Experimental Investigation of Heat Transfer during Evaporation in the Vicinity of Moving Three-Phase Contact Lines

Zur Erlangung des akademischen Grades Doktor-Ingenieur (Dr.-Ing.)
genehmigte Dissertation von Dipl.-Ing. Sebastian Fischer aus Wiesbaden
März 2015 — Darmstadt — D 17

TECHNISCHE
UNIVERSITÄT
DARMSTADT

Fachbereich Maschinenbau
Institut für Technische Thermodynamik

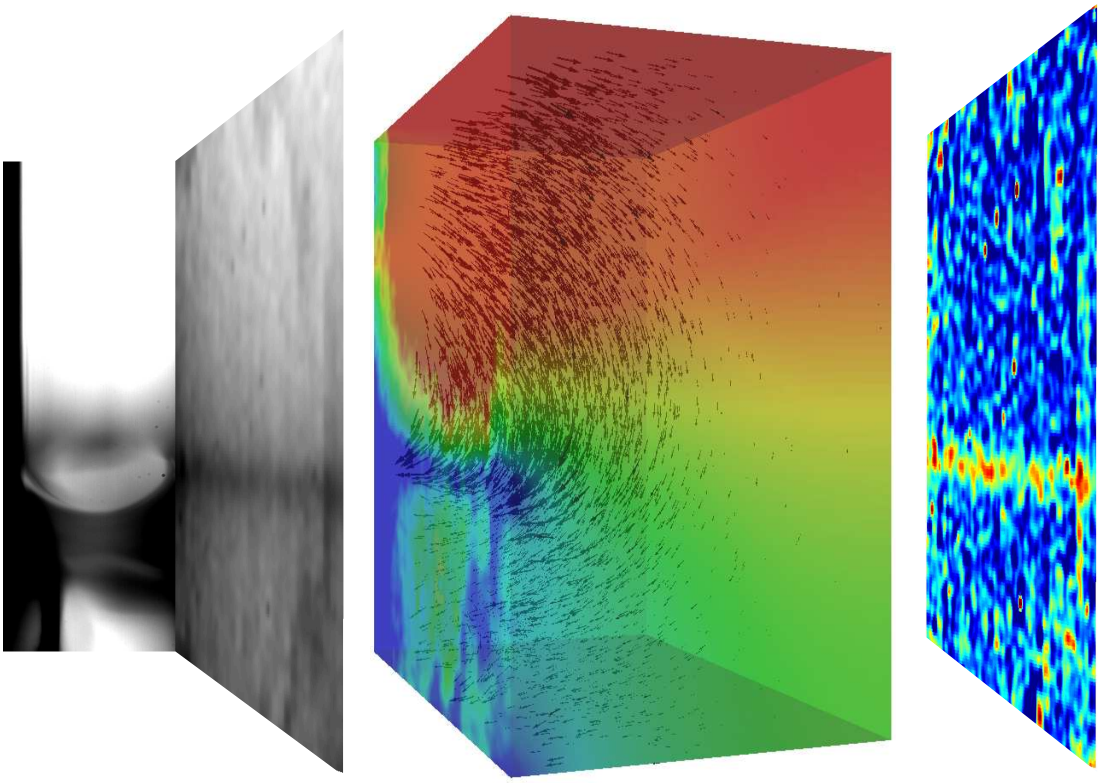

Experimental Investigation of Heat Transfer during Evaporation in the Vicinity of Moving Three-Phase Contact Lines
Technische Universität Darmstadt, Fachbereich Maschinenbau
Zur Erlangung des akademischen Grades Doktor-Ingenieur (Dr.-Ing.)

Genehmigte Dissertation von Dipl.-Ing. Sebastian Fischer aus Wiesbaden

1. Gutachten: Prof. Dr.-Ing. Peter Stephan
2. Gutachten: Prof. Dr.-Ing. Michael Dreyer

Tag der Einreichung: 02.10.2014
Tag der Prüfung: 04.02.2015

Darmstadt, 2015 — D 17

Bitte zitieren Sie dieses Dokument als:
URN: urn:nbn:de:tuda-tuprints-43961
URL: http://tuprints.ulb.tu-darmstadt.de/4396

Erklärung zur Dissertation

Hiermit versichere ich, die vorliegende Dissertation ohne Hilfe Dritter nur mit den angegebenen Quellen und Hilfsmitteln angefertigt zu haben. Alle Stellen, die aus Quellen entnommen wurden, sind als solche kenntlich gemacht. Diese Arbeit hat in gleicher oder ähnlicher Form noch keiner Prüfungsbehörde vorgelegen.

Darmstadt, den 02. März 2015

(Sebastian Fischer)

Abstract

The subject of the present work is heat transfer close to moving three-phase contact lines. The term three-phase contact line designates the area in which the liquid/vapour- or liquid/gas-interface approaches a solid wall. Due to the small thermal resistance of the extremely thin liquid film high heat fluxes are reached within this area. These can have significant influence onto the overall heat transfer process within two-phase systems. Examples of such systems are pool and flow boiling, droplet evaporation during spray cooling applications or heat pipes used for high power electronics cooling. The more the interface approaches to the heated wall, the stronger the influence of intermolecular interactions between wall molecules and those at the liquid/vapour-interface onto the local phase equilibrium becomes. This results in a shift of the equilibrium to higher temperatures, so that local evaporation is entirely inhibited through intermolecular forces at a certain minimum liquid film thickness. A few molecule layers thin liquid film that cannot be evaporated remains on the apparently dry surface. Apart from the wall superheat, the direction of contact line movement and its velocity, as well as the system pressure influence the local heat transfer in the contact line area decisively. While there is some experimental work on the influence of contact line velocity and its movement direction, the influence of system pressure has remained uninvestigated up to date. Aim of this work is therefore a target oriented experimental investigation of the pressure and velocity influence on heat transfer in the proximity of moving three-phase contact lines.

Core of the dedicated experiment setup is an infrared transparent heater element, which provides the possibility to measure the temperature fields at the heater/fluid interface with high spatial and temporal resolution using infrared thermography. The heater developed for this purpose consists of an infrared transparent substrate, onto which a two-layer composition of black Chromium Nitride and pure Chromium with an overall thickness of approximately 800 nm is applied through Physical Vapour Deposition. While the black Chromium Nitride layer enhances the surface emissivity and thereby increases the signal-to-noise-ratio of the IR thermography drastically, the pure Chromium is employed as resistance heater to achieve the wall superheat necessary for evaporation. As experiment fluid degassed FC-72 (n-perfluorohexane) is used. Within the experiment setup a single capillary slot with a width of 1.4 mm is created between the infrared transparent heater and a polished copper wall. Liquid rises between the walls of the slot due to capillary forces and forms a single extended meniscus. The system pressure is adjusted through the saturation state of the fluid by variation of the system temperature, while the movement of the meniscus is realized through a volume displacement within the system. Movement of the meniscus results in an advancing or a receding contact line situation at the surface of the IR transparent heater, that influences the local temperature distribution at the heater wall. The temperature distribution on the backside of the Chromium Nitride layer at a distance of less than 1 μm away from the heater/fluid-interface is measured with a high speed IR camera at a framerate of 1000 Hz and a resolution of 29.27 μm/pixel. The high speed IR camera is synchronized to a high speed black-and-white camera, that allows detection of the liquid/vapour-interface with a resolution of 4 μm/pixel. From the temperature fields the local heat flux distribution is calculated numerically with the same spatial and temporal resolution.

Experiments were performed at reduced pressures in the range of $p_\mathrm{R} = 0.05$ to $p_\mathrm{R} = 0.7$ and with liquid/vapour-interface velocities of up to $v_\mathrm{int} = \pm 40\,\mathrm{mm/s}$. Comparisons to earlier experiments on three-phase contact line heat transfer show, that the results obtained using thin foil heaters are transferable to heaters with substantial larger thermal inertia, like the IR transparent heaters used within this work. Merely the extremely high temperature differences, that are present in proximity of

the contact line, are significantly smaller on walls with higher thermal inertia.

The conducted experiments clearly show a local heat flux peak in proximity of the contact line, which is accompanied by a local temperature minimum. At increased system pressure and equal wall superheat and contact line velocity, the local heat flux peak at the contact line decreases with increasing pressure. This effect can be attributed to the reduction of latent heat of evaporation with increasing pressure.

Considering the influence of the contact line velocity, one must distinguish between advancing and receding contact lines. At a receding contact line and equal reduced pressure and wall superheat, no influence of the contact line velocity onto the local heat flux distribution in proximity of the contact line is discernible. At an advancing contact line on the other hand, an increase of the heat flux maximum at the wall and thereby the heat transfer in proximity of the contact line with increasing contact line velocity is observed. Both the increase of the heat flux maximum with increasing contact line velocity at an advancing contact line and the independence of the maximum heat flux on the contact line velocity at a receding contact line is observed at low and high levels of the reduced pressure.

In some experiments with negative meniscus velocity (and therefore receding contact line) it was observed, that a thin, evaporating liquid film can be deposited on the heater surface by the moving liquid/vapour-interface. If and to which extend the thin film is deposited, depends on the wall superheat, the velocity and acceleration of the liquid/vapour-interface, the latent heat of evaporation of the fluid and the wetting characteristics of the heated wall. Furthermore it was observed, that film rupture due to instabilities can occur. If the thin film was present, the contribution of thin film evaporation to the overall heat transfer was dominating compared to the contribution of contact line heat transfer. This makes it necessary to describe the thin film with a model, if it appears during an evaporation process in order to capture the underlying physics correctly.

Based on an estimation of the thickness of a liquid film staying behind on a wall drawn out of a quiescent liquid by Landau and Levich, a model for stationary thin film evaporation was developed. It is assumed, that thin film evaporation has no influence onto the initial film thickness, so it can be calculated according to Landau and Levich. Starting from the mass and energy balance at an infinitesimal thin segment of the film, an equation for the film thickness gradient in direction parallel to the wall is derived. By making the equation dimensionless, non-dimensional quantities governing thin film evolution are identified.

Comparison of the length of the thin film region calculated using the model to lengths of the thin film region observed in the experiment shows good agreement up to a certain velocity, at which an increasing deviation between theoretical value and experimental data is observed. This deviation is probably caused by the limited length of the IR transparent heater, which does not allow for reaching steady state thin film evaporation.

Kurzzusammenfassung

Thema der vorliegenden Arbeit ist die Wärmeübertragung in unmittelbarer Umgebung bewegter Drei-Phasen Kontaktlinien. Als Drei-Phasen Kontaktlinie wird der Bereich bezeichnet, in dem sich die Flüssigkeits/Dampf- oder Flüssigkeits/Gas-Phasengrenze einer Wand annähert. Aufgrund des geringen Wärmewiderstands des enorm dünnen Flüssigkeitsfilms in diesem Bereich werden hier extrem hohe Wärmestromdichten erreicht. Diese können daher einen maßgeblichen Anteil am übertragenen Gesamtwärmestrom innerhalb zweiphasiger Systeme haben. Beispiele solcher Systeme sind unter anderem die Wärmeübertragung mittels Behälter- und Strömungssieden, die Tropfenverdampfung in Sprühkühlungsanwendungen oder aber die Verdampfung in Wärmerohren, welche zur Kühlung elektronischer Hochleistungsbauteile eingesetzt werden. Je dichter sich die Phasengrenze der Heizerwand annähert, umso stärker wird das lokale Phasengleichgewicht durch intermolekulare Wechselwirkungen zwischen den Wandmolekülen und jenen an der Phasengrenze beeinflusst. Dies führt zu einer Verschiebung des Gleichgewichtszustandes hin zu höheren Temperaturen, so dass ab einer minimalen Flüssigkeitsfilmdicke die intermolekularen Kräfte die lokale Verdampfung vollständig verhindern. Ein wenige Moleküllagen dünner adsorbierter Flüssigkeitsfilm bleibt auf der scheinbar trockenen Oberfläche, der nicht verdampft werden kann. Neben der Wandüberhitzung haben insbesondere die Bewegungsrichtung und die Geschwindigkeit, mit der sich die Kontaktlinie fortbewegt, als auch der Systemdruck einen ausschlaggebenden Einfluss auf den lokalen Wärmeübergang im Kontaktlinienbereich. Während es bereits einige experimentelle Arbeiten zum Einfluss der Kontaktliniengeschwindigkeit und Bewegungsrichtung gibt, ist der Einfluss des Systemdrucks bislang unerforscht. Das Ziel der vorliegenden Arbeit ist daher, den Einfluss des Systemdrucks und der Kontaktliniengeschwindigkeit auf die lokale Wärmeübertragung an bewegten Drei-Phasen Kontaktlinien gezielt zu untersuchen.

Kern des hierfür konstruierten Versuchsaufbaus stellt ein infrarot-transparenter Heizer dar, der es ermöglicht, zeitlich und örtlich hoch aufgelöste Temperaturfelder an der Heizer/Fluid-Grenzfläche mittels Infrarot-Thermografie zu messen. Der hierfür entwickelte Heizer besteht aus einem infrarot-transparenten Substrat, auf das ein Zwei-Schichten-System aus schwarzem Chromnitrid und reinem Chrom mit einer Gesamtdicke von ca. 800 nm mittels Physical Vapour Deposition aufgebracht wird. Während die schwarze Chromnitridschicht die Emissivität der Oberfläche erhöht und dadurch das Signal/Rausch-Verhältniss der IR-Thermografie deutlich verbessert, dient die reine Chromschicht als Widerstandsheizer, um die für die Verdampfung notwendige Wandüberhitzung zu erreichen. Als Versuchsfluid wird entgastes FC-72 (n-Perfluorohexan) verwendet. In der Versuchsanlage werden die Wände eines Kapillarspalts mit einer Breite von 1.4 mm von dem infrarot-transparenten Heizer und einer polierten Kupferwand gebildet. Zwischen diesen beiden Wänden steigt das Versuchsfluid aufgrund von Kapillarkräften und bildet einen Einzelmeniskus aus. Durch Variation der Systemtemperatur wird der Systemdruck über den Sättigungszustand des Fluids eingestellt, während die Bewegung des Meniskus mittels einer Volumenverschiebung innerhalb des Systems realisiert wird. Die Meniskusbewegung erzeugt auf der Oberfläche des IR transparenten Heizers eine voranschreitende oder eine zurückschreitende Kontaktlinie, welche die lokale Temperaturverteilung an der Heizerwand beeinflusst. Die Temperaturverteilung auf der Rückseite der Chromnitridschicht, also weniger als 1 μm von der Heizer/Fluid-Grenzfläche entfernt, wird mit einer Hochgeschwindigkeits-IR-Kamera mit einer Bildfrequenz von 1000 Hz und einer räumlichen Auflösung von 29.27 μm/Pixel vermessen. Die Hochgeschwindigkeits-IR-Kamera ist mit einer Hochgeschwindigkeits-Schwarz/Weiß-Kamera synchronisiert, welche die Detektierung der Phasengrenze mit einer räumlichen Auflösung von 4 μm/Pixel ermöglicht. Aus dem Temperaturfeld wird auf numerischem Weg die lokale Wärmestromdichte mit

gleicher zeitlicher und örtlicher Auflösung berechnet.
Es wurden Messungen bei reduzierten Drücken im Bereich von $p_{\mathrm{R}} = 0.05$ bis $p_{\mathrm{R}} = 0.7$ und bei Geschwindigkeiten der Phasengrenze von bis zu $v_{\mathrm{int}} = \pm 40\,\mathrm{mm/s}$ durchgeführt. Im Vergleich mit früheren Experimenten zur Wärmübertragung an Drei-Phasen Kontaktlinien zeigt sich, dass die mithilfe von dünnen Folienheizern gewonnen Erkenntnisse auf Heizer mit deutlich höherer thermischer Kapazität, wie den in dieser Arbeit verwendeten IR transparenten Heizer, übertragbar sind. Lediglich die auf Folienheizern enorm stark ausgeprägten Temperaturdifferenzen, die in der Umgebung der Kontaktlinie auftreten, treten an Wänden mit höherer thermischer Kapazität deutlich vermindert auf.
Die Ergebnisse der durchgeführten Versuche zeigen klar ein lokales Maximum der Wärmestromdichte im Bereich der Kontaktlinie, welches mit einem lokalen Temperaturminimum einher geht. Bei erhöhtem Systemdruck, jedoch gleicher Wandüberhitzung und Kontatktliniengeschwindigkeit verringert sich die lokale Überhöhung der Wärmestromdichte in Kontaktliniennähe zunehmend mit ansteigendem Druck. Dies ist auf die Verringerung der Verdampfungsenthalpie des Versuchsfluids mit steigendem Druck zurückzuführen.
Was den Einfluss der Geschwindigkeit, mit der sich die Kontaktlinie fortbewegt, anbelangt, muss zwischen voranschreitender und zurückschreitender Kontaktlinie unterschieden werden. Bei zurückschreitender Kontaktlinie und gleichem reduziertem Druck und Wandüberhitzung, ist kein Einfluss der Kontaktliniengeschwindigkeit auf den Verlauf der lokalen Wärmestromdichte festzustellen. Bei voranschreitender Kontaktlinie dagegen steigt das Maximum der lokalen Wärmestromdichte an der Wand und damit der in Kontaktliniennähe übertragene Gesamtwärmestrom mit zunehmender Kontaktliniengeschwindigkeit an. Sowohl der Anstieg der maximalen Wärmestromdichte mit steigender Kontaktliniengeschwindigkeit bei voranschreitender Kontaktlinie, als auch die Unabhängigkeit der maximalen Wärmestromdichte von der Kontaktliniengeschwindigkeit bei zurückschreitender Kontaktlinie wurden bei geringen und hohen Werten des reduzierten Drucks beobachtet.
Es hat sich in einigen Experimenten gezeigt, dass es bei negativer Meniskusgeschwindigkeit (also zurückschreitender Kontaktlinie) zu der Ausprägung eines dünnen, verdampfenden Flüssigkeitsfilms auf der Heizeroberfläche kommen kann. Ob und in welchem Maß sich der dünne Film ausprägt, hängt dabei von der Wandüberhitzung, der Geschwindigkeit und Beschleunigung mit der sich die Phasengrenze bewegt, der Verdampfungsenthalpie des Fluids und Benetzungseigenschaften der beheizten Wand ab. Des Weiteren wurde beobachtet, dass es zum Aufreißen des Films aufgrund von Instabilitäten kommen kann. Wenn der dünne, verdampfende Flüssigkeitsfilm auftrat, so war der Anteil der Dünnfilmverdampfung am Gesamtwärmestrom dominierend gegenüber dem Anteil der Kontaktlinienverdampfung. Daraus entsteht die Notwendigkeit, den dünnen Flüssigkeitsfilm mit einem Modell zu beschreiben, wenn er innerhalb eines Verdampfungsprozesses auftritt, um dessen physikalische Grundlagen korrekt zu erfassen.
Aufbauend auf der Abschätzung der Dicke eines Flüssigkeitsfilms, welcher auf einer Wand zurückbleibt, wenn diese aus einem Behälter mit ruhender Flüssigkeit gezogen wird, nach Landau und Levich, wurde ein Modell für die stationäre Dünnfilmverdampfung entwickelt. Es wird angenommen, dass die Dünnfilmverdampfung keinen Einfluss auf die initiale Filmdicke hat, so dass diese nach Landau und Levich berechnet werden kann. Ausgehend von der Massen- und Energiebilanz an einem infinitesimal schmalen Filmsegment in einem mit dem Meniskus bewegten Bezugssystem, wird unter einigen Annahmen eine Bestimmungsgleichung für den Gradienten der Filmdicke parallel zur Heizerwand hergeleitet. Durch Entdimensionierung dieser Gleichung wurden dimensionslose Größen bestimmt, welche den Filmdickenverlauf beeinflussen.
Ein Vergleich der mittels Modell bestimmten Länge des Dünnfilms mit im Experiment aufgetretenen Dünnfilmlängen zeigt gute Übereinstimmung bis zu einer Grenzgeschwindigkeit, ab der eine zunehmende Abweichung zwischen Modell und Experiment festzustellen ist. Diese Abweichung lässt sich mit hoher Wahrscheinlichkeit auf die begrenzte Länge des IR transparenten Heizers zurückführen, was das Erreichen eines stationären Dünnfilmverdampfungszustands nicht ermöglicht.

Vorwort

Diese Arbeit entstand während meiner Tätigkeit als Wissenschaftlicher Mitarbeiter am Institut für Technische Thermodynamik der Technischen Universität Darmstadt. Mein besonderer Dank gilt Herrn Prof. Dr.-Ing. Peter Stephan, der mir als Leiter des Fachgebiets nicht nur die finanziellen und technischen Möglichkeiten zum Abschluß der vorliegenden Dissertation zur Verfügung stellte, sondern mir darüber hinaus ermöglichte durch die Umsetzung eigener Ideen zum aktuellen Stand der Forschung beizutragen. Neben einem Höchstmaß an persönlichen Freiräumen und Eigenverantwortlichkeit in der Forschung, die er mir einräumte und die ich als enorm positiv empfand, war er auch stets ein Anlaufpunkt für Anregungen und fachliche Diskussionen. In diesem Zusammenhang danke ich ebenfalls der Deutschen Forschungsgemeinschaft, die die Entstehung dieser Arbeit im Rahmen des Sonderforschungsbereichs Transregio SFB-TRR 75 “Tropfendynamische Prozesse unter extremen Umgebungsbedingungen” finanziert hat. Ebenso gilt mein Dank Priv.-Doz. Dr.-Ing. habil. Tatiana Gambaryan-Roisman, die ebenfalls stets zu fruchtbaren fachlichen Diskussionen bereit war, und Herrn Prof. Dr.-Ing. Michael Dreyer, für seine Bereitschaft die Stelle des Ko-Referenten der vorliegenden Arbeit einzunehmen.

Des Weiteren möchte ich allen aktuellen und ehemaligen Kollegen des Instituts danken, die mir stets hilfreich zur Seite gestanden haben. Ohne ihr Engagement und ihre tatkräftige Unterstützung wären aufwändige Projekte, wie z. B. die Organisation von Parabelflugkampagnen, nicht möglich gewesen. Insbesondere gilt mein Dank Stefan Batzdorf, der mich mit seiner Expertise im CFD-code OpenFOAM® massiv in der Entwicklung der numerischen Wärmestromdichteberechnung unterstützt hat. Ihm und Martin Freystein danke ich besonders dafür, dass sie sich bereit erklärt haben diese Arbeit Korrektur zu lesen. Eine weitere besondere Erwähnung verdient Nils Schweizer, von dem ich während meiner Zeit als Student am TTD enorm viel über experimentelles Arbeiten gelernt habe. Auch möchte ich der Institutswerkstatt und insbesondere deren Leiter Roland Berntheisel danken. Ohne ihre tatkräftige Unterstützung und ihren fachlichen Rat, wenn es um die Fertigung von Versuchsaufbauten geht, wäre zielgerichtetes experimentelles Arbeiten am Institut undenkbar.

Während meiner Zeit am TTD entwickelte sich eine fruchtbare Zusammenarbeit mit dem Institut für Werkstoffkunde, aus der unter anderem die Entwicklung des in dieser Arbeit verwendeten infrarottransparenten Heizerelements hervorgegangen ist. Neben dem Leiter des Instituts Herrn Prof. Dr.-Ing. Matthias Oechsner und dem Fachverantwortlichen des Kompetenzfeldes Funktionelle Oberflächentechnik Herrn Dr. rer. nat. Herbert Scheerer, die der Möglichkeit einer Zusammenarbeit sehr aufgeschlossen gegenüber standen, möchte ich vor allem Elena Slomski für die gute Zusammenarbeit und ihre tatkräftige Unterstützung bei der Konzeption und der Herstellung der Heizerbeschichtungen danken.

Auch möchte ich allen HiWis und Studenten danken, die ich während meiner Zeit am Institut betreut habe und die sowohl beim Aufbau und der Durchführung von Experimenten, als auch bei deren Auswertung eine große Hilfe waren.

Nicht zuletzt möchte ich meiner Familie und insbesondere meinen Eltern danken. Ohne ihren Rückhalt und ihre Unterstützung wäre die Anfertigung dieser Arbeit nicht möglich gewesen.

Contents

Nomenclature

Latin Characters

a	acceleration	[m/s^2]
A	surface	[m^2]
A_{12}	Hamaker Constant	[J]
C_6, C_{12}	constants of the Lennard-Jones-Potential	[J m^6] [J m^{12}]
c	thermal capacity	[J kg^{-1} K^{-1}]
c_p	thermal capacity at constant pressure	[J kg^{-1} K^{-1}]
$\overline{c}_p$	molar thermal capacity at constant pressure	[J kmol^{-1} K^{-1}]
$\overline{c}_v$	molar thermal capacity at constant volume	[J kmol^{-1} K^{-1}]
d	diameter	[m]
$\dot{E}$	energy flow per unit depth	[W m^{-1}]
E_{surface}	energy per surface area	[J m^{-2}]
f	accommodation coefficient	[ ]
$f_{\text{IR,B/W}}$	camera framerate	[s^{-1}]
g	gravitational acceleration on earth	[m s^{-2}]
h	heat transfer coefficient	[W m^{-2} K^{-1}]
Δh_v	latent heat of evaporation	[J kg^{-1}]
I	electric current	[A]
I_{dig}	digital intensity representation	[ ]
J	radiative energy flow	[W]
j	radiative energy flux	[W m^{-2}]
k	absorption coefficient	[m^{-1}]
l	length	[m]
$\overline{M}$	molar mass	[kg kmol^{-1}]
$\dot{M}$	mass flow per unit depth	[kg s^{-1} m^{-1}]
m	mass flux	[kg m^{-2} s^{-1}]
n	index of refraction	[ ]
p	pressure	[Nm^{-2}]
q	heat flux	[W m^{-2}]
r	radius	[m]
R	electrical resistance	[Ω]
R_{int}	interfacial thermal resistance	[K m^2 W^{-1}]
$\overline{R}$	universal gas constant	[J kmol^{-1} K^{-1}]

T	temperature	[K]
t	temperature	[°C]
U	voltage	[V]
v	velocity	[m s^{-1}]
$\overline{V}$	molar volume	[m^3 $kmol^{-1}$]
w	width	[m]
Δx_{res}	resolution	[m $pixel^{-1}$]
x, y, z	coordinates	[m],[pixel]
Z	compressibility factor	[ ]

Greek Characters

α	thermal diffusivity	[m^2 s^{-1}]
δ	liquid film thickness	[m]
Γ	inverse thermal conductivity	[m K W^{-1}]
$\varepsilon_{\mathrm{rad}}$	emissivity	[ ]
η	coordinate perpendicular to the heater surface	[m]
κ	interface curvature	[m^{-1}]
λ	thermal conductivity	[W m^{-1} K^{-1}]
$\tilde{\mu}$	chemical potential	[J kg^{-1}]
μ	dynamic viscosity	[Pa s^{-1}]
ν	kinematic viscosity	[m^2 s^{-1}]
Π_{LJ}	Lennard-Jones-Potential	[eV]
θ	apparent contact angle	[°]
ρ	density	[kg m^{-3}]
ρ_{rad}	reflectivity	[ ]
σ	surface tension	[N m^{-1}]
σ_{SB}	Stefan-Boltzmann constant	[W m^{-2} K^{-4}]
τ	time	[s]
τ_{rad}	transmittance	[ ]
ω	accentric factor	[ ]
Ω_{v}	viscosity collision integral	[ ]
ξ	coordinate parallel to the heater surface	[m]

Dimensionless Numbers

$\mathrm{Bo} = \frac{(\rho_\mathrm{l} - \rho_\mathrm{v}) g {l_0}^2}{\sigma}$	Bond number
$\mathrm{Ca} = \frac{\nu \rho v_0}{\sigma}$	Capillary number
$\mathrm{Co} = \frac{\Delta\tau_\mathrm{num} v_0}{\Delta x_\mathrm{num}}$	Courant number
$\mathrm{Ja} = \frac{c_{p,\mathrm{l}}(T_\mathrm{W} - T_\mathrm{sat})}{\Delta h_v}$	Jakob number
$\mathrm{Nu} = \frac{h l_0}{\lambda}$	Nusselt number
$\mathrm{Pr} = \frac{\nu}{\alpha}$	Prandtl number
$\mathrm{Re} = \frac{v_0 l_0}{\nu}$	Reynolds number
$\mathrm{We} = \frac{\rho {v_0}^2 l_0}{\sigma}$	Weber number

Indices

0	reference
1.4301	stainless steel alloy 1.4301 (X 5 CrNi 18-10)
20°C	at 20 °C
abs	absolute
av	averaged
B/W	high speed black and white camera
CaF	calcium fluoride
calc	calculated
CL	contact line
cond	condensation
crit	critical
Cr	chromium
CrN	chromium nitride
D	droplet
DAQ	data acquisition system
det	detected
dis	disjoining
eq	equilibrium
evap	evaporation
exp	experimental
hl	heating layer
in	input
int	liquid/vapour-interface
IR	high speed infrared camera
l	liquid
LJ	Lennard-Jones
loss	due to losses
lp	line profile (averaged in x-direction)

max	maximal
mic	micro-region
min	minimal
NBP	at normal boiling point (1013 mbar)
num	numerical
pix	pixel
PS	power supply
Pt100	measured by Pt100
R	reduced (ratio of value / value at the crit. point)
rec	recoil
rel	relative
ref	reference fluid
sat	at saturation
sim	simple fluid
StM	stepper motor
sur	surroundings
TC	measured by thermocouple
theory	theory
v	vapour
W	at the heater wall

List of Acronyms

ACL	advancing contact line
BC	boundary condition
B/W	black and white
CaF_2	calcium fluoride
CCD	charge-coupled device
CFD	computational fluid dynamics
CNES	Centre National D'Études Spatiales
Cr	chromium
CrN	chromium nitride
CVB	constrained vapour bubble
DAQ	data acquisition system
DKD	Deutscher Kalibrierdienst
DLR	Deutsches Zentrum für Luft- und Raumfahrt
ESA	European Space Agency
FOV	field of view
HF	heat flux
IR	infrared
ITO	indium tin oxide
JEPPF	Joint European Partial-g Parabolic Flight Campaign
LIF	laser induced fluorescence
LWIR	long-wave infrared
MPA-IfW	Staatliche Materialprüfungsanstalt Darmstadt, Fachgebiet und Institut für Werkstoffkunde, Technische Universität Darmstadt
MWIR	mid-wave infrared

NMCL	non-moving contact line
NBP	normal boiling point
NETD	noise equivalent temperature difference
NEHFD	noise equivalent heat flux difference
ODE	ordinary differential equation
PEEK	poly-ether-ether-ketone
PIV	particle image velocimetry
PMMA	polymethylmethacrylat
Pt100	Platinum temperature sensor, 100 Ω resistance at 0 °C
PVD	physical vapour deposition
RCL	receding contact line
RGB	red-green-blue color triples
ROI	region of interest
StM	stepper motor
SWIR	short-wave infrared
TC	thermocouple
TEC	thermoelectric cooler
TLC	thermochromic liquid crystal
TTD	Institut für Technische Thermodynamik, Technische Universität Darmstadt

1 Introduction

1.1 Motivation

Moving three-phase contact lines are present in many physical processes in numerous technical applications. The term three-phase contact line describes the apparent intersection of liquid/gas-interface, liquid/solid-interface and solid/gas-interface. Examples, where moving contact lines are coupled to heat transfer, are pool and flow boiling apparatuses, where contact line movement occurs during bubble growth and detachment at the heated wall; heat pipes, where contact line movement can be induced by deviations of the cooling or heating power; or spray cooling, where the impingement of droplets results in moving contact lines. This small excerpt of technical applications shows that heat transfer involving moving three-phase contact lines can be found in a wide variety of macroscopic configurations.

In figure 1.1 two such configurations, namely pool boiling and spray cooling, are shown. To accurately model and predict the overall heat transfer of such macroscopic systems, one must be able to model heat transfer on the scale of single bubbles or droplets. However, heat transfer on that scale is in many cases largely influenced by heat transfer on the microscale close to the three-phase contact line, making it essential to understand and model the phenomena on this microscale. As shown in figure 1.1, the apparent three-phase contact line vanishes on this scale and is replaced by a transition region, which is more closely described in chapter 2.1.

The most interesting aspect that can be seen in figure 1.1 is, that even though the two systems shown (and several other systems that are not further addressed at this point) are macroscopically quite

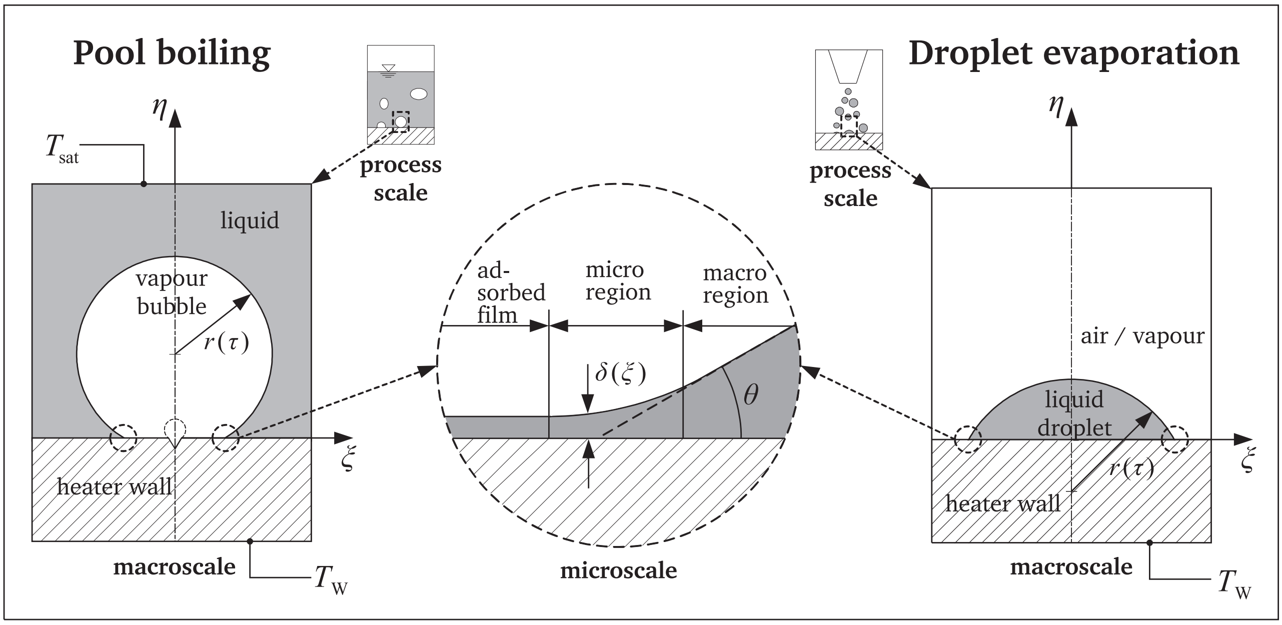

Figure 1.1.: Problem scales of pool boiling and spray cooling

dissimilar, the microscale system influencing them dramatically is not only similar, but entirely equal. The multiscale character of such problems involving moving three-phase contact lines makes it difficult to model them theoretically and numerically, especially since the phenomena on contact line scale are still not sufficiently understood. Therefore, a better understanding of heat transfer on contact line scale and the dominating influences onto it have the potential to allow a more target-oriented design of technical applications involving them. As a consequence an increase of the application efficiency and a reduction of consumption of resources can be reached.

Macroscopically the liquid film thickness seems to approach zero at the three-phase contact line. When evaporative heat transfer is involved, this would lead to a vanishing thermal resistance between the solid heater wall and the liquid/vapour-interface resulting in an infinite heat flux, assuming homogeneous wall superheat compared to the saturation temperature. Microscopically however, the apparent three-phase contact line is merely a transition region between the macroscopic liquid film and an adsorbed liquid film governed by intermolecular forces between the liquid and the solid heater wall [1]. The intermolecular forces between the wall molecules and the interface of the adsorbed liquid film shift the phase equilibrium to higher saturation temperatures, thereby inhibiting its evaporation. The transition region, which is visible as apparent three-phase contact line, is characterized by an increasing thickness of the liquid film and a local strong curvature of the liquid/vapour-interface. In this “interline region” [2] or “micro region” [3], the intermolecular forces between the liquid and the solid heater wall strongly decrease with increasing film thickness, so that molecules at the interface can be evaporated. As the liquid film is still relatively thin in this region (and thereby provides a low thermal resistance between heater wall and liquid/vapour-interface compared with the liquid bulk region), high local evaporation rates are reached. Due to the strong local curvature a pressure gradient is generated that leads to a liquid flow from the liquid bulk into the micro region. With increasing thickness of the liquid film, the thermal resistance between heater wall and liquid/vapour-interface increases, which leads to a decrease of the heat flux when approaching the bulk- or macro-region. When the contact line is moving, a macroscopic flow is superimposed. In case of an advancing contact line, the flow sucks cold liquid into the contact line area enhancing local heat transfer from the wall to the fluid by transient thermal conduction. In case of a receding meniscus, the flow transports hot liquid from the wall to the liquid/vapour-interface, which enhances evaporation at the interface, but does not enhance wall heat transfer through transient conduction [4].

While the influence of pressure onto boiling systems on the macroscale has been extensively studied, its influence onto the local heat transfer at the three-phase contact line is still widely unknown. Especially when approaching the critical point, the surface tension decreases, leading to a thickening of the liquid/vapour-interface. But apart from surface tension, changing the saturation pressure has tremendous influence onto almost any fluid property in a saturated system. The change of fluid properties can be expected to lead to a change in contact line heat transfer. The overall effect however is very difficult to predict and must be investigated experimentally.

Such an investigation could be carried out on single bubbles or droplets. Yet, during boiling or drop impingement, contact line movement is induced by macroscopic bubble or droplet dynamics, making it very hard to control contact line movement and to focus solely on the effects in proximity of the contact line. Furthermore the extension of the contact line in such systems is rather small. To solely investigate the effect of pressure onto contact line heat transfer, an experiment is therefore needed, in which a three-phase contact line can be observed as isolated as possible. In a single meniscus configuration, two extended contact lines are formed on the walls of the channel, between which the meniscus is formed. Movement of the contact line can be controlled through movement of the meniscus. A generic experiment focusing onto a single capillary slot, in which such a single meniscus with an extended contact line is formed, is therefore the main topic of the present thesis.

1.2 Structure of the thesis

In the following section a short summary of the content and the scope of the chapters of the present thesis is given:

Chapter 1
This chapter contains a short introduction of contact line heat transfer. It is shortly explained, why contact line heat transfer is of importance in many phase change processes, e.g. pool boiling and drop impingement. In advance of the following chapter, the concept of including intermolecular forces in contact line modeling to avoid a singularity when evaporative heat transfer is involved is introduced. It is hypothesized that a change of the system pressure has an influence onto contact line heat transfer, which has not been the focus of an experimental study, yet.

Chapter 2
The theory of heat transfer at three-phase contact lines and the consequent state-of-the-art modeling approach is closer described in the first section of this chapter. Details on the origin and the effect of intermolecular forces that play an important role in the contact line region are provided. This is followed by a literature review of experimental work conducted on contact line heat transfer. From the literature review, open scientific questions and ensuing objectives of this thesis are formulated. An evaluation of available temperature measurement techniques with respect to the measurement task at hand is given.

Chapter 3
Chapter 3 focuses on the experiment concept and the design of the experiment heater, which is a direct consequence of the main measurement method chosen at the end of chapter 2. The experiment setup and procedure are introduced along with the parameter space, in which experiments have been conducted. The applied measurement methods are described along with data treatment and data reduction techniques.

Chapter 4
In chapter 4 the final results of this thesis are presented. Main focus of the results are the influence of the system pressure and the influence of the contact line velocity. During some experiments, a thin evaporating film has been observed, that was deposited on the heater surface by the receding liquid/vapour-interface. As this heat transfer mode could be of major importance, a comparative analysis is carried out to determine primary influence factors for generation and sustainment of such a thin film. Based on the influence factors, the development of an analytical model for thin film evaporation is described. The results of this model are compared to experimental data.

Chapter 5
The content of the thesis and the main findings are summarized in this chapter. An outlook on possible future experiments and enhancements of the model presented in chapter 4 is given.

2 State of the art

2.1 Theory of heat transfer at the three-phase contact line

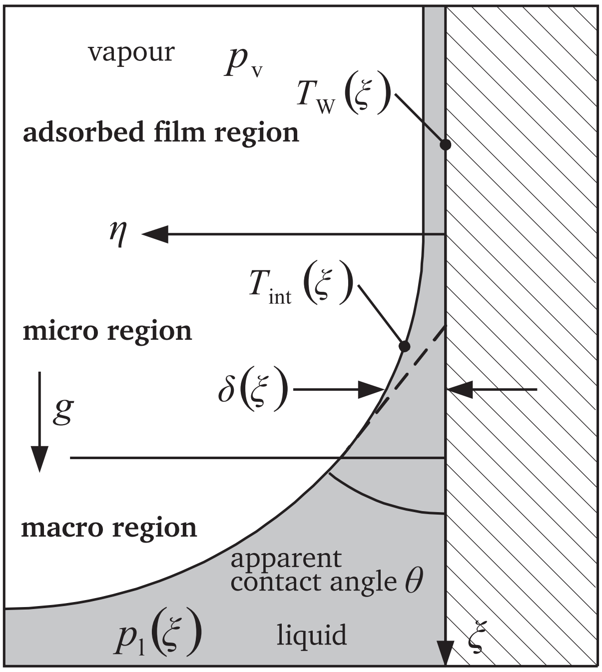

Figure 2.1.: Theoretical model of the three-phase contact line on a vertical surface

In figure 2.1 the two-dimensional model representation of a three-phase contact line is shown. The point of origin of the coordinate system is set to the heater surface at the end of the adsorbed film region, where the curvature $\kappa(\xi)$ of the liquid/vapour-interface starts to deviate from zero. The ξ-coordinate runs parallel to the wall and the η coordinate normal to the wall. The interface position is given by the local liquid film thickness $\delta(\xi)$, which is a function of the ξ-coordinate. While in the micro region the gradient of curvature is rather high, the curvature approaches the constant bulk value at its end, where the curvature gradient approaches zero. The slope of the interface at this point gives the apparent contact angle θ, as the thin liquid film in the micro- and the adsorbed film region is too thin to be visible on the macroscopic scale.

An important dimensionless number in capillary flows is the Bond number

$$\mathrm{Bo} = \frac{(\rho_\mathrm{l} - \rho_\mathrm{v})\, g {l_0}^2}{\sigma}, \tag{2.1}$$

which represents the ratio of gravitational forces to surface tension forces. When the characteristic length scale l_0 is small, as it is the case for contact line heat transfer, gravitational forces are negligible and are therefore not included in the following equations.

2.1.1 Transport phenomena

In order to be in thermodynamic equilibrium, the following conditions must be met by the liquid and the vapour phase [5]

$$T_\mathrm{l} \overset{!}{=} T_\mathrm{v}\ ,\ p_\mathrm{l} \overset{!}{=} p_\mathrm{v}\ ,\ \tilde{\mu}_\mathrm{l} \overset{!}{=} \tilde{\mu}_\mathrm{v}. \tag{2.2}$$

For a curved interface, the criterion of equal pressures in liquid and vapour phase is altered due to the surface tension, resulting in the Young-Laplace equation

$$\Delta p = p_\mathrm{v} - p_\mathrm{l} = \sigma\kappa, \tag{2.3}$$

which must be fulfilled at the whole interface. In this equation σ is the surface tension and κ is the curvature of the interface. As in the observed case the three-phase contact line of the meniscus is a straight line, the curvature can be expressed by the derivatives of the liquid film thickness [6]

$$\kappa = \frac{\frac{\mathrm{d}^2\delta}{\mathrm{d}\xi^2}}{\left[1 + \frac{\mathrm{d}\delta}{\mathrm{d}\xi}^2\right]^{3/2}}. \tag{2.4}$$

One can use the criterion of equilibrium of the chemical potential $\tilde{\mu}$ in liquid and vapour phase and the Young-Laplace equation given by equation (2.3) to derive the Kelvin equations for the pressure deviations from the saturation pressure in liquid and vapour phase [7]

$$\Delta p_\mathrm{v} = -\frac{\rho_\mathrm{v}}{\rho_\mathrm{l} - \rho_\mathrm{v}}\sigma\kappa, \tag{2.5}$$

$$\Delta p_\mathrm{l} = -\frac{\rho_\mathrm{l}}{\rho_\mathrm{l} - \rho_\mathrm{v}}\sigma\kappa. \tag{2.6}$$

Close to a solid wall the pressures deviate from the expressions given by equations (2.5) and (2.6) due to the disjoining pressure, or dispersion pressure:

$$p_\mathrm{dis} = -\frac{A_{12}}{6\pi\delta^3}. \tag{2.7}$$

In this equation A_{12} is the Hamaker constant (which is negative for attractive net forces between wall and liquid molecules) and δ is the local distance of the interface to the solid heater wall in η-direction. The origin of the disjoining pressure are intermolecular van der Waals forces between the wall molecules and the fluid molecules at the liquid/vapour-interface. These forces are generated by induced dipole moments of the electric fields of the outer electrons of two molecules [8]. The effect of these fields is usually represented by the Lennard-Jones-Potential, given by

$$\Pi_\mathrm{LJ}(r) = \frac{C_{12}}{r^{12}} - \frac{C_6}{r^6}. \tag{2.8}$$

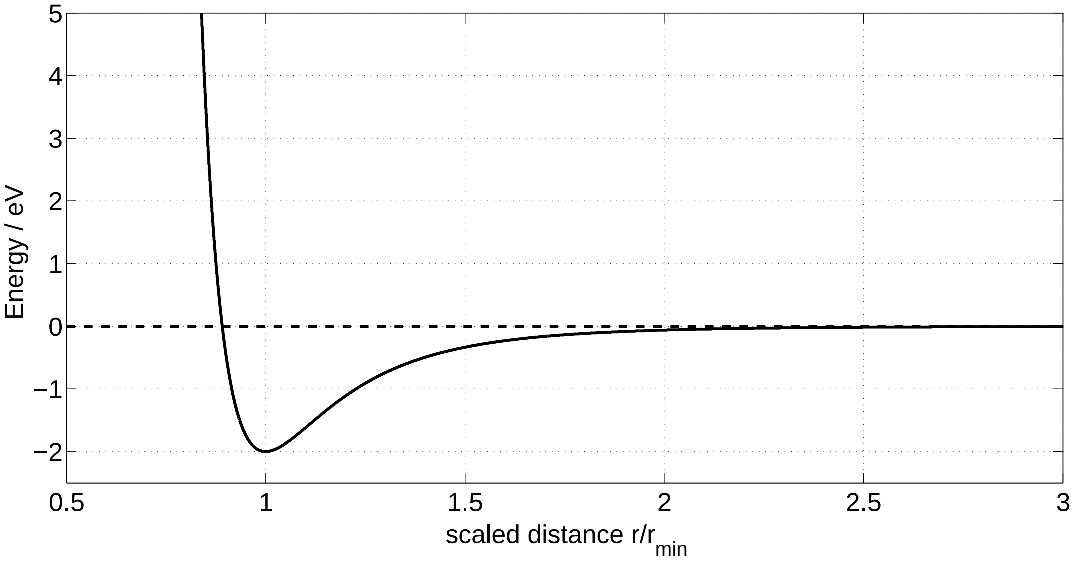

Figure 2.2.: Lennard-Jones Potential energy versus scaled radial distance

In figure 2.2 the Lennard-Jones-Potential energy Π_{LJ} is plotted versus the scaled radial distance of two single molecules for arbitrary constants C_{12} and C_6. The radial coordinate is scaled with the coordinate of minimum energy. Hamaker derived an expression for the surface free energy per square meter of the attractive part of the Leonard-Jones-Potential between a spherical molecule and a semi-infinite wall through a volume integration over the wall [9], which results in

$$E_{\mathrm{surface}} = -\frac{A_{12}}{12\pi\delta^2}. \tag{2.9}$$

The disjoining pressure can be found from equation (2.9) through differentiation to be

$$p_{\mathrm{dis}} = -\frac{\mathrm{d}E_{\mathrm{surface}}}{\mathrm{d}\delta}. \tag{2.10}$$

It should be noted that equation (2.7) is according to its derivation strictly only valid for non-polar fluids with spherical molecules, but is often also applied for non-spherical molecules like long-chained hydrocarbons and strongly polar liquids like water. Van Oss et al. reasoned, that for polar cases the influence of Lewis acid-base interactions and electrostatic interactions onto the surface free energy should be taken into account [10]. The Hamaker constant A_{12} can therefore in these cases not be seen as a physical constant, but is often used as a physically based fitting parameter, that is adapted to the case observed.

Combining equations (2.5) and (2.6) with the disjoining pressure and the equation of Clausius-Clapeyron and assuming that $\rho_{\mathrm{l}} \gg \rho_{\mathrm{v}}$, one can derive the superheat compared to the saturation state without interface curvature and intermolecular forces in the liquid and vapour phase in equilibrium

$$\Delta T_{\mathrm{l}} = \frac{T_{\mathrm{sat}}}{\Delta h_{\mathrm{v}}\rho_{\mathrm{v}}}\left(\sigma\kappa - \frac{A_{12}}{6\pi\delta^3}\right), \tag{2.11}$$

$$\Delta T_{\mathrm{v}} = \frac{T_{\mathrm{sat}}}{\Delta h_{\mathrm{v}}\rho_{\mathrm{l}}}\left(\sigma\kappa - \frac{A_{12}}{6\pi\delta^3}\right). \tag{2.12}$$

Therefore, in equilibrium the temperature on the vapour side of the interface $T_{\mathrm{int,eq}}$ is given by

$$T_{\text{int,eq}} = T_{\text{sat}} + \Delta T_{\text{v}} = T_{\text{sat}} \left(1 + \frac{\sigma\kappa - \frac{A_{12}}{6\pi\delta^3}}{\Delta h_{\text{v}} \rho_{\text{l}}} \right). \tag{2.13}$$

According to gas-kinetic theory, evaporation leads to an additional thermal resistance at the interface:

$$R_{\text{int}} = \frac{2-f}{2f} \frac{T_{\text{sat}} \sqrt{2\pi T_{\text{sat}} \overline{R}/\overline{M}}}{\Delta h_{\text{v}}{}^2} \frac{\rho_{\text{l}} - \rho_{\text{v}}}{\rho_{\text{l}} \rho_{\text{v}}}. \tag{2.14}$$

Again assuming that $\rho_{\text{l}} \gg \rho_{\text{v}}$, equation (2.14) is simplified to [3]

$$R_{\text{int}} = \frac{2-f}{2f} \frac{T_{\text{sat}} \sqrt{2\pi T_{\text{sat}} \overline{R}/\overline{M}}}{\Delta h_{\text{v}}{}^2 \rho_{\text{v}}}. \tag{2.15}$$

Herein, f is the accommodation coefficient. In the way the accommodation coefficient is used in this equation, there is no distinction between the condensation coefficient f_{cond} and the evaporation coefficient f_{evap} and they are assumed to be equal [11].

2.1.2 Modeling approach

Due to the small dimensions of the micro-region, the wall temperature is usually assumed to be spatially constant in the microregion [1, 2, 3]. Assuming heat transfer is governed by quasi-stationary, one-dimensional thermal conduction within the liquid film, the local heat flux is given by

$$q_{\text{mic}}(\xi) = \frac{\lambda_{\text{l}}}{\delta(\xi)} \left(T_{\text{W,mic}} - T_{\text{int}}(\xi) \right). \tag{2.16}$$

The interface temperature T_{int} differs from the equilibrium interface temperature $T_{\text{int,eq}}$, given by equation (2.13), as the evaporative mass flux results in an interfacial thermal resistance R_{int} as introduced in equation (2.15) [3]

$$T_{\text{int}}(\xi) = T_{\text{sat}} \left(1 + \frac{\sigma\kappa(\xi) - \frac{A_{12}}{6\pi\delta(\xi)^3}}{\Delta h_{\text{v}} \rho_{\text{l}}} \right) + R_{\text{int}} q_{\text{mic}}(\xi). \tag{2.17}$$

The local heat flux q_{mic} that appears in equations (2.16) and (2.17) is coupled to the evaporating mass flux, which must be equal to the change of mass flux in ξ-direction

$$q_{\text{mic}}(\xi) = \Delta h_{\text{v}} m_{\text{evap}}(\xi) = \Delta h_{\text{v}} \rho_{\text{l}} \frac{\mathrm{d}}{\mathrm{d}\xi} \left(\int_0^{\delta(\xi)} v_\xi(\xi, \eta)\, \mathrm{d}\eta \right). \tag{2.18}$$

In equation (2.18), v_ξ is the liquid velocity in ξ-direction. Assuming that the velocity component in η-direction can be neglected and that the Reynolds number is low, lubrication theory can be applied to describe the velocity distribution [4] with

$$v_\xi(\xi, \eta) = -\frac{\delta(\xi)^2}{\mu_{\text{l}}} \frac{\mathrm{d}\Delta p}{\mathrm{d}\xi} \left[\frac{1}{2} \frac{\eta^2}{\delta(\xi)^2} - \frac{\eta}{\delta(\xi)} \right]. \tag{2.19}$$

Combining Equations (2.16) - (2.19) yields

$$\begin{aligned} T_{\mathrm{W,mic}} - T_{\mathrm{sat}} \left(1 + \frac{\sigma\kappa(\xi) - \frac{A_{12}}{6\pi\delta(\xi)^3}}{\Delta h_{\mathrm{v}} \rho_{\mathrm{l}}} \right) \dots \\ \dots - \frac{\Delta h_{\mathrm{v}} \rho_{\mathrm{l}}}{3\mu_{\mathrm{l}}} \left(\frac{\delta(\xi)}{\lambda_{\mathrm{l}}} + R_{\mathrm{int}} \right) \frac{\mathrm{d}}{\mathrm{d}\xi} \left[\delta(\xi)^3 \frac{\mathrm{d}}{\mathrm{d}\xi} \left(\sigma\kappa(\xi) - \frac{A_{12}}{6\pi\delta(\xi)^3} \right) \right] = 0. \end{aligned} \tag{2.20}$$

With the curvature κ defined by equation (2.4), this equation represents a fourth order ordinary differential equation (ODE) for the liquid film thickness, which can be solved numerically, with the adsorbed layer providing the boundary conditions.

Solutions of equation (2.20) can be integrated into numerical Volume-of-Fluid codes as a sub-grid model as it has been shown by Kunkelmann for the CFD software OpenFOAM® [4]:
In a first step equation (2.20) is transformed into a system of four first order ODEs. As the adsorbed film is the trivial solution to the problem, the film thickness and the integrated heat flux are slightly perturbed and the ODE system is solved using a shooting method until the curvature at the end of the micro region matches the macroscopic curvature as described by Stephan [12]. To be able to couple the sub-grid model with a macroscopic CFD simulation, Kunkelmann correlated the integrated heat flux per unit contact line length transfered in the micro region, the liquid film thickness at the end of the micro region and the apparent contact angle with the wall superheat $\Delta T_{\mathrm{W,mic}}$. With the local wall temperature as input, the heat flow transfered at the contact line can be calculated with the sub-grid model, given that an accurate interface reconstruction algorithm is implemented. This heat flow is then superimposed to the conjugate heat transfer between solid and liquid as heat sink in the solid domain and as mass source equivalent to the heat flow on the vapour side of the fluid cell containing a part of the three-phase contact line.
Kunkelmann [4] and Kunkelmann and Stephan [13, 14] used this model to numerically investigate pool boiling phenomena. Kunkelmann et al. used the model to investigate the effect of contact line velocity onto local heat transfer at the three-phase contact line and compared the results to experiments [15].

In a later work by Raj et al. the model was extended to include the effect of recoil pressure, which is caused by the impulse change of the evaporating molecules [16]

$$\Delta p_{\mathrm{rec}} = -\frac{{q_{\mathrm{mic}}}^2}{{\Delta h_{\mathrm{v}}}^2} \left(\frac{1}{\rho_{\mathrm{v}}} - \frac{1}{\rho_{\mathrm{l}}} \right). \tag{2.21}$$

Equation (2.17) must take this additional pressure difference into account and is therefore altered to

$$T_{\mathrm{int}}(\xi) = T_{\mathrm{sat}} \left(1 + \frac{\sigma\kappa(\xi) - \frac{A_{12}}{6\pi\delta(\xi)^3} - \frac{{q_{\mathrm{mic}}}^2}{{\Delta h_{\mathrm{v}}}^2} \left(\frac{1}{\rho_{\mathrm{v}}} - \frac{1}{\rho_{\mathrm{l}}} \right)}{\Delta h_{\mathrm{v}} \rho_{\mathrm{l}}} \right) + R_{\mathrm{int}} q_{\mathrm{mic}}(\xi). \tag{2.22}$$

As the pressure difference at the liquid/vapour-interface with recoil pressure is also a function of the local heat flux, it can not be removed from the equations anymore, making a notation as one fourth order ODE as given by equation (2.20) for the local film thickness not possible. Nevertheless, formulation of the problem as a system of four first order ODEs as described by Kunkelmann [4] is equally possible by combining equations (2.16), (2.18), (2.19) and (2.22) [16].
Herbert et al. investigated single drop impingement numerically using this contact line model [17, 18]. A comparison to a corresponding experiment yielded well agreement [17].

2.2 Review of experimental work on three-phase contact line heat transfer

An early experimental study of heat and mass transfer at a single meniscus was conducted by Wayner and Coccio [19]. By immersing flat test samples of stainless steel and aluminum into pools of water and methanol respectively, a steady state meniscus was created. The fluid was kept at saturation temperature through a heating coil within the liquid pool and the test samples were heated from the top through cartridge heaters. Each sample was manufactured from plates of the respective material that were joined by silicone rubber. Within the rubber layer iron-constantan thermocouples were embedded at certain lengths of the test sample. Through the temperatures measured by the thermocouples, Wayner and Coccio determined the steady-state heat flow along the direction perpendicular to the three-phase contact line. In all test configurations a steep heat flow reduction has been found at the position of the meniscus, indicating high heat transfer to the fluid in this region. However, the spatial measurement resolution of this technique was not sufficient to measure the temperature drop at the contact line, which has been reported by later studies.
DasGupta et. al. [2, 20] and Kim and Wayner [21] measured the local film thickness profiles at the apparent contact lines of evaporating extended menisci of completely wetting fluids (propanol, butanol, octane, heptane and R-113) on silicone surfaces. High resolutions of the liquid film thickness down to the adsorbed film region were achieved by combining image-scanning null-ellipsometry with microcomputer-enhanced video microscopic interferometry. Since the liquid was evaporated into the atmosphere at low input heat fluxes and no high resolution temperature measurement technique was employed, the temperature drop close to the three-phase contact line could not be observed. Instead, a constant substrate temperature was assumed given that only small temperature deviations were measured by thermocouples positioned on the backside of the silicone substrates at distances of 1.5 mm. As it will be shown later in this work, this assumption is not necessarily justified as the spatial resolution of the temperature measurement and the distance between measurement plane and the heater/fluid-interface are essential for detection of a local temperature minimum at the contact line. Even with the assumption of a constant heater surface temperature the high resolution of the liquid film thickness measurement allowed the authors to calculate the evaporative mass flux as a function of the film thickness using an approach similar to the one outlined in section 2.1, which has been developed by Wayner [22]. The results of these investigations have shown a peak of the dimensionless evaporative mass flux at small film thickness, which equals a peak in the absolute evaporative mass flux close to the adsorbed film region.

Höhmann developed a method to measure the temperature distribution below metallic heating foils with thermochromic liquid crystals (TLCs) with high spatial resolution [23, 24]. A single extended water meniscus was formed in the experiment setup between two walls. One of the walls consisted of a 10 μm thin stainless steel foil, that acted as electrical heater. The backside of the foil was covered with a layer of TLCs and the foil was then applied to a 20 mm thick PMMA window. By using uncapsuled TLCs a resolution of 0.83 μm/pixel was achieved. The temperature distribution at the wall beneath the non-moving contact line of the meniscus was measured by acquiring the color play of the TLCs with a three-chip CCD-camera and saving them into RGB matrices. Using an in-situ calibration, a pixel-wise equation was derived to correlate the RGB values to the pixel temperature. With this high resolution temperature measurement technique Höhmann has been able to actually measure the temperature drop near the three-phase contact line of an evaporating water meniscus, as it had been predicted in earlier publications [3, 6].

Buffone and Sefiane conducted experiments on evaporation of volatile fluids (ethanol, methanol, acetone and pentane) from capillary tubes using infrared thermography [25]. The fluid was fed to capillary tubes of inner tube sizes of 600 , 900 and 1630 μm and formed an evaporating meniscus at the end of the tube. Temperature fields were acquired both from the liquid/air-interface from the end of the tube and from the side. The temperature fields acquired showed increasing temperature gradients at the contact line of the meniscus with increasing heater power. However, in the description of the measurement technique, no calibration procedure is given by the authors. While the spatial resolution of the IR camera is investigated in detail, an accuracy of 1 °C is given, which requires detailed knowledge of the emissivity of the investigated surface. The emissivity and penetration depth in the wavelength regime of the used IR camera is not analyzed by the authors and it is claimed that reflection of ambient radiation is negligible "because of the meniscus interface high curvature and locally rough shape" [25]. It is not explained, why high interface curvature should inhibit reflection or what is meant by a "locally rough shape". For these reasons, the absolute temperature values reported by Buffone and Sefiane may be well out of the accuracy threshold given by the authors. In a later work Buffone and Sefiane conducted thermochromic liquid crystal thermography on an equivalent system with pentane evaporating from an unheated capillary tube with an inner diameter of 1630 µm [26]. Unsealed TLCs were applied to the outside of the capillary tube and the hue color value of the used TLCs was calibrated with a separate calibrator bar, at which a constant temperature gradient was applied. During stationary evaporation from the capillary tube, the authors reported a local temperature minimum close to the tube edge, where the meniscus was pinned. From the temperature distribution the local heat flux introduced into the capillary tube by the surrounding air was calculated. As the heat transfer coefficient from air to the capillary tube and the air far field temperature were assumed to be homogeneous, a local heat flux maximum has been found at the temperature minimum close to the contact line at the end of the tube.

Kandlikar and Kuan and Kandlikar et al. investigated the mean heat flux at a moving water meniscus evaporating into air on a heated copper surface [27, 28]. Through a static nozzle degassed and de-ionized water was deposited onto a rotating, heated copper surface. By changing the rotational velocity and the distance between nozzle and central axis different relative velocities between meniscus and heated wall were adjusted. From the water flow rate needed to establish a stationary meniscus the mean heat flux transferred to the liquid was calculated by multiplying the flow rate with the latent heat of evaporation and the liquid thermal capacity multiplied with the inlet subcooling. It has been found that the mean heat flux transferred to the liquid increases with increasing surface velocity [27]. However, due to the motion of the heated surface, the investigated system contained an advancing and a receding contact line at the same time. As only global values were acquired with the measurement technique, the authors could not distinguish between these two cases.

The group of Plawsky and Wayner developed a technique to measure the pressure jump across the liquid/vapour-interface caused by interface curvature by measuring the local film thickness through image analyzing interferometry [29, 30, 31, 32, 33, 34, 35]. The authors used this technique to measure liquid film thickness profiles, curvature and apparent contact angles of different fluids filled into a quartz or fused silica cuvette test cell with a square inner cross section. As the cell was only partially filled, a single constrained vapour bubble (CVB) formed in the heated top of the cuvette. Due to the higher capillary pressure in the sharp edges of the cells the liquid rose there and formed menisci. Close to the edges the authors observed the menisci with a microscope objective mounted to a CCD camera. By projecting monochromatic light through the objective, fringe patterns were created due to interference of light reflected from the liquid/solid-interface and light reflected from the liquid/vapour-interface.

The validity of the measurement method was checked by comparing the results for pure pentane for the isothermal case to the theoretical hydrostatic prediction by Zheng et al. [29]. When adding an external condenser assembly feeding recondensed liquid back to the liquid bulk of the quartz test cell, Zheng et al. reported that higher input heat flows into the system lead to a steeper liquid film thickness profile and a larger contact angle. At the highest input heat flows the liquid film started to become unstable and started oscillating with periodic dry-out and rewetting of the wall with contact line velocities of up to $\pm 5\,\mathrm{mm\,s^{-1}}$ accompanied by an overproportional increase of the local heat flow rates.

By filling the CVB system with a mixture of *n*-butanol as experiment fluid and air, Gokhale et al. conducted experiments on evaporation and condensation of droplets and corner menisci [31]. By heating from below the authors were able to study condensing droplets at the top while by heating from the top it was possible to study evaporating droplets. For condensation the authors have reported an increase of contact angle with increasing condensation rate, while for evaporation a decrease in contact angle with increasing evaporation rate was observed. This seems to contradict results of other researchers, who have reported an increase of contact angle with increasing wall superheat (and therefore higher evaporation rates) [16, 17]. However it must be noted that the *n*-butanol drops under investigation in this work had (apparent contact line) diameters less than 100 μm. Under these circumstances an increased evaporation rate results in a larger (negative) contact line velocity, which has a decreasing effect onto the contact angle [17]. This explains the decrease of the contact angle with increasing evaporation rates.

Plawsky et al. investigated oscillations of the contact line region of HFE-7000 ($C_3F_7OCH_3$, methyl perfluoropropyl ether) in such a CVB system [32]. From evaluation of the local film thickness and the curvature of the interface the authors calculated the liquid pressure profiles. A minimum of the liquid pressure close to the three-phase contact line has been found for both the advancing and the receding case, indicating liquid flow into this region.

Panchamgam et al. conducted experiments on the microscale heat transfer at a CVB system filled with a mixture of pure pentane vapour and non-condensible gases [33]. By applying lubrication theory the local evaporative heat flux at the extended corner meniscus was calculated. In contrast to predictions no heat flux maximum could be identified by the authors which was attributed to insufficient spatial resolution of the optical system. In a later work Panchamgam et al. have identified a peak in the evaporative heat flux close to the three-phase contact line for pure pentane and for a binary mixture of pentane (98 vol.-%) and octane (2 vol.-%) [34]. For the binary mixture, the heat flux maximum has been found to be not as high as for the single species fluid, but it was distributed across a wider area, resulting in an increase of the overall heat flux. This has been attributed to favorable Marangoni stresses in the mixture.

Ojha et al. investigated the influence of nano-scale surface roughness onto evaporation close to the three-phase contact line using the interferometric method described above. [35]. As rough surfaces fused silica samples were treated by plasma etching and plasma enhanced chemical vapour deposition. It has been found that higher roughness reduces the slope of the liquid film close to the apparent contact line and the curvature peak near the adsorbed film. Due to the smaller slope of the interface, the overall transfered heat flux in the contact line region has been found to be larger for rough surfaces.

Raj et al. investigated the contact angle of FC-72 (C_6F_{14}, *n*-perfluorohexane) during droplet impingement and evaporation on a heated copper wall in a pure FC-72 vapour atmosphere and compared the results to numerical predictions [16]. The contact line model used within this work was based on the work of Kunkelmann and Stephan [13, 14]. In contrast to the original model, the one used in this work was altered to account for recoil pressure, which is caused by the impulse change of the evaporating molecules (see section 2.1.2). As it is implied by the model, it has been found experimentally that while under isothermal conditions the fluid is highly wetting with contact angles approaching zero, the contact angle on a superheated wall is larger and increases with wall superheat. The numerical calculations have shown a peak in curvature and heat flux close to the three-phase contact line, which is coherent with the results of Plawskys group discussed beforehand. A comparison of the experimentally determined and the numerically calculated contact angle dependency on wall superheat yielded good agreement. Deviations between the numerical and experimental results have been attributed to uncertainties in the experiment and the neglect of Marangoni stress and fluid inertia, as well as the one dimensional approximation of the contact line model.

Dhavaleswarapu et al. [36] and Chamarthy et al. [37] conducted experiments on buoyant-thermocapillary convection of pure methanol evaporating from capillary tubes of 75 μm - 1575 μm diameters. The authors used a micro particle image velocimetry (μPIV) technique to visualize the flow patterns inside the capillary tubes which were heated through a water bath surrounding the capillary. It was reported that for the smallest tube size of 75 μm the flow pattern was rotational symmetric, which indicates the dominance of thermocapillary induced flow. For tube diameters of 200 μm and more, however the flow patterns were found to be asymmetrical in parallel to the direction of gravity. The upper clockwise rotating vortex was found to be decreasing in size with increasing tube diameter, while the lower counterclockwise rotating vortex was found to be increasing in size with increasing tube diameter, which indicates the increasing importance of buoyancy for the overall flow field with increasing tube diameter. Based on the assumption that the underlying evaporation process is dominated by diffusion of the experiment fluid vapour in the surrounding air the authors developed an analytical model to approximate the local heat flux in dependence on the radial coordinate. The results of their model has shown a heat flux peak close to the contact line and an amount of 95 % of the overall heat being transferred on a scaled radial distance of less than 30 % away from the contact line in such a diffusion driven case.
In a later work Dhavaleswarapu et al. conducted microscale temperature measurements near the contact line of heptane evaporating into the atmosphere on a 500 μm thick fused quartz wafer [38]. Above the wafer a circular acrylic knife edge was positioned to hold the liquid film in place and re-supply evaporating liquid allowing to adjust steady state conditions. The backside of the wafer was coated with a 100 nm thick titanium coating, which acted as an electrical resistance heater. Above the liquid film and below the wafer an IR camera was positioned to record the temperature profile at the contact line and at the lower surface of the quartz wafer. The authors reasoned that the temperature recorded from above close to the contact line corresponds to the substrate temperature, as heptane exhibits a high transmissivity in the biggest part of the infrared regime recorded by the camera up to a thickness of 80 μm. The shape of the meniscus formed between the acrylic knife edge and the quartz wafer was recorded from the side using a goniometer. The resulting temperature profiles showed a local temperature drop close to the contact line in the order of ∼ 1 K with rather small temperature gradients in direction of the liquid and the gaseous phase. Even though the temperature measurements showed significant temperature differences between upper and lower surfaces of the wafer, the authors applied a one-dimensional energy balance to determine the heat transferred through a 50 μm wide subregion at the contact line. Depending on the input heat flux and the evaporation rate the authors have reported ratios of subregion to total evaporative heat transfer between 66 % and 87 %.
Migliaccio et al. used the same infrared measurement technique and heater design to study evaporation into the atmosphere from a heptane meniscus inside a V-groove geometry [39]. In contrast to the results of Dhavaleswarapu et al., who reported a temperature drop of ∼ 1 K [38], the contact line temperature drop that has been found in this study lay roughly at ∼ 0.2 K, which is more consistent with results obtained by Höhmann [23, 24]. The ratio of heat transfered through a 50 μm subregion around the contact line to total evaporative heat transfer calculated by Migliaccio et al. was relatively constant at ∼ 45 %, regardless of liquid feeding rate. Due to a high uncertainty of ±50 % the results have been quantitatively inconclusive, but qualitatively confirmed the high importance of the near-contact-line region for the overall heat transfer during evaporation.

Schweizer conducted experiments on single bubble nucleate boiling of FC-72 under microgravity conditions with special attention on contact line heat transfer [40]. Due to the microgravity environment, the bubble departure diameter was enlarged and bubble growth and detachment processes were significantly slowed down, virtually increasing the spatial and temporal resolution of the measurements. As heater Schweizer used a 20 μm thick stainless steel foil which was electrically heated. The back side of the heating foil was coated with a graphite layer to increase its emissivity. With an in-situ calibrated high-speed IR camera the temperature field on the backside of the foil was measured during bubble growth and detachment at a framerate of 1000 Hz and a spatial resolution of 29.6 μm/pixel. Because of the low thickness of the foil, temperature differences across its thickness could be neglected. A cold temperature imprint of $T_{\mathrm{W,mean}} - T_{\mathrm{CL}} \approx 2\,\mathrm{K}$ generated by strong evaporation rates at the bubble foot was detected in the temperature field of the heating foil backside. By applying a two-dimensional, instationary energy balance for each pixel of the temperature field and approximating the derivatives with a finite differencing scheme the local heat flux distributions were calculated. In the heat flux fields a distinctive heat flux peak was observed at the bubble foot, where the apparent contact line is located. The heat flux below the bubble and the bulk liquid were significantly lower. By fitting an ellipse to the maximum heat flux Schweizer calculated the contact line velocity through the change of radii. Two more ellipses were fitted to the locations, where the heat flux fell below a pre-defined threshold and through integration between these two boundaries the transfered heat flow per unit contact line length was calculated. The results of this calculation indicate that for a negative contact line velocity the heat flow per unit contact line length is independent of the velocity. For a positive contact line velocity the data points suggest a linear increase of the heat flow per unit contact line length with contact line velocity. Schweizer has attributed this increase to transient conduction to the fluid in the advancing contact line case [40].

Ibrahem et al. conducted experiments on the local heat transfer at a stationary three-phase contact line of a meniscus inside a single capillary slot [41]. The capillary slot with a width of 600 μm was formed by a copper plate and a 10 μm thick stainless steel foil accommodated in a stainless steel test section. As experiment fluid HFE-7100 ($C_4F_9OCH_3$, methyl-nonafluorobutyl-ether) was used, which was pre-heated in a copper container submerged inside a water bath. Due to capillary forces the liquid formed a single meniscus in the test section which was heated by Joule heating of the stainless steel foil. The temperature field on the graphite coated backside of the foil was recorded using an in-situ calibrated IR camera at a framerate of 244 Hz and a spatial resolution of 14.8 μm/pixel. Following the approach of Schweizer [40], Ibrahem et al. calculated the local heat flux distribution. The input heat flux adjusted through the supply current of the heating foil was varied from $183\,\mathrm{W\,m^{-2}}$ to $12\,170\,\mathrm{W\,m^{-2}}$. The working fluid is reported to have been subcooled between 3 K and 6.5 K against its saturation temperature at the experiment pressure of 510 mbar. Ibrahem et al. found a temperature minimum at the position of the contact line in the order of ~ 0.4 K to ~ 12 K lower than the mean bulk liquid temperature [41]. With increasing heat flux, the temperature difference at the contact line has been reported to be increasing, as well as the the local heat flux at the contact line, which has been found to be 5.4 to 6.5 times higher than the mean input heat flux.

In a subsequent work Ibrahem et al. investigated the microscale heat transfer at a moving three-phase contact line [42], using the same experimental setup and heat flux calculation technique. The meniscus movement was realized by pushing the liquid into or sucking it out of the test section using a stepper motor controlled syringe pump. The authors have found that for an advancing contact line case the local temperature minimum at the contact line disappears. This is according to the authors caused by the fact that in the advancing case the contact line moves across the hotter part of the heating foil formerly insulated by the vapour bulk. The local temperature minimum seen in the stationary and the receding contact line case, which is caused by the energy that is removed from the wall through contact line evaporation, is therefore compensated by the higher wall temperature. While for the advancing contact line Ibrahem et al. reported an increasing heat flux peak with increasing contact line velocity, the heat flux peak in the receding contact line case was found to be almost independent on contact line velocity. This was attributed to the higher local wall superheat and the steeper temperature gradient in the advancing contact line case.

Ibrahem et al. compared their experimental findings to a numerical simulation of the evaporating meniscus in a later work [43]. The contact line model that was applied followed the approach used by Kunkelmann and Stephan [13]. The comparison showed a reasonably good agreement between experimental and numerical results.

Kunkelmann et al. combined experimental investigations of pool boiling at a single nucleation site in microgravity and a moving evaporating meniscus in a single capillary slot with numerical investigations of the phenomena to characterize the influence of contact line speed onto contact line heat transfer [15]. The experimental results presented by the authors is in case of the pool boiling experiments based on the setup used by Schweizer [40] and in case of the evaporating moving meniscus based on the setup used by Ibrahem et al. [41, 42, 43]. By mimicking the post-processing of the experiments for the numerical data instead of evaluating the heat flux at the heater/fluid-interface directly, excellent agreement between numerical and experimental results could be achieved. As the numerical simulation provides much more detailed data, a reason for the discrepancy between advancing and receding contact line heat transfer could be identified: The flow field in the numerical simulation clearly showed that for a receding contact line liquid flows away from the heater wall towards the moving liquid/vapour-interface. This decreases the local temperature gradient in the liquid close to the wall, but increases the evaporation rate at the interface. In case of an advancing contact line however, colder liquid from the interface flows into the thermal boundary layer at the heater wall, thereby increasing the local temperature gradient in the fluid close to the contact line and consequently the local heat transfer [15].

2.3 Survey of high resolution temperature measurement techniques

The review of experimental work conducted on contact line heat transfer in the previous section shows that the highly resolved temperature distribution below the contact line is of major interest. To measure the wall surface temperature, the applied measurement technique must fulfill several requirements:

1. High spatial and temporal resolution
2. Fast reaction time
3. High measurement sensitivity
4. No mechanical disruption of the heater surface
5. No introduction of additional heat

Several measurement techniques are available to acquire the wall temperature distibution:

- **Micro temperature sensors**
  Locally resolved measurements with micro temperature sensors (e.g. micro thermocouples or micro thermistors) could in principle give an indication of the local wall temperature distribution, but if commercially available sensors are used, the wall temperature measurement would be limited to several point measurements. Furthermore integration of such sensors into a heater without disrupting the heat flux distribution is almost impossible to achieve. An alternative is to use micro-electronics fabrication techniques to generate a very narrow array of temperature sensors, a technique that has been developed by Kim and Co-workers [44, 45, 46, 47]. However, this measurement technique still suffers from inferior resolution compared to optical measurement techniques.

- **Laser induced fluorescence and laser induced phosphorescence**
  While these two measurement techniques can provide highly resolved 2 dimensional temperature fields, they both suffer from one major drawback, which is the additional energy introduced by the laser. While this energy is in many cases negligible, the small sizes of the system and the low heat flux required for stable contact line evaporation make its applicability in the given case questionable. Furthermore close to the contact line, evaporation of the experiment fluid can lead to agglomeration of the fluorescence/phosphorescence dye or particles. The ensuing concentration gradients introduce apparent temperature deviations. Two-color one-dye LIF techniques are in theory independent of the dye/particle concentration [48], but time-dependent photobleaching of the dyes can result in deviations of the intensity at a given temperature from the calibration values [49, 50].

- **Liquid crystal thermography**
  TLCs have been used in the past to measure the heater surface temperature at a stationary evaporating meniscus [23, 24]. By combining uncapsuled TLCs with a CCD camera equipped with a microscope objective high resolutions of roughly 1 μm/pixel can be achieved. Uncapsuled TLCs however suffer from aging and hysteresis, strongly reducing the experiment repeatability [24]. This problem can be overcome by using encapsuled TLCs, but the resulting resolution is limited by the size of the encapsuled TLCs to roughly 5 μm/pixel – 50 μm/pixel. Furthermore TLCs cannot be applied directly to the heater fluid interface and have a rather narrow temperature range which they cover with acceptable accuracy. Also the applicability for moving contact lines is questionable, as the response time of TLCs is rather large due to their comparably large thermal inertia.

- **Infrared (IR) thermography**
  IR thermography is a very powerful measurement technique to acquire two-dimensional temperature fields with a large range of possible applications. With semi-conductor based camera systems high framerates of up to several thousand frames/second in part frame mode can be achieved at resolutions down to roughly 20 μm/pixel. With pixel-wise in-situ calibration techniques, very high relative accuracies down to 0.1 K can be realized (see section 3.5.5) across wide temperature ranges.

Following the survey of available high-resolution temperature measurement techniques given above, IR thermography has been chosen, as it is the only non-intrusive measurement method providing sufficient reaction times. In combination with the sputtered heater design (see section 3.2), the 2-dimensional temperature distribution can be measured less than 1 μm away from the heater/fluid interface with high temporal and spatial resolution using IR thermography.

2.4 Objectives of this thesis

Heat transfer in the proximity of moving three-phase contact lines plays a major role in many phase change processes. The main objective of this thesis is to systematically investigate contact line heat transfer using a state-of-the-art high resolution temperature measurement technique. For reasons outlined in the previous section, IR thermography has been chosen as primary measurement technique.

In many technical applications, where contact line heat transfer is of interest (e.g. boiling phenomena or heat pipes), evaporation takes place in a single species system. Nevertheless, most experimental work conducted up to date investigated contact line heat transfer during evaporation into a mixture of inert gas (mostly air) and vapour [2, 19, 20, 21, 25, 26, 27, 28, 31, 33, 34, 36, 37, 38, 39]. As pointed out by Birdi et al. however, evaporation might in such a system very well not be controlled only by heat transfer, but also by diffusive and convective mass transport of the vapour in the gaseous phase [51]. This makes it very difficult to transfer the findings to systems containing only a single species, as the contribution of mass transport in the gaseous phase to the overall process is not known. Furthermore the presence of an inert gas can result in the change of contact line dynamics, influencing the local transport phenomena [16]. To rule out such an influence and facilitate the comparability of the results of this work to models and numerical simulations, it has been chosen to study contact line evaporation in an enclosed single species system.

Contact line heat transfer often occurs in highly dynamical systems like boiling or drop impingement, where the velocity of the contact line is pre-determined by droplet or bubble hydrodynamics. Even though studying the influence of velocity on contact line heat transfer in such systems is in principle possible and has been carried out in the past experimentally [40] and numerically [4], the dynamic nature of these systems makes it extremely difficult to control and investigate the velocity influence systematically. Contact line heat transfer has already been studied at extended menisci between two flat plates in the past [23, 24, 41, 42, 43]. In such a configuration the contact line takes the shape of a straight line and curvature of the liquid/vapour-interface is only a function of the perpendicular distance from the wall. As a result this configuration can be treated two-dimensional, making it perfect to study fundamental aspects of heat transfer at the three-phase contact line. Furthermore, the contact line velocity can be controlled more easily through rise and fall of the liquid level between the two plates. Since a systematic study of the influence of contact line velocity is one of the primary objectives of this thesis, it has been chosen to study contact line heat transfer at a single extended meniscus configuration.

Up to now the influence of pressure on contact line heat transfer has not been the prime focus of any experimental study, yet. As contact line heat transfer might be an important phenomenon in many applications that often incorporate high pressure environments, investigation of the influence of the system pressure onto contact line heat transfer is another objective of this thesis.

Following the objectives stated above, the aim of this thesis is to experimentally investigate the influence of contact line velocity and system pressure onto the local heat transfer in proximity of the contact line of a single species extended meniscus by means of high speed IR thermography.

3 Experimental apparatus, measurement methods and data reduction

3.1 Basic concept

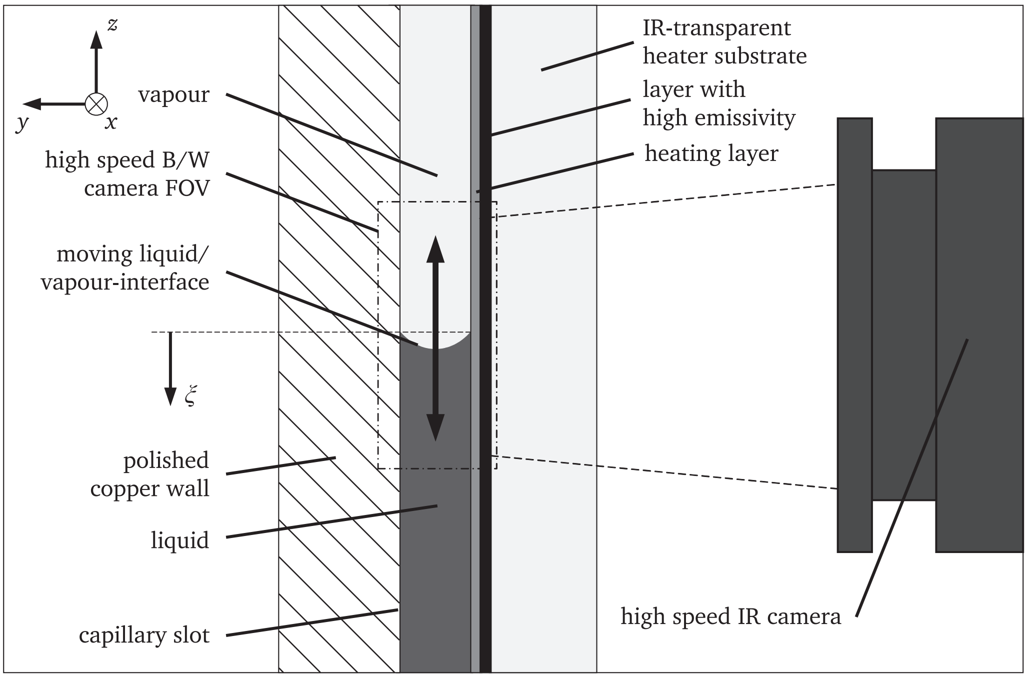

Figure 3.1.: Schematics of the experiment concept

From the aim of this thesis formulated in section 2.4 a basic experiment concept has been derived, which is depicted in figure 3.1.:
A liquid meniscus is formed due to capillary forces in a small slot inside an enclosed system filled with a degassed single species fluid. The walls of the capillary channel are formed by a copper wall on one side and a heating element on the other side. The heating element must provide the possibility to accurately measure the wall temperature distribution with high spatial and temporal resolution. IR thermography has been chosen for this measurement task for reasons closer described in section 2.3. To visualize the liquid/vapour-interface the capillary slot should be optically accessible for a high speed black and white (B/W) camera.
Since the influence of pressure is to be investigated the heater must withstand the system pressure, preferably up to the critical pressure of the experiment fluid. As indicated in figure 3.1 the solution for this has been found in form of a novel sputtered heater design which is described in more detail in section 3.2.
Inside the capillary channel the liquid/vapour-interface is to be moved along the channel in order to generate an advancing contact line (ACL) or a receding contact line (RCL) situation.

As experiment fluid the fully-fluorinated liquid FC-72 is chosen. Apart from being non-flammable and practically non-toxic it has a rather low critical temperature ($T_{\text{crit}} = 449\,\text{K}$) and critical pressure ($p_{\text{crit}} = 18.3\,\text{bar}$), making it in combination with the heater design, and IR thermography as measurement technique possible to measure the wall temperature distribution at high values of the reduced pressure $p_{\text{R}} = p/p_{\text{crit}}$. Furthermore measured data is available for this fluid to develop and check correlations for the fluid properties based on corresponding states methods. The correlations used within this work and a comparison to measured data are given in Appendix A.

The coordinate system defined in figure 3.1 is used consistently throughout this thesis. In chapter 4 the z-coordinate is partly substituted by the ξ-coordinate, which is based on the definition given by figure 2.1. $\xi = 0$ is defined as the position of the maximum heat flux and is counted positive in direction of the liquid bulk. This substitution facilitates the comparison of different measurement sequences.
The width of the capillary channel must be chosen as compromise between two requirements: On one hand, the slot should be small to promote the dominance of capillary forces, on the other hand, the channel is required to have a sufficient width to allow optical observation of the liquid/vapour-interface. Within this work a slot width of 1.4 mm was chosen. Though it could be changed in principle by exchanging the modular access of the test section (see section 3.3), it was chosen not to vary it within this work. For an extended, but narrow channel, it can be shown that its hydraulic diameter corresponds to twice the channel width [52]. With the characteristic length of the channel of $l_0 = 2 \cdot 1.4\,\text{mm}$, a maximum interface velocity of $v_0 = 100\,\text{mm}\,\text{s}^{-1}$ and the thermophysical fluid data, that can be calculated using the correlations from Annex A between 50 °C and 170 °C, the following dimensionless numbers can be calculated:

Table 3.1.: Extreme values of the dimensionless numbers influencing the fluid flow for the experimental channel width of 1.4 mm and the experiment fluid FC-72 between 50 °C and 170 °C

dimensionless number	**equation**	**meaning**	**minimum value**	**maximum value**
Bond number	$\text{Bo} = \frac{(\rho_{\text{l}}-\rho_{\text{v}}) g l_0{}^2}{\sigma}$	$\frac{\text{gravitational forces}}{\text{surface tension forces}}$	14	204
Capillary number	$\text{Ca} = \frac{\nu_{\text{l}} \rho_{\text{l}} v_0}{\sigma}$	$\frac{\text{viscous forces}}{\text{surface tension forces}}$	$5 \cdot 10^{-3}$	$64 \cdot 10^{-3}$
Liquid Reynolds number	$\text{Re}_{\text{l}} = \frac{v_0 l_0}{\nu_{\text{l}}}$	$\frac{\text{inertia forces}}{\text{viscous forces}}$	943	1696
Vapour Reynolds number	$\text{Re}_{\text{v}} = \frac{v_0 l_0}{\nu_{\text{v}}}$	$\frac{\text{inertia forces}}{\text{viscous forces}}$	303	6376
Weber number	$\text{We} = \frac{\rho_{\text{l}} v_0{}^2 l_0}{\sigma}$	$\frac{\text{inertia forces}}{\text{surface tension forces}}$	5	103

From the values given in table 3.1 for Bond number, Capillary number and Weber number, it is evident, that fluid flow inside the channel is rather influenced by surface tension, gravity and inertia of the liquid, than by viscous forces. The Reynolds number of the liquid is well below the critical Reynolds number of $\text{Re}_{\text{crit}} \approx 2320$ [53], indicating purely laminar flow in the liquid phase. The vapour Reynolds number can exceed that value while staying below the threshold for fully turbulent flow of $\text{Re} \approx 8000$ [53]. The vapour flow can therefore be expected to enter the transition regime between laminar and turbulent flow at high velocities and temperatures.

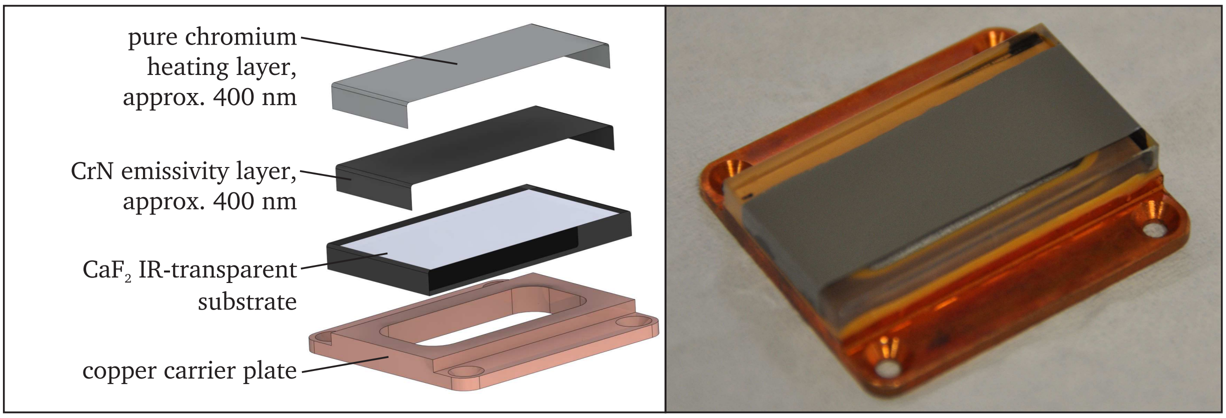

Figure 3.2.: Exploded view of the experiment heater design (left) and picture of an assembled heater element (right)

Heating foils as they have been employed for example by Ibrahem et al. [41, 42, 43] would require a sophisticated pressure equalization system to avoid deformation and rupture of the foil at elevated pressures. An alternative to these thin foil heaters is to use a sputtered heating layer on top of an IR transparent substrate. Theofanous et al. used titanium thin films deposited by physical vapour deposition (PVD) onto 130 µm thin borosilicate glasses (which is only partially transparent to IR radiation) to investigate boiling phenomena [54, 55]. Chatzikyriakou et al. employed an IR transparent CaF_2 disk onto which a 100 nm layer of aluminum was deposited to investigate heat transfer during impact of non-wetting droplets onto a heated surface [56]. Duan et al. used a 700 nm indium tin oxide (ITO) layer deposited onto a 250 µm thick sapphire substrate to investigate single bubble heat transfer during pool boiling [57].
All three sputtered heater designs suffer from one major drawback when compared to thin foil heaters: The rather limited emissivity of the deposited layer results in low signal-to-noise ratios. Therefore an alternative heater design has been developed in the frame of this work in cooperation with the Staatliche Materialprüfungsanstalt Darmstadt, Fachgebiet und Institut für Werkstoffkunde (MPA-IfW) [58].

The heater consists of a two-layer composition, which is sputtered on top of a 4 mm thick infrared transparent calcium fluoride (CaF_2) substrate[1]. A scanning electron microscopy image of a notched specimen of the heater coating system applied onto a silicon wafer is shown in figure 3.3. The thermal diffusivity of CaF_2 is with $\alpha_{\mathrm{CaF}} = 3.575 \cdot 10^{-6}\,\mathrm{m^2\,s^{-1}}$ ($\lambda_{\mathrm{CaF}} = 9.71\,\mathrm{W\,m^{-1}\,K^{-1}}$, $\rho_{\mathrm{CaF}} =$

---

[1] lateral dimensions: 41 mm x 23 mm

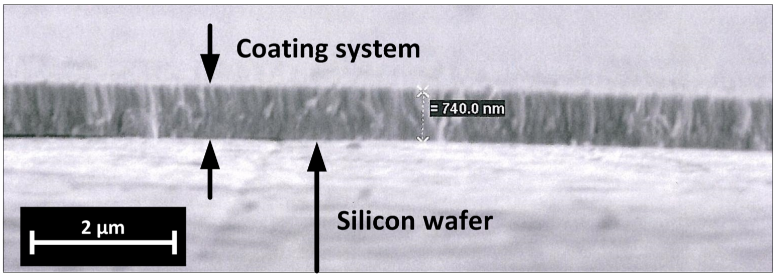

Figure 3.3.: Scanning electron microscopy image of a notched specimen of the heater coating system applied onto a silicon wafer

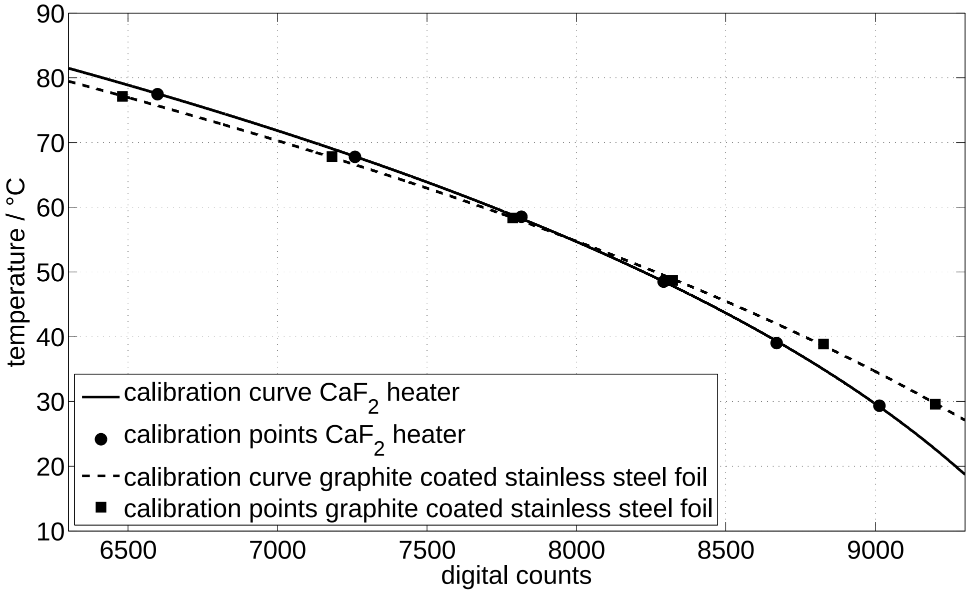

Figure 3.4.: Comparison of calibration curves of the CaF_2 heater design and a graphite coated stainless steel foil (integration time $0.8515\,\mathrm{ms}$)

$3180\,\mathrm{kg\,m^{-3}}$, $c_{\mathrm{CaF}} = 854\,\mathrm{J\,kg^{-1}\,K^{-1}}$)) [59] in the same order of magnitude as commonly used stainless steel alloys (e.g. $\alpha_{1.4301,20^{\circ}\mathrm{C}} = 4.040 \cdot 10^{-6}\,\mathrm{m^2\,s^{-1}}$ [60]). In combination with a comparably high thermal capacity this results in a heater design very close to heater walls found in technical applications. The substrate thickness of 4 mm has been chosen to ensure stability of the heater substrate up to the critical pressure of the experiment fluid. The first layer that is applied to the substrate is a black layer to enhance the surface emissivity for IR thermopraphy. The layer consists of chromium nitride (CrN) crystals sputtered onto the substrate by High Power Impulse Magnetron Sputtering. The black color is achieved by adjusting the sputtering parameters according to Slomski et. al. [58, 61, 62]. The second layer of the two-layer composition is a pure chromium (Cr) layer, which acts as electric heating layer. The coated substrate is glued onto a copper carrier plate equipped with an optical access using the two component epoxy adhesive Polytech EP 655-T. This adhesive provides a high thermal stability (up to 220 °C) and is particularly suited to bond materials with different thermal expansion coefficients. Along with a high thermal conductivity of the carrier material this is necessary to avoid rupture of the heater substrate through thermal stresses. An exploded view of the heater design and an assembled heater element are shown in figure 3.2. The thickness of the layers is in the order of 400 nm each. In case of the CrN black layer this ensures intransparency, while it has been found that such a thickness of the pure chromium layer results in convenient electrical resistances of the heating layer.

The emissivity of the black layer in the spectral range of the IR thermography system is not known. As an in-situ calibration procedure is applied, it is not mandatory to have the exact value of the surface emissivity. Nevertheless, a rather high emissivity is desirable to enhance the signal-to-noise ratio of the temperature measurement. One way to obtain information about the emissivity is by comparing a calibration curve obtained on the CrN black layer to a calibration curve obtained with the same IR camera settings on a high emissivity surface. In figure 3.4 the calibration curves (averaged over 50 x 50 pixel) of the CaF_2 heater design and a graphite coated stainless steel foil are shown for an integration time of 0.8515 ms. While the digital count signal received from the black CrN surface is slightly lower (smaller discharge and thereby higher digital count) than the one received from the graphite coated stainless steel foil, it is still of the same order of magnitude. At low temperatures

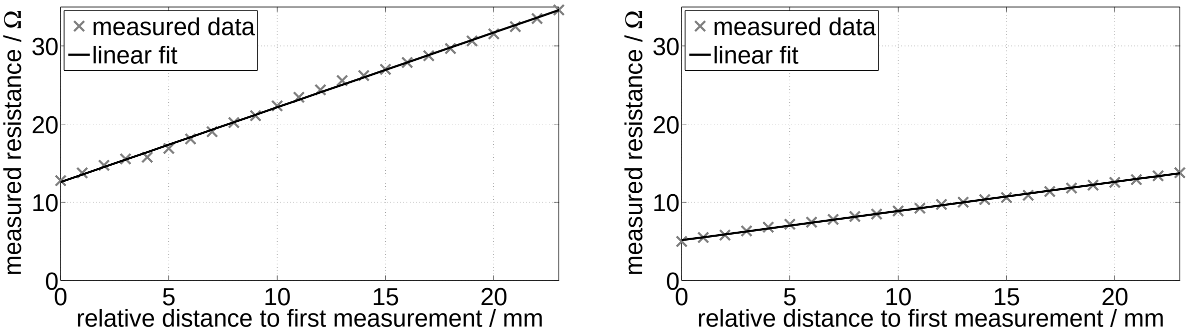

Figure 3.5.: Measured heater resistance and linear fit versus distance to first measurement point for two heaters of different production batches

the signal from the CrN black layer even exceeds the one from the graphite coated stainless steel foil (stronger discharge and thereby lower digital count).

Although the parameters for the deposition process were always kept the same, it was found that different batches of produced heaters possessed different electrical resistances. Therefore the resistance of each heater used must be measured individually:
The heater is clamped with a copper foil electrode at one of its sides. A second copper foil electrode is mounted onto a x-y-micrometer table and pressed onto the top of the heater surface several times in 1 mm intervals. At each step the resistance between the two electrodes is measured. The contact resistance of the copper foil electrodes is not known, but the heater resistance per length of the heating layer (in $\Omega\,\mathrm{m}^{-1}$) can easily be calculated as the slope of a linear fit to the measured resistances. In figure 3.5 two exemplary heater resistance measurements for heaters manufactured in different batches are displayed along with the linear fit to the measurements. Even though the slope of the two heaters is quite different, the linear fit matches the measured data extremely well in both cases. The heater resistance can be deduced from the measurements by multiplying the slope of the linear fit with the heater length. Through this technique the resistance of only the heating layer is calculated eliminating the need to account for contact resistances of the heater electrodes. It does however pose a threat to the heater surface quality, as the procedure can introduce tiny scratches in the heater surface. Therefore

Table 3.2.: Advantages and disadvantages of the CaF_2 sputtered heater design in comparison to thin foil heaters

	Advantages		Disadvantages
+	Wall temperatures can be measured by IR thermography extremely close to the heater/fluid-interface (approx. 800 nm).	-	High temperature gradients can destroy the heater through thermal stresses due to low material ductility.
+	No “blurring” of the temperature signal due to conduction parallel to the heater/fluid-interface (as it is the case for thin foil heaters).	-	Substrate material is very brittle and highly susceptible to mechanical shocks.
+	Pressure resistant heater design with no deformation of the heater surface.	-	Heat flux calculation is computationally very expensive compared to thin foil heaters.
+	Thermal capacity of the heater element is much closer to real applications than thin foil heaters.	-	CaF_2 Substrates are way more expensive than thin-foil heaters.

the heater resistance measurement can only be carried out after the experiments.

Table 3.2 lists the advantages and disadvantages of the heater design when compared to state-of-the-art thin foil heaters. The sputtered heater concept was also applied in single bubble pool boiling experiments under microgravity and drop impingement experiments, which are shortly outlined in Annex D.

3.3 Experiment setup

To realize the basic experiment concept as introduced by figure 3.1 a dedicated experiment setup has been constructed. In figure 3.6 a schematical drawing of the experiment setup is displayed. The core of the experiment is the sputtered heater design, which must form one wall of the capillary slot. In order to be heated through Joule heating of the pure chromium layer, it is connected to electrical feedthroughs in one of the test section walls. Exploded and sectional views of the heater flange and the test section are provided in Annex B along with a more detailed descritption of the integration of the experiment heater.

In the test section the single capillary slot with a width of 1.4 mm is formed between the experiment heater and a polished copper modular access. Through different modular access inserts any width of the capillary slot can be realized.
By exchanging the modular access with a copper calibration block, that is pressed onto the heater surface after the measurements, an in-situ calibration of the IR-camera is performed, which is absolutely mandatory for accurate temperature measurements through IR thermography (see section 3.5.2). In the copper modular access three thermocouples are installed at a distance of approx. 10 mm from the fluid to check the wall temperature and its homogeneity.
The walls of the test section contain four thermalization channels connected to a thermostat to adjust the saturation temperature inside the test section. At the top of the test section, a vapour tube connector is installed, that feeds the generated vapour to the condenser, where it is recondensed and fed back to the test section through the liquid tube connector at the bottom of the test section.

To allow optical access to the meniscus the test section is equipped with two sapphire windows that are installed on both sides of the capillary slot. The channel widens linearly in positive and negative x-directions. This leads to a local reduction of the capillary forces there, which compensates for the liquid rise due to wetting of the sapphire windows. Otherwise the liquid rising at the windows would inhibit the visibility of the centre of the slot, where the heater is located.
The test section is equipped with six thermocouple feedthroughs (four on the side of the modular access, two on top of the test section, see figures B.2 and B.3). The measurement tips of the six type K thermocouples fed through the test section walls are arranged at different heights of the test section fluid volume to measure the bulk liquid and bulk vapour temperatures.

Power is supplied to the experiment heater through the electrode feedthroughs connected to a laboratory DC power supply[2], which is controlled by the data acquisition system (DAQ)[3]. The vapour generated by evaporation inside the test section is recondensed inside a copper block filled with copper powder to enhance heat transfer and facilitate a homogeneous fluid thermalization. The powder (particle diameter 270 μm) is kept inside the condenser by stainless steel meshes with pore sizes of 50 μm glued into the condenser. The temperature of the test section is controlled by a high temperature thermostat[4], feeding silicone oil (LAUDA Kryo 55) through the thermalization channels of the test

---

[2] Elekto-Automatik EA-PS3065-05B

[3] PC with National Instruments™ M-series PCI-6289 measurement card and
National Instruments™ SCXI-1000 multiplexer and signal conditioning chassis

[4] LAUDA Integral XT 350 HW

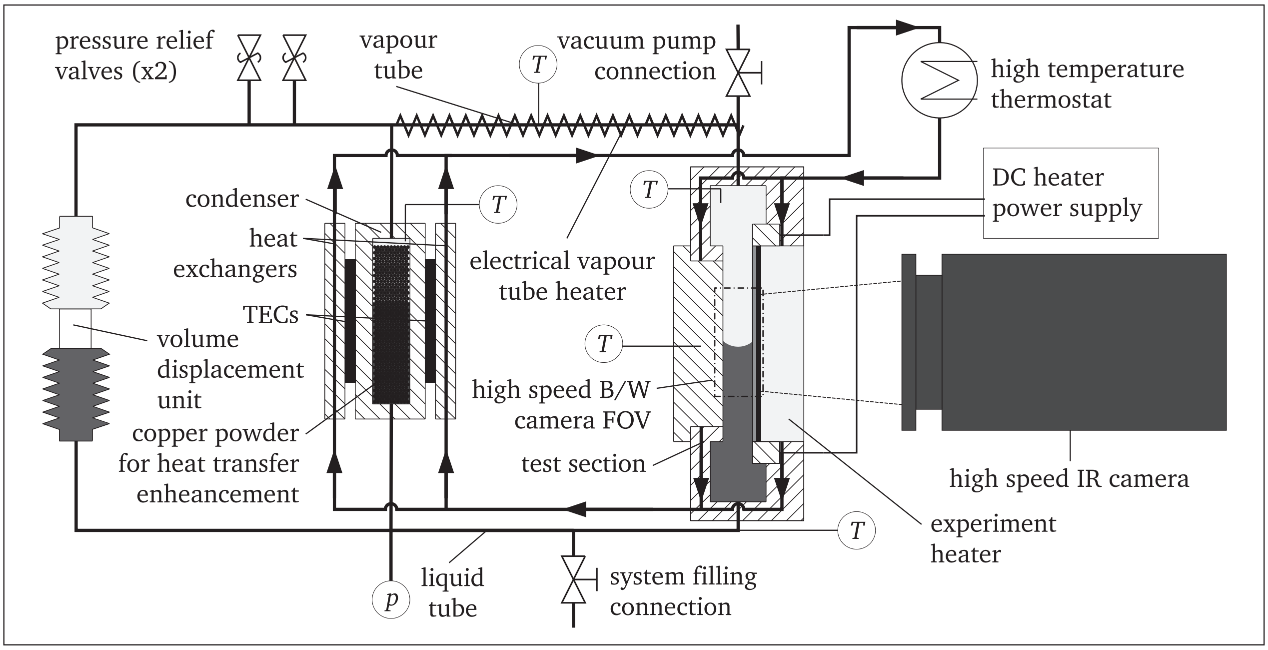

Figure 3.6.: Schematics of the experiment setup

section (see figures B.2 and B.3). After exiting the test section, the silicone oil is routed through heat exchangers connected to the condenser before being returned to the thermostat. To be able to adjust test section temperature and condenser temperature individually the thermalization circuit heat exchangers are coupled to the condenser through thermoelectric coolers (TECs). Intensity and direction of the current supplied to the TECs (and thereby their heating or cooling power, respectively) is adjusted with a DC laboratory power supply[5] controlled by the DAQ based on the sensor feedback of a thermocouple installed inside the condenser. During the first test runs it was found that the thermal losses at the vapour tube connecting condenser and test section result in it filling up with liquid effectively decoupling condenser and test section. To avoid recondensation inside the vapour tube, heating foils[6] were connected to the outside of the tube. The thermocouple readout of the vapour tube temperature is used to automatically switch the heating foils on/off through the DAQ to keep the vapour tubes always slightly superheated (approx. 2 K ... 4 K against saturation). For safety reasons the vapour tube is equipped with overpressure relief valves (redundant design), designed to open at 19 bar absolute. In case of clogging of both valves the system is also equipped with two additional blow-out discs designed to rupture at 20 bar absolute. A pressure sensor[7] is connected to the liquid tube, that is read out by the DAQ.

One of the most challenging requirements for the experimental setup is to realize a controlled movement of the contact line at elevated system pressures. Due to the high system pressures, using a stepper motor controlled syringe pump, as it was employed by Ibrahem et al. [42], is out of question. As the pressure inside the system is to be kept constant during the measurements and a contamination of the experiment fluid with lubricants or non-condensable gases is to be avoided, movement of the liquid/vapour-interface must be realized by an internal shift of the vapour and liquid volumes without any mechanical feedthrough. A schematic of the final design of such a volume displacement unit is displayed in figure 3.7: Two stainless steel bellows are installed opposite of each other. Through this arrangement the net forces in axial direction, that result from the internal pressure in each bellow,

---

[5] Elekto-Automatik EA-PS3032-20B

[6] Minco HK913-A

[7] WIKA® Precision Pressure Transmitter Type P-10, $0 - 25$ bar, abs.

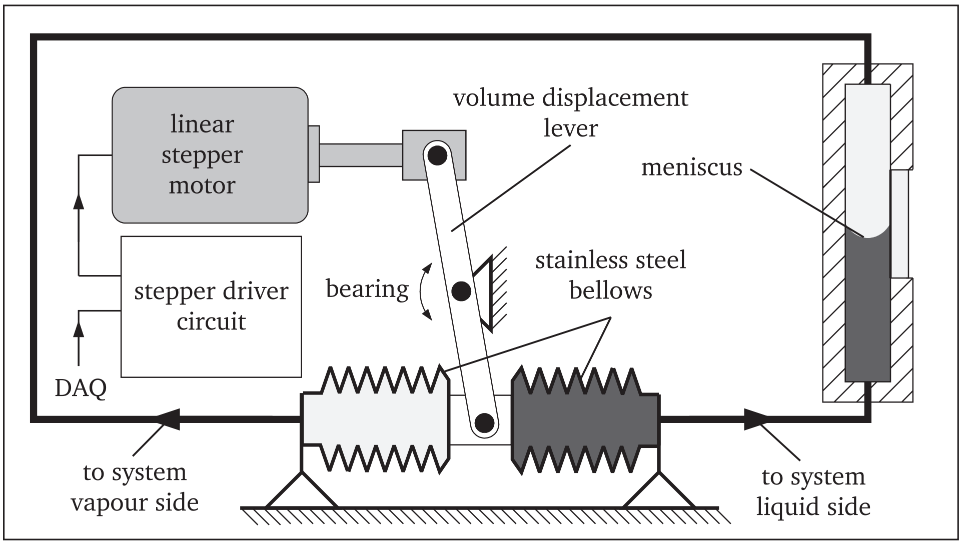

Figure 3.7.: Schematics of the volume displacement unit

cancel each other out. While one of the bellows is connected to the system liquid side, the other one is connected to the system vapour side. Between the two bellows a lever connects the closed inner flanges of the bellows to a linear stepper motor[8]. By moving the stepper motor the liquid bellow is compressed, while the vapour bellow is correspondingly elongated or vice versa. The stepper motor is controlled by the DAQ over a dedicated stepper motor driving circuit[9]. Because of the bellow arrangement the stepper motor only needs to overcome the bellow stiffness regardless of the system pressure. For a constant stepper motor velocity the liquid bellow generates a constant volumetric flow rate, which is always compensated by the volumetric flow rate entering the vapour bellow. The resulting, corresponding changes in liquid and vapour volume inside the systems lead to a rise or a fall of the liquid/vapour-interface inside the test section and the condenser, thereby generating an advancing contact line or a receding contact line situation at the experiment heater.

Photographies of the experiment setup are provided in Annex B.

3.4 Experimental procedure and parameters

Before being filled into the experiment setup, the experiment fluid is carefully degassed. This is important, as the presence of non-condensable gases results in a change of the local saturation conditions, depending on the local vapour concentration in the gaseous phase, which is often neglected in similar experiments (see section 2.4). For degassing the experiment fluid FC-72 is filled into a degassing facility, in which non-condensable gases are separated from the fluid by evaporation and re-condensation. Non-condensable gases accumulate at the condenser section of the degassing facility and are removed from the facility by periodically opening a valve to a vacuum pump. Over time the concentration of non-condensable gases within the liquid gradually decreases. After approximately one hour of degassing, liquid is taken from the evaporator section of the degassing facility and fed into the experiment setup. To check the quality of this degassing procedure a gas chromatography-mass spectrometry of a not degassed and a degassed sample of FC-72 has been carried out. An excerpt of the resulting mass spectra are shown in figure 3.8 (the full mass spectra are provided in Annex C). In the spectrum of the not degassed sample (figure 3.8, left) peaks are evident at a mass-to-charge

---

[8] Haydon™ 57000 Series Size 23 Double Stack hybrid linear actuator T57M41-12-912

[9] Nanotec® SMCI 32-1

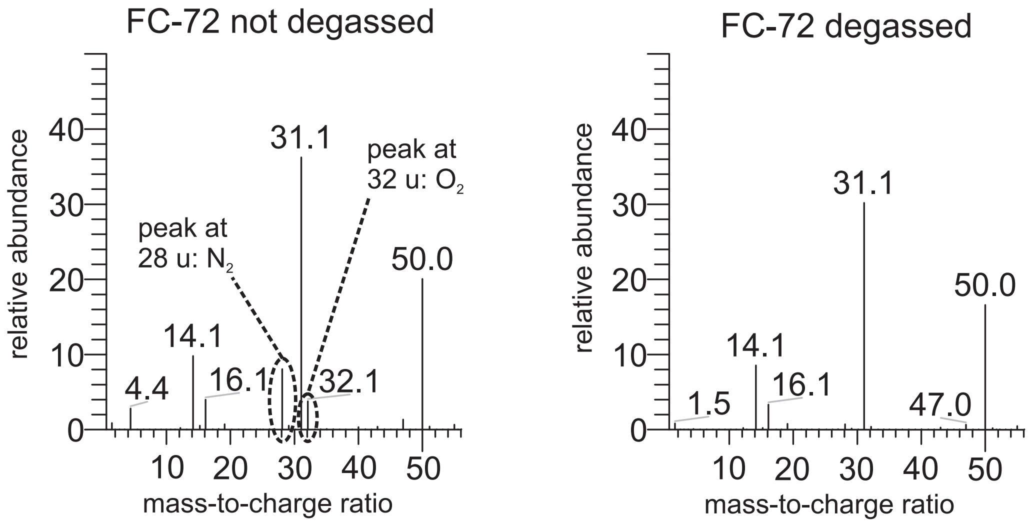

Figure 3.8.: Excerpt of the mass spectra from the gas chromatography-mass spectrometry of a not degassed FC-72 sample (left) and a degassed FC-72 sample (right)

ratio of 28 u, indicating the presence of nitrogen (N_2) and a mass-to-charge ratio of 32 u, indicating the presence of oxygen (O_2). The small peak at a mass-to-charge ratio of 4 u visible on the spectrum of the not degassed sample is caused by helium used to flush the measurement chamber prior to the measurements. In the spectrum of the degassed sample (figure 3.8, right) the peaks indicating nitrogen and oxygen are barely present at all. From the reduction of the relative abundance a reduction of the non-condensable gas content of $\sim 90\,\%$ can be deduced, which suggests a very high quality of the applied degassing procedure.
For the system itself an air leakage rate of $9.02 \cdot 10^{-5}\,\mathrm{mbar\,l\,s^{-1}}$ has been measured over a time period of 26 hours at the evacuated system. This corresponds to a rise of the partial pressure of the non-condensable gases in the system of less than 5 mbar each day. As the system is refilled each day for a new pressure level, the rise of non-condensable gas content in the system is negligible.

After the degassing procedure, experiment fluid is filled into the evacuated experimental setup until the test section is fully flooded. The desired pressure level is then adjusted by setting the outlet

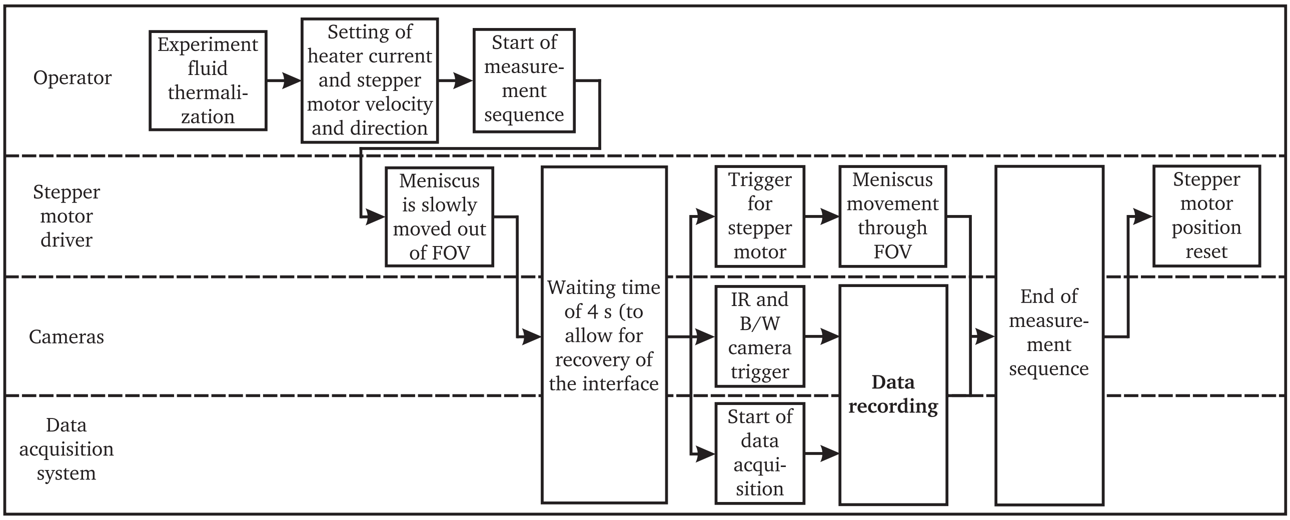

Figure 3.9.: Flow chart of an experiment run

temperature of the thermostat a little higher than the corresponding saturation temperature. When a homogeneous fluid thermalization is reached, which is checked through the thermocouples inside the test section, fluid is let out of the test section until the meniscus is centered in the field of views (FOVs) of the B/W and the IR camera.

In figure 3.9 a flow chart of an experiment run is displayed. After heater current and stepper motor velocity have been set by the operator, the measurement sequence is triggered. All further actions are controlled automatically by the DAQ:
First, the meniscus is moved out of the FOVs of the cameras in the opposite direction of the measurement (up for a RCL experiment, down for an ACL experiment) at a low velocity. Once the motor has reached the final position, a waiting time of 4 seconds is implemented to allow for recovery of the interface from the previous movement. Then, the DAQ sends a trigger signal to the B/W and IR camera, as well as the stepper motor. While the stepper motor is running at the pre-defined, constant velocity, both cameras are recording images at a framerate of 1000 Hz and the DAQ is recording measurement data at a rate of 2000 Hz. After the meniscus has reached either the upper or the lower end of the FOVs of the cameras, the measurement sequence is finished and the meniscus position is reset by moving the stepper motor back to its point of origin. After the image sequences have been saved, the setup is ready for the next measurement sequence.

The general influence of pressure onto contact line heat transfer is a central aspect of this work, but using the absolute saturation pressure p_{sat} of the experiment fluid FC-72 as variable would be of little significance. Instead, the reduced pressure is used as parameter, to allow for comparison with results possibly obtained with different experiment fluids in the future:

$$p_{\mathrm{R}} = \frac{p}{p_{\mathrm{crit}}} \tag{3.1}$$

By relating temperature, pressure and specific volume of a fluid to its values at the critical point, one can formulate a universal form of the van der Waal's equation of state [63]. This "principle of corresponding states" [64] is extensively used within this work to determine the thermophysical properties of FC-72 up to the critical point (see Annex A).

As the fluid inside the test section is always at saturated conditions, it was found that input heat fluxes exceeding $3000\,\mathrm{W\,m^{-2}}$ always resulted in nucleate boiling on the heater surface. This inhibits the adjustment of high input heat fluxes in the experimental setup. At high experiment pressures, boiling was also observed to occur at the heater edges at lower heat fluxes (due to the smaller latent heat of evaporation), but observation of the temperature fields revealed little impact onto contact line dynamics, as long as the bubbles were out of the FOV of the IR camera. On the other hand it was found that low input heat fluxes result in very low temperature differences at the contact line. The significance of measurements with low input heat flux is therefore limited due to the measurement uncertainty of the wall temperature measurement technique (see sections 3.5.2 and 3.5.5). For these reasons the input heat flux was only slightly varied on purpose within this work in contrast to the investigations conducted by Ibrahem et al. [41, 42, 43]. Slight deviations of the input heat flux however could not be entirely ruled out, as an exchange of the experiment heater also results in a change of the heater electrical resistance, which is not exactly known at the time of the measurements (see section 3.2).
In table 3.3 the parameter space investigated in this work is given. The parameter space is set up by all possible combinations of five reduced pressures p_{R}, seventeen stepper motor velocity or acceleration settings v_{StM}, a_{StM} and two input heat fluxes q_{in}, resulting in a total number of 170 experiment parameter sets. The acceleration sequences were included, as it turned out that the acceleration of the interface could have an influence onto the generation of a thin evaporating liquid film on the heater

Table 3.3.: Experiment parameters

parameter	values	total no. of parameter sets	influenced system properties
reduced system pressure p_R	0.05 0.1 0.3 0.5 0.7	5	saturation pressure p_sat, saturation temperature t_sat, all fluid properties (see Appendix A)
stepper motor velocity v_StM	$0\,\mathrm{mm\,s^{-1}}$ $\pm1\,\mathrm{mm\,s^{-1}}$ $\pm2\,\mathrm{mm\,s^{-1}}$ $\pm3\,\mathrm{mm\,s^{-1}}$ $\pm4\,\mathrm{mm\,s^{-1}}$ $\pm5\,\mathrm{mm\,s^{-1}}$ $\pm6\,\mathrm{mm\,s^{-1}}$	13	direction of contact line movement, contact line velocity v_CL
stepper motor acceleration a_StM (receding contact line only)	$-2\,\mathrm{mm\,s^{-2}}$ $-4\,\mathrm{mm\,s^{-2}}$ $-6\,\mathrm{mm\,s^{-2}}$ $-8\,\mathrm{mm\,s^{-2}}$	4	receding contact line acceleration a_CL, transient contact line velocity $v_\mathrm{CL}(\tau)$
input heat flux q_in	$1800\,\mathrm{W\,m^{-2}}$ ... $1900\,\mathrm{W\,m^{-2}}$ $2500\,\mathrm{W\,m^{-2}}$ ... $2600\,\mathrm{W\,m^{-2}}$ $0\,\mathrm{W\,m^{-2}}$	2 (only at $p_\mathrm{R} = 0.05$)	wall superheat ΔT_W

surface (see section 4.5.1). As reference experiment a stationary meniscus at $p = 0.9\,\mathrm{bar}$ ($p_\mathrm{R} = 0.05$) is chosen (see section 4.1). In addition, all seventeen stepper motor velocity or acceleration settings are run at zero input heat flux at a reduced pressure of $p_\mathrm{R} = 0.05$ to identify trends of the determined contact angle behavior. Each experiment set is run at least twice to check for reproducibility.

3.5 Measurement methods and data reduction

3.5.1 High speed shadowgraphy for interface velocity and contact angle measurement

To determine the liquid/vapour-interface velocity and the apparent contact angle in-situ, the images taken by the high speed black and white camera are used. Due to refraction and reflection at the interface, the liquid region close to the liquid/vapour-interface appears dark. In the vapour and the liquid far away from the interface light emitted by the background illumination can pass through the slot undisturbed. As illumination a collimated white light source[10] is used. The meniscus is recorded through a telecentric objective[11] with a high speed black-and-white (B/W) camera[12] at an optical resolution of $\Delta x_\mathrm{res,B/W} = 4\,\mu\mathrm{m/pixel}$ and a framerate of $f_\mathrm{B/W} = 1000\,\mathrm{Hz}$. A typical raw image acquired by the B/W camera is displayed in figure 3.10, a). Image processing was done by an automated

---

[10] Schott® Moritex MCBP-CW3430

[11] Edmund Optics® 2x telecentric long distance objective

[12] Mikrotron MotionBLITZ EoSens® Cube7

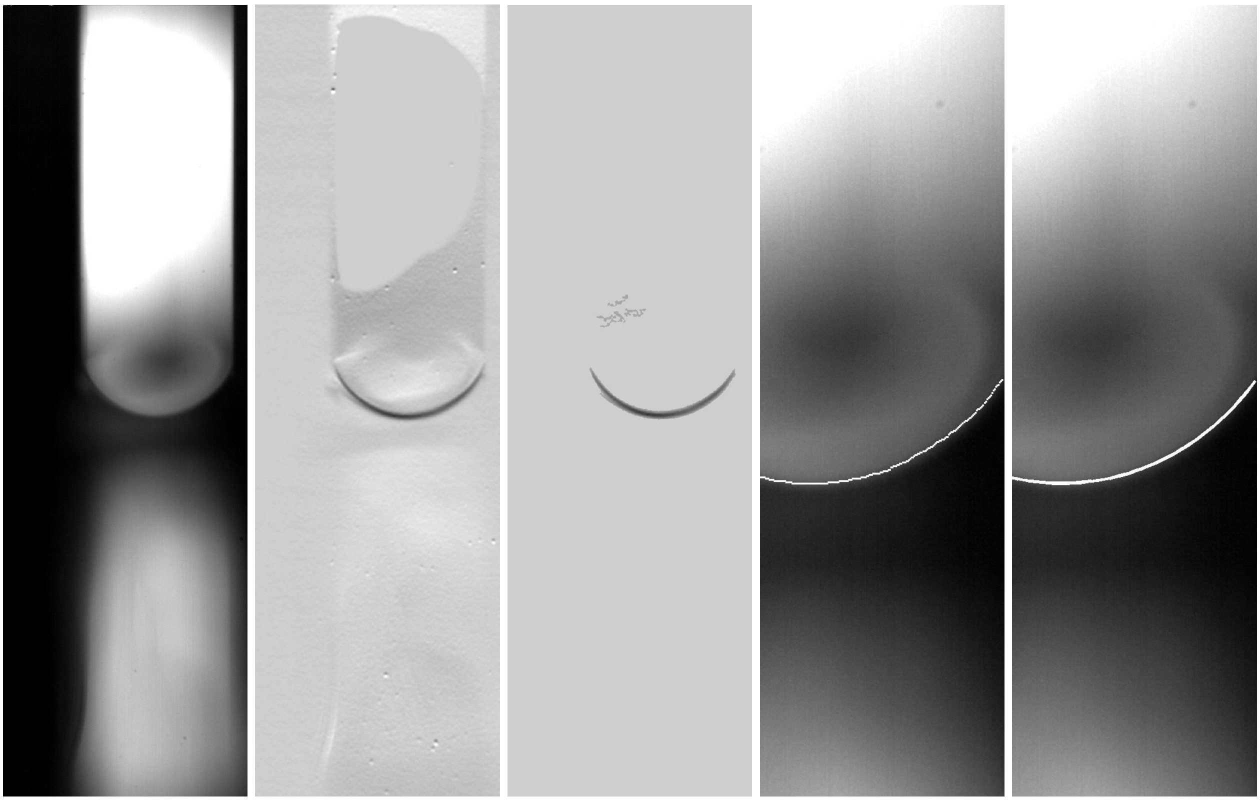

a) b) c) d) e)

Figure 3.10.: Processing steps of the interface fitting algorithm: Raw black and white image (a), image of the gradient parallel to the walls of the capillary slot (b), revised gradient image (c), cut-out of the raw image with detected interface (d) and cut-out of the raw image with fit of the Young-Laplace equation to the detected interface (e)

algorithm using the Image Processing Toolbox of the MATLAB® software.

In a first step, the image is loaded by the software with a resolution of 8 bit, in which the gray scale values are represented by integer values $I_{\mathrm{dig}}(y,z)$ between 0 and 255, with 255 being white and 0 being black. A part of the image is pre-defined as the region of interest (ROI), to which the contour detection algorithm is limited. Along the channel, only the central part of the channel can be used for evaluation, as in the upper and lower parts of the channel light refraction from the liquid/vapour-interface make its accurate detection impossible. From the raw image, the gradient of the gray scale values in the direction parallel to the channel walls are calculated. The resulting gradient image is then filtered to eliminate gradients that are introduced through noise of the black and white camera. The result of this step is shown in figure 3.10, b). As the z-coordinate runs from the upper edge of the image downwards, changes from light to dark (like at the interface) result in negative gradients. Dust fragments in the optical path introduce strong local gradients, that can lead to errors in the interface detection. To remove these small fragments from the gradient image, a function is defined, which assigns a logical 1 or a logical 0 to every pixel, based on a statistical threshold

$$b(y,z) = \begin{cases} 1 & \text{if } \frac{\mathrm{d}I_{\mathrm{dig}}}{\mathrm{d}z}(y,z) <= \mathrm{mean}\left(\frac{\mathrm{d}I_{\mathrm{dig}}}{\mathrm{d}z}\right) - 2 \cdot \mathrm{std}\left(\frac{\mathrm{d}I_{\mathrm{dig}}}{\mathrm{d}z}\right) \\ 0 & \text{if } \frac{\mathrm{d}I_{\mathrm{dig}}}{\mathrm{d}z}(y,z) > \mathrm{mean}\left(\frac{\mathrm{d}I_{\mathrm{dig}}}{\mathrm{d}z}\right) - 2 \cdot \mathrm{std}\left(\frac{\mathrm{d}I}{\mathrm{d}z}\right). \end{cases} \tag{3.2}$$

In this equation $\frac{\mathrm{d}I_{\mathrm{dig}}}{\mathrm{d}z}\left(y,z\right)$ is the intensity gradient in z direction as displayed in figure 3.10, b), mean $\left(\frac{\mathrm{d}I_{\mathrm{dig}}}{\mathrm{d}z}\right)$ is the mean value of the intensity gradient and std $\left(\frac{\mathrm{d}I_{\mathrm{dig}}}{\mathrm{d}z}\right)$ is the standard deviation of the intensity gradient. In the matrix generated by the boolean function b, all connected areas smaller than a threshold of 200 pixel are removed. Pixel-wise multiplication of the gradient image with the boolean function b removes all gradient values above the statistical threshold defined by equation (3.2) and connected areas below the threshold which are smaller than 200 pixel. The outcome of this step is shown in figure 3.10, c). The liquid/vapour-interface can be easily found from the revised gradient image by finding the minimum gradient within the ROI for each column of the revised gradient image. The result of this step is displayed in figure 3.10, d) along with the ROI of the raw image. Due to the digital nature of the image, only discrete velocities and a contact angle of 90 ° could be found from the detected boundary. Therefore a fit must be applied to the interface to determine the local curvature, the velocity of the meniscus and the apparent contact angle.

The easiest approach would be to fit a polynomial to the liquid/vapour-interface. However, a low order polynomial would lead to a rather bad representation of the interface, while a high order polynomial can introduce short-waved fluctuations of the detected interface. In both cases this would lead to a dramatically bad representation of the local interface curvature and the contact angle.
A very general equation to approximate the position of a liquid/vapour-interface is to use a circular, ellipsoidal or hyperbolic curve, which are special cases of conical section equations. In its most general form, the equation to describe an arbitrary conical section is given by

$$Ay^2 + By + Cyz + Dz^2 + Ez + F = 0. \tag{3.3}$$

with $A...F$ being constants. Equation (3.3) can be rewritten to an explicit equation for the position of the interface z_{int}

$$z_{\mathrm{int}} = C_1 + C_2 y + \sqrt{C_3 y^2 + C_4 y + C_5}, \tag{3.4}$$

with $C_1...C_5$ being the fitting constants derived from $A...F$, y being the coordinate perpendicular to the heater wall and z_{int} being the interface coordinate parallel to the heater wall (see figure 3.1).

A more physical approach to represent the detected interface is to actually solve the balance of the Young-Laplace equation with the hydrostatic pressure difference at the interface. This balance can be expressed as

$$\kappa\sigma = p_{\mathrm{v}} - p_{\mathrm{l}} = \left(\rho_{\mathrm{l}} - \rho_{\mathrm{v}}\right) gz + p_0 \tag{3.5}$$

with p_0 being the deviation from the static presure balance due to viscous forces. Replacing the curvature κ with a similar expression as given by equation (2.4), a non-linear second order differential equation for the local height of the interface is obtained

$$z^{''} = \frac{\mathrm{d}^2 z}{\mathrm{d}y^2} = \left(\frac{\left(\rho_{\mathrm{l}} - \rho_{\mathrm{v}}\right) g}{\sigma} z + \frac{p_0}{\sigma}\right) \left[1 + \left(\frac{\mathrm{d}z}{\mathrm{d}y}\right)^2\right]^{3/2}. \tag{3.6}$$

By defining a function $f(y) := z^{'}$, this second order differential equation can be transformed into a non-linear system of first order differential equations

$$z^{'}(y) = f(y), \tag{3.7a}$$

$$f^{'}(y) = \left(Az(y) + B\right)\left(1 + f(y)^2\right)^{3/2}, \tag{3.7b}$$

with

$$A = \frac{(\rho_\mathrm{l} - \rho_\mathrm{v})\, g}{\sigma}, \tag{3.8a}$$

$$B = \frac{p_0}{\sigma}. \tag{3.8b}$$

While the parameter A is defined by the fluid data at the given system temperature, the parameter B is a priori unknown. The system can be solved numerically using an ODE solver in MATLAB® on the range defined by the y-values of the ROI. The starting values of the solution are given by

$$f(y=0) = z^{'}(y=0) = \cot\theta, \tag{3.9a}$$

$$z(y=0) = 0. \tag{3.9b}$$

A solution is calculated for distinguished values of θ between 1° and 80° in 0.1° steps and values of B between $0\,\mathrm{m}^{-1}$ and $1500\,\mathrm{m}^{-1}$ in steps of $30\,\mathrm{m}^{-1}$, creating a look-up table of 791 x 51 possible solutions for the parameter A at the given system temperature.

Each solution is then compared to the detected interface based on the sum of the square errors between the solution and the detected interface

$$ERROR = \sum_{i=1}^{n} \left(z_\mathrm{int,calc}(y_i) - z_\mathrm{int,det}(y_i)\right)^2. \tag{3.10}$$

Finally, the interface representation with the least square error sum is chosen as the right solution, with the apparent contact angle θ being the one resulting in the most accurate interface representation. The parameter B resulting in this interface representation can be seen as a deviation term from the static pressure balance (see section 4.4). It accounts not only for residual curvature, caused by the second wall of the single capillary slot, but also for other disturbances of the balance like for example inertia forces due to surface motion, making this procedure also applicable for non-static cases. The average velocity of the liquid/vapour-interface can then be calculated from the interface fit as follows:

$$v_\mathrm{int}(\tau) = \frac{1}{n\Delta\tau_\mathrm{B/W}} \sum_{i=1}^{n} \left[z_\mathrm{int,calc}\left(y_i, \tau + \Delta\tau_\mathrm{B/W}\right) - z_\mathrm{int,calc}\left(y_i, \tau\right)\right] \tag{3.11}$$

This Young-Laplace-based fitting procedure is with a computation time of approx. 3 minutes/picture much slower than a fitting procedure using a conical section equation, which takes approx. 1.5 seconds/picture. The reason for this method being so time consuming is that the *ERROR* matrix contains local minima. Therefore a gradient based minimum search is not possible. Each *ERROR* Value of the possible solutions must be calculated individually and the absolute minimum must be searched afterwards. Furthermore each solution stored in the lookup table must be individually re-mapped to the detected pixel values, as the ODE solver uses an adaptive resolution in y-direction, depending on local derivatives (higher resolutions are used at locations with high derivative). Nevertheless, a reduction of the computation time to approx. 20 seconds/picture is achieved by pre-evaluating the contact angle: A linear fit is applied to the rightmost 10 pixels of the interface. An approximation of the contact angle is calculated, which is then used to narrow the range of possible contact angles to

±5° of the linear approximation. This procedure reduces the number of possible solutions from 40 341 to 5151.

Even though a conical section fit would be much faster, it suffers from several disadvantages. Especially the choice of the initial guess of the parameters was found to have an impact. In some cases, the conical section fitting algorithm was found to be not converging for a badly chosen initial guess. As the parameters in equation (3.4) have no physical basis, there is no possibility to make an educated initial guess. "Good" initial conditions must be found by trial and error. Furthermore, the quality of a conical section fit depends on the y-range of the interface fitted. The quality of the fit decreases with increasing y-range of the ROI. The quality of the Young-Laplace-based fit in contrast is independent of the y-range of the ROI and always results in an excellent fit, as long as the interface is detected correctly. Also, in contrast to a conical section, this Young-Laplace-based fitting procedure is physically based, making it a very elegant method. Therefore, the Young-Laplace based method is chosen to determine contact angle and interface velocity. The output of the Young-Laplace-fit is shown in figure 3.10, e) along with the ROI of the raw image.

The whole fitting procedure can be summarized in the following steps:

1. Calculate look-up table with possible solutions of the Young-Laplace pressure balance according to the ODE system given by equations (3.7) - (3.9) (once for each measurement sequence).
2. Load image, calculate gray-scale gradients in the direction parallel to the channel walls.
3. Filter gradient image to eliminate camera noise.
4. Calculate boolean matrix b from mean gradients and standard deviation.
5. Delete areas with less than 200 connected pixels from boolean matrix b
6. Remove particles in the optical path from the gradient image by multiplying it elementwise with b.
7. Detect liquid/vapour-interface by finding the minimum of each column of the revised gradient image within the ROI.
8. Calculate linear approximation of the rightmost 10 pixel of the ROI and the approximate contact angle.
9. Calculate square errors of the detected interface to all possible solutions stored in the look-up table for angles of ±5° of the linear approximation.
10. Select solution with the least square error and save the result.

The counter detection accuracy close to the heater wall is crucial for the accuracy of the contact angle determination, as the experiment fluid is highly wetting. If the optical axis of the B/W-camera is slightly tilted against the central axis of the capillary slot, a certain region close to the wall is shadowed by half the width $w = 23\,\mathrm{mm}$ of the heater, as illustrated in figure 3.11.
The width b of the shadow thrown by the heater surface at a given tilt angle α can be calculated easily:

$$b = \frac{1}{2} w \sin\alpha. \tag{3.12}$$

A tilt angle as small as $\alpha = 0.1\,°$ already results in a width of the heater shadow of $b = 20\,\mu\mathrm{m}$, which corresponds to 5 pixel directly at the wall, where no information about the shape of the interface is available. Alignment of the BW camera with the capillary slot cannot be guaranteed to be below 0.1 °

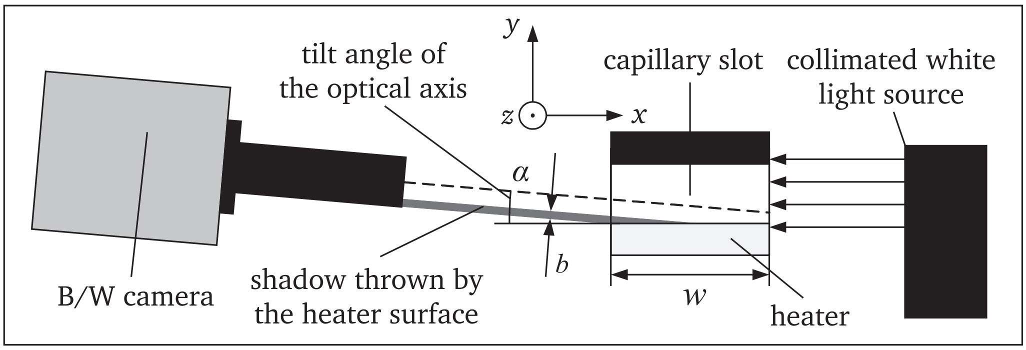

Figure 3.11.: Illustration of the geometric relationship that lead to shadowing effects due to a small tilt angle of the BW camera optical axis

in the experiment setup. Therefore, the determined contact angles do not necessarily exactly represent the apparent contact angle and only trends of the contact angles determined in-situ can be compared to other experimental results or numerical calculations.

3.5.2 IR thermography for wall temperature measurements

High speed IR thermography has been chosen to measure the wall temperature distribution for reasons closely described in section 2.3.

There are three possibilities to distinguish between IR camera systems [65]: Either by the optical arrangement, by the detector technology or by the wavelength band of the camera. The two optical arrangement possibilities are scanning systems and staring systems: In a staring system the object, which is to be measured, is projected through a lens system onto a focal plane detector array. In a scanning system, each point of the measurement object is scanned point by point in sequence over a system of moving mirrors and prisms onto a single detector element, which introduces additional measurement noise. Therefore most modern IR cameras are staring systems.
The detector itself can be either a micro-bolometer array or a semi-conductor photon detector chip. Micro bolometers work in the long wavelength IR (LWIR, 8 μm ... 12 μm) bandwidth and measure the incident radiation through the change of temperature on the sensing pixel element caused by the radiation. The advantage of this sensor technology is that it must not be cooled and can therefore be built into very compact IR cameras, but as the measurement is temperature based the thermal inertia of the sensor deny its use in high-speed IR cameras. Photon detector chips are manufactured from different semi-conductor materials and work depending on the material in the short wavelength IR (SWIR, 0.4 μm ... 2...3 μm) bandwidth, the medium wavelength IR (MWIR, 2...3 μm ... 5 μm) bandwidth or the LWIR bandwidth. The disadvantage of these systems is, that they must be actively cooled to reach acceptable photon counts (and therefore signal to noise ratios), which results in a larger size of such camera systems. On the other hand the integration time is not restricted by thermal inertia of the sensor, as it is the case for micro-bolometer arrays. As a result so much higher frame rates can be achieved with semi-conductor detectors.

The IR camera[13] used in the frame of this work is a staring semi-conductor photon detector camera working in the spectral range of 3.4 - 5.1 μm with 14 bits ($2^{14} = 16384$) digital resolution. A field of view of 224 pixel × 224 pixel is resolved by $\Delta x_{\mathrm{res,IR}} = 29.27\,\mu\mathrm{m/pixel}$, resulting in a FOV of 6.56 mm × 6.56 mm. The camera records images with a framerate of $f_{\mathrm{IR}} = 1000\,\mathrm{Hz}$ (synchronized to

---

[13] Thermosensorik® CMT 256 M HS

the high speed B/W camera). During the integration time, each pixel of the detector chip is discharged corresponding to the received signal (net radiative energy flow at the pixel). The remaining charge of all pixels is read out and mapped to the digital resolution of the camera with 16 383 being still fully charged and 0 being fully discharged. Higher temperatures result in higher energy fluxes introduced into the pixel and therefore lower digital values. Each integration time has therefore a saturation temperature at which the pixel is fully discharged and no higher temperature can be measured (see section 3.5.5, figure 3.18).

According to the Stefan-Boltzmann law, the radiative energy emitted by a black body surface is given by [66]

$$j = n^2 \sigma_{\mathrm{SB}} T^4. \tag{3.13}$$

Herein, j is the radiative energy flux, n is the index of refraction of the medium the radiation is emitted into and σ_{SB} is the Stefan-Boltzmann constant. In many applications n^2 is set to one, as radiation is emitted into air, but as in case of the heater radiation is emitted into the $\mathrm{CaF_2}$ substrate, n is different from 1 and must be considered. The emitting surface is the CrN surface, which is characterized by an unknown emission coefficient $\varepsilon_{\mathrm{rad,CrN}}$. The total radiative energy flow emitted by the surface is thereby given by

$$J_{\mathrm{CrN}} = A\,\varepsilon_{\mathrm{rad,CrN}} n^2 \sigma_{\mathrm{SB}} T^4 + \rho_{\mathrm{rad,CrN}} J_{\mathrm{sur}}. \tag{3.14}$$

In this equation J_{CrN} is the radiative energy flow, A the surface area seen by the pixel, $\varepsilon_{\mathrm{rad,CrN}}$ the emissivity of the surface area seen by the pixel, $\rho_{\mathrm{rad,CrN}}$ the reflectivity of the surface area seen by the pixel and J_{sur} the radiative energy flow coming from the surroundings. This radiation is damped by absorption within the $\mathrm{CaF_2}$ substrate [67]

$$J(z) = J_{\mathrm{CrN}} e^{-kz} = \tau_{\mathrm{rad,CaF}} J_{\mathrm{CrN}}. \tag{3.15}$$

According to transmittance data provided by the manufacturer of the $\mathrm{CaF_2}$ substrates [59] the mean absorption coefficient of the substrate material is calculated to be $k = 5.1293 \cdot 10^{-4}\,\mathrm{mm^{-1}}$ in the spectral range of the IR camera. At a thickness of $z = 4\,\mathrm{mm}$, this results in a transmissivity of $\tau_{\mathrm{rad,CaF}} = 0.998$. Combining radiative energy conservation with Kirchhoff's law for a system in thermodynamic equilibrium results in the following relationship

$$\tau_{\mathrm{rad,CaF}} + \rho_{\mathrm{rad,CaF}} + \varepsilon_{\mathrm{rad,CaF}} = 1. \tag{3.16}$$

Within the medium, no reflection occurs, so the emissivity of the substrate material is given by

$$\varepsilon_{\mathrm{rad,CaF}} = 1 - \tau_{\mathrm{rad,CaF}} = 0.002. \tag{3.17}$$

Equation (3.17) shows, that the radiation emitted by the substrate is negligible and must not be taken into account, in contrast to a method using a semi-transparent medium which was developed by Kim et al. [68].

Combining equations (3.14) and (3.15) and considering the radiation J_{pix} emitted by the physical pixel of the measurement detector chip itself, the net radiation introduced into each pixel of the chip is given by

$$J = \tau_{\mathrm{rad}} A\,\varepsilon_{\mathrm{rad,CrN}} n^2 \sigma_{\mathrm{SB}} T^4 + \tau_{\mathrm{rad}} \rho_{\mathrm{rad,CrN}} J_{\mathrm{sur}} - J_{\mathrm{pix}}. \tag{3.18}$$

In this equation, τ_{rad} is the overall transmissivity of the heater substrate, the IR camera lens system and the air in between the detector and the heater. Unfortunately, the exact chip characteristics and internal data transformations of the camera electronics is not known, but based on equation (3.18) and the digital resolution of the camera of 14 bits a physically based calibration function between the temperature t and the digital intensity representation I_{dig} can be formulated [40]

$$t = A\left[\left(16\,383 - I_{\mathrm{dig}}\right) + B\right]^{1/4} + C. \tag{3.19}$$

From the physical point of view, the constants A and B account for unknown radiation properties (as they appear in equation (3.18)) as well as linear pixel characteristics including gain, offset and integration time. The constant C accounts for unknown data processing conducted by the framegrabber of the camera.

To calibrate the IR camera a copper block is pressed onto the chromium heating layer of the heater after the measurements. The copper block is thermalized through interior channels by a thermostat. Neither the heater, nor the IR camera are moved in between measurements and calibration. As reference temperature a type K thermocouple is installed in the centre of the calibration block at a distance of approx. 1 mm to the interface to the heater. Several uniform constant temperature levels are adjusted. Stationarity and uniformity of each temperature level are ensured by checking that no more changes of the thermocouple temperature and the raw data of the IR camera can be observed. At each temperature level, 500 frames are recorded with the IR camera, with the exact same framerate and integration time as it is used in the measurements. The intensity values of each pixel are averaged over the 500 frames and correlated to the temperature measurement of the thermocouple: The constants $A(x,z)$, $B(x,z)$ and $C(x,z)$ in equation (3.19) are determined *for each pixel* of the IR camera through a least square errors curve fitting algorithm in MATLAB®. In figure 3.12 exemplary calibration curves for three pixels of the IR camera FOV are shown for an integration time of 0.5931 ms. It can be seen that the calibration points are matched extremely well by the calibration curves using the respective calibration constants. On the other hand it can also be seen that there can be a considerable deviation between the calibration curves of different pixels, making this pixel-wise in-situ calibration procedure indispensable.

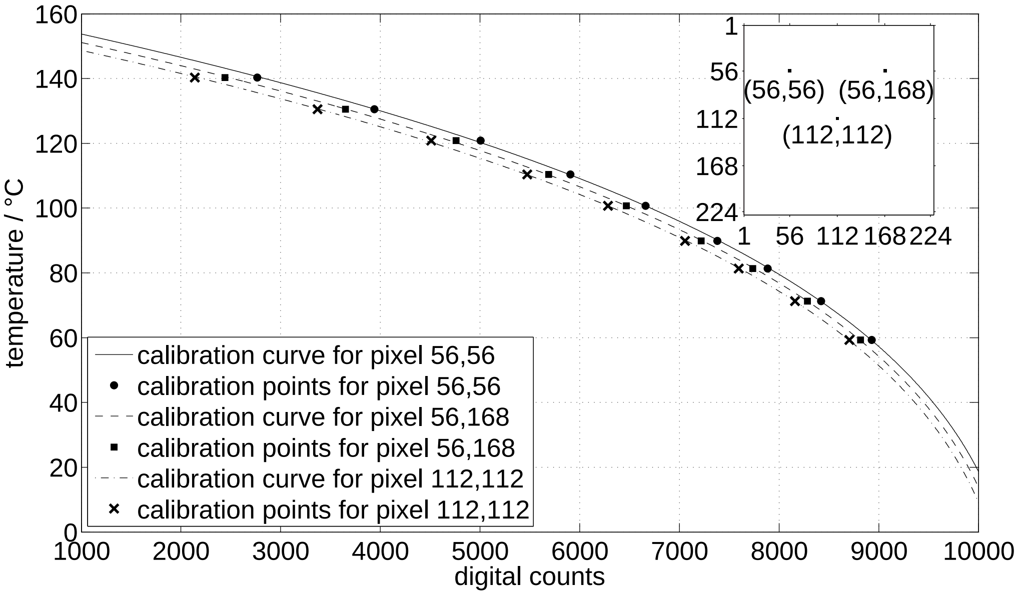

Figure 3.12.: Exemplary calibration curves for three pixels of an IR camera calibration with 0.5931 ms integration time (pixel positions within the IR FOV are shown in the upper right corner)

To reduce temperature gradients introduced by measurement noise of the IR camera (see section 3.5.5) the calculated temperature fields are smoothed using a Gaussian filter. This is extremely important for the heat flux calculation procedure, as it reacts very sensible onto the high local temperature gradients introduced by IR camera noise. The resulting temperature fields are then averaged along x-direction to produce line temperature profiles

$$t_{\mathrm{lp}}(z,\tau) = \frac{1}{184} \sum_{x=21}^{204} t(x,z,\tau). \tag{3.20}$$

3.5.3 Heat flux calculation procedure

When investigating contact line heat transfer the local heat flux from the wall to the fluid is of major interest. When using thin foil heaters the assumption can be made that the temperature is uniform across the thickness of the heater. By applying a two-dimensional energy balance for each pixel and using a finite differences approximation for the derivatives, the local heat flux from the wall to the fluid can be calculated. This method has for example been used by Kenning et al. [69, 70, 71], Golobic et al. [72, 73], Wagner et al. [74, 75, 76] and Ibrahem et al. [41, 42, 43]).

In contrast to thin foil heaters, the assumption of uniform temperature across the entire thickness of the heater element does not hold true for the comparably massive CaF_2 heater substrate. Therefore a three-dimensional energy balance must be applied to calculate the local heat flux. A comparable method was used by Chatzikyriakou et al. to calculate the heat flux during impact of non-wetting droplets onto a heated surface [56].

Numerical Scheme

The governing equation for heat transfer within the CaF_2 heater substrate is given by

$$\frac{\partial T}{\partial \tau} = \alpha_{\mathrm{CaF}} \nabla^2 T. \tag{3.21}$$

Herein α_{CaF} is the thermal diffusivity of the substrate material. The substrate block below the IR camera FOV is discretized into finite volumes and equation (3.21) is solved on this grid using the CFD-code OpenFOAM®. As the sputtered layers at the heater/fluid-interface are extremely thin in comparison to the substrate thickness of 4 mm, the thermal resistance and energy storage of the sputtered layers are negligible and they are not included in the numerical calculation. In order for the numerical calculation to be stable the Courant number

$$\mathrm{Co} = \frac{v_0 \Delta \tau_{\mathrm{num}}}{\Delta x_{\mathrm{num}}} \tag{3.22}$$

must be below 1. The maximum velocity v_0 with which information can propagate in the numerical calculation can be calculated by

$$v_0 = \frac{\alpha_{\mathrm{CaF}}}{\Delta x_{\mathrm{num}}}. \tag{3.23}$$

Inserting the data for $\alpha_{\mathrm{CaF}} = 3.575 \cdot 10^{-6}\,\mathrm{m^2\,s^{-1}}$ and $\Delta x_{\mathrm{num}} = \Delta x_{\mathrm{res,IR}} = 29.27 \cdot 10^{-6}\,\mathrm{m}$, this criterion for the Courant number can be used for determination of the maximum time step size:

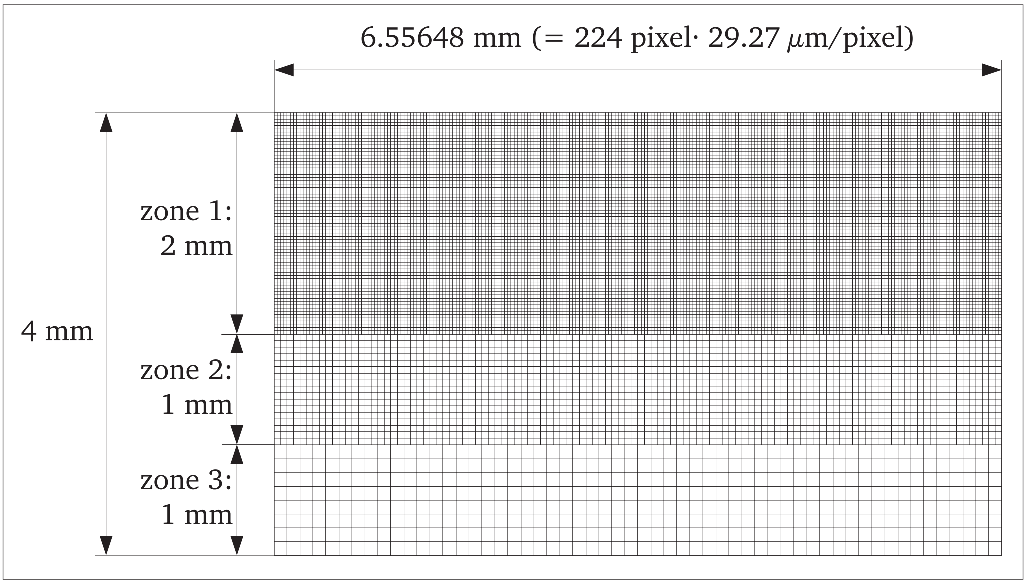

Figure 3.13.: Numerical mesh for the heat flux calculation

$$\Delta\tau_{\mathrm{num,max}} \overset{!}{<} 0.239\,\mathrm{ms} \tag{3.24}$$

As the framerate of the IR camera only provides temperature fields with a time spacing of $\Delta\tau_{\mathrm{IR}} = 1\,\mathrm{ms}$, the temperature fields are linearly interpolated in between frames to realize a time step size of $\Delta\tau_{\mathrm{num}} = 0.1\,\mathrm{ms}$ (and hereby a Courant number of $\mathrm{Co} = 0.417$) to ensure convergence of the calculation.

Mesh

The volume of the CaF_2 substrate below the IR camera FOV is discretized into a numerical mesh with three different zones (see figure 3.13). In the uppermost zone (zone 1) the lateral cell size is defined by the IR camera resolution. Up to a depth of 2 mm the volume is resolved by 68 cells in thickness direction, which corresponds to an aspect ratio close to 1. Such a fine resolution of the entire heater substrate would result in a total number of 6.8 million cells and very large computation times. To decrease computation time the resolution is divided by two from a depth between 2 mm and 3 mm (zone 2) and by four from a depth of 3 mm onwards (zone 3), as the temperature gradients that are to be expected in these depths are much smaller than close to the heater/fluid-interface. By this step-wise coarsening of the mesh the total number of cells is reduced to 3.6 million cells. A comparison of calculations performed on a fully resolved mesh and the step-wise coarsened mesh yielded no significant differences for the heat flux calculated at the heater/fluid-interface.

Boundary conditions

In figure 3.14 the boundary conditions used for the numerical heat flux calculation are illustrated. On the top boundary of the calculation domain, which corresponds to the interface between CaF_2 substrate and the CrN emissivity layer, the smoothed temperature fields acquired through IR thermography are used to determine the boundary condition. As stated before it is necessary to interpolate the temperature fields in between the frames of the IR camera to ensure convergence of the calculation

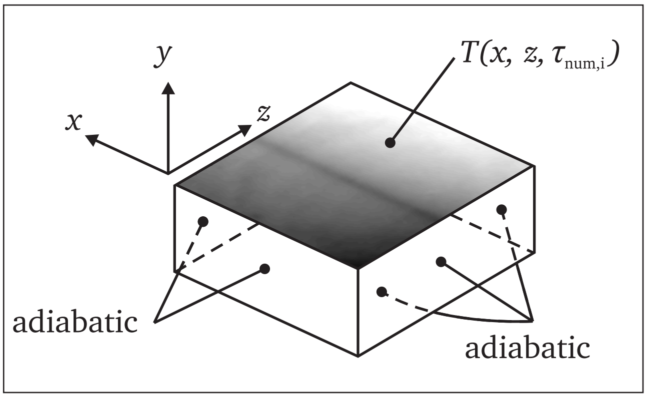

Figure 3.14.: Boundary conditions for the heat flux calculation

$$T\left(x,z,\tau_{\mathrm{num,i}}\right)=T\left(x,z,\tau_{\mathrm{IR}}\right)+\frac{i}{10}\left[T\left(x,z,\tau_{\mathrm{IR+1}}\right)-T\left(x,z,\tau_{\mathrm{IR}}\right)\right]\ \text{with}\ i=1...10. \tag{3.25}$$

Between the two subsequent frames of the IR camera at time τ_{IR} and $\tau_{\mathrm{IR+1}}$ ($\Delta\tau_{\mathrm{IR}}=1\,\mathrm{ms}$) the temperature field at the numerical time $\tau_{\mathrm{num,i}}$ is calculated by a linear interpolation of ten values at each pixel, so that $\Delta\tau_{\mathrm{num}}=0.1\,\mathrm{ms}$. For the other surfaces of the calculation domain adiabatic boundary conditions are assumed. The validity of this assumption and its influences onto the heat flux calculation are further discussed in section 3.5.5.

Initial condition

As initial condition the 3D temperature field $T(x,y,z,\tau_{\mathrm{num,0}})$ in the computation domain is set to the steady state solution computed from the first 2D temperature field $T(x,z,\tau_{\mathrm{IR,0}})$ obtained from IR thermography.

Post processing

The outcome of the numerical calculation are two-dimensional heat flux fields at the interface between CaF_2 substrate and the CrN emissivity layer. Under the assumption of uniform electrical heating in the pure Cr layer and negligible thermal resistance and energy storage of the sputtered layers, the heat flux at the heater/fluid-interface is calculated as

$$q\left(x,z,\tau\right)=q_{\mathrm{num}}\left(x,z,\tau\right)+q_{\mathrm{in}}\left(\tau\right). \tag{3.26}$$

In equation (3.26) q_{num} is the outcome of the numerical calculation and q_{in} is the heat flux introduced into the system by Joule heating of the Cr layer. The input heat flux q_{in} is given by

$$q_{\mathrm{in}}\left(\tau\right)=\frac{R_{\mathrm{hl}}I\left(\tau\right)^2}{l_{\mathrm{hl}}w_{\mathrm{hl}}}. \tag{3.27}$$

In this equation R_{hl} is the electrical resistance of the heating layer, l_{hl} and w_{hl} are length and width of the heating layer and I is the electric current supplied to the heating layer, which is measured by the DAQ. The resulting heat flux field is then averaged along x-direction to produce heat flux line profiles:

$$q_{\mathrm{lp}}(z,\tau) = \frac{1}{184}\sum_{x=21}^{204} q(x,z,\tau) \tag{3.28}$$

3.5.4 Heat flux tracking for contact line velocity determination

The shadowgraphy method to determine the meniscus velocity described in section 3.10 requires high contrast at the liquid/vapour-interface. At elevated reduced pressures the density ratio (and by that the ratio of the indices of refraction) is reduced, which leads to lower contrast at the interface. For acetone droplets in a nitrogen atmosphere the sharpness of the interface was reported to be significantly reduced at a reduced temperature of the droplet of only $T_{\mathrm{R}} = 0.917$ [77]. For FC-72, this corresponds to a temperature of $t_{\mathrm{sat}} = 138.6\,°\mathrm{C}$, or under saturated conditions a reduced pressure of $p_{\mathrm{R}} = 0.47$. This effect is illustrated in figure 3.15, in which two stationary FC-72 menisci at a reduced pressure of $p_{\mathrm{R}} = 0.05$ (left) and at a reduced pressure of $p_{\mathrm{R}} = 0.5$ (right) are displayed. While the liquid/vapour-interface is clearly visible in case of a low reduced pressure, it can hardly be identified in case of the high reduced pressure. Because of the low contrast, the contour detection algorithm outlined in section 3.10 is not capable to retrieve reliable information about the meniscus and contact line movement from processing of the B/W images.

Across all investigated reduced pressures however, the heat flux fields were found to exhibit a distinct maximum at the contact line and strong gradients close to the contact line. In figure 3.16 an exemplary heat flux line profile (solid line, left axis) is plotted along with its gradient in ξ-direction (dashed line, right axis) to illustrate the distinctive peaks in heat flux and heat flux gradient, which are used for an alternative method to calculate the the contact line velocity:

From the heat flux line profiles q_{lp} (heat flux field averaged along x-direction, solid line in figure 3.16) the heat flux gradient along z/ξ-direction is calculated (dashed line in figure 3.16). The contact line position is then found by searching for the local maximum of the heat flux line profile between minimum and maximum of the heat flux gradient. A quadratic fit (to allow for constant acceleration of the interface) is applied to the time-dependent positions of the maximum heat flux and the positions of maximum and minimum heat flux gradient along z/ξ-direction. Apart from the interface velocity, which can be calculated from the fit of the heat flux gradient, the width of the region with increased heat transfer can be calculated, which is of importance if a thin evaporating liquid film remains on the heater surface (see section 4.5.1). In figure 3.17 an exemplary plot of the determined positions

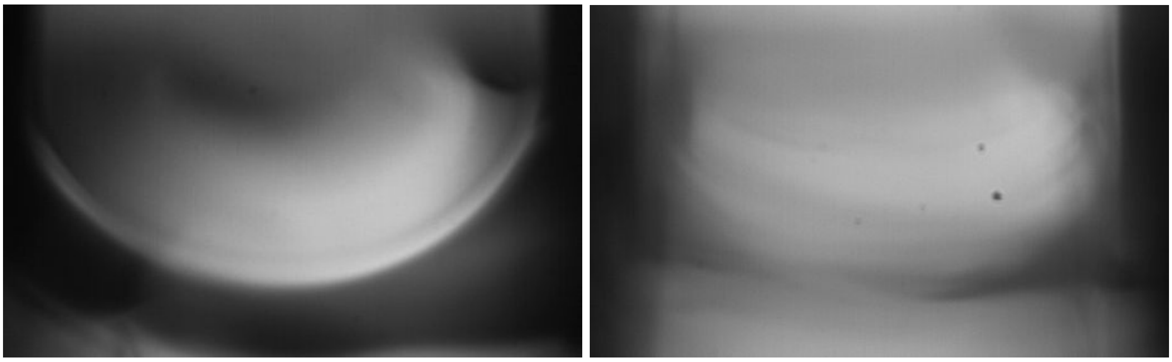

Figure 3.15.: Stationary FC-72 menisci at a reduced pressure of $p_{\mathrm{R}} = 0.05$ (left, high contrast at the interface) and at a reduced pressure of $p_{\mathrm{R}} = 0.5$ (right, low contrast at the interface)

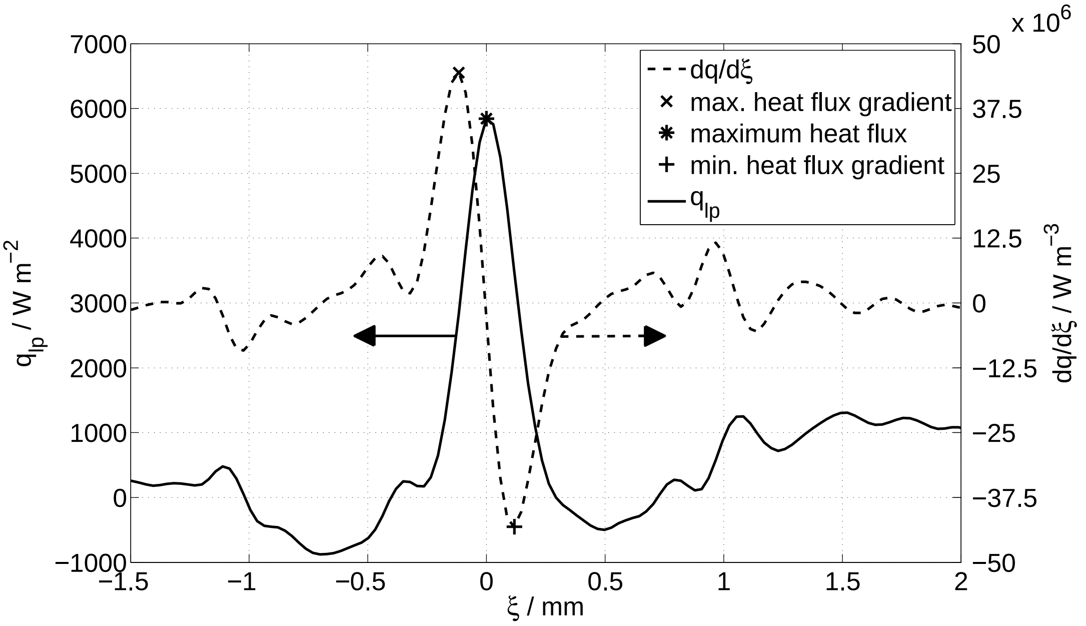

Figure 3.16.: Exemplary plot of the heat flux line profile and its gradient in ξ-direction versus the ξ-coordinate

(relative to the image centre) of the heat flux maximum, as well as the positions of the maximum and minimum heat flux gradient versus time is displayed. As it can be seen in figure 3.17, the quadratic term of the fit and thereby the acceleration of the liquid/vapour-interface was found to be negligible in most sequences with constant stepper motor velocity.

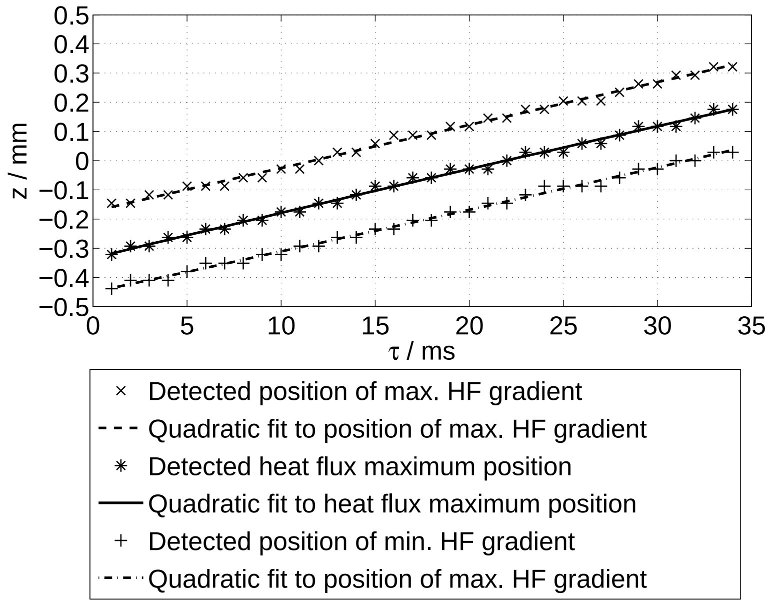

Figure 3.17.: Exemplary plot of detected heat flux maximum position and detected positions of the maximum and minimum heat flux (HF) gradient along with the respective quadratic fits versus time for an advancing contact line

Measurement uncertainties calculated in this section are based on the worst case assumption of linear error propagation.

Temperature measurements

The type K thermocouples (TC) used in the setup were carefully calibrated along with the complete measurement chain prior to the measurements against a Pt100 temperature probe as reference temperature. The Pt100 itself was calibrated by the German calibration service (Deutcher Kalibrierdienst, DKD) to a certified absolute accuracy of $\Delta T_{\mathrm{Pt100}} = \pm 0.15\,\mathrm{K}$. From the recorded temperatures a calibration polynomial was calculated and again checked versus the Pt100 reference temperature. All thermocouples were found to be within $\Delta T_{\mathrm{TC}\leftrightarrow\mathrm{Pt100}} = \pm 0.13\,\mathrm{K}$ from the reference temperature. This results in relative and absolute measurement uncertainties for the thermocouples of

$$\Delta T_{\mathrm{TC,rel}} = \Delta T_{\mathrm{TC}\leftrightarrow\mathrm{Pt100}} = \pm 0.13\,\mathrm{K}, \tag{3.29a}$$

$$\Delta T_{\mathrm{TC,abs}} = \Delta T_{\mathrm{TC}\leftrightarrow\mathrm{Pt100}} + \Delta T_{\mathrm{Pt100}} = \pm 0.28\,\mathrm{K}. \tag{3.29b}$$

Pressure measurements

The pressure transducer used in the experiment provides a measurement accuracy of 0.05 % full scale at a measurement range of 0 bar ... 25 bar and 0 V ... 10 V output. This results in a measurement uncertainty of the sensor of $\Delta p_{\mathrm{sensor}} = \pm 12.5\,\mathrm{mbar}$. In addition to the measurement uncertainty of the sensor, an additional uncertainty is introduced by the DAQ voltage read out uncertainty of $\Delta U_{\mathrm{DAQ}} = \pm 980\,\mu\mathrm{V}$. The overall pressure measurement uncertainty can be calculated as

$$\Delta p_{\mathrm{abs}} = \Delta p_{\mathrm{sensor}} + \frac{\mathrm{d}p}{\mathrm{d}U}\Delta U_{\mathrm{DAQ}} = \pm 14.95\,\mathrm{mbar}. \tag{3.30}$$

IR thermography

In figure 3.18 the mean temperature sensitivity curves for different integration times of the IR camera are plotted versus temperature in the corresponding calibration ranges (standard deviations are not included for better readability, but were always smaller than 0.005 K).

It can be seen that it is always recommendable to choose an integration time as large as possible (which was done in this work), as this increases the sensitivity of the measurement. However, an adequate threshold must be kept to the maximum temperature, at which the pixels would reach saturation (readout of 0 digital counts, see section 3.5.2). As the calibration curves tend to be very flat at high temperatures, differ for each pixel (see figure 3.12) and are not known at the time of the measurement the integration times were chosen such, that a margin of at least 10 °C was kept between the expected temperatures and the maximum measurable temperature.

Like all electronic measurement devices, the chip of an IR camera has a certain noise level, that introduces measurement uncertainties. The noise equivalent temperature difference (NETD) representing this measurement uncertainty is due to the measurement principle a function of temperature and the optical setup of the measurement, which makes the quantity difficult to compute. The NETDs

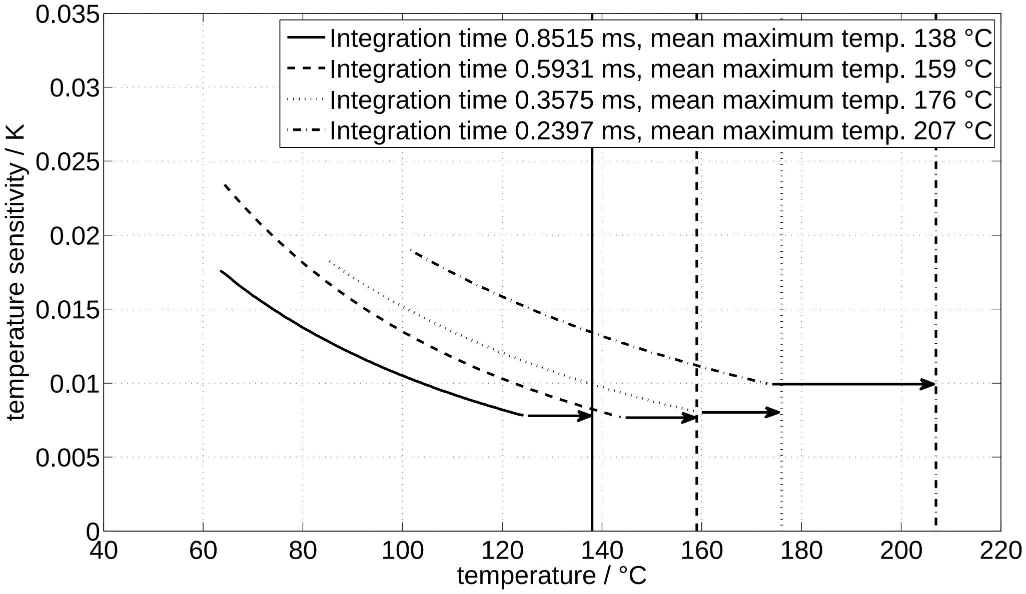

Figure 3.18.: Mean temperature measurement sensitivity for different integration times of the IR camera. Arrows indicate distance between calibration range and mean maximum measurable temperature at chip saturation

given by IR camera manufactures usually only cover the chip itself at a certain temperature level.
To calculate the NETD the calibration images are used. For each calibration, the difference between minimum and maximum temperature value of each pixel for all 500 images of the calibration sequence is calculated. As temperature is kept constant throughout the calibration, the temperature differences must be caused by noise of the IR camera chip. The mean NETD for different integration times of the IR camera are plotted versus temperature in figure 3.19 (standard deviations are not included

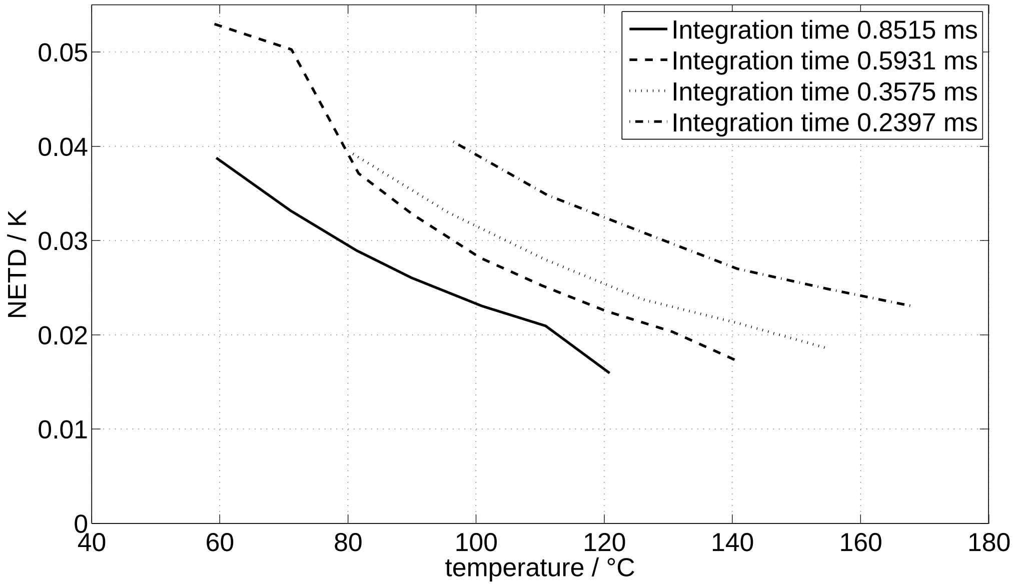

Figure 3.19.: Mean noise equivalent temperature differences (NETD) for different integration times of the IR camera

for better readability, but were in the order of 0.015 °C ... 0.04 °C). By summing up the maximum NETD in the temperature range, in which the evaluated calibration was used, with the possible error introduced by the digital resolution of the IR camera (as given in figure 3.18) the measurement uncertainty (including standard deviations) for the wall temperature measurements can be assessed. As calibration was performed using a thermocouple, the absolute measurement uncertainty is increased by the measurement uncertainty of the thermocouple

$$\Delta T_{\mathrm{IR,rel}} = \pm 0.125\,\mathrm{K}, \tag{3.31a}$$

$$\Delta T_{\mathrm{IR,abs}} = \Delta T_{\mathrm{IR,rel}} + \Delta T_{\mathrm{TC,abs}} = \pm 0.405\,\mathrm{K}. \tag{3.31b}$$

Heat flux calculation

To evaluate the uncertainty of the heat flux calculation procedure, the validity of the assumption of adiabatic boundary conditions at the sides and the backside of the calculation domain (see figure 3.14) has been analyzed. In figure 3.20 the information available at the surfaces of the CaF_2 substrate for estimation of the heat losses is illustrated. To evaluate the heat losses analytically or numerically, information at the side surfaces and most of the heater/fluid-interface of the heater substrate (top surface in figure 3.20) is missing.

Nevertheless, an estimation of the heat losses has been performed using a set of numerical calculations. For these calculations the whole volume of the heater substrate was discretized and the following boundary conditions were applied:

- Constant temperature (saturation temperature T_{sat}), where the CaF_2 substrate is glued onto the copper carrier plate (blue surface in figure 3.20).
- Constant heat transfer coefficient h at the rest of this surface (transparent lower surface in figure 3.20). h has been calculated using a Nusselt correlation for a vertical plate [78] .
- Constant homogeneous temperature ($T_{\mathrm{sat}} + \Delta T_{\mathrm{W}}$) at the whole heater/fluid-interface (top surface in figure 3.20).
- Adiabatic on all other surfaces (side surfaces of the CaF_2 substrate in figure 3.20).

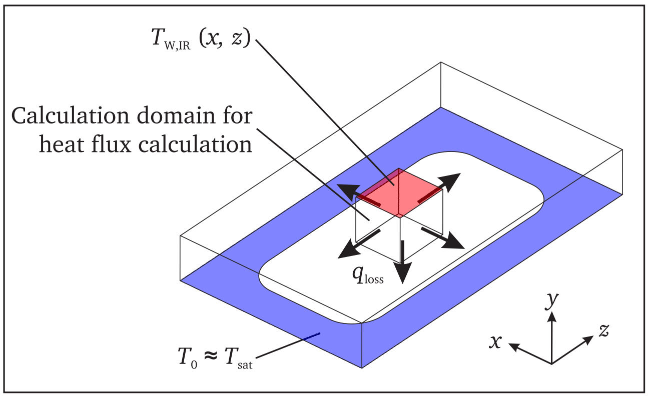

Figure 3.20.: Available information for estimating the heat losses across the boundaries of the calculation domain for the heat flux calculation procedure

Several steady state calculations have been performed using OpenFOAM® with different wall superheats of $\Delta T_\mathrm{W} = 1\,\mathrm{K} \ldots 10\,\mathrm{K}$ in steps of 1 K. During post processing the local temperature gradients (and thereby the heat flux) normal to the boundaries of the calculation domain of the heat flux calculation procedure (inner cuboid in figure 3.20) have been evaluated. The dependency of the heat transfer coefficient on the wall superheat and the temperature gradients on the position within the boundary and the wall superheat were approximated by polynomial equations

$$\frac{\mathrm{d}T}{\mathrm{d}x}\left(y,z,\Delta T_\mathrm{W}\right) = \left[A\Delta T_\mathrm{W} + B\right]\left[Cy^2 + Dz^2 + Eyz + Fy + Gz + H\right], \tag{3.32a}$$

$$\frac{\mathrm{d}T}{\mathrm{d}z}\left(x,y,\Delta T_\mathrm{W}\right) = \left[A\Delta T_\mathrm{W} + B\right]\left[Cx^2 + Dy^2 + Exy + Fx + Gy + H\right], \tag{3.32b}$$

$$h\left(\Delta T_\mathrm{W}\right) = \left[A\Delta {T_\mathrm{W}}^3 + B\Delta {T_\mathrm{W}}^2 + C\Delta T_\mathrm{W} + D\right]. \tag{3.32c}$$

Equation (3.32a) and (3.32b) correlate the spatially resolved temperature gradients at the side surfaces of the heat flux calculation domain to the mean surface superheat and equation (3.32c) correlates the heat transfer coefficient at the bottom surface of the heat flux calculation domain to the mean surface superheat.

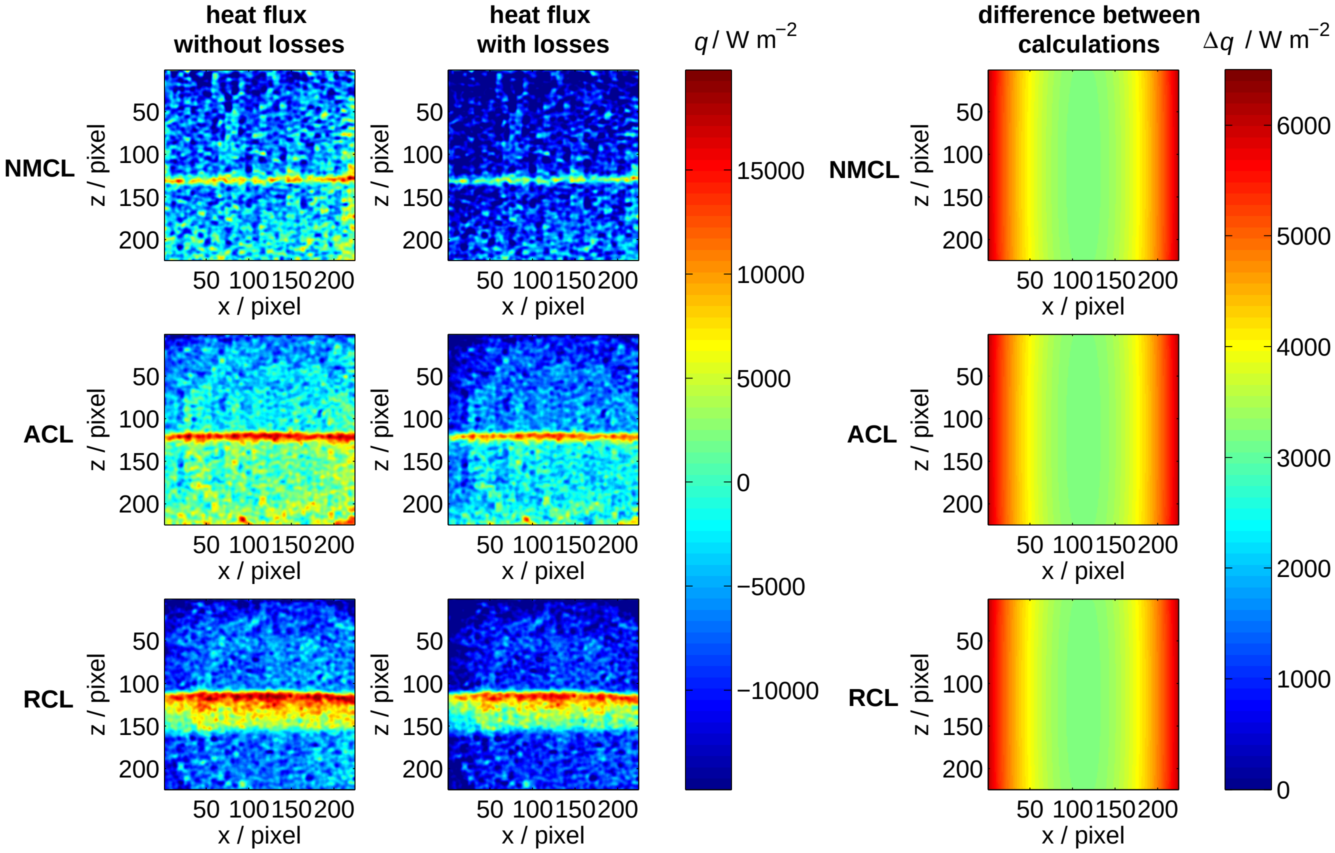

Figure 3.21.: Comparison of three exemplary heat flux calculations (upper row: Non-moving contact line, central row: Advancing contact line, lower row: Receding contact line) with adiabatic boundary conditions (left column) and non-adiabatic boundary conditions (central column) and the heat flux difference between both cases (right column)

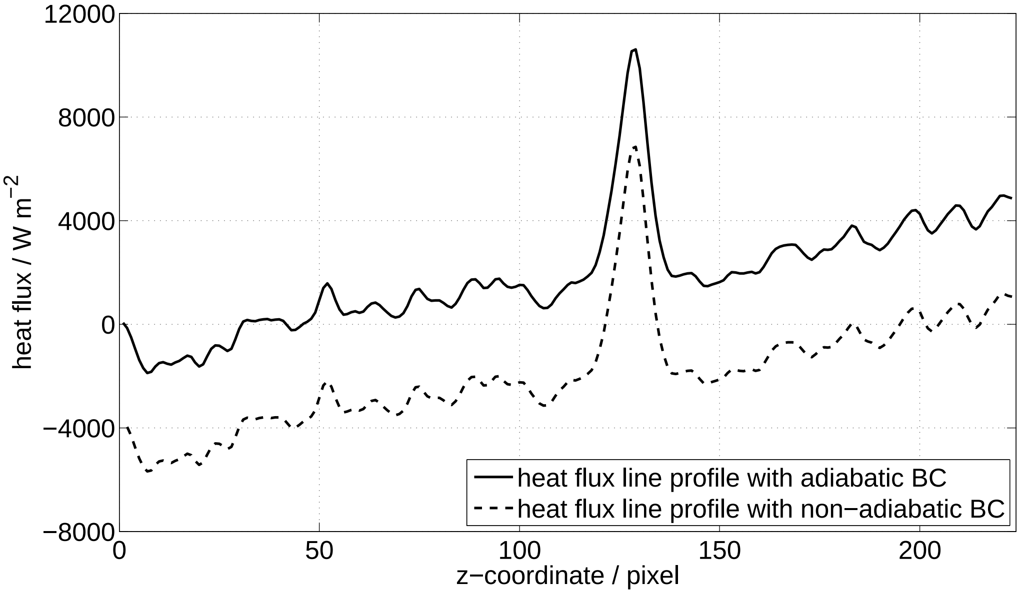

Figure 3.22.: Comparison of the heat flux line profiles with adiabatic and non-adiabatic boundary conditions for the non-moving contact line test case

Equations (3.32) have been implemented in the heat flux calculation procedure to replace the adiabatic boundary conditions as illustrated in figure 3.14. The heat flux field of three exemplary measurements (one with non-moving contact line (NMCL), one with advancing contact line (ACL), one with receding contact line (RCL)) have been re-calculated with the altered heat flux calculation procedure, that includes the heat loss approximations given by equations (3.32).

The outcome of these altered calculations and a comparison to the outcome of the original calculation method using adiabatic boundary conditions is displayed in figure 3.21. Apart from a global reduction of the heat flux, when non-adiabatic boundary conditions are used, all three test cases show an increasing discrepancy between the calculations close to the boundaries in x-direction. The reason for this discrepancy is that here the distance between calculation domain and heater carrier plate is smallest.
With non-adiabatic boundary conditions the mean heat flux has been found to be smaller than zero in all test cases, which is physically not possible. This paradox is caused by the assumption, that the temperature on top of the heater surface was homogeneous for estimating the losses. This is however not the case, as only a part of the substrate surface is coated with the heating layer (see figure 3.2). Therefore the losses are largely overestimated with the available information. In consequence the adiabatic boundary conditions must be closer to reality than the applied estimation method for non-adiabatic boundary conditions. For this reason the adiabatic boundary conditions are used.

Nevertheless, it could be shown that the influence of the boundary conditions is strongest close to the boundaries in x-direction. Therefore the outermost 20 pixel in x-direction are not taken into account for the heat flux line profile generation. In figure 3.22 the heat flux line profiles with and without loss estimation are plotted versus the z-coordinate for the non-moving contact line test case. It can be seen that both heat flux line profiles show the same curve progression with a constant offset in between the curves. The lack of exact knowledge of the heat losses is therefore of little impact onto comparative analysis of the heat flux line profiles, as long as sequences with equal wall superheat are compared.

The NETD of the IR camera due to camera noise naturally causes apparent deviations of the heat flux. One can refer to these heat flux fluctuations as noise equivalent heat flux difference (NEHFD). To evaluate the magnitude of the NEHFD, the heat flux fields during the central 200 images of each calibration sequence have been calculated using the method described in section 3.5.3. As temperature is constant and homogeneous during the calibration sequences, the heat flux should be equal to zero. For each calibration sequence the difference between minimum and maximum heat flux value of each pixel is calculated, which is equal to the NEHFD of this pixel. The mean NEHFD for different integration times of the IR camera are plotted versus temperature in figure 3.23 (standard deviations are not included for better readability, but were in the order of $2000\,\mathrm{W\,m^{-2}}$ ... $3500\,\mathrm{W\,m^{-2}}$).
The overall uncertainty of the heat flux transfered to the fluid is the sum of the NEHFD and the uncertainty in the input heat flux calculation. The uncertainty of the input heat flux is governed by the uncertainty of the current measurement. The laboratory power supply used for the heater has a maximum current output deviation of $\Delta I_{\mathrm{PS}} = 6\,\mathrm{mA}$ and maps its output range of 0 A ... 5 A to an analogue voltage signal of 0 V ... 10 V read out by the DAQ with an uncertainty of $\Delta U_{\mathrm{DAQ}} = 980\,\mu\mathrm{V}$. With the heating layer length of $l_{\mathrm{hl}} = 41.7\,\mathrm{mm}$ and its width of $w_{\mathrm{hl}} = 15\,\mathrm{mm}$ and the maximum product of heater resistance times input current of $\left(R_{\mathrm{hl}} I\right)_{\max} = 39.91\,\Omega{\cdot}200\,\mathrm{mA}$ this results in a maximum uncertainty of the input heat flux of

$$\Delta q_{\mathrm{in,max}} = 2\frac{R_{\mathrm{hl}} I}{l_{\mathrm{hl}} w_{\mathrm{hl}}} \left(\Delta I_{\mathrm{PS}} + \frac{\mathrm{d}I}{\mathrm{d}U} \Delta U_{\mathrm{DAQ}} \right) = \pm 165.64\,\mathrm{W\,m^{-2}}. \tag{3.33}$$

The NEHFD in the temperature range, in which the evaluated calibration was used, represents an estimation of the relative uncertainty of the heat flux calculation procedure (including standard deviations). An estimation of the absolute uncertainty of the heat flux fields can be calculated by adding the uncertainty of the input heat flux:

$$\Delta q_{\mathrm{rel}} = \pm 10\,500\,\mathrm{W\,m^{-2}} \tag{3.34a}$$

$$\Delta q_{\mathrm{abs}} = \Delta q_{\mathrm{rel}} + \Delta q_{\mathrm{in,max}} = \pm 10\,665\,\mathrm{W\,m^{-2}} \tag{3.34b}$$

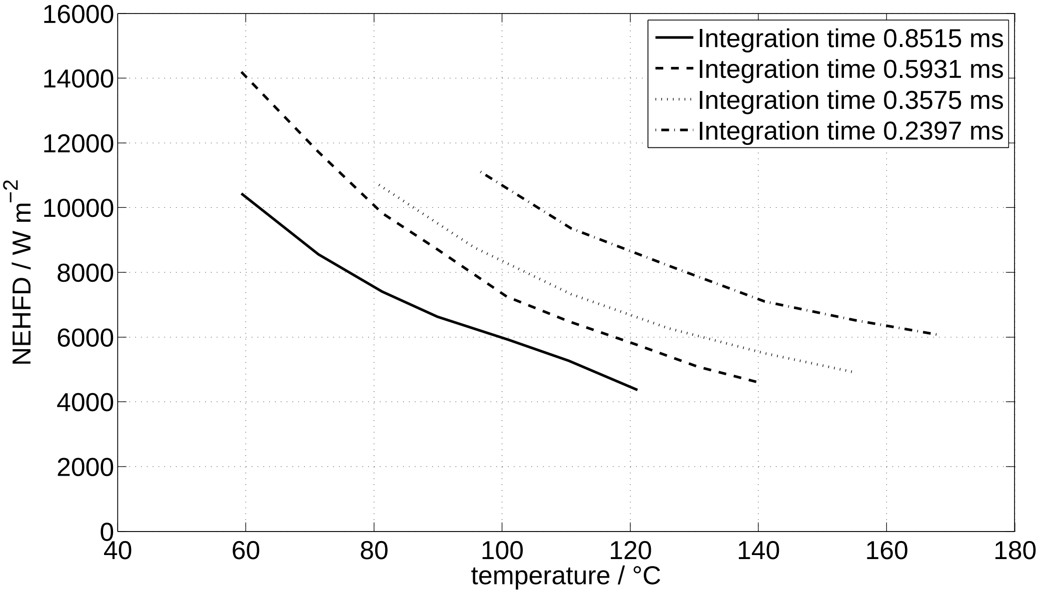

Figure 3.23.: Mean noise equivalent heat flux differences (NEHFD) for different integration times of the IR camera

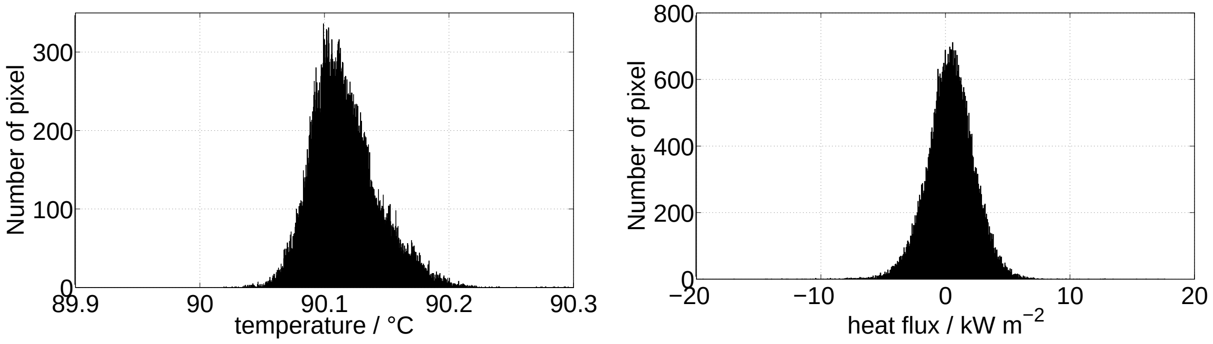

Figure 3.24.: Exemplary temperature (left) and corresponding heat flux (right) histogram for a single frame of a calibration point of the IR camera with an integration time of 0.5931 ms

Even though these values seem to be very high compared to the values presented in chapter 4, one should keep in mind that they are only maximum uncertainty estimations and are only valid for single time steps and single pixel of the heat flux fields. For the evaluation of the results, that are presented in the following chapter, the uncertainties of single pixel values are not relevant. What is of significance is the uncertainty of the temperature and heat flux line profiles, that are generated by averaging the fields in x-direction.

Temperature and heat flux line profiles

In figure 3.24 exemplary histograms for the temperature distribution and the heat flux distribution of a single frame of a calibration point of the IR camera are displayed. The normal distribution of the temperature and the heat flux data around the mean value is immediatly recognizable. For such a statistical distribution of the measurement noise the resulting relative uncertainty of the line profiles is diminished by the number of pixel $N = 184$ averaged to generate them [79]:

$$\Delta T_{\mathrm{lp,rel}} = \frac{\Delta T_{\mathrm{IR,rel}}}{\sqrt{N}} = \pm 9.215 \cdot 10^{-3}\,\mathrm{K} \tag{3.35a}$$

$$\Delta q_{\mathrm{lp,rel}} = \frac{\Delta q_{\mathrm{rel}}}{\sqrt{N}} = \pm 774.07\,\mathrm{W\,m^{-2}} \tag{3.35b}$$

The absolute uncertainty of the line profiles is therefore:

$$\Delta T_{\mathrm{lp,abs}} = \Delta T_{\mathrm{lp,rel}} + \Delta T_{\mathrm{TC,abs}} = \pm 0.289\,\mathrm{K} \tag{3.36a}$$

$$\Delta q_{\mathrm{lp,abs}} = \Delta q_{\mathrm{lp,rel}} + \Delta q_{\mathrm{in,max}} = \pm 939.71\,\mathrm{W\,m^{-2}} \tag{3.36b}$$

4 Results and discussion

4.1 Reference experiment

As reference experiment the local heat transfer at a non-moving meniscus at a system pressure of $p = 0.9\,\text{bar}$ is chosen. This corresponds to a reduced pressure of $p_\text{R} = 0.05$ and a saturation temperature of $t_\text{sat} = 53.0\,°\text{C}$. This experiment pressure has been chosen, as it is close to atmospheric pressure, which allows to compare the results presented in this section to local heat transfer measurements near the contact line during evaporation into the atmosphere possibly conducted in the future. The input heat flux was $q_\text{in} = 2500\,\text{W}\,\text{m}^{-2}$.

In figure 4.1 an instantaneous temperature field and heat flux field for the reference experiment are provided. It is immediately evident that the temperature minimum at the contact line that can be seen in the temperature field is in the order of $\sim 0.1\,\text{K}$. This is almost one order of magnitude lower than the values reported by Ibrahrem et al. [41], but is in the same order of magnitude as values measured by Höhmann [23, 24] and Migliaccio [39], who both used comparably thick heater designs.
In figure 4.2 the temperature and heat flux line profiles (temperature and heat flux field of figure 4.1 averaged in x-direction) are displayed. The factor between maximum heat flux at the contact line and input heat flux lies at $q_\text{max}/q_\text{in} \approx 2.7$. The heat flux below liquid and vapour approximately match the input heat flux. Below the vapour such a high heat flux is unlikely, as it can only be transported away from the heater surface by natural convection. This rather high heat flux is probably the result of the adiabatic boundary condition (see section 3.5.4, heat flux calculation). At the end of the measurement FOV, there is still a temperature gradient detectable in the temperature line profile, which indicates a heat flux across the upper boundary of the calculation domain, which is not taken into account by the

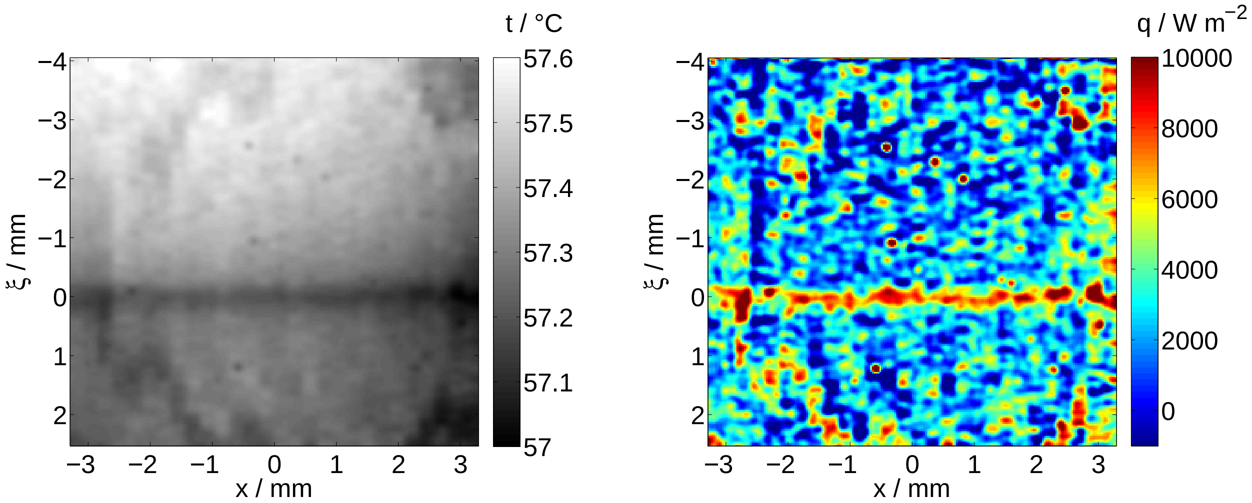

Figure 4.1.: Instantaneous temperature field (left) and heat flux field (right) at the heater/fluid-interface for a non-moving contact line at a reduced pressure of $p_\text{R} = 0.05$ and a mean wall superheat of $\Delta T_\text{W} = 4.5\,\text{K}$ ($q_\text{in} = 2500\,\text{W}\,\text{m}^{-2}$)

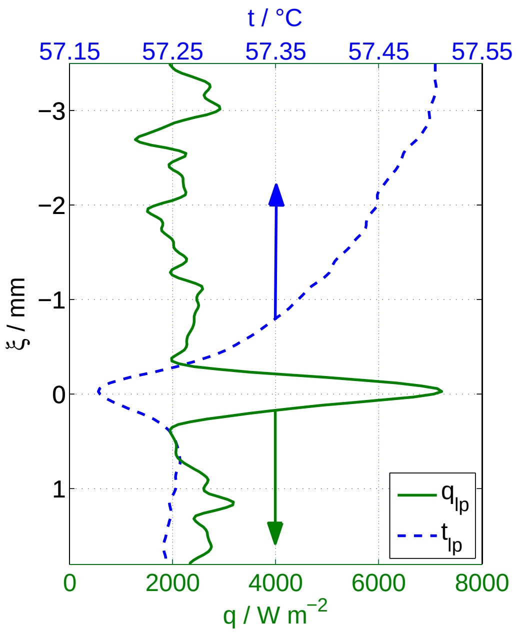

Figure 4.2.: Temperature and heat flux line profiles for a non-moving contact line at a reduced pressure of $p_\mathrm{R} = 0.05$ and a mean wall superheat of $\Delta T_\mathrm{W} = 4.5\,\mathrm{K}$ ($q_\mathrm{in} = 2500\,\mathrm{W\,m^{-2}}$)

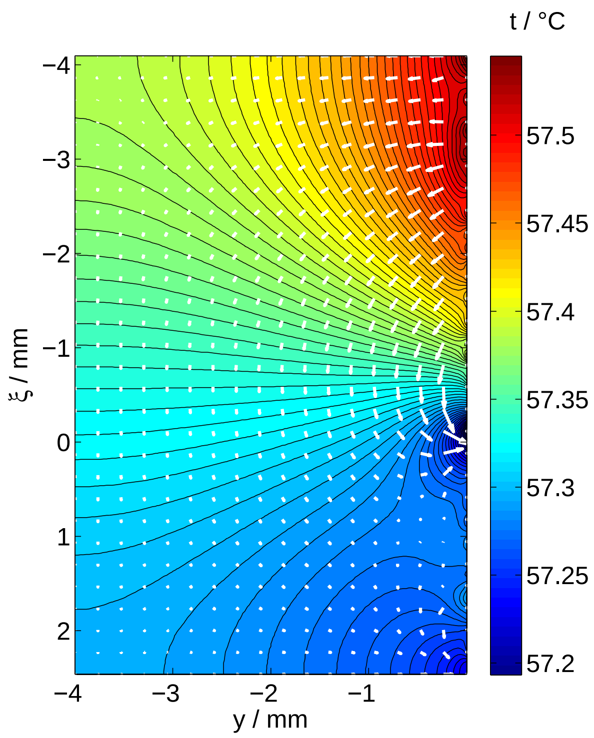

Figure 4.3.: Contour plot of the temperature distribution and heat flux vectors inside the heater substrate at the centre in x-direction for a non-moving contact line at a reduced pressure of $p_\mathrm{R} = 0.05$ and a mean wall superheat of $\Delta T_\mathrm{W} = 4.5\,\mathrm{K}$ ($q_\mathrm{in} = 2500\,\mathrm{W\,m^{-2}}$)

heat flux calculation.

A big advantage of the computationally expensive heat flux calculation technique is, that apart from the heat flux data at the heater/fluid-interface, it also supplies data on the 3-D-temperature distribution and energy flow within the heater material. In figure 4.3 a contour plot of the temperature distribution in the central plane of the heater substrate in x-direction is displayed along with the heat flux vectors. The position of the contact line is at $\xi = 0$, $y = 0$. One can clearly see that, while temperature homogeneity in y-direction is a reasonable assumption for thin foil heaters, it is far from being satisfied for the given heater substrate. A large amount of heat generated below the vapour is transferred through the solid to the contact line region, while the contribution from below the liquid to heat transfer at the contact line is rather low (as indicated by the small heat flux vectors below the liquid).

Even though the qualitative results show good agreement to the direct precursor experiments carried out by Ibrahem et al. [41, 42, 43], several factors inhibit quantitative comparability: Ibrahem used a different fluid which was subcooled before entering his test section. This allowed to adjust relatively high input heat fluxes. Due to the experiment concept of setting the system pressure through the saturation pressure of the liquid, large sub-coolings of the liquid and correspondingly high heat fluxes could not be realized with the experiment setup used in this work. The biggest difference between the two setups however is the heater design. The heaters used by Ibrahem et al. were thin foil heaters

with a thickness of 10 µm. The sputtered heater design used within this work with its CaF_2 substrate thickness of 4 mm is massive in comparison. Not only do the CaF_2 heaters provide a much higher thermal inertia, but also thermal conduction within the heater is completely different. Within a thin foil heater energy transport to the contact line through thermal conduction is limited to the directions parallel to the heater surface. In contrast to thin foil heaters, energy transport to the contact line region can also take place in perpendicular direction to the heater surface in the CaF_2 heaters (see figure 4.3). This explains the smaller temperature minimum close to the contact line compared to values reported by Ibrahem et al: Due to the three-dimensional nature of heat conduction within the solid substrate, a much smaller temperature gradient is required to transport the same amount of energy to the contact line as it would be the case in a two-dimensional configuration as found in thin foil heaters.
An oscillation of the contact line as reported by Ibrahem et al. [41] was not observed. Misale et al. conducted experiments on pool boiling of saturated HFE-7100 in a confined vertical gap with a width of 0.5 mm, which is comparable to Ibrahems test section of 0.6 mm [80, 81]. They reported fully developed nucleate boiling for heat fluxes already as low as 5000 W m^{-2}. Ibrahem et al. on the other hand adjusted input heat fluxes as high as 12 170 W m^{-2}. As their very narrow channel of 0.6 mm did not allow for optical observation of the liquid/vapour-interface, it can not be ruled out that the oscillations were actually caused by nucleate boiling at the submerged electrode causing a periodic disturbance of the interface due to the rising bubbles. Furthermore the CaF_2 heater provides a much higher stiffness than a 10 µm thin stainless steel foil heater. As the channel used by Ibrahem et al. was with 0.6 mm very narrow, small deformations of the foil (e.g. due to pressure fluctuations) result in a shift of the liquid level, which could be interpreted as contact line oscillations.

4.2 Influence of the system pressure

In figure 4.4 the heat flux line profiles of non-moving contact lines at different reduced pressures are displayed. The areas beneath vapour (negative ξ) and beneath liquid (positive ξ) are marked to facilitate orientation. Except for the strongly reduced heat flux peak at the contact line for $p_R = 0.7$,

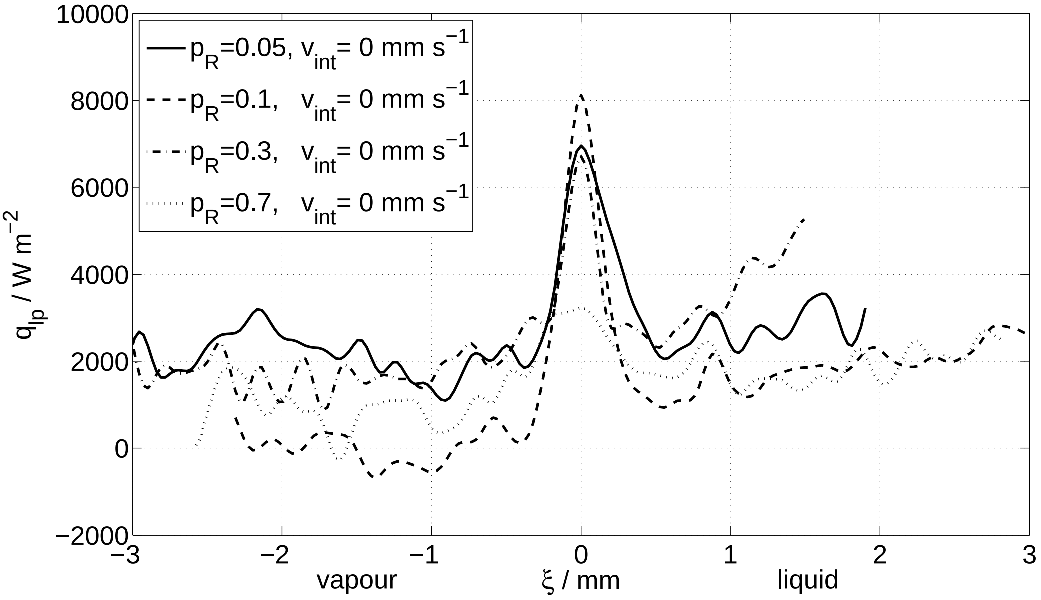

Figure 4.4.: Heat flux line profiles at a non-moving contact line at different reduced pressures for an average wall superheat of $\Delta T_{W,av} = 4.5\,K \pm 1.2\,K$

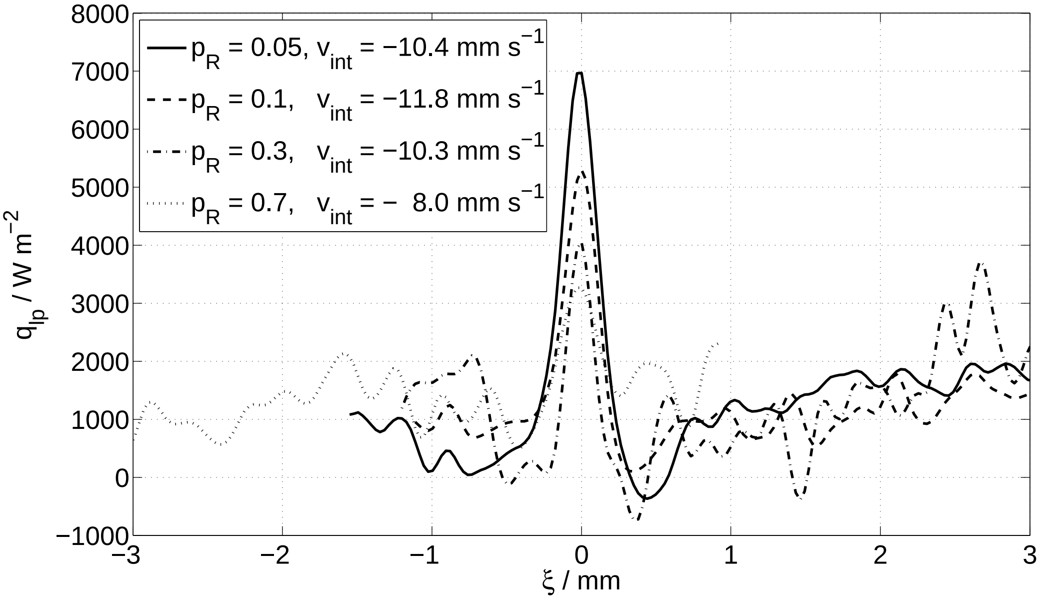

Figure 4.5.: Heat flux line profiles at a receding contact line at different reduced pressures for an average wall superheat of $\Delta T_{W,av} = 3.7\,K \pm 0.4\,K$

no clear statements can be drawn from the data. Even though the input heat flux was kept constant at $q_{in} = 2580\,W\,m^{-2}$ throughout the depicted sequences, considerable differences have been found in the average wall superheat. This is caused by the fact, that the total energy that can be transferred through a single extended contact line is extremely small. Consequently the wall temperature depends on temperatures far away from the contact line, as heat transfer is almost entirely controlled by thermal conduction. This makes it close to impossible to reach comparable steady state conditions at a non-moving contact line.

At a moving contact line on the other hand, contact line heat transfer is rather controlled through the energy stored within the heater material than through thermal conduction. As a result, the influence of the system presure is more easiliy accessible in sequences with a moving contact line. These are comparable, as long as the wall superheat is comparable. Since the interface velocity is measured in-situ and can not be set directly, but is controlled indirectly through the volume shift in the stainless steel bellows caused by the stepper motor, there are some deviations of the interface velocity in the following compared sequences.

In figure 4.5 the heat flux line profiles of receding contact lines with comparable interface velocities ($v_{int} = -11.8\,mm/s$ ... $-8.0\,mm/s$) and wall superheat are plotted versus the ξ-coordinate for four different reduced pressure levels. Of all sequences recorded at $p_R = 0.5$, none showed a comparable

Table 4.1.: Influence of the reduced pressure p_R on maximum heat flux $q_{max,RCL}$ transferred close to a receding contact line and ratio of $q_{max,RCL}/\Delta h_v\,(p_R)$

p_R	0.05	0.1	0.3	0.7
$q_{max,RCL}$	$6970\,W\,m^{-2}$	$5301\,W\,m^{-2}$	$4051\,W\,m^{-2}$	$3269\,W\,m^{-2}$
$q_{max,RCL}/\Delta h_v\,(p_R)$	$81.5\,g\,m^{-2}\,s^{-1}$	$67.3\,g\,m^{-2}\,s^{-1}$	$64.1\,g\,m^{-2}\,s^{-1}$	$79.2\,g\,m^{-2}\,s^{-1}$

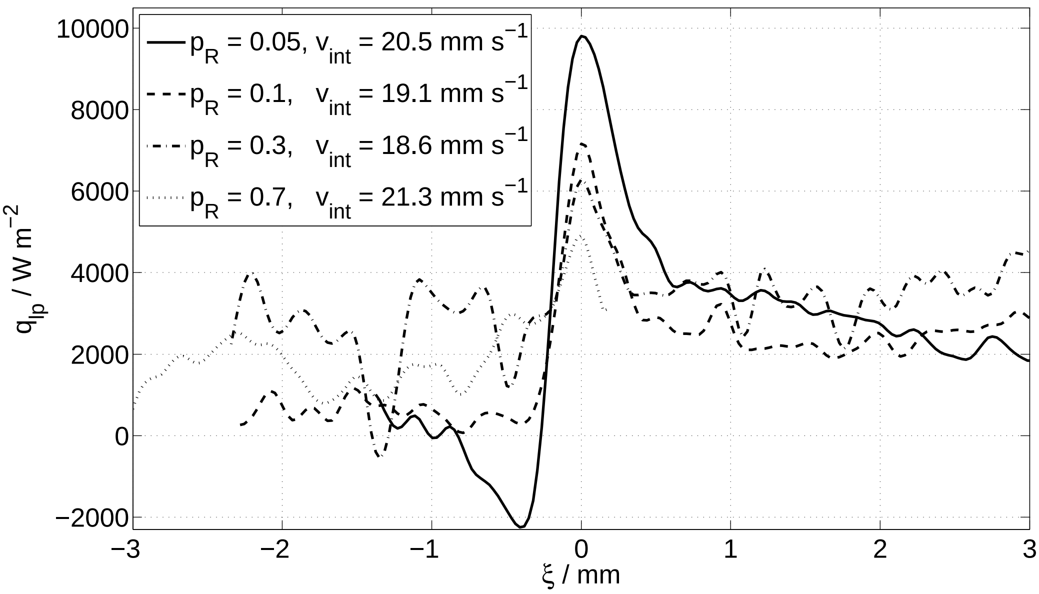

Figure 4.6.: Heat flux line profiles at an advancing contact line at different reduced pressures for an average wall superheat of $\Delta T_{\mathrm{W,av}} = 4.1\,\mathrm{K} \pm 0.4\,\mathrm{K}$

wall superheat and interface velocity, and therefore this pressure level is not included. In figure 4.5 one clear trend is observable: The heat flux peak close to the contact line decreases with increasing reduced pressure. Quite interestingly, this decrease scales well with the decrease of latent heat of evaporation. In table 4.1 the maximum heat flux close to the contact line $q_{\mathrm{max,RCL}}$ and the ratio of maximum heat flux divided by latent heat of evaporation is listed for a receding contact line. While the maximum heat flux changes quite considerably, the ratio changes lie within only ±12.5 % of the mean value of $q_{\mathrm{max,RCL}}/\Delta h_{\mathrm{v}} = 73.0\,\mathrm{g m^{-2} s^{-1}}$.

In figure 4.6 the heat flux line profiles at advancing contact lines with comparable interface velocities ($v_{\mathrm{int}} = 18.6\,\mathrm{mm\,s^{-1}}$ ... $21.3\,\mathrm{mm\,s^{-1}}$) and wall superheat are plotted versus the ξ-coordinate for four different reduced pressure levels. Again, no sequence with comparable wall superheat and interface velocity was recorded at $p_{\mathrm{R}} = 0.5$. Like in case of a receding contact line, comparison of the heat flux line profiles at an advancing contact line show the same trend of reduction of the heat flux peak with increasing reduced pressure.

At any pressure level the heat flux peak is higher for an advancing contact line, than for a receding contact line. This is in-line with the results obtained by Ibrahem et al. on thin foil heaters [42]. An explanation for this phenomenon is given in section 4.4.

In table 4.2 the maximum heat flux close to the contact line $q_{\mathrm{max,ACL}}$ and the ratio of maximum heat flux divided by latent heat of evaporation is listed for an advancing contact line. Again, the change in

Table 4.2.: Influence of the reduced pressure p_{R} on maximum heat flux $q_{\mathrm{max,ACL}}$ transferred close to an advancing contact line and ratio of $q_{\mathrm{max,ACL}}/\Delta h_{\mathrm{v}}\,(p_{\mathrm{R}})$

p_{R}	0.05	0.1	0.3	0.7
$q_{\mathrm{max,ACL}}$	$9803\,\mathrm{W\,m^{-2}}$	$7163\,\mathrm{W\,m^{-2}}$	$6292\,\mathrm{W\,m^{-2}}$	$4913\,\mathrm{W\,m^{-2}}$
$q_{\mathrm{max,ACL}}/\Delta h_{\mathrm{v}}\,(p_{\mathrm{R}})$	$114.6\,\mathrm{g\,m^{-2}\,s^{-1}}$	$90.6\,\mathrm{g\,m^{-2}\,s^{-1}}$	$99.7\,\mathrm{g\,m^{-2}\,s^{-1}}$	$116.6\,\mathrm{g\,m^{-2}\,s^{-1}}$

maximum heat flux is quite pronounced, but the changes of the ratio lie within ±15 % of the mean value of $q_{\mathrm{max,ACL}}/\Delta h_{\mathrm{v}} = 105.4\,\mathrm{g m^{-2} s^{-1}}$.

The influence of the (reduced) system pressure can be summarized as follows: Due to the reduced latent heat of evaporation the heat flux peak close to the contact line decreases with increasing system pressure, regardless of contact line velocity and movement direction. The ratio of maximum heat flux divided by latent heat of evaporation is practically unaltered by a change of the system pressure. Due to increased convective energy transport to the liquid/vapour-interface (because of the increased thermal capacity of the fluid), the contribution of contact line heat transfer to the overall evaporative mass flow decreases with increasing pressure.

4.3 Influence of the contact line movement direction

In figure 4.7 the heat flux line profiles of two sequences with equal interface and thereby contact line velocities ($v_{\mathrm{int,RCL}} = -9.8\,\mathrm{mm\,s^{-1}}$, $v_{\mathrm{int,ACL}} = 9.1\,\mathrm{mm\,s^{-1}}$) at equal mean wall superheat ($\Delta T_{\mathrm{W,RCL}} = 3.5\,\mathrm{K}$, $\Delta T_{\mathrm{W,ACL}} = 3.6\,\mathrm{K}$), but with different movement directions is displayed. It is evident that the heat flux peak at the advancing contact line is twice as high as in the receding case. This higher heat transfer at advancing contact lines has been reported in the past on thin foil heaters [15, 40, 42]. Kunkelmann and Kunkelmann et al. attributed this enhanced heat transfer to the effect of transient conduction [4, 15]:
In figure 4.8 the streamlines and temperature fields close to the three-phase contact line obtained from numerical simulations of pool boiling performed by Kunkelmann are displayed [4]. The streamlines show, that at an advancing contact line (figure 4.8, right) liquid is sucked to the wall by the moving interface, which must be heated up to replenish the thermal boundary layer at the wall. This leads to increased wall heat transfer at advancing contact lines. At receding contact lines (figure 4.8, left) on the other hand, hot liquid from the wall flows towards the interface, which does not increase wall heat transfer, but the evaporation rates at the interface.

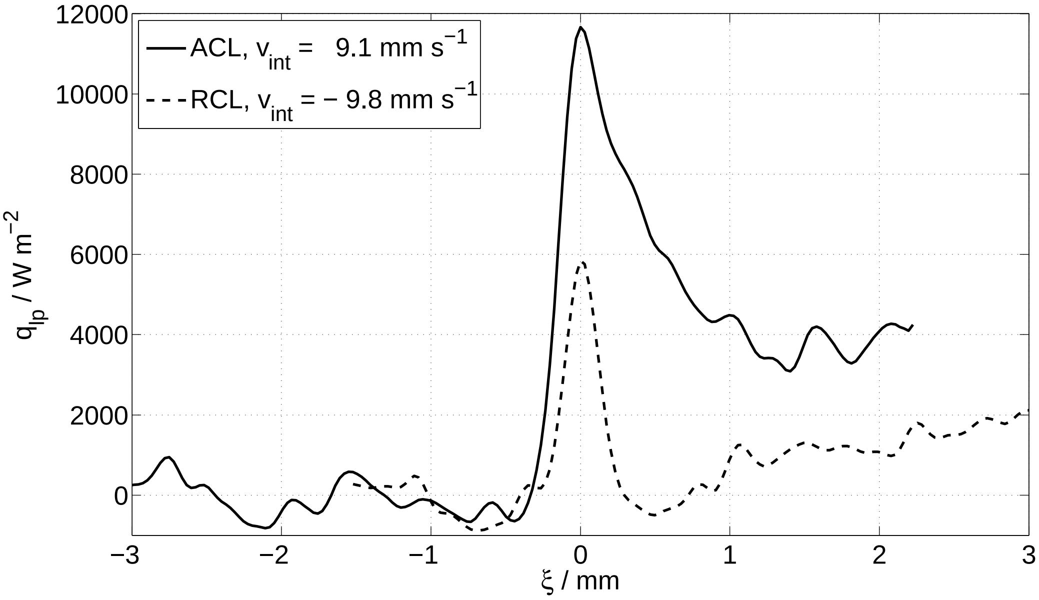

Figure 4.7.: Heat flux line profiles for an advancing and a receding contact line moving with equal interface velocities ($\Delta T_{\mathrm{W,av}} = 3.5\,\mathrm{K} \ldots 3.6\,\mathrm{K}$, $p_{\mathrm{R}} = 0.05$, $q_{\mathrm{in}} = 2580\,\mathrm{W\,m^{-2}}$)

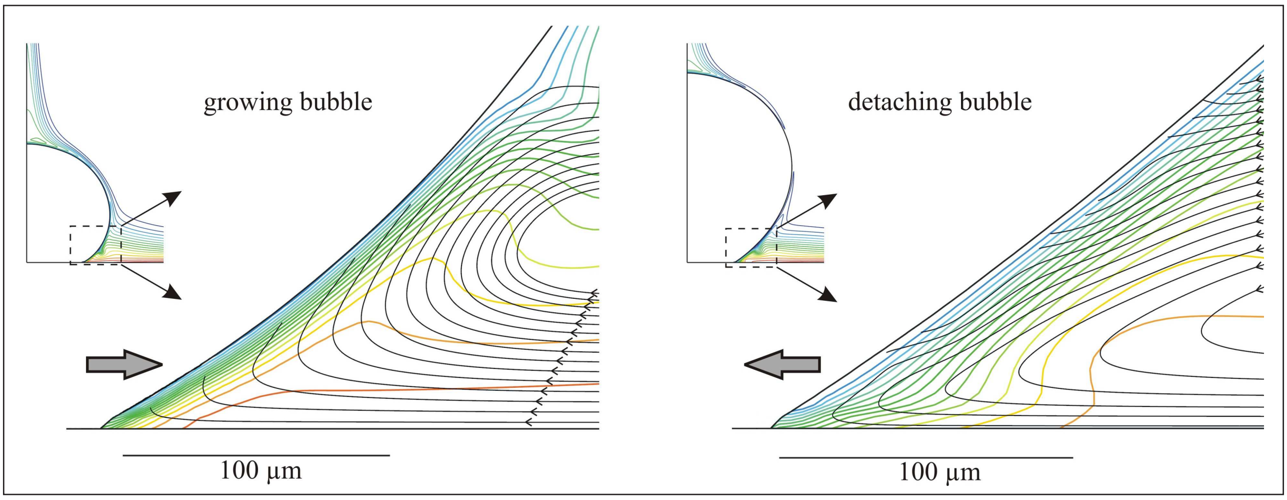

Figure 4.8.: Numerical results of Kunkelmann: Temperature fields and relative velocity streamlines at a receding contact line (left) and at an advancing contact line (right) during bubble growth and detachment in pool boiling [4]

In figure 4.9 the temperature profiles matching the heat flux profiles of figure 4.7 are displayed. As it is the case in the reference experiment, the temperature distributions show good qualitative agreement to the ones measured by Ibrahem et al. [42], but the temperature differences are much smaller in the present case. Even though the mean wall superheat is almost equal, the temperature distribution across the heater surface is entirely different depending on the movement direction. At the receding contact line there is a local temperature minimum close to the contact line. At the advancing contact line, however, the local minimum does not exist and is replaced by a strong temperature gradient between the contact line region and heater surface covered by vapour. In addition to transient conduction to the fluid, heat transfer is also enhanced at advancing contact lines because the contact line moves in direction of this steep temperature gradient. When the advancing contact line moves across the wall area that was previously insulated by the vapour, it experiences a higher local wall superheat at the

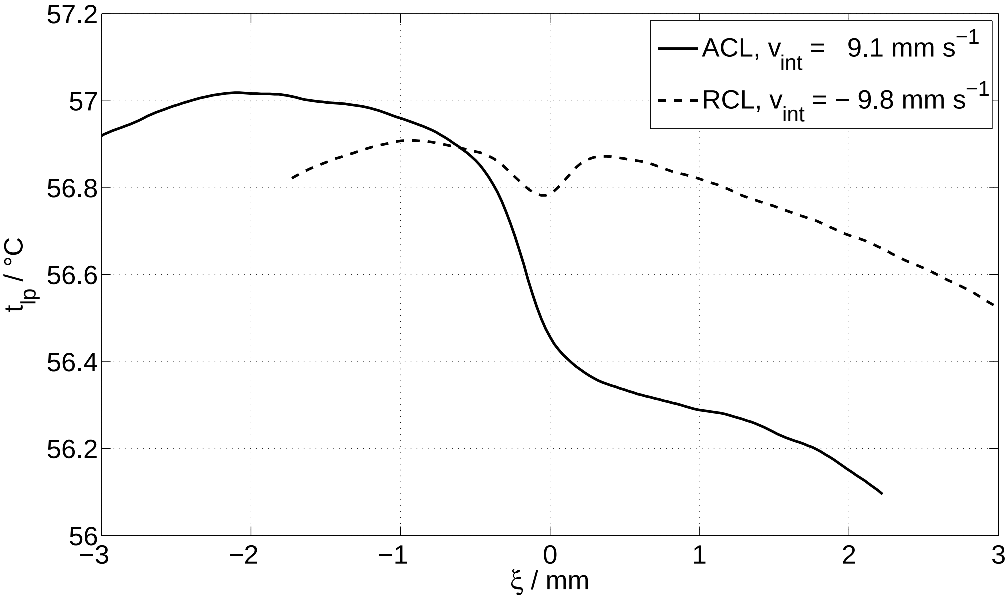

Figure 4.9.: Temperature line profiles for an advancing and a receding contact line moving with equal interface velocities ($\Delta T_{\mathrm{W,av}} = 3.5\,\mathrm{K} \ldots 3.6\,\mathrm{K}$, $p_{\mathrm{R}} = 0.05$, $q_{\mathrm{in}} = 2580\,\mathrm{W\,m^{-2}}$)

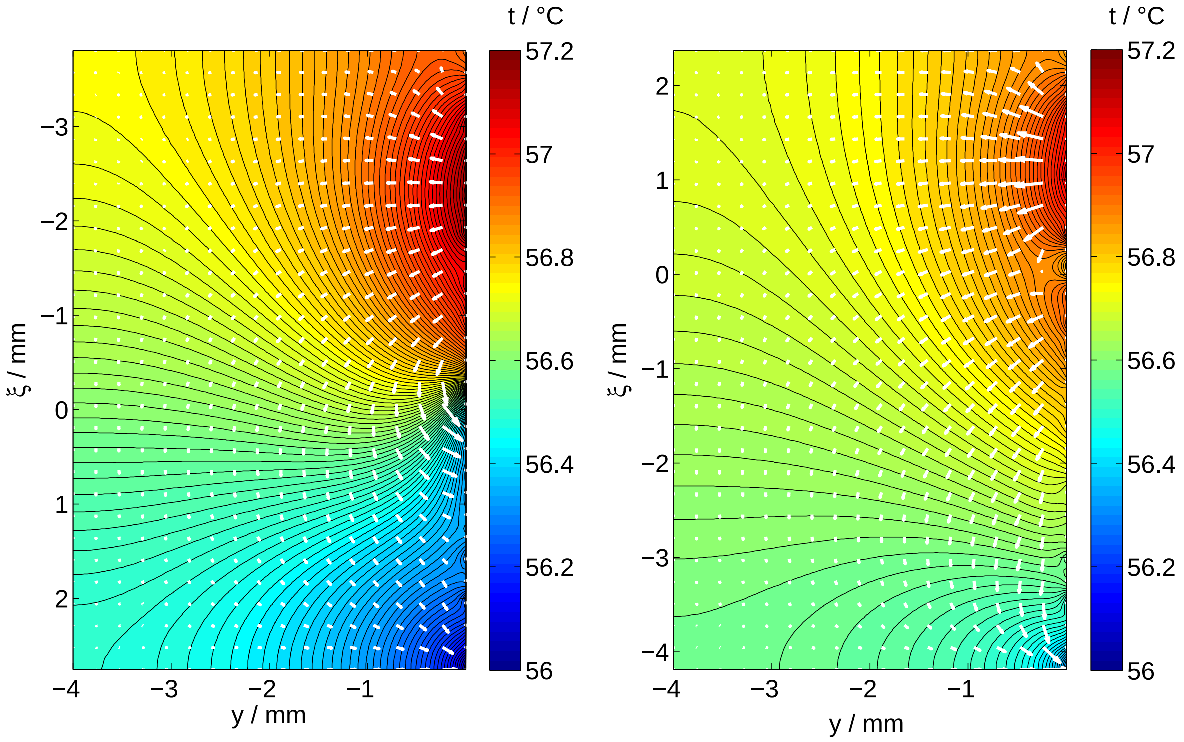

Figure 4.10.: Contour plots of the temperature distribution and heat flux vectors inside the heater substrate at the centre in x-direction for an advancing contact line (left) and a receding contact line (right) moving with equal interface velocities ($\Delta T_{\mathrm{W,av}} = 3.5\,\mathrm{K} \dots 3.6\,\mathrm{K}$, $p_{\mathrm{R}} = 0.05$, $q_{\mathrm{in}} = 2580\,\mathrm{W\,m^{-2}}$)

wall, than it is the case for a receding contact line.

Contour plots of the temperature distribution and the heat flux vectors in the centre of the heater substrate in x-direction for both cases are provided in figure 4.10. Again, the position of the contact line is at $\xi = 0$, $y = 0$. In both cases the shapes of the isotherms are shifted from those, that are present at a stationary contact line (see figure 4.3). While the distance between the isotherms is reduced in case of an advancing contact line, it is increased for a receding contact line. At an advancing contact line the high energy removal rate at the contact line generates a strong temperature gradient between substrate material covered by vapour and substrate material covered by liquid. This strong local gradient favors energy transport into the contact line area by transient conduction within the heater material, as indicated by elongated heat flux vectors in the contact line area (see figure 4.10, left).

In case of a receding contact line, there are only slight temperature gradients in proximity of the contact line (see figure 4.10, right). Close to the contact line, the isotherms are perpendicular to the heater surface and the heat flux vector is zero, which means that all heat generated in the heating layer must be transferred to the fluid there.

4.4 Influence of the contact line velocity

In figure 4.11 the heat flux line profiles for three receding contact lines with equal wall superheat and different interface velocities are plotted versus the ξ-coordinate for a reduced pressure of $p_{\mathrm{R}} = 0.05$ and an average wall superheat of $\Delta T_{\mathrm{W,av}} = 2.2\,\mathrm{K} \pm 0.2\,\mathrm{K}$. In case of a receding contact line at low pressure, higher interface velocities are not included, as those often led to the deposition of a thin,

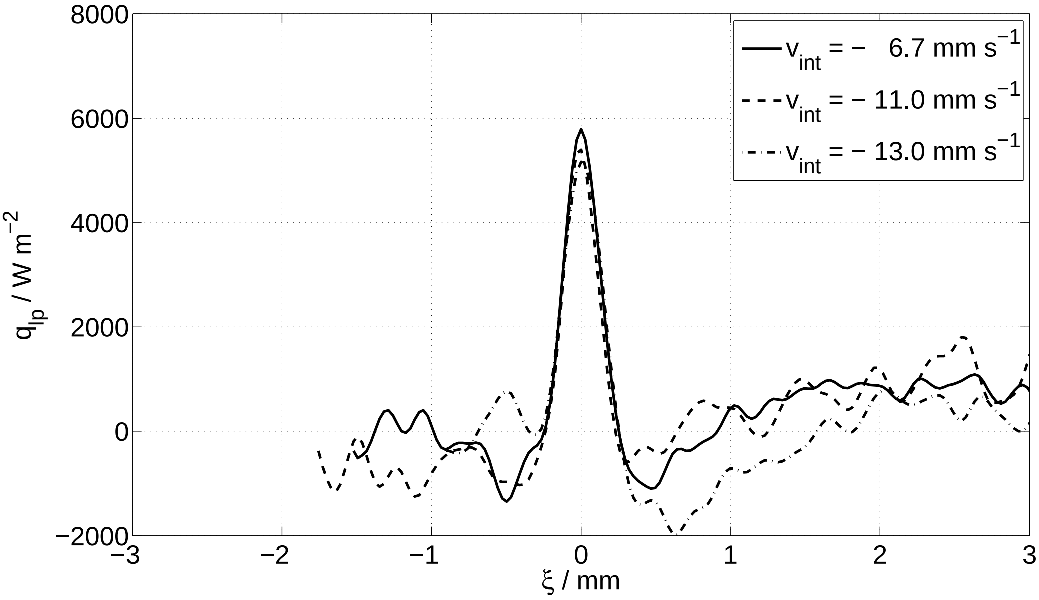

Figure 4.11.: Heat flux line profiles at a receding contact line at a reduced pressure of $p_{\mathrm{R}} = 0.05$ with different interface velocities for an average wall superheat of $\Delta T_{\mathrm{W,av}} = 2.2\,\mathrm{K} \pm 0.2\,\mathrm{K}$

evaporating liquid film on the heater surface (see section 4.5). All three heat flux line profiles are practically identical.

In figure 4.12 the heat flux line profiles for four advancing contact lines with equal wall superheat and different interface velocities are plotted versus the ξ-coordinate for a reduced pressure of $p_{\mathrm{R}} = 0.05$ and an average wall superheat of $\Delta T_{\mathrm{W,av}} = 2.3\,\mathrm{K} \pm 0.2\,\mathrm{K}$. In case of an advancing contact line, there is a very distinctive influence of the interface velocity onto the local heat flux peak at the contact line. The heat flux line profile at the lowest positive interface velocity of $v_{\mathrm{int}} = 5.9\,\mathrm{mm\,s^{-1}}$ is almost identical to

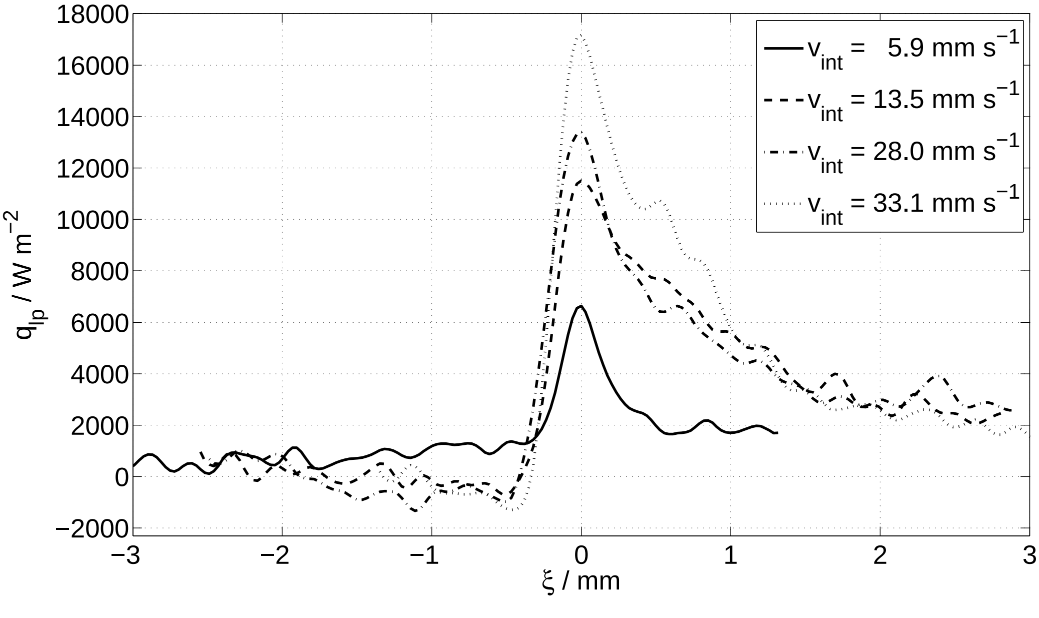

Figure 4.12.: Heat flux line profiles at an advancing contact line at a reduced pressure of $p_{\mathrm{R}} = 0.05$ with different interface velocities for an average wall superheat of $\Delta T_{\mathrm{W,av}} = 2.3\,\mathrm{K} \pm 0.2\,\mathrm{K}$

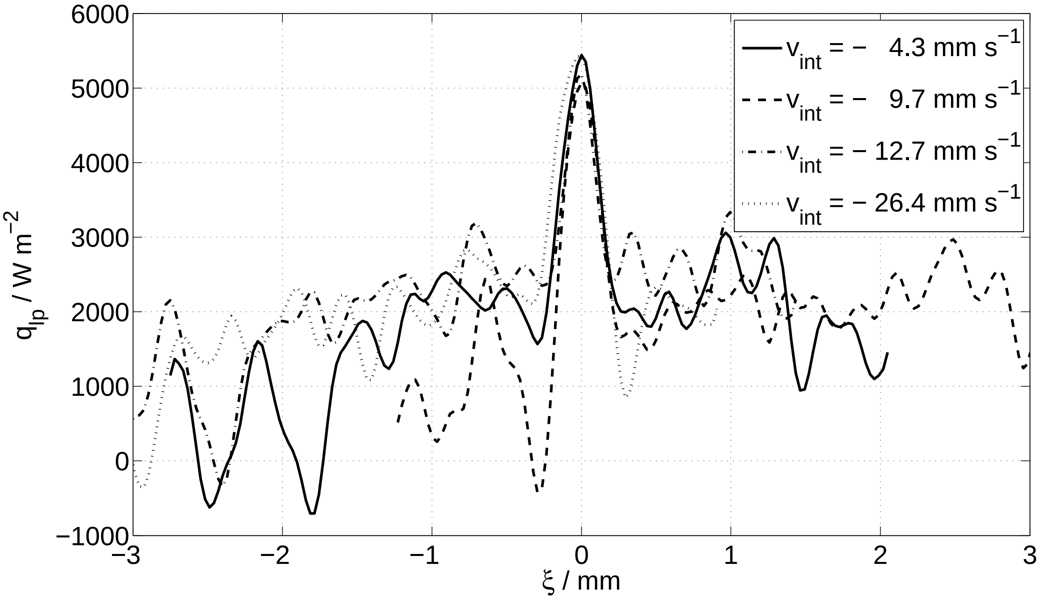

Figure 4.13.: Heat flux line profiles at a receding contact line at a reduced pressure of $p_{\mathrm{R}} = 0.5$ with different interface velocities for an average wall superheat of $\Delta T_{\mathrm{W,av}} = 5.0\,\mathrm{K} \pm 0.2\,\mathrm{K}$

the heat flux line profiles of receding contact line depicted in figure 4.11. When the interface velocity is further increased, the heat flux gradient in positive ξ direction decreases, which means that more heat is transferred in the wake of the contact line. Furthermore the maximum heat flux transferred in the contact line region increases with contact line velocity.
This is a logical consequence of the explanation of Kunkelmann et al. [15]. A higher interface velocity results in stronger micro-convection close to the contact line, thereby increasing wall heat transfer. At receding contact lines, as shown in figure 4.11, this effect is not present and therefore the local heat flux maximum does not depend on the interface velocity.

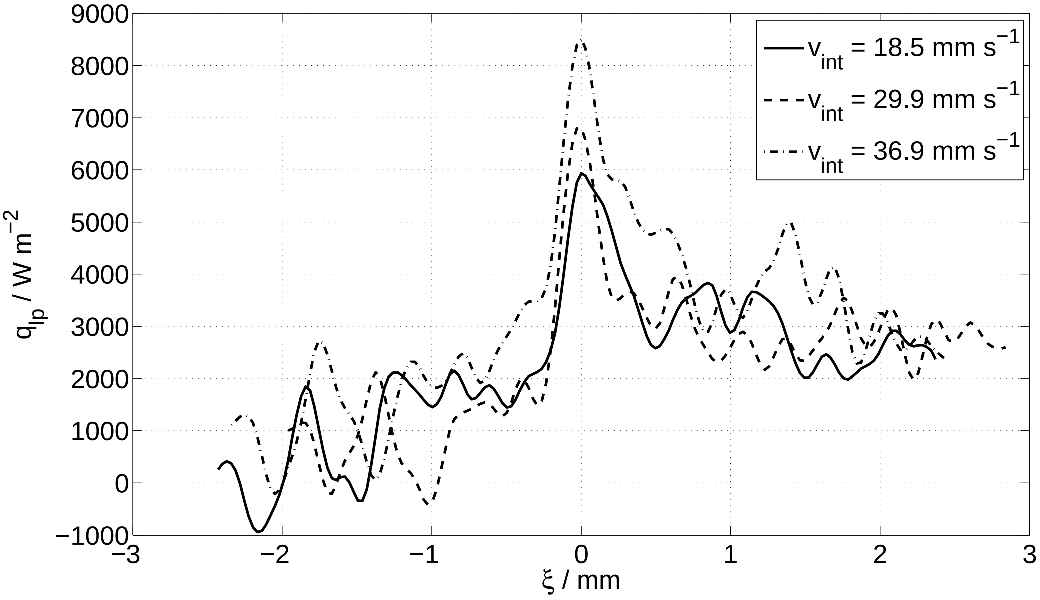

Figure 4.14.: Heat flux line profiles at an advancing contact line at a reduced pressure of $p_{\mathrm{R}} = 0.5$ with different interface velocities for an average wall superheat of $\Delta T_{\mathrm{W,av}} = 5.2\,\mathrm{K} \pm 0.2\,\mathrm{K}$

In figure 4.13 the heat flux line profiles for receding contact lines at a reduced pressure of $p_\mathrm{R} = 0.5$ are plotted versus the ξ-coordinate for equal wall superheat of $\Delta T_\mathrm{W,av} = 5.0\,\mathrm{K} \pm 0.2\,\mathrm{K}$ and different interface velocities. As for the heat flux line profiles on a low reduced pressure value shown in figure 4.11, no distinctive change of the heat flux maximum with increasing interface velocity can be deduced. In figure 4.14 the heat flux line profiles for advancing contact lines at a reduced pressure of $p_\mathrm{R} = 0.5$ are plotted versus the ξ-coordinate for equal wall superheat of $\Delta T_\mathrm{W,av} = 5.2\,\mathrm{K} \pm 0.2\,\mathrm{K}$ and different interface velocities. As it is the case at low reduced pressure (see figure 4.12) a clear trend of increasing heat flux maximum with interface velocity is visible.

The influence of contact line velocity and movement direction onto contact line heat transfer can be summarized as follows: The maximum heat flux at receding contact lines is independent of the (negative) contact line velocity, regardless of the (reduced) pressure level. There is a distinctive difference in the heat flux and temperature line profiles at receding and advancing contact lines. Wall heat transfer is increased at advancing contact lines when compared to receding contact lines. The heat flux maximum at the contact line increases with increasing contact line velocity, regardless of the (reduced) pressure level.

4.5 Near contact line evaporation versus thin film evaporation

For quite some time there has been a dispute in the scientific community, whether the evaporation of a thin microlayer beneath the bubble (as first proposed by Snyder and Edwards [82]) or contact line dominated heat transfer is the predominant heat transfer mechanism during boiling phenomena. A comprehensive review of the two mechanisms is given by Kim [83]. The observation of an evaporating microlayer was linked to the Jakob number of the reviewed experiments, which is merely a function of the fluid data and the wall superheat:

$$\mathrm{Ja} = \frac{c_{p,\mathrm{l}} \left(T_\mathrm{W} - T_\mathrm{sat}\right)}{\Delta h_\mathrm{v}} \tag{4.1}$$

It should be noted that the definition of the Jakob number is somewhat ambiguous in literature and sometimes includes the density ratio of liquid and vapour $\rho_\mathrm{l}/\rho_\mathrm{v}$ (both variations can for example be found in [5]). Within this work the definition of the Jakob number as given by equation (4.1) is being maintained.

In some measurement sequences with a receding meniscus, a thin evaporating liquid film was deposited on the heater surface by the moving liquid/vapour-interface, which corresponds to the microlayer evaporation reported in some boiling experiments. The results indicate however, that other influence factors apart from the Jakob number also play a role for the generation of a microlayer. The generation of the thin liquid film by the receding liquid/vapour-interface turned out to be not entirely reproducible, but a couple of influence factors that could be identified are outlined below.

4.5.1 Influence factors for the generation of an evaporating thin film at a receding contact line

First of all, at the lowest stepper motor velocity setting, no thin film deposition could be observed at any input heat flux and pressure level on any experiment heater. The velocity of the liquid/vapour-interface must be large enough for sufficient deposition of liquid mass on the surface to counteract contact line evaporation. Longer films were observed at higher liquid/vapour-interface velocities. In figure 4.15 exemplary heat flux fields from three different measurement sequences with different interface velocities are displayed ($v_\mathrm{int} = -9.1\,\mathrm{mm\,s^{-1}}$ in figure 4.15 left, $v_\mathrm{int} = -13.3\,\mathrm{mm\,s^{-1}}$ in figure

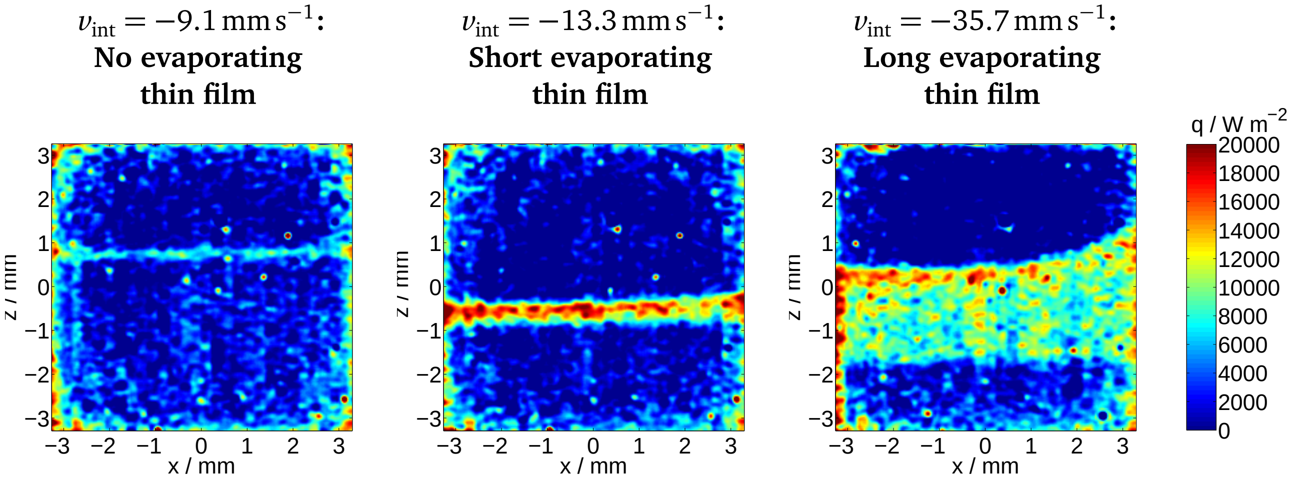
$v_{\mathrm{int}} = -9.1\,\mathrm{mm\,s^{-1}}$: **No evaporating thin film**

$v_{\mathrm{int}} = -13.3\,\mathrm{mm\,s^{-1}}$: **Short evaporating thin film**

$v_{\mathrm{int}} = -35.7\,\mathrm{mm\,s^{-1}}$: **Long evaporating thin film**

Figure 4.15.: Heat flux fields for a receding liquid/vapour-interface with an equal mean wall superheat of $\Delta T_{\mathrm{W}} = 3.3\,\mathrm{K}$ at different interface velocities ($p_{\mathrm{R}} = 0.05$, $q_{\mathrm{in}} = 2580\,\mathrm{W\,m^{-2}}$).

4.15 centre and $v_{\mathrm{int}} = -35.7\,\mathrm{mm\,s^{-1}}$ in figure 4.15, right). The higher the interface velocity, the longer the thin film region is.

At the same time, the wall superheat should be rather low to promote the generation of the liquid film, as a large wall superheat will lead to dry-out of the film. This criterion corresponds to the criterion of a low Jakob number, which was already identified by Kim [83]. In figure 4.16 two exemplary heat flux fields with an equal interface velocity of $v_{\mathrm{int}} = -28.5\,\mathrm{mm\,s^{-1}}$, but different wall superheat are displayed. It is evident, that the thin film region is longer for a lower wall superheat (figure 4.16, left).

Low Jakob numbers are also encountered at high latent heats of evaporation. High latent heat of evaporation counteracts dry-out, therefore the probability of encountering a thin film should be higher at low reduced pressures (corresponding to high latent heat of evaporation). This is in-line with experimental investigations of Fath and Judd [84], who reported a bigger contribution of microlayer evaporation to the total energy of a bubble in nucleate boiling under lower pressure. In figure 4.17 two exemplary heat flux fields with an equal interface velocity of $v_{\mathrm{int}} = -16.0\,\mathrm{mm\,s^{-1}}$ at two different

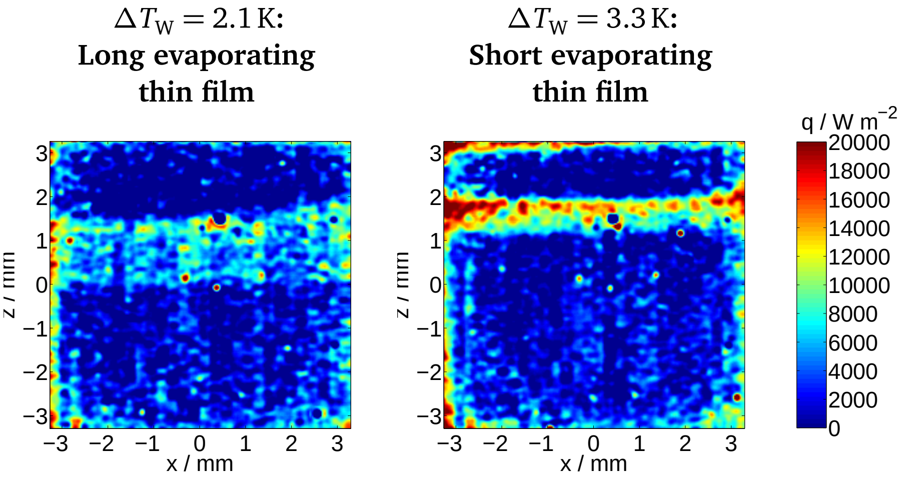
$\Delta T_{\mathrm{W}} = 2.1\,\mathrm{K}$: **Long evaporating thin film**

$\Delta T_{\mathrm{W}} = 3.3\,\mathrm{K}$: **Short evaporating thin film**

Figure 4.16.: Heat flux fields for a receding liquid/vapour-interface with equal interface velocities of $v_{\mathrm{int}} = -28.5\,\mathrm{mm\,s^{-1}}$ at $p_{\mathrm{R}} = 0.05$ with different mean wall superheats.

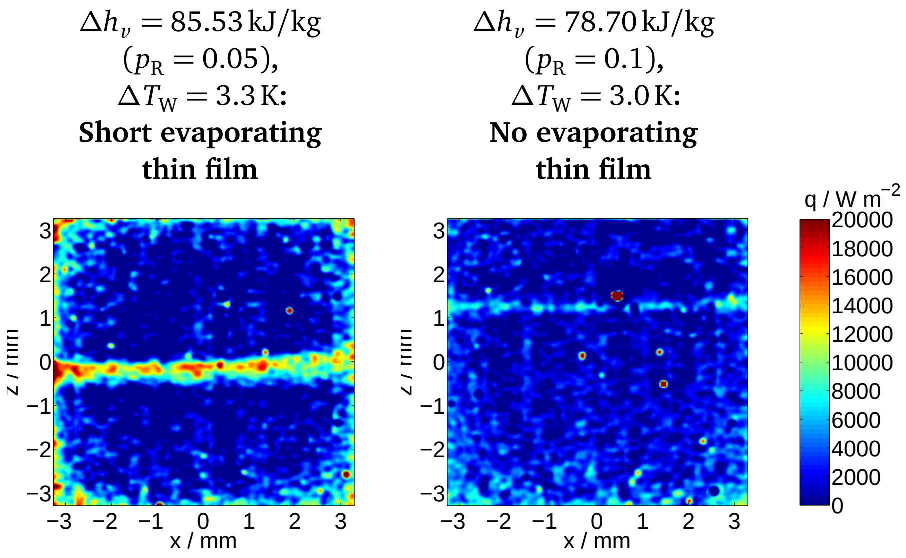

$\Delta h_v = 85.53\,\mathrm{kJ/kg}$ $(p_\mathrm{R} = 0.05)$, $\Delta T_\mathrm{W} = 3.3\,\mathrm{K}$: **Short evaporating thin film**

$\Delta h_v = 78.70\,\mathrm{kJ/kg}$ $(p_\mathrm{R} = 0.1)$, $\Delta T_\mathrm{W} = 3.0\,\mathrm{K}$: **No evaporating thin film**

Figure 4.17.: Heat flux fields for a receding liquid/vapour-interface with equal interface velocities of $v_\mathrm{int} = -16.0\,\mathrm{mm\,s^{-1}}$ at different reduced pressures.

reduced pressures are displayed. The mean wall superheat at $p_\mathrm{R} = 0.05$ is with $\Delta T_\mathrm{W} = 3.3\,\mathrm{K}$ (figure 4.17, left) slightly higher than the superheat of $\Delta T_\mathrm{W} = 3.0\,\mathrm{K}$ at $p_\mathrm{R} = 0.1$ (figure 4.17, right). This should reduce the film length in comparison. Nevertheless, the effect of wall superheat is counteracted by the reduction of the latent heat, so that a short evaporating thin film is generated at low reduced pressure, while no thin film is generated at the slightly higher reduced pressure.

The considerations up to this point have led to the development of an analytical model for stationary thin film evaporation which is presented in section 4.5.2 and which includes all influence factors up to this point. However, it turned out that not all sequences with high interface velocities and low Jakob number feature the thin evaporating film. While a low Jakob number and a high interface velocity are mandatory to sustain the thin film, other factors must play a role in triggering its generation.

In table 4.3 it is listed, whether the acceleration of the liquid/vapour interface a_int caused by the stepper motor acceleration a_StM triggered the generation of the thin liquid film. Only at the lowest reduced pressure setting of $p_\mathrm{R} = 0.05$ a thin film generation could be triggered within the FOV of the IR camera by the accelerating interface, when the stepper motor acceleration was above $a_\mathrm{StM} = 4\,\mathrm{mm\,s^{-2}}$. At an accelerated interface fluid movement out of the depth of field of the HSBW camera made it impossible to calculate time-resolved interface velocity data using the Young-Laplace fit described in

Table 4.3.: Influence of the stepper motor acceleration a_StM on triggering the thin evaporating film ($q_\mathrm{in} = 2580\,\mathrm{W\,m^{-2}}$, sequences where no thin film was triggered are marked with O, sequences where a thin film was triggered are marked with X)

$a_\mathrm{StM}/\mathrm{mms^{-2}}$	$p_\mathrm{R} = 0.05$	$p_\mathrm{R} = 0.1$	$p_\mathrm{R} = 0.3$	$p_\mathrm{R} = 0.5$	$p_\mathrm{R} = 0.7$
2	O	O	O	O	O
4	X	O	O	O	O
6	X	O	O	O	O
8	X	O	O	O	O

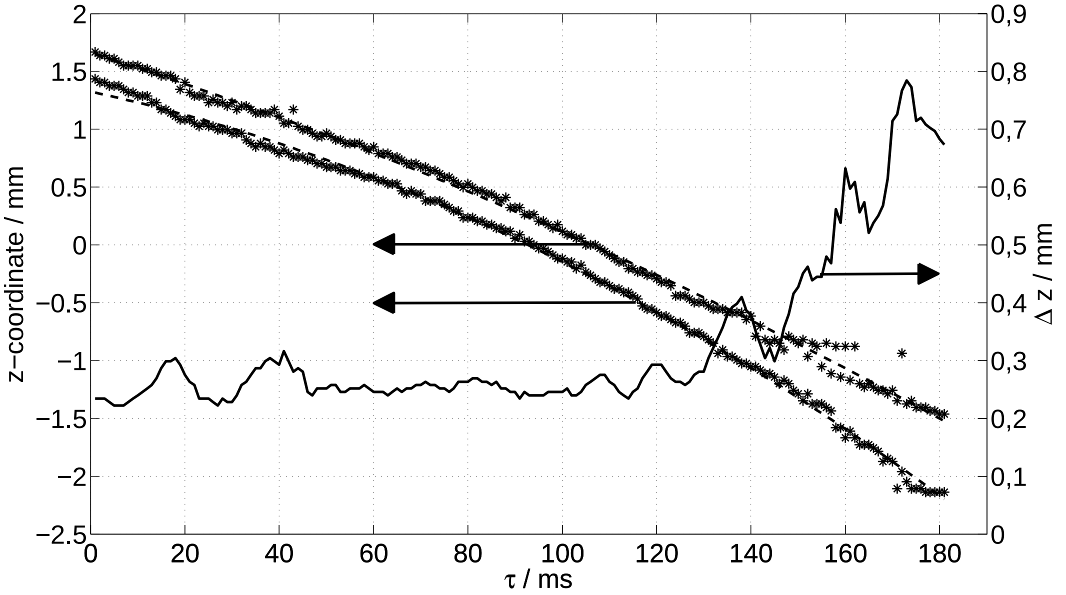

Figure 4.18.: Position of and distance between minimum and maximum heat flux gradient at an accelerated liquid/vapour-interface ($a_{\mathrm{int}} = -117\,\mathrm{mms^{-2}}$, $p_{\mathrm{R}} = 0.05$, $q_{\mathrm{in}} = 2580\,\mathrm{W\,m^{-2}}$)

section 3.10. The heat flux tracking method described in section 3.5.4 was therefore used to calculate velocity and acceleration of the interface. From the sequences evaluated in table 4.3, it can only be estimated that the necessary interface acceleration to trigger the generation of the thin evaporating liquid film within the FOV of the IR camera at a reduced pressure of $p_{\mathrm{R}} = 0.05$ and an input heat flux of $q_{\mathrm{in}} = 2580\,\mathrm{W\,m^{-2}}$ must lie somewhere between $a_{\mathrm{int}} = -53\,\mathrm{mm\,s^{-2}}$ and $a_{\mathrm{int}} = -117\,\mathrm{mm\,s^{-2}}$. It can however not be ruled out, that lower accelerations of the liquid/vapour-interface can disturb the force balance close to the contact line enough to trigger thin film evaporation, if one of the other factors, that have been identified come into play.

In figure 4.18 the positions of minimum and maximum heat flux gradient relative to the centre of the IR camera FOV and their quadratic fits (left axis) are plotted versus time together with the distance between minimum and maximum heat flux gradient (right axis) for a sequence with an accelerated interface. Up to approx. $\tau \approx 130\,\mathrm{ms}$ the distance between minimum and maximum gradient is roughly constant and is with approx. $\Delta z \approx 250\,\mu\mathrm{m}$ equal to the value found at a stationary contact line. Above $\tau \approx 130\,\mathrm{ms}$ the distance broadens, which indicates the onset of thin film evaporation. While the acceleration of the interface could play a role in the generation of the thin liquid film, figure 4.18 implies, that other factors must play a role in its generation. The possibility of a necessary minimum velocity to deposit a sufficient amount of liquid mass on the surface to counteract contact line evaporation has already been discussed above. This would explain the onset of thin film evaporation after a certain time, when a certain velocity has been reached.

A disturbance of the force balance at the contact line can also occur through a change of the heater wetting characteristics. In figure 4.19 a heat flux field for a reduced pressure of $p_{\mathrm{R}} = 0.05$ and an input heat flux of $q_{\mathrm{in}} = 2580\,\mathrm{W\,m^{-2}}$ is displayed. The mean wall superheat was with $\Delta T_{\mathrm{W}} = 3.4\,\mathrm{K}$ relatively moderate. One can immediately recognize contact line dominated evaporation in the left half of the heat flux field and thin film dominated heat transfer in the right half of the heat flux field. It appears that the thin film generation was triggered by an inhomogeneity of the heater surface (and therefore its wetting characteristics), where the contact line pinned during its receding movement. This sequence demonstrates, that wetting characteristics of the heater surface are also of major importance for the

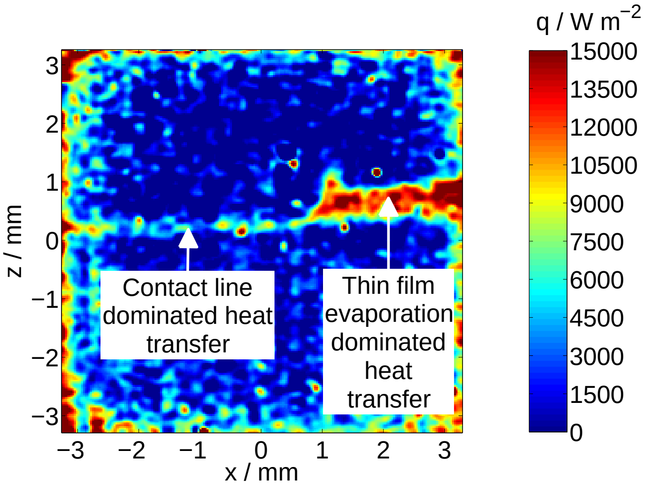

Figure 4.19.: Heat flux field for a receding liquid/vapour-interface with contact line and thin film evaporation at the same time at a reduced pressure of $p_\mathrm{R} = 0.05$ and a mean wall superheat of $\Delta T_\mathrm{W} = 3.4\,\mathrm{K}$ ($q_\mathrm{in} = 2580\,\mathrm{W\,m^{-2}}$).

generation of the thin film.

If a thin film is generated and can be sustained through high deposited mass flux (high interface velocities) and low evaporative mass flux (low wall superheat, high latent heat of evaporation), the question arises, whether the thin liquid film is stable. Bankoff carried out a stability analysis of thin evaporating liquid films on inclined heated plates [85] and horizontal and vertical walls [86]. He found that for a vertical wall, an evaporating thin film is always unstable. Some initial disturbance will grow in the film, regardless of the film Reynolds number. If the growth time of an initial disturbance to reach the same order of magnitude as the film thickness is comparable to the residence time of the thin film on the surface, film rupture occurs. As the growth time is a function of the dimensionless initial disturbance wave amplitude [85], it is difficult to predict, when film rupture occurs in the physical system investigated.
In some of the experiments film rupture did occur. In figure 4.20 a typical evolution of the heat flux field during a film rupture event at an accelerated liquid/vapour-interface is shown: Starting from the undisturbed thin film, the local heat flux increases close to the intrinsic meniscus at $\tau = 0\,\mathrm{ms}$ (figure 4.20, left), which indicates local thinning of the liquid film in this region. First dry spots appear

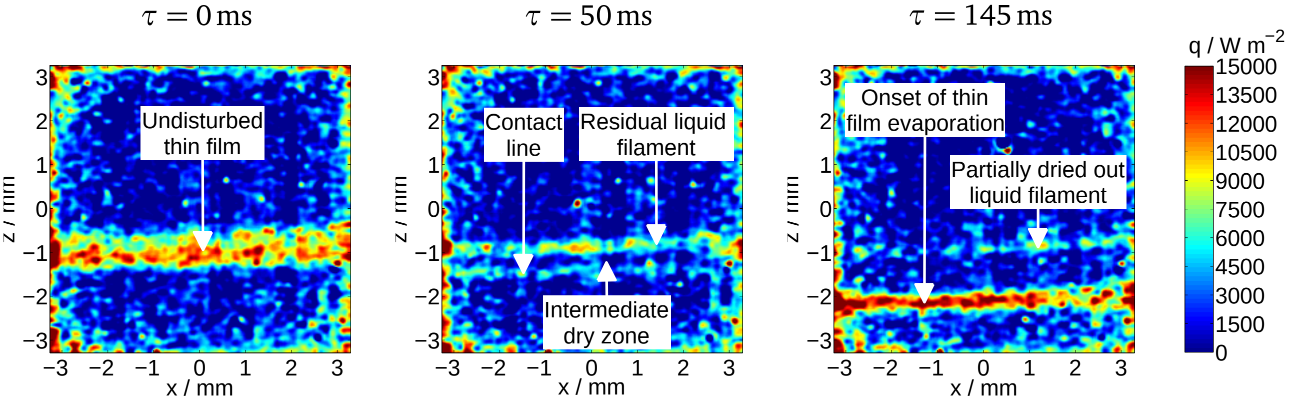

Figure 4.20.: Evolution of the heat flux field for an accelerated, receding liquid/vapour-interface during a film rupture event at a reduced pressure of $p_\mathrm{R} = 0.05$ and a mean wall superheat of $\Delta T_\mathrm{W} = 2.4\,\mathrm{K}$ ($q_\mathrm{in} = 1900\,\mathrm{W\,m^{-2}}$).

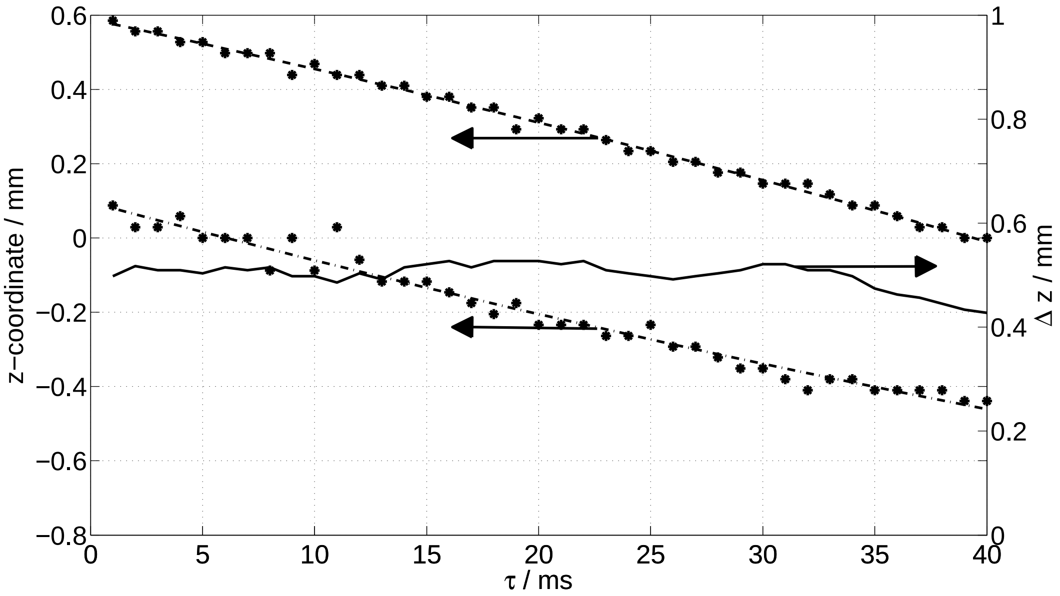

Figure 4.21.: Position of and distance between minimum and maximum heat flux gradient for a stationary evaporating thin film, $p_{\mathrm{R}} = 0.05$, $q_{\mathrm{in}} = 2580\,\mathrm{W\,m^{-2}}$, $v_{\mathrm{int}} = -13.3\,\mathrm{mm\,s^{-1}}$)

at $\tau = 27\,\mathrm{ms}$ and quickly grow, until the contact line of the meniscus is separated from a residual liquid filament by an intermediate dry patch at $\tau = 50\,\mathrm{ms}$ (figure 4.20, centre). While a new thin film starts to develop at the intrinsic meniscus, the residual liquid filament dries out through ongoing evaporation ($\tau = 145\,\mathrm{ms}$, figure 4.20, right).

The large amount of influence factors, especially the importance of acceleration of the liquid/vapour-interface, the wetting characteristics of the heater wall, as well as the instability of the thin evaporating film, explain why the appearance of the thin film was found to be not entirely reproducible. From figures 4.15 and 4.19 it can be deduced, that when thin film heat transfer occurs, it is the predominant mode of heat transfer. Even though theory predicts higher local heat transfer at the contact line, its lateral extension is so small compared to the thin film, that the overall heat transfer is clearly controlled by thin film evaporation. If thin film evaporation occurs, it must therefore be modeled to capture the physical process correctly. In figure 4.21 an example is shown, where thin film evaporation occurs with a constant length of the thin film region. This implies that thin film evaporation can occur as a stationary process, which is modeled in the following section.

4.5.2 Analytical model for stationary thin film evaporation

Based on the observations of the evaporating thin film, an analytical model is developed in a reference frame moving with the interface velocity v_{int}. In the moving reference frame the liquid film is deposited on the wall moving with the relative velocity v_{int} by the non-moving liquid/vapour-interface with an initial film thickness of δ_0. This corresponds to the deposition of a thin liquid film remaining on the surface of a solid drawn from a quiescent liquid, which has been analyzed for the non-evaporating case by Landau and Levich [87]. The thickness of the deposited liquid film δ_0 calculated according to Landau and Levich is used as initial condition for the model.

In figure 4.22 the mass balance (left) and the energy balance (right) at an infinitesimal short segment of the thin film is depicted. Across the segment of the thin film with the length dz the thickness of

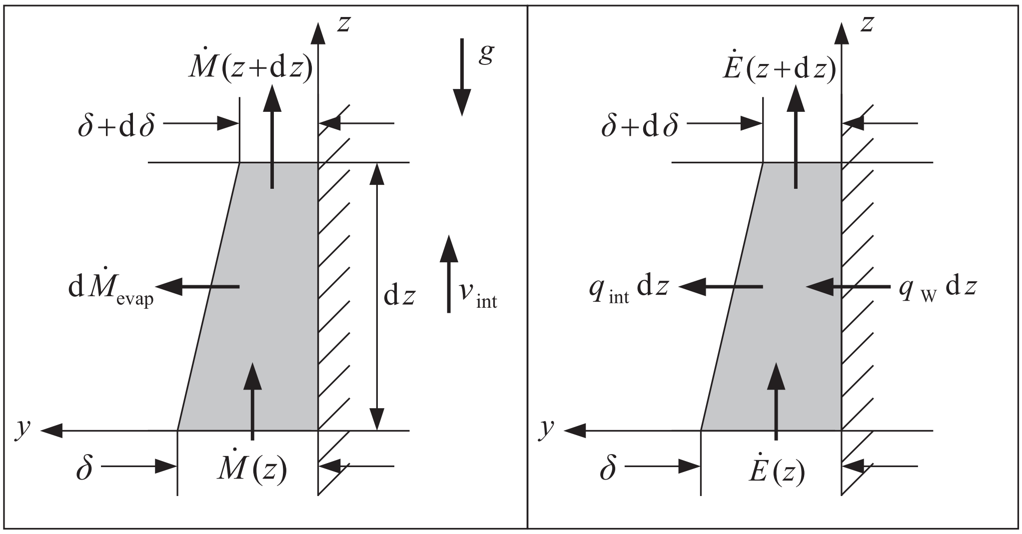

Figure 4.22.: Mass balance (left) and energy balance (right) at an infinitesimal short segment of an evaporating thin film

the film will experience a change in film thickness $d\delta$. At the surface of the thin film, a mass flow per unit depth $d\dot{M}_{evap}$ is evaporated. Due to the fluid motion the thin film segment experiences an input mass flow at the position z of $\dot{M}(z)$ and an output mass flow at the position $z+dz$ of $\dot{M}(z+dz)$. The two-dimensional stationary mass balance for the thin film segment is given by

$$\dot{M}(z+dz) + d\dot{M}_{evap} = \dot{M}(z). \tag{4.2}$$

The evaporating mass flow per unit depth $d\dot{M}_{evap}$ is coupled to the local heat flux at the interface by

$$\Delta h_v d\dot{M}_{evap} = q_{int} dz. \tag{4.3}$$

The general equation to describe the two-dimensional motion of a thin liquid film is given by Levich [87]

$$\frac{\partial v_z}{\partial \tau} + v_z \frac{\partial v_z}{\partial z} + v_y \frac{\partial v_z}{\partial y} = \frac{\sigma}{\rho_l} \frac{d^3\delta}{dz^3} + \nu_l \frac{\partial^2 v_z}{\partial y^2} - g. \tag{4.4}$$

To find an expression for $\dot{M}(z)$, some assumptions must be made:

- The thin film flow is laminar and stationary.
- The y-component of the velocity is negligibly small $v_y \approx 0$.
- The interface curvature of the thin film is negligibly small $\frac{d^2\delta}{dz^2} \approx 0$.

With these assumptions equation (4.4) can be simplified to

$$\frac{d^2 v_z}{dy^2} = \frac{g}{\nu_l}. \tag{4.5}$$

Integration of equation (4.5) results in

$$v_z = \frac{g}{2\nu_l} y^2 + C_1 y + C_2. \tag{4.6}$$

The constants C_1 and C_2 in equation (4.6) can be determined using the following boundary conditions:

1. There is no slip velocity at the wall

$$v_\mathrm{z}\left(y=0\right) \overset{!}{=} v_\mathrm{int} \Rightarrow C_2 = v_\mathrm{int}.$$

2. The shear stress at the interface exerted by the vapour flow is negligibly small

$$\mu_\mathrm{l} \left.\frac{\mathrm{d}v_\mathrm{z}}{\mathrm{d}y}\right|_{y=\delta} \approx 0 \Rightarrow C_1 = -\frac{g}{\nu_\mathrm{l}}\delta.$$

The velocity profile in the thin film can thereby be expressed as

$$v_\mathrm{z}\left(y\right) = \frac{g}{\nu_\mathrm{l}}\left(\frac{y^2}{2} - \delta y\right) + v_\mathrm{int}. \tag{4.7}$$

The mass flow per unit depth can by calculated by integrating the velocity profile along y-direction

$$\dot{M} = \rho_\mathrm{l}\int_0^\delta v_\mathrm{z}\mathrm{d}y = \rho_\mathrm{l}\left|\frac{g}{\nu_\mathrm{l}}\left(\frac{y^3}{6} - \frac{\delta y^2}{2}\right) + v_\mathrm{int}y\right|_0^\delta$$

$$\begin{aligned}\Rightarrow \dot{M}\left(z\right) &= \rho_\mathrm{l}v_\mathrm{int}\delta - \frac{1}{3}\frac{\rho_\mathrm{l}g\delta^3}{\nu_\mathrm{l}}\\ \Rightarrow \dot{M}\left(z+\mathrm{d}z\right) &= \rho_\mathrm{l}v_\mathrm{int}\left(\delta+\mathrm{d}\delta\right) - \frac{1}{3}\frac{\rho_\mathrm{l}g\left(\delta+\mathrm{d}\delta\right)^3}{\nu_\mathrm{l}}.\end{aligned} \tag{4.8}$$

From $\mathrm{d}\delta^2 \approx 0$, for an infinitesimal small $\mathrm{d}\delta$, follows $\left(\delta+\mathrm{d}\delta\right)^3 \approx \delta^3 + 3\delta^2\mathrm{d}\delta$ and $\dot{M}\left(z+\mathrm{d}z\right)$ can be expressed as

$$\dot{M}\left(z+\mathrm{d}z\right) = \dot{M}\left(z\right) + \rho_\mathrm{l}v_\mathrm{int}\mathrm{d}\delta - \frac{\rho_\mathrm{l}g\delta^2}{\nu_\mathrm{l}}\mathrm{d}\delta. \tag{4.9}$$

Combining equation (4.9) with the mass balance given by equation (4.2) and equation (4.3) results in an expression for the heat flow per unit depth at the interface

$$q_\mathrm{int}\mathrm{d}z = \Delta h_\mathrm{v}\left(\frac{\rho_\mathrm{l}g\delta^2}{\nu_\mathrm{l}}\mathrm{d}\delta - \rho_\mathrm{l}v_\mathrm{int}\mathrm{d}\delta\right). \tag{4.10}$$

Coupled to the mass flows $\dot{M}$ are energy flows $\dot{E}$ into and out of the control volume. Assuming the change in kinetic energy is negligible, the energy flow per unit depth is given by

$$\dot{E} = \rho_\mathrm{l}c_{p,\mathrm{l}}\int_0^\delta v_\mathrm{z}\cdot\left(T - T_0\right)\mathrm{d}y. \tag{4.11}$$

The reference temperature T_0 must be set to the interface temperature T_int, as this is the reference point for the energy of the evaporating mass flow per unit depth $\mathrm{d}\dot{M}_\mathrm{evap}$. Under the assumption of linear temperature profiles in y-direction the energy flow can be calculated through integration of

$$\begin{aligned}\dot{E} &= \rho_l c_{p,l} \int_0^{\delta} \left[\frac{g}{\nu_l} \left(\frac{y^2}{2} - \delta y \right) + v_{\text{int}} \right] \cdot \left[\frac{T_{\text{W}} - T_{\text{int}}}{\delta} (\delta - y) \right] \mathrm{d}y \\ &= \rho_l c_{p,l} \left| \frac{g \left(T_{\text{W}} - T_{\text{int}} \right)}{\nu_l \delta} \left(-\frac{y^4}{8} + \delta \frac{y^3}{2} - \delta^2 \frac{y^2}{2} \right) + v_{\text{int}} \frac{T_{\text{W}} - T_{\text{int}}}{\delta} \left(\delta y - \frac{y^2}{2} \right) \right|_0^{\delta}\end{aligned}$$

$$\begin{aligned}\Rightarrow \dot{E}(z) &= \frac{1}{2} \rho_l c_{p,l} v_{\text{int}} \left(T_{\text{W}} - T_{\text{int}} \right) \delta - \frac{1}{8} \rho_l c_{p,l} \frac{g \left(T_{\text{W}} - T_{\text{int}} \right)}{\nu_l} \delta^3 \\ \Rightarrow \dot{E}(z + \mathrm{d}z) &= \frac{1}{2} \rho_l c_{p,l} v_{\text{int}} \left(T_{\text{W}} - T_{\text{int}} \right) (\delta + \mathrm{d}\delta) - \frac{1}{8} \rho_l c_{p,l} \frac{g \left(T_{\text{W}} - T_{\text{int}} \right)}{\nu_l} (\delta + \mathrm{d}\delta)^3 .\end{aligned} \tag{4.12}$$

From $\mathrm{d}\delta^2 \approx 0$, for an infinitesimal small $\mathrm{d}\delta$, follows $(\delta + \mathrm{d}\delta)^3 \approx \delta^3 + 3\delta^2 \mathrm{d}\delta$ and $\dot{E}(z + \mathrm{d}z)$ can be expressed as

$$\dot{E}(z + \mathrm{d}z) = \dot{E}(z) + \frac{1}{2} \rho_l c_{p,l} v_{\text{int}} \left(T_{\text{W}} - T_{\text{int}} \right) \mathrm{d}\delta - \frac{3}{8} \rho_l c_{p,l} \frac{g \left(T_{\text{W}} - T_{\text{int}} \right)}{\nu_l} \delta^2 \mathrm{d}\delta. \tag{4.13}$$

The two-dimensional, stationary energy balance for the thin film segment is given by

$$\dot{E}(z + \mathrm{d}z) = \dot{E}(z) + q_{\text{W}} \mathrm{d}z - q_{\text{int}} \mathrm{d}z. \tag{4.14}$$

Assuming a linear temperature profile, the wall heat flux can be approximated by

$$q_{\text{W}} = \frac{\lambda_l}{\delta} \left(T_{\text{W}} - T_{\text{int}} \right). \tag{4.15}$$

Combining the energy balance given by equation (4.14) with equations (4.10), (4.13) and (4.15) yields

$$\begin{aligned}\frac{1}{2} \rho_l c_{p,l} v_{\text{int}} \left(T_{\text{W}} - T_{\text{int}} \right) \mathrm{d}\delta - \frac{3}{8} \rho_l c_{p,l} \frac{g \left(T_{\text{W}} - T_{\text{int}} \right)}{\nu_l} \delta^2 \mathrm{d}\delta \ldots \\ \ldots = \frac{\lambda_l}{\delta} \left(T_{\text{W}} - T_{\text{int}} \right) \mathrm{d}z - \Delta h_{\text{v}} \left(-\rho_l v_{\text{int}} \mathrm{d}\delta + \frac{\rho_l g \delta^2}{\nu_l} \mathrm{d}\delta \right)\end{aligned}$$

$$\Rightarrow \frac{\mathrm{d}\delta}{\mathrm{d}z} = \underline{\underline{\frac{\lambda_l \left(T_{\text{W}} - T_{\text{int}} \right)}{\Delta h_{\text{v}} \rho_l \left(\frac{g}{\nu_l} \left[1 - \frac{3}{8} \frac{c_{p,l} \left(T_{\text{W}} - T_{\text{int}} \right)}{\Delta h_{\text{v}}} \right] \delta^3 - v_{\text{int}} \left[1 - \frac{1}{2} \frac{c_{p,l} \left(T_{\text{W}} - T_{\text{int}} \right)}{\Delta h_{\text{v}}} \right] \delta \right)}}}. \tag{4.16}$$

This differential equation describes the evolution of the evaporating thin film.

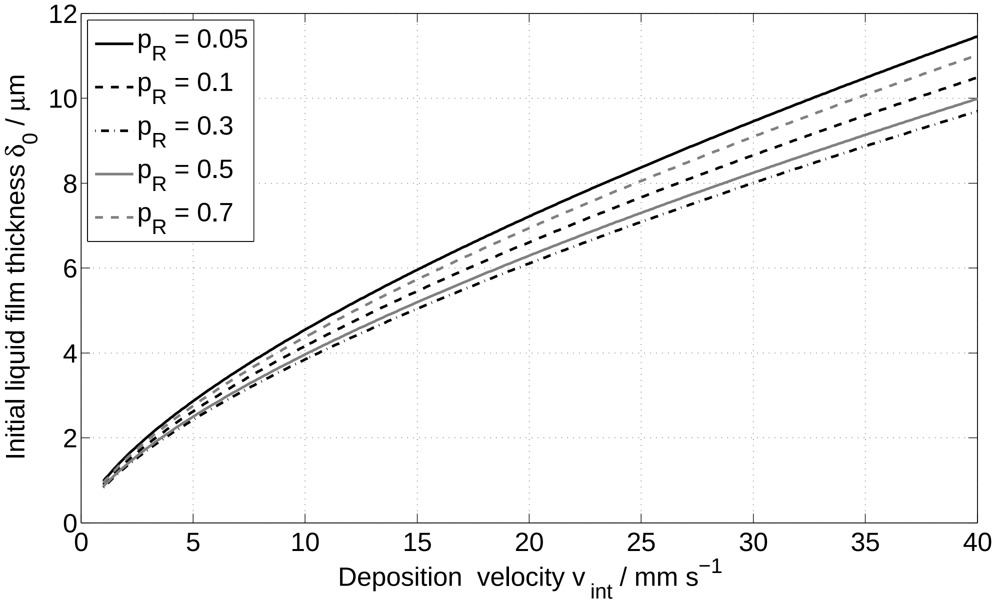

Figure 4.23.: Initial thickness of the deposited liquid film for FC-72 at different reduced pressures

If the influence of evaporation onto the initial film thickness δ_0 is small, it can be described by the solution found by Landau and Levich [87]. According to them, the initial film thickness can be calculated as

$$\delta_0 = \left(\frac{\mu_l v_{\text{int}}}{\rho_l g}\right)^{1/2} f\left(\text{Ca}\right). \tag{4.17}$$

where the function f can be approximated by

$$f\left(\text{Ca}\right) \approx 0.93\text{Ca}^{1/6} \qquad \text{for} \quad \text{Ca} \ll 1, \tag{4.18a}$$

$$f\left(\text{Ca}\right) \approx 1 \qquad \text{for} \quad \text{Ca} \gg 1. \tag{4.18b}$$

In figure 4.23 the initial film thickness δ_0 for FC-72 at different reduced pressures is displayed versus the deposition (= interface) velocity v_{int}.

In order to solve equation (4.16) analytically some additional assumptions must be made:

- The wall temperature is roughly constant in z-direction $T_{\text{W}} \approx$ const..
- The molecular kinetic thermal resistance at the interface is small compared to the thermal resistance of the liquid film. As the curvature of the interface is already assumed to be negligible, the interface temperature corresponds to the saturation temperature $T_{\text{int}} \approx T_{\text{sat}} = \text{const.}$

Dimensionless coordinates can be defined with the initial film thickness δ_0 given by equation (4.17)

$$\delta^* = \frac{\delta}{\delta_0}, \tag{4.19a}$$

$$z^* = \frac{z}{\delta_0}. \tag{4.19b}$$

The dimensionless form of equation (4.16) is then given by

$$\frac{\mathrm{d}\delta^*}{\mathrm{d}z^*} = \frac{\lambda_\mathrm{l}\left(T_\mathrm{W} - T_\mathrm{sat}\right)}{\Delta h_\mathrm{v}\rho_\mathrm{l}v_\mathrm{int}\delta_0\left(\frac{g{\delta_0}^2}{\nu_\mathrm{l}v_\mathrm{int}}\left[1 - \frac{3}{8}\frac{c_{p,\mathrm{l}}\left(T_\mathrm{W}-T_\mathrm{sat}\right)}{\Delta h_\mathrm{v}}\right]\delta^{*3} - \left[1 - \frac{1}{2}\frac{c_{p,\mathrm{l}}\left(T_\mathrm{W}-T_\mathrm{sat}\right)}{\Delta h_\mathrm{v}}\right]\delta^*\right)}$$

$$\Rightarrow \underline{\underline{\frac{\mathrm{d}\delta^*}{\mathrm{d}z^*} = \frac{A}{B\left[1 - \frac{3}{8}C\right]\delta^{*3} - \left[1 - \frac{1}{2}C\right]\delta^*}}}, \tag{4.20}$$

with

$$A = \frac{\lambda_\mathrm{l}\left(T_\mathrm{W} - T_\mathrm{sat}\right)}{\Delta h_\mathrm{v}\rho_\mathrm{l}v_\mathrm{int}\delta_0} = \frac{\mathrm{Ja}}{\mathrm{Pr\ Re}}, \tag{4.21a}$$

$$B = \frac{g{\delta_0}^2}{\nu_\mathrm{l}v_\mathrm{int}} = \frac{\mathrm{Bo}}{\mathrm{Ca}}, \tag{4.21b}$$

$$C = \frac{c_{p,\mathrm{l}}\left(T_\mathrm{W} - T_\mathrm{sat}\right)}{\Delta h_\mathrm{v}} = \mathrm{Ja}. \tag{4.21c}$$

From the physical point of view the parameters A and B represent mass flux ratios

$$A = \frac{\text{evaporating mass flux}}{\text{deposited mass flux}},$$

$$B = \frac{\text{mass flux caused by gravity}}{\text{deposited mass flux}}.$$

The dimensionless parameters A and B for FC-72 at an exemplary wall superheat of $\Delta T_\mathrm{W} = 4\,\mathrm{K}$ are displayed in figures 4.24 and 4.25. An interesting outcome of the dimensionless treatment is, that equation (4.20) contains with the dimensionless parameters A and C two quantities, that depend on the ratio of wall superheat to latent heat of evaporation. While it has been reasoned that the

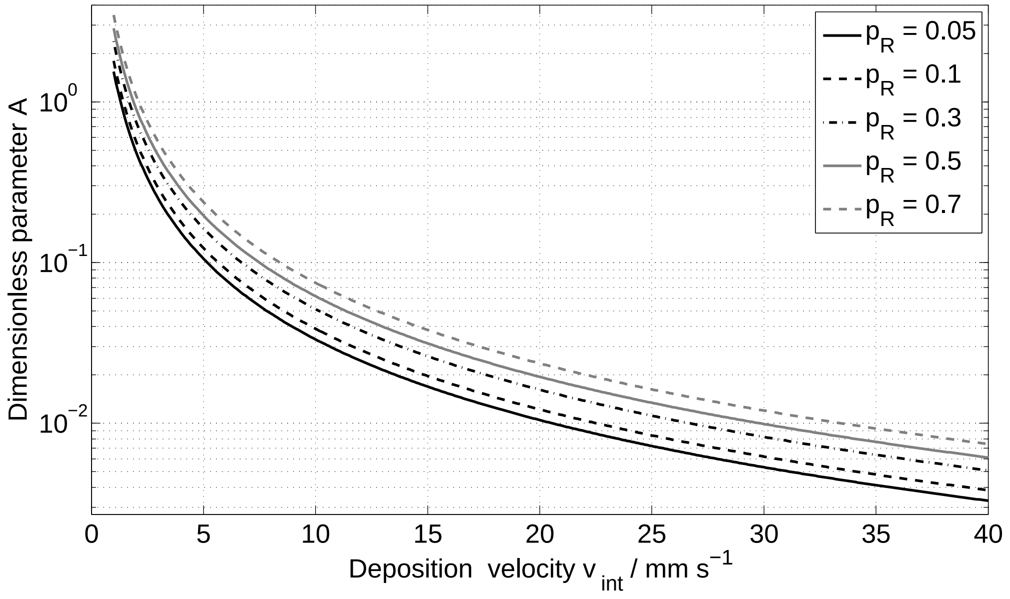

Figure 4.24.: Dimensionless parameter A versus deposition velocity for FC-72 at 4 K wall superheat

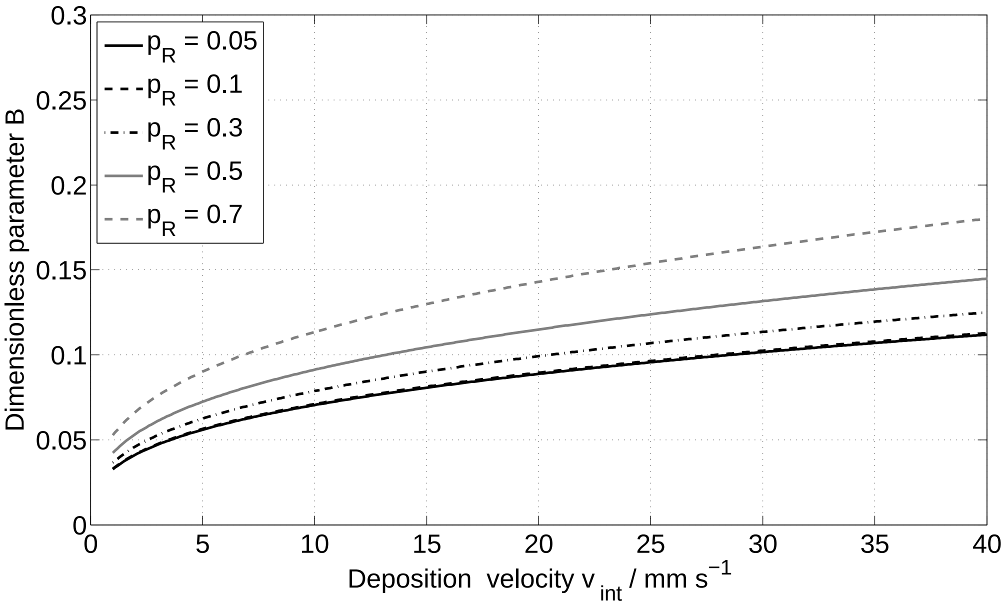

Figure 4.25.: Dimensionless parameter B versus deposition velocity for FC-72

appearance of thin film/microlayer evaporation depends on the Jakob number C by Kim [83], a new dimensionless influence factor containing this ratio has been identified in the parameter A.

The parameter C is one version of the definition for the Jakob number Ja, sometimes encountered in phase change problems [5]. It depends only on the wall superheat and the liquid properties and represents a ratio of energy storage

$$C = \frac{\text{energy stored in superheated liquid}}{\text{energy stored in latent heat}}.$$

Equation (4.20) can be integrated to obtain the film thickness profile

$$\int\limits_{\delta^*=1}^{\delta^*} B\left(1-\frac{3}{8}C\right)\delta^{*3} - \left(1-\frac{1}{2}C\right)\delta^* \mathrm{d}\delta^* = \int\limits_{z^*=0}^{z^*} A\mathrm{d}z^*$$

$$\Rightarrow \frac{B}{4}\left(1-\frac{3}{8}C\right)\left(\delta^{*4}-1\right) - \frac{1}{2}\left(1-\frac{1}{2}C\right)\left(\delta^{*2}-1\right) = Az^*. \tag{4.22}$$

With equation (4.22) the dimensionless film length l^*_{TF} can be calculated

$$l^*_{\mathrm{TF}} = z^*(\delta^*=0) = \frac{1}{2A}\left(1-\frac{1}{2}C\right) - \frac{B}{4A}\left(1-\frac{3}{8}C\right). \tag{4.23}$$

In figure 4.26 the dimensionless film length l^*_{TF} is plotted versus the deposition (= interface) velocity v_{int} for FC-72 under different reduced pressures at 4 K wall superheat. Equation (4.20) is actually not valid at $\delta^* = 0$, as the assumptions of negligible curvature of the interface and negligible thermal resistance of the interface are violated close to the contact line. Nevertheless equation (4.23) can give an estimation of the length of the thin film.

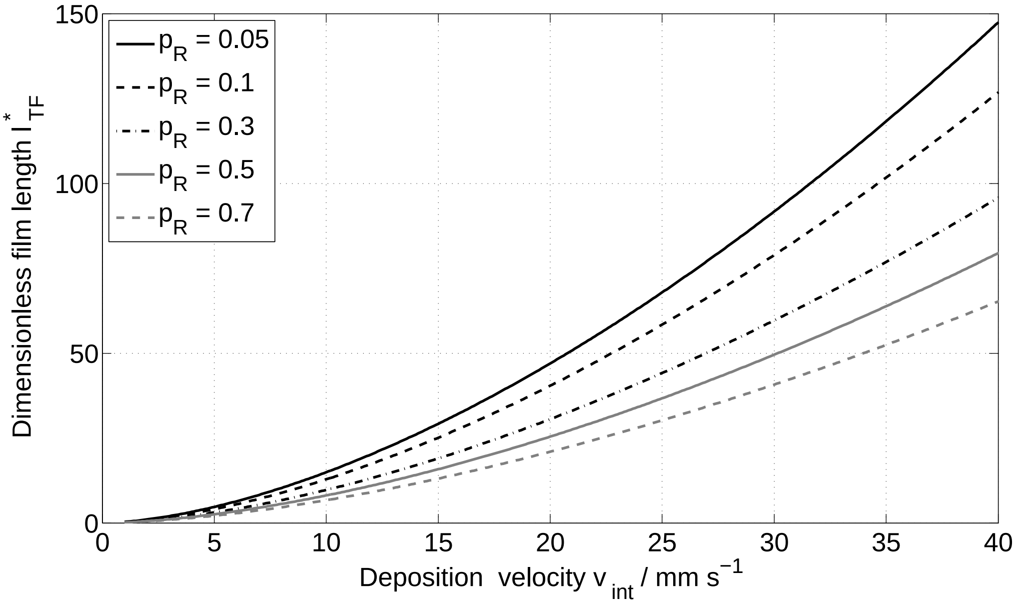

Figure 4.26.: Dimensionless film length l^*_{TF} versus deposition velocity for FC-72 at 4 K wall superheat

Equation (4.22) can also be rewritten in an explicit form for the dimensionless film thickness δ^* as

$$\delta^* = \sqrt{\frac{1-\frac{1}{2}C}{B\left(1-\frac{3}{8}C\right)} - \sqrt{\left[\frac{1-\frac{1}{2}C}{B\left(1-\frac{3}{8}C\right)}\right]^2 + \frac{4Az^*}{B\left(1-\frac{3}{8}C\right)} + 1 - \frac{2-C}{B\left(1-\frac{3}{8}C\right)}}}. \tag{4.24}$$

Heat transfer from the wall to the thin film is characterized by the local Nusselt number, with the initial film thickness as characteristic length scale

$$\mathrm{Nu} = \frac{h\delta_0}{\lambda_\mathrm{l}} = \frac{q_\mathrm{W}\delta_0}{\lambda_\mathrm{l}\left(T_\mathrm{W}-T_\mathrm{sat}\right)}. \tag{4.25}$$

Inserting equation (4.15) results in

$$\mathrm{Nu} = \frac{1}{\delta^*}. \tag{4.26}$$

As a result of the assumption, that wall heat transfer can be approximated by thermal conduction through the thin film, the local Nusselt number becomes the reciprocal of the dimensionless film thickness, which is given by equation (4.24).

As already outlined in section 4.5.1 it is not quite clear when the appearance of the thin film is triggered. In the experiments, the thin film was observed most often (but not always) at a reduced pressure of $p_\mathrm{R} = 0.05$. At this reduced pressure, the thin film appeared to be stationary in enough comparable sequences to allow for a comparison of experimental data with the model described above. Experimental data, which is directly comparable, is the length of the thin film region. In the experiments this length is determined as distance between maximum and minimum heat flux gradient in z/ξ-direction minus the distance between maximum and minimum heat flux gradient in z/ξ-direction, when the contact line is not moving. This correction is necessary as the heat flux

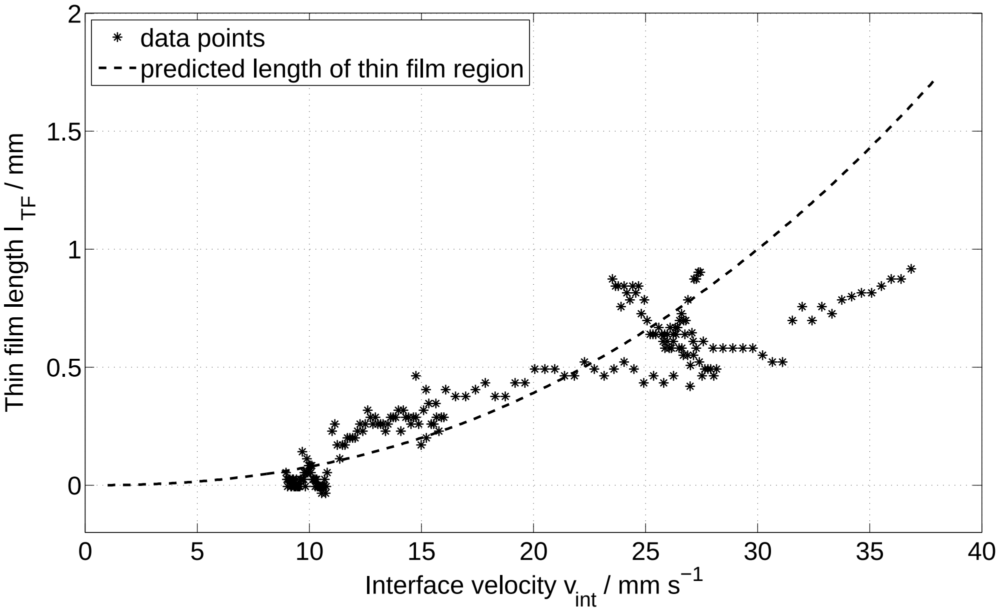

Figure 4.27.: Comparison of the predicted film length l_{TF} and the measured length of the thin film region versus meniscus velocity for FC-72 at 3.3 K wall superheat ($p_{\mathrm{R}} = 0.05$)

gradient is "smeared out" over several pixel due to the limited spatial resolution of the IR camera and the smoothing necessary to ensure the stability of the heat flux calculation. The result of the thin film prediction given by equation (4.23) for a mean wall superheat of $\Delta T_{\mathrm{W,av}} = 3.3\,\mathrm{K}$ and the experimental data points at $p_{\mathrm{R}} = 0.05$ are displayed in figure 4.27. Reasonable agreement between experiment and theory can be identified up to an interface velocity of $v_{\mathrm{int}} \approx 28\,\mathrm{mm\,s^{-1}}$. Above this value, the theoretical prediction of the liquid film length seems to be departing from the length determined from

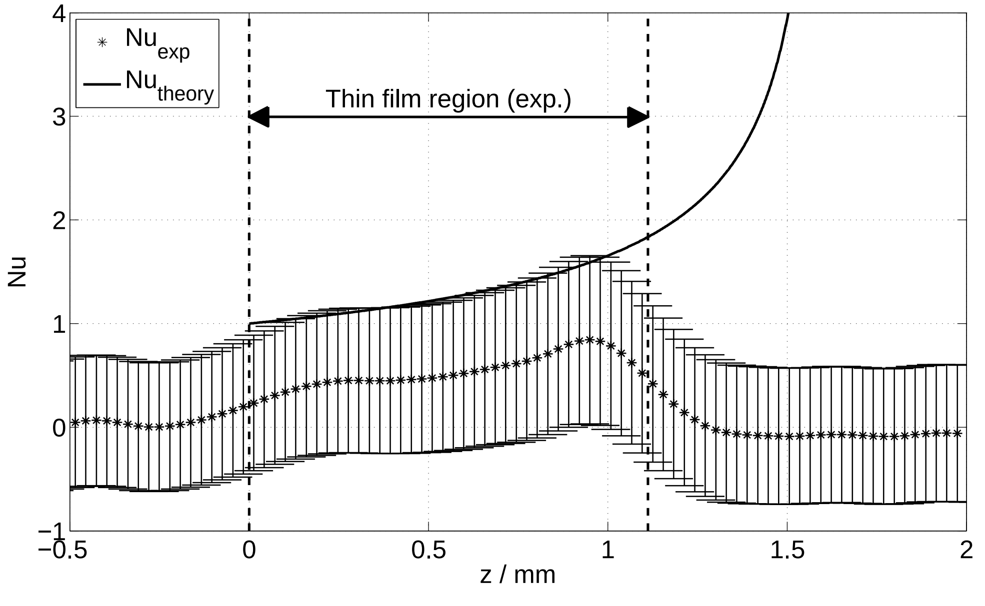

Figure 4.28.: Comparison of theoretical Nusselt number and Nusselt number determined in the experiment for FC-72 at 3.3 K wall superheat and $v_{\mathrm{int}} = 36.9\,\mathrm{mm\,s^{-1}}$ ($p_{\mathrm{R}} = 0.05$)

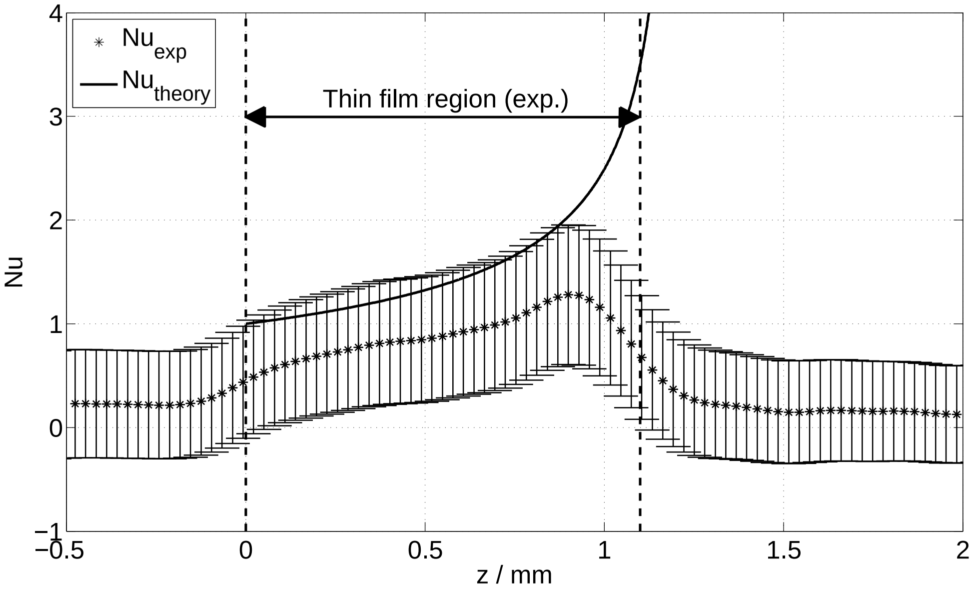

Figure 4.29.: Comparison of theoretical Nusselt number and Nusselt number determined in the experiment for FC-72 at 4.7 K wall superheat and $v_{\mathrm{int}} = 35.5\,\mathrm{mm\,s^{-1}}$ ($p_{\mathrm{R}} = 0.1$)

experiments. This could be caused by the limited length of the heater element. The model is only valid for stationary thin film evaporation. At large interface velocities, the film length is expected to be bigger and the distance between edge of the heater and measurement area is covered more quickly. Therefore it is possible, that the timescale for the film to become stationary is bigger than that for it to travel beyond the measurement area and no steady state thin film evaporation occurs.

In figures 4.28 and 4.29 a comparison of the theoretical, local Nusselt number (eq. (4.24) and (4.26)) and local Nusselt numbers determined from experiments (eq. (4.25) with experimental data on local heat flux and temperature distribution) is shown for two sequences with different reduced pressures and wall superheats, but comparable interface velocities. The slope of the experimental data is matched rather well by the theoretical prediction in both cases. In the majority of the thin film region the theoretical Nusselt number lies at the upper boundary of the measurement uncertainty of the experimental Nusselt number. A stronger deviation is found close to the intrinsic meniscus. Here, the assumptions of a linear temperature profile across the film thickness and heat transfer being solely controlled by one-dimensional thermal conduction are not satisfied. Close to dry-out of the thin film, the model deviates further from the experimental values. This was to be expected, as the liquid film is extremely thin with a high interface curvature close to the contact line. The model does not incorporate the deviation of the local saturation conditions caused by interface curvature, disjoining pressure and the interfacial thermal resistance,which play a role under these circumstances.

5 Summary and Outlook

5.1 Summary

Heat transfer close to moving three-phase contact lines is of tremendous importance in numerous evaporation processes. Examples for such processes are pool and flow boiling, evaporation in heat pipes with wick structures or open grooves or droplet evaporation in spray cooling applications. The huge number of technical applications involving these processes illustrates the importance of understanding contact line heat transfer for industry in order to design apparatuses and predict their behavior reliably. Many of these applications involve high values of the reduced pressure and/or high velocities of the three-phase contact line, which are pre-determined through the hydrodynamics of the respective process. Evaporation from a single extended meniscus is the simplest configuration involving contact line heat transfer, in which both pressure and contact line velocity can be systematically varied.

With the **heater technology** developed in the frame of this work, a huge step has been taken towards high resolution wall temperature measurements at the heater/fluid-interface of heaters more closely resembling heater walls found in technical applications. Not only is the thermal diffusivity of the heater substrate material in the same range as that of stainless steels, which are used to manufacture evaporation devices, but due to its large thickness its thermal capacity per surface area is also much closer to applications than thin foil heaters. Because the two-layer coating composition thickness is less than 1 μm, the heater design makes it possible to measure the temperature distribution extremely close to the actual heater/fluid-interface with high spatial and temporal resolution using IR-thermography.

To generate a moving contact line situation under different values of the reduced pressure at the heater surface, a dedicated **experiment setup** has been designed. In combination with the degassing procedure, this closed, two-phase, single species system allows for the investigation of heat transfer at the contact line of an extended meniscus inside a single capillary slot. While the value of the reduced pressure is set in the range of $p_{\mathrm{R}} = 0.05 - 0.7$ via the system temperature, a volume displacement system has been constructed to realize velocities of the liquid/vapour-interface of up to $v_{\mathrm{int}} = \pm\, 40\,\mathrm{mm\,s^{-1}}$. The temperature distribution at the heater/fluid-interface of the IR transparent heater has been measured with an in-situ calibrated high-speed IR thermography camera at a framerate of 1000 Hz with a spatial resolution of 29.27 μm/pixel. The IR camera has been synchronized with a high speed black and white camera, that recorded the meniscus shape from the side with a spatial resolution of 4 μm/pixel.

In contrast to the situation on thin foil heaters, the temperature can not be assumed to be uniform across the heater thickness in case of the IR transparent heater. Therefore a state of the art calculation method of the local heat flux as used on thin foil heaters, which is based on a two-dimensional, instationary energy balance for each pixel of the temperature field, can not be applied. Instead, a **new heat flux calculation procedure** has been developed to numerically calculate the local heat flux fields out of the temperature distributions with a three-dimensional substrate discretization using the CFD-code OpenFOAM®.

To determine velocity and contact angle from the high speed black and white images, a purely **physically based interface fitting algorithm** has been developed and implemented in MATLAB®. Apart from a description of the interface shape, information about the interface velocity and the apparent contact angle, the algorithm also provides information about the deviation from the static pressure balance. It has been shown that the determined contact angle does however not necessarily represent the apparent contact angle at the wall, as the requirement of an extended meniscus requires an extended straight heater wall that can lead to information loss due to shading close to the wall. At high pressures a reduction of contrast at the interface requires an alternative method to determine the interface velocity. A tracking algorithm for the heat flux maximum and the maximum and minimum heat flux gradient in ξ-direction has been applied in these cases.

At a **non-moving contact line** the heat flux and temperature distributions agree qualitatively very well to the precursor experiment carried out by Ibrahem et al. [41]. The existence of a heat flux maximum close to the three-phase contact line could be confirmed for heaters with higher thermal capacity. The accompanying temperature minimum however was found to be in the order of $\sim 0.1\,\mathrm{K}$ and thereby one order of magnitude lower than the values reported by Ibrahem et al. on thin foil heaters. This discrepancy could be explained through the 3-d heat flux data in the solid available from the heat flux calculation procedure. It could be shown, that in contrast to thin foil heaters, in a thick heater element energy can be transported to the contact line region in perpendicular direction to the heater/fluid-interface. Therefore smaller temperature gradients in the solid are required to transport the same amount of energy to the contact line.

It has been found that with **increasing pressure** the heat flux maximum at the contact line decreases for both advancing and receding contact lines. It could be shown that this reduction of the heat flux peak scales with the decrease of the latent heat of evaporation with increasing system pressure. The ratio of maximum heat flux divided by latent heat of evaporation is practically unaltered through a change of the system pressure. Since convective heat transfer to the liquid/vapour-interface increases with system pressure due to an increase of the liquid thermal capacity, the contribution of contact line heat transfer to overall heat transfer decreases with increasing pressure.

Concerning the **heat transfer at advancing and receding contact lines** it has been confirmed that as long as heat transfer is dominated by contact line evaporation, the heat flux peak at receding contact lines is smaller than at advancing contact lines. While the heat flux peak (and thereby the overall heat transfer close to the contact line) increases with velocity at an advancing contact line, it has been found to be independent of the contact line velocity at receding contact lines. This is in agreement to results of Kunkelmann et at. [15], Schweizer [40] and Ibrahem et al. [42]. An exception to this are sequences, in which an evaporating thin film was deposited on the surface by the receding meniscus.

A comparative analysis of several sequences, in which a thin evaporating film was deposited, has been carried out to identify **parameters influencing thin film generation**. In accordance to considerations of the contribution of thin film evaporation to boiling processes by Kim [83], it could be confirmed that a low Jakob number (low wall superheat and/or high latent heat of evaporation) promotes thin film heat transfer. Furthermore the velocity with which the liquid/vapour-interface is receding has been found to be of importance. The length of the thin film region has been found to increase with interface receding velocity. Beyond Jakob number and interface velocity, the acceleration of the interface and wetting characteristics of the heater surface have been found to play a role in triggering the thin film deposition. As it was shown by Bankoff [86], the thin evaporating film is unstable on a vertical wall. In some sequences film rupture has been observed, which was always followed by the re-development of a thin evaporating film.

An **analytical model for stationary thin film evaporation** has been developed, that extends the model for deposition of a non-evaporating thin film by Landau and Levich [87] for cases with evaporation. An expression for the film thickness evolution with distance from the intrinsic meniscus has been found, that contains the influence factors interface velocity, wall superheat and latent heat of evaporation as described beforehand. By making the equations dimensionless with the initial film thickness, dimensionless parameters governing stationary thin film evaporation have been identified. Using the model, an estimation of the length of the thin film region could be calculated. By inserting fluid data and experiment parameters into the estimation, the model prediction of the thin film length has been compared to experimental results, in which a stationary thin film could be identified. Reasonable agreement between model prediction and experiment has been found up to a threshold of the interface velocity. This deviation has been attributed to the limited length of the heater element, that does not allow for the development of a stationary thin film.

It has been discussed for quite some time in the scientific community whether **thin film (or microlayer) evaporation or contact line evaporation** is the dominant mode of heat transfer in boiling phenomena [88]. The results of this work show, that it depends on the fluid and experiment parameters, which one of these heat transfer modes is dominant. With the analytical model for stationary thin film evaporation, a first step towards the quantification of the parameters influencing thin film evaporation has been undertaken. Still further research is necessary to quantify the influence of parameters, that appear to be responsible for triggering the generation of the thin film and the influence of film rupture. The aim should be a regime map, which makes it possible to identify the dominant mode of heat transfer (contact line or thin film dominated) based on thermophysical fluid data and the process parameters. Based on such a regime map, it will be possible to model boiling and other phase change phenomena physically more accurately.

5.2 Outlook

In order to achieve the goal of generating a regime map for thin film (microlayer) or contact line evaporation and collect more data to validate the thin film model, a **new experiment** is needed that incorporates a longer heater surface to allow for the generation of longer thin films at higher interface velocities and a bigger IR camera field-of-view to track the longer films. In order to further validate the thin film model a highly resolved measurement of the film thickness profile would be of interest, that can be compared to predictions of the model. Such data could be gathered with an interferometric or a laser extinction method.

In order to check, whether the influence of gravity is expressed correctly by the model (gravitational forces reduce the initial film thickness and try to drain the film), an **experiment in microgravity** could be performed. As the liquid film can be expected to be longer and thicker in microgravity, the measurement resolution would also be artificially increased in a microgravity environment.

In its current state the developed model does not **incorporate contact line evaporation at the end of the thin film region**. The contact line model as described in chapter 2.1 should be coupled to the thin film model there to incorporate the effects of interface curvature, disjoining pressure and interfacial thermal resistance.

Futhermore figures 4.28 and 4.29 show, that an **adaptation of the model close to the intrinsic meniscus** appears to be necessary. While the theory necessarily predicts a Nusselt number of one at the beginning of the thin film region, this value is not reached by experimental data, as local heat transfer is here probably still influenced by the flow patterns of the intrinsic meniscus. This effect should be accounted for by a correction of the local Nusselt number.

If the development of a regime map to distinguish between contact line dominated and thin film evaporation dominated heat transfer is successful, the developed model can be the starting point to **incorporate thin film evaporation as sub-grid model** (analogue to the contact line model) in numerical codes. Based on the regime map, the model that describes the physical process correctly can then be chosen by the program. In nucleate boiling for example, high interface velocities are present during the early stages of bubble growth and thin film evaporation can be dominant. In later stages of the bubble growth the interface velocity decreases and contact line evaporation gains dominance [88]. If a thin film is present during early bubble growth, a numerical program used to predict boiling heat transfer needs to take both heat transfer modes into account to reflect the underlying physics correctly.

Bibliography

[1] P. C. Wayner, Y. K. Kao, and L. V. LaCroix. The interline heat-transfer coefficient of an evaporating wetting film. *International Journal of Heat and Mass Transfer*, 19(5):487–492, 1976.

[2] S. DasGupta, I.Y Kim, and P. C. Wayner [JR.]. Use of the Kelvin-Clapeyron Equation to Model an Evaporating Curved Microfilm. *Journal of Heat Transfer*, 116:1007–1015, 1994.

[3] P. Stephan and J. Hammer. A new model for nucleate boiling heat transfer. *Heat and Mass Transfer*, 30(2):119–125, 1994.

[4] C. Kunkelmann. *Numerical Modeling and Investigation of Boiling Phenomena*. PhD thesis, Institut für Technische Thermodynamik, Technische Universität Darmstadt, Darmstadt, 2011.

[5] V. P. Carey. *Liquid-vapor phase-change phenomena: An introduction to the thermophysics of vaporization and condensation processes in heat transfer equipment*. Taylor and Francis, New York, 2nd edition, 2008.

[6] P. C. Stephan and C. A. Busse. Analysis of the heat transfer coefficient of grooved heat pipe evaporator walls. *International Journal of Heat and Mass Transfer*, 35(2):383–391, 1992.

[7] K. Stephan. Influence of dispersion forces on phase equilibria between thin liquid films and their vapour. *International Journal of Heat and Mass Transfer*, 45(24):4715–4725, 2002.

[8] F. London and M. Polanyi. Über die atomtheoretische Deutung der Adsorptionskräfte. *Naturwissenschaften*, 18(50):1099–1100, 1930.

[9] H.C. Hamaker. The London-van der Waals attraction between spherical particles. *Physica*, 4(10):1058–1072, 1937.

[10] C. J. van Oss, M. K. Chaudhury, and R. J. Good. Interfacial Lifshitz-van der Waals and polar interactions in macroscopic systems. *Chemical Reviews*, 88(6):927–941, 1988.

[11] R. Marek and J. Straub. Analysis of the evaporation coefficient and the condensation coefficient of water. *International Journal of Heat and Mass Transfer*, 44(1):39–53, 2001.

[12] P. Stephan. *Wärmedurchgang bei Verdampfung aus Kapillarrillen in Wärmerohren*. PhD thesis, Universität Stuttgart, 1992.

[13] C. Kunkelmann and P. Stephan. CFD Simulation of Boiling Flows Using the Volume-of-Fluid Method within OpenFOAM. *Numerical Heat Transfer, Part A: Applications*, 56(8):631–646, 2009.

[14] C. Kunkelmann and P. Stephan. Numerical simulation of the transient heat transfer during nucleate boiling of refrigerant HFE-7100. *International Journal of Refrigeration*, 33(7):1221–1228, 2010.

[15] C. Kunkelmann, K. Ibrahem, N. Schweizer, S. Herbert, P. Stephan, and T. Gambaryan-Roisman. The effect of three-phase contact line speed on local evaporative heat transfer: Experimental and numerical investigations. *International Journal of Heat and Mass Transfer*, 55(7-8):1896–1904, 2012.

[16] R. Raj, C. Kunkelmann, P. Stephan, J. Plawsky, and J. Kim. Contact line behavior for a highly wetting fluid under superheated conditions. *International Journal of Heat and Mass Transfer*, 55(9-10):2664–2675, 2012.

[17] S. Herbert, S. Fischer, T. Gambaryan-Roisman, and P. Stephan. Local heat transfer and phase change phenomena during single drop impingement on a hot surface. *International Journal of Heat and Mass Transfer*, 61:605–614, 2013.

[18] S. Herbert, T. Gambaryan-Roisman, and P. Stephan. Influence of the governing dimensionless parameters on heat transfer during single drop impingement onto a hot wall. *Colloids and Surfaces A: Physicochemical and Engineering Aspects*, 432:57–63, 2013.

[19] P. C. Wayner and C. L. Coccio. Heat and mass transfer in the vicinity of the triple interline of a meniscus. *AIChE Journal*, 17(3):569–574, 1971.

[20] S. DasGupta, J. A. Schonberg, and P. C. Wayner. Investigation of an Evaporating Extended Meniscus Based on the Augmented Young-Laplace Equation. *Journal of Heat Transfer*, 115:201–208, 1993.

[21] I. Y. Kim and P. C. Wayner. Shape of an evaporating completely wetting extended meniscus. *Journal of Thermophysics and Heat Transfer,* 10(2):320–325, 1996.

[22] P. C. Wayner. The effect of interfacial mass transport on flow in thin liquid films. *Colloids and Surfaces*, 52:71–84, 1991.

[23] C. Höhmann and P. Stephan. Microscale temperature measurement at an evaporating liquid meniscus. *Experimental Thermal and Fluid Science*, 26(2-4):157–162, 2002.

[24] C. Höhmann. *Temperaturmessverfahren zur räumlich hochauflösenden Untersuchung des Wärmetransports an einem verdampfenden Flüssigkeitsmeniskus*. PhD thesis, Institut für Technische Thermodynamik, Technische Universität Darmstadt, Darmstadt, 2004.

[25] C. Buffone and K. Sefiane. IR measurements of interfacial temperature during phase change in a confined environment. *Experimental Thermal and Fluid Science*, 29(1):65–74, 2004.

[26] C. Buffone and K. Sefiane. Temperature measurement near the triple line during phase change using thermochromic liquid crystal thermography. *Experiments in Fluids*, 39(1):99–110, 2005.

[27] S. G. Kandlikar and W. K. Kuan. Heat Transfer From a Moving and Evaporating Meniscus on a Heated Surface. In *Proceedings of Heat Transfer 2003 ASME Summer Heat Transfer Conference*, 2003.

[28] S. G. Kandlikar, W. K. Kuan, and A. Mukherjee. Experimental Study of Heat Transfer in an Evaporating Meniscus on a Moving Heated Surface. *Journal of Heat Transfer*, 127(3):244, 2005.

[29] L. Zheng, Y.-X. Wang, J. L. Plawsky, and P. C. Wayner. Accuracy of measurements of curvature and apparent contact angle in a constrained vapor bubble heat exchanger. *International Journal of Heat and Mass Transfer*, 45(10):2021–2030, 2002.

[30] L. Zheng, J. L. Plawsky, P. C. Wayner, and S. DasGupta. Stability and Oscillations in an Evaporating Corner Meniscus. *Journal of Heat Transfer*, 126(2):169, 2004.

[31] S. J. Gokhale, J. L. Plawsky, and P. C. Wayner. Experimental investigation of contact angle, curvature, and contact line motion in dropwise condensation and evaporation. *Journal of Colloid and Interface Science*, 259(2):354–366, 2003.

[32] J. L. Plawsky, S. S. Panchamgam, S. J. Gokhale, P. C. Wayner, and S. DasGupta. A study of the oscillating corner meniscus in a vertical constrained vapor bubble system. *Superlattices and Microstructures*, 35(3-6):559–572, 2004.

[33] S. S. Panchamgam, J. L. Plawsky, and P. C. Wayner. Microscale heat transfer in an evaporating moving extended meniscus. *Experimental Thermal and Fluid Science*, 30(8):745–754, 2006.

[34] S. S. Panchamgam, J. L. Plawsky, and P. C. Wayner. Spreading Characteristics and Microscale Evaporative Heat Transfer in an Ultrathin Film Containing a Binary Mixture. *Journal of Heat Transfer*, 128(12):1266, 2006.

[35] M. Ojha, A. Chatterjee, G. Dalakos, P. C. Wayner, and J. L. Plawsky. Role of solid surface structure on evaporative phase change from a completely wetting corner meniscus. *Physics of Fluids*, 22(5):052101, 2010.

[36] H. K. Dhavaleswarapu, P. Chamarthy, S. V. Garimella, and J. Y. Murthy. Experimental investigation of steady buoyant-thermocapillary convection near an evaporating meniscus. *Physics of Fluids*, 19(8):082103, 2007.

[37] P. Chamarthy, H. K. Dhavaleswarapu, S. V. Garimella, J. Y. Murthy, and S. T. Wereley. Visualization of convection patterns near an evaporating meniscus using μPIV. *Experiments in Fluids*, 44(3):431–438, 2008.

[38] H. K. Dhavaleswarapu, S. V. Garimella, and J. Y. Murthy. Microscale Temperature Measurements Near the Triple Line of an Evaporating Thin Liquid Film. *Journal of Heat Transfer*, 131(6):061501, 2009.

[39] C. P. Migliaccio, H. K. Dhavaleswarapu, and S. V. Garimella. Temperature measurements near the contact line of an evaporating meniscus V-groove. *International Journal of Heat and Mass Transfer*, 54(7-8):1520–1526, 2011.

[40] N. Schweizer. *Multi-Scale Investigation of Nucleate Boiling Phenomena in Microgravity*. PhD thesis, Institut für Technische Thermodynamik, Technische Universität Darmstadt, Darmstadt, 2010.

[41] K. Ibrahem, M.F Abd Rabbo, T. Gambaryan-Roisman, and P. Stephan. Experimental investigation of evaporative heat transfer characteristics at the 3-phase contact line. *Experimental Thermal and Fluid Science*, 34(8):1036–1041, 2010.

[42] K. Ibrahem, M. F. Abd Rabbo, T. Gambaryan-Roisman, and P. Stephan. Experimental Investigation of Micro-Scale Heat Transfer at an Evaporating Moving 3-Phase Contact Line. In *Proceedings of the 14th International Heat Transfer Conference*, pages 783–790, 2010.

[43] K. Ibrahem, M. F. Abd Rabbo, T. Gambaryan-Roisman, and P. Stephan. Experimental and numerical investigation of evaporative heat transfer in the vicinity of the 3-phase contact line. In *Proceedings of the 3rd International Conference on Thermal Issues in Emerging Technologies Theory and Applications (ThETA)*, pages 207–215, 2010.

[44] J. Kim, J. F. Benton, and D. Wisniewski. Pool boiling heat transfer on small heaters: effect of gravity and subcooling. *International Journal of Heat and Mass Transfer*, 45(19):3919–3932, 2002.

[45] F. Demiray and J. Kim. Microscale heat transfer measurements during pool boiling of FC-72: effect of subcooling. *International Journal of Heat and Mass Transfer*, 47(14-16):3257–3268, 2004.

[46] J. G. Myers, V. K. Yerramilli, S. W. Hussey, G. F. Yee, and J. Kim. Time and space resolved wall temperature and heat flux measurements during nucleate boiling with constant heat flux boundary conditions. *International Journal of Heat and Mass Transfer*, 48(12):2429–2442, 2005.

[47] P. Delgoshaei and J. Kim. Microscale Heat Transfer Measurements During Subcooled Pool Boiling of Pentane: Effect of Bubble Dynamics. In *Proceedings of the 14th International Heat Transfer Conference*, pages 397–405, 2010.

[48] R. Nasarek. *Temperature field measurements with high spatial and temporal resolution using liquid crystal thermography and laser induced fluorescence*. PhD thesis, Technische Universität Darmstadt, Darmstadt, 2010.

[49] J. P. Crimaldi. The effect of photobleaching and velocity fluctuations on single-point LIF measurements. *Experiments in Fluids*, 23(4):325–330, 1997.

[50] L. G. Larsen and J. P. Crimaldi. The effect of photobleaching on PLIF. *Experiments in Fluids*, 41(5):803–812, 2006.

[51] K. S. Birdi, D. T. Vu, and A. Winter. A study of the evaporation rates of small water drops placed on a solid surface. *The Journal of Physical Chemistry*, 93(9):3702–3703, 1989.

[52] E. Truckenbrodt. *Grundlagen und elementare Strömungsvorgänge dichtebeständiger Fluide, Band 1 von Fluidmechanik*. Springer, Berlin [u.a.], 4., ergänzte Auflage 1996, Nachdruck 2008 in veränderter Ausstattung, 2008.

[53] W. Kast (Revised by H. Nirschl). L1.2 Pressure Drop in Flow Through Pipes. In *VDI Heat Atlas*, pages 1053–1116. Springer, Berlin and Heidelberg, 2010.

[54] T. G. Theofanous, J. P. Tu, A. T. Dinh, and T. N. Dinh. The boiling crisis phenomenon: Part I: nucleation and nucleate boiling heat transfer. *Experimental Thermal and Fluid Science*, 26(6-7):775–792, 2002.

[55] T. G. Theofanous, T. N. Dinh, J. P. Tu, and A. T. Dinh. The boiling crisis phenomenon: Part II: dryout dynamics and burnout. *Experimental Thermal and Fluid Science*, 26(6-7):793–810, 2002.

[56] D. Chatzikyriakou, S. P. Walker, C. P. Hale, and G. F. Hewitt. The measurement of heat transfer from hot surfaces to non-wetting droplets. *International Journal of Heat and Mass Transfer*, 54(7-8):1432–1440, 2011.

[57] X. Duan, B. Philips, T. McKrell, and J. Buongiorno. Synchronized high-speed video, infrared thermometry and PIV data for validation of interface-tracking simulations of nucleate boiling phenomena. In *Proceeding of the 8th International Conference on Boiling and Condensation Heat Transfer*, 2012.

[58] E. M. Slomski. *Funktionsorientierte Mikrostrukturierung von Chromnitrid-Beschichtungen mittels hybrider PVD-Technologie*. PhD thesis, Institut für Werkstoffkunde, Technische Universität Darmstadt, Darmstadt, 2012.

[59] Korth Kristalle GmbH. Material data Calcium Fluoride, 2014.

[60] M. Neubronner and T. Bodmer. D6.1 Thermodynamic Properties of Pure Metals and Metal Alloys. In *VDI Heat Atlas*, pages 551–565. Springer, Berlin and Heidelberg, 2010.

[61] E. M. Slomski, H. Scheerer, T. Troßmann, and C. Berger. Einfluss der PVD-Prozessparameter auf die Schichtnukleation und Struktur von CrN-Schichten. *Materialwissenschaft und Werkstofftechnik*, 41(3):161–165, 2010.

[62] E. M. Slomski, H. Scheerer, T. Troßmann, and C. Berger. Einfluss der HiPIMS-Parameter beim PVD-Verfahren. *Vakuum in Forschung und Praxis*, 22(4):22–25, 2010.

[63] A. Bejan. *Advanced Engineering Thermodynamics*. Wiley, New York, 3$^{\text{rd}}$ edition, op. 2006.

[64] J. S. Rowlinson. *J. D. van der Waals. On the continuity of the gaseous and liquid states*, volume 14 of *Studies in statistical mechanics*. North-Holland, Amsterdam, 1988.

[65] C. Tropea, A. L. Yarin, and J. F. Foss (Eds.). *Springer handbook of experimental fluid mechanics*. Springer, Berlin, 2007.

[66] E. M. Sparrow and R. D. Cess. *Radiation heat transfer*. Hemisphere Pub. Corp., Washington, augmented edition, 1978.

[67] H. C. Hottel and A. F. Sarofim. *Radiative Transfer*. McGraw-Hill, New York, 1967.

[68] T. H. Kim, E. Kommer, S. Dessiatoun, and J. Kim. Measurement of two-phase flow and heat transfer parameters using infrared thermometry. *International Journal of Multiphase Flow*, 40:56–67, 2012.

[69] D. B. R. Kenning and Y. Yan. Pool boiling heat transfer on a thin plate: features revealed by liquid crystal thermography. *International Journal of Heat and Mass Transfer*, 39(15):3117–3137, 1996.

[70] D. B. R. Kenning, T. Kono, and M. Wienecke. Investigation of boiling heat transfer by liquid crystal thermography. *Experimental Thermal and Fluid Science*, 25(5):219–229, 2001.

[71] D. B. R. Kenning and O.-E. Bustnes. Liquid crystal studies of sliding vapour bubbles. *Heat and Mass Transfer*, 45(7):867–880, 2009.

[72] I. Golobic, J. Petkovsek, M. Baselj, A. Papez, and D. B. R. Kenning. Experimental determination of transient wall temperature distributions close to growing vapor bubbles. *Heat and Mass Transfer*, 45(7):857–866, 2009.

[73] I. Golobic, J. Petkovsek, and D. B. R. Kenning. Bubble growth and horizontal coalescence in saturated pool boiling on a titanium foil, investigated by high-speed IR thermography. *International Journal of Heat and Mass Transfer*, 55(4):1385–1402, 2012.

[74] E. Wagner, A. Sprenger, P. Stephan, O. Koeppen, F. Ziegler, and H. Auracher. Nucleate boiling at singel artificial cavities: Bubble dynamics and local temperature measurements. In *Proceedings in the 6th International Conference on Multiphase flow, ICMF*, 2007.

[75] E. Wagner and P. Stephan. Experimental study of local temperature distribution and heat transfer mechanisms during nucleate boiling of binary mixtures. In *Proceedings of th 5th European Termal-Sciences Conference EUROTHERM*, 2008.

[76] E. Wagner. *Hochauflösende Messungen beim Blasensieden von Reinstoffen und binären Gemischen*. PhD thesis, Technische Universität Darmstadt, Darmstadt, 2009.

[77] E. Oldenhof, F. Weckenmann, G. Lamanna, B. Weigand, B. Bork, and A. Dreizler. Experimental investigation of isolated acetone droplets at ambient and near-critical conditions, injected in a nitrogen atmosphere. *Progress in Propulsion Physics*, Vol. 4:257–270, 2013.

[78] W. Kast and H. Klan (Revised by A. Thess). F2 Heat Transfer by Free Convection: External Flows. In *VDI Heat Atlas*, pages 667–672. Springer, Berlin and Heidelberg, 2010.

[79] J. R. Taylor. *Fehleranalyse: Eine Einführung in die Untersuchung von Unsicherheiten in physikalischen Messungen*. VCH, Weinheim and Basel (Schweiz) and Cambridge and New York and NY, 1st edition, 1988.

[80] M. Misale, G. Guglielmini, and A. Priarone. HFE-7100 pool boiling heat transfer and critical heat flux in inclined narrow spaces. *International Journal of Refrigeration*, 32(2):235–245, 2009.

[81] M. Misale, G. Guglielmini, and A. Priarone. Erratum to 'HFE-7100 pool boiling heat transfer and critical heat flux in inclined narrow spaces' [Int. Journal of Refrigeration 32/2 (2009) 235–245]. *International Journal of Refrigeration*, 33(3):650–651, 2010.

[82] N. R. Snyder and D. K. Edwards. Summary of conference on bubble dynamics and boiling heat transfer: Memo 20-137, 1956.

[83] J. Kim. Review of nucleate pool boiling bubble heat transfer mechanisms. *International Journal of Multiphase Flow*, 35(12):1067–1076, 2009.

[84] H. S. Fath and R. L. Judd. Influence of System Pressure on Microlayer Evaporation Heat Transfer. *Journal of Heat Transfer*, 100(1):49, 1978.

[85] S. G. Bankoff. Stability of Liquid Flow Down a Heated Inclined Plate. *International Journal of Heat and Mass Transfer*, Vol. 14:377–385, 1971.

[86] S. G. Bankoff. 1987 Max Jakob Memorial Award Lecture: Dynamics and Stability of Thin Heated Liquid Films. *Journal of Heat Transfer*, 112(3):538, 1990.

[87] V. G. Levich. *Physiochemical hydrodynamics*. Prentice-hall international series in the physical and chemical engineering science. Prentice-Hall, Englewood Cliffs and N.J, 1962.

[88] A. Sielaff. *Experimental Investigation of Single Bubbles and Bubble Interactions in Nucleate Boiling*. PhD thesis, Institut für Technische Thermodynamik, Technische Universität Darmstadt, Darmstadt, 2014.

[89] B. E. Poling, J. P. O'Connell, and J. M. Prausnitz. *The properties of gases and liquids*. McGraw-Hill, New York and NY [u.a.], 5th edition, 2001.

[90] University of Minnesota. http://www.me.umn.edu/courses/me/me5348/fc72.html.

[91] H. G. Rackett. Equation of state for saturated liquids. *Journal of Chemical & Engineering Data*, 15(4):514–517, 1970.

[92] B. I. Lee and M. G. Kesler. A generalized thermodynamic correlation based on three-parameter corresponding states. *AIChE Journal*, 21(3):510–527, 1975.

[93] S. Fischer, S. Herbert, E. M. Slomski, P. Stephan, and M. Oechsner. Local Heat Flux Investigation During Pool Boiling Single Bubble Cycles Under Reduced Gravity. *Heat Transfer Engineering*, 35(5):482–491, 2014, also published in *Proceedings of the 8th International Conference on Boiling and Condensation Heat Transfer*, 2012.

[94] S. Fischer, S. Herbert, T. Gambaryan-Roisman, and P. Stephan. Local heat flux investigation during single drop impingement onto a heated wall. In *Proceedings of the 25th European Conference on Liquid Atomization and Spray Systems (ILASS-Europe 2013)*, 2013.

List of Figures

List of Tables

Annex

A FC-72 physical properties determination equations

This chapter provides the equations that were used in this work to determine the physical parameters of the experiment fluid FC-72, as no measured fluid data is available up to the critical point. The correlations used were taken from “The Properties of Gases and Liquids” by Polling, O’Connel and Prausnitz [89], except stated otherwise. The methods applied are corresponding states methods, which correlate the relation between value and critical state. Quality of the correlations was tested against data measured by the University of Minnesota [90].

A.1 Input parameters

To be able to correlate the necessary quantities, some input parameters are required, as given in the following table. The subscript NBP refers to the normal boiling point (value at $p = 1013.25\,\text{mbar}$, $T = 329.75\,\text{K}$). Since several input parameters are not available for FC-72, instead values for n-perfluorohexane, which is the main component of FC-72, are taken from [89], Annex A11. All required input parameters are listed in tables A.1 and A.2.

Table A.1.: input parameters for FC-72 data correlation

quantity	value	source
critical temperature	$T_{\text{crit}} = 449\,\text{K}$	3M FC-72 data sheet
critical pressure	$p_{\text{crit}} = 18.3\,\text{bar}$	3M FC-72 data sheet
molar mass	$\overline{M} = 338\,\text{kg}\,\text{kmol}^{-1}$	3M FC-72 data sheet
saturation temperature at NBP	$T_{\text{NBP}} = 329.75\,\text{K}$	3M FC-72 data sheet
universal gas constant	$\overline{R} = 8314.46\,\text{J}\,\text{kmol}^{-1}\,\text{K}^{-1}$	[89]
critical molar volume	$\overline{V}_{\text{crit}} = 0.5732\,\text{m}^3\,\text{kmol}^{-1}$	[89], appendix A.11
critical compressibility factor	$Z_{\text{crit}} = 0.274$	[89], appendix A.11
accentric factor	$\omega = 0.513$	[89], appendix A.11

Table A.2.: input parameters for FC-72 data correlation (continued)

quantity	value	source
latent heat of evaporation at NBP	$\Delta h_{v,\mathrm{NBP}} = 84.515\,\mathrm{kJ\,kg^{-1}}$	Value measured by University of Minnesota [90]
latent heat of evaporation at 20 °C	$\Delta h_{v,20^\circ\mathrm{C}} = 94.363\,\mathrm{kJ\,kg^{-1}}$	Value measured by University of Minnesota [90]
saturated liquid density at NBP	$\rho_{\mathrm{l,NBP}} = 1619.822\,\mathrm{kg\,m^{-3}}$	Value measured by University of Minnesota [90]
liquid thermal conductivity at NBP	$\lambda_{\mathrm{l,NBP}} = 5.216 \cdot 10^{-2}\,\mathrm{W\,m^{-1}\,K^{-1}}$	Value measured by University of Minnesota [90]
liquid thermal conductivity at 20 °C	$\lambda_{\mathrm{l,20^\circ C}} = 5.643 \cdot 10^{-2}\,\mathrm{W\,m^{-1}\,K^{-1}}$	Value measured by University of Minnesota [90]
vapor thermal conductivity at NBP	$\lambda_{\mathrm{v,NBP}} = 8.641 \cdot 10^{-3}\,\mathrm{W\,m^{-1}\,K^{-1}}$	Value measured by University of Minnesota [90]
liquid dynamic viscosity at NBP	$\mu_{\mathrm{l,NBP}} = 4.530 \cdot 10^{-4}\,\mathrm{Pa\,s^{-1}}$	Value measured by University of Minnesota [90]
liquid dynamic viscosity at 20 °C	$\mu_{\mathrm{l,20^\circ C}} = 6.895 \cdot 10^{-4}\,\mathrm{Pa\,s^{-1}}$	Value measured by University of Minnesota [90]

A.2 Saturation pressure

The saturation pressure can be estimated using the Kirchhoff vapour pressure equation ([89], pp. 7.3)

$$p_{\mathrm{sat}} = e^{h\left(1-1/T_{\mathrm{R}}\right)} p_{\mathrm{crit}}. \tag{A.1}$$

The constant h herein is calculated using the normal boiling point

$$h = T_{\mathrm{R,NBP}} \frac{\ln\left(p_{\mathrm{crit}}/1.013\,25\,\mathrm{bar}\right)}{1 - T_{\mathrm{R,NBP}}}. \tag{A.2}$$

In figure A.1 the calculated saturation pressure is plotted versus temperature along with measured data. Comparison of the correlation to measured data yields errors smaller than 0.03 bar.

A.3 Saturation temperature

The saturation temperature as a function of pressure can be estimated using the inverse Kirchhoff vapour pressure equation ([89], pp. 7.3), using the constant h determined by equation (A.2)

$$T_{\mathrm{sat}} = \frac{h T_{\mathrm{crit}}}{h - \ln\left(p_{\mathrm{R}}\right)}. \tag{A.3}$$

In figure A.2 the calculated saturation is plotted versus pressure along with measured data. Comparison of the correlation to measured data yields errors smaller than 3 K.

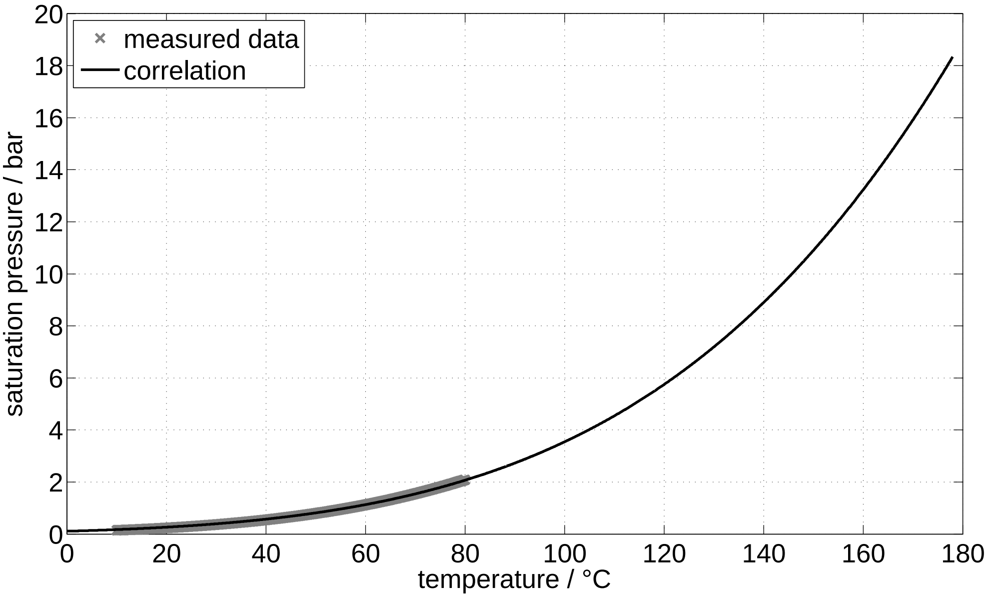

Figure A.1.: Correlation of saturation pressure p_{sat} versus temperature

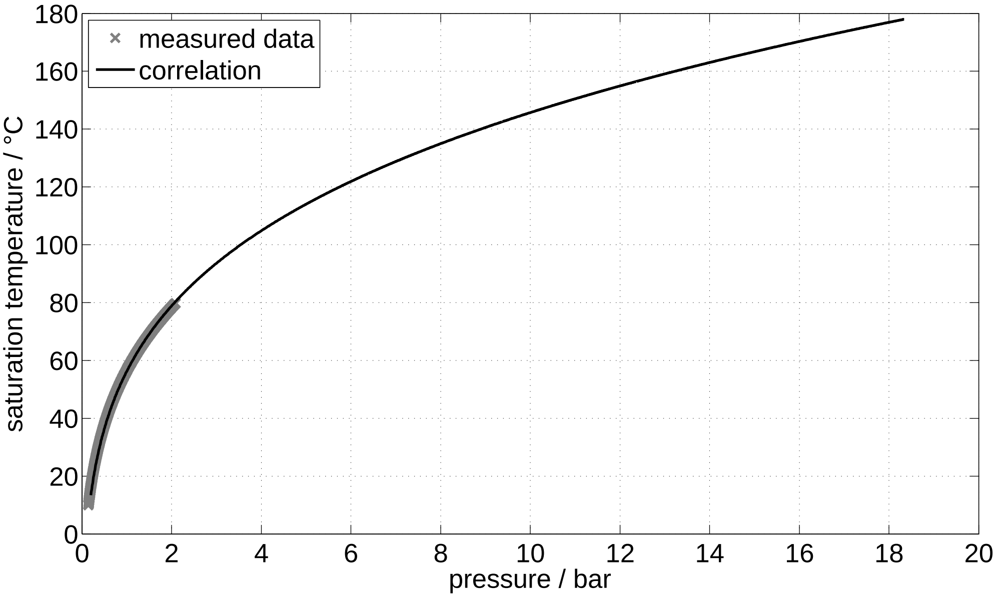

Figure A.2.: Correlation of saturation temperature t_{sat} versus pressure

A.4 Latent heat of evaporation

The latent heat of evaporation is calculated using the Watson relation, introduced by Thek and Stiel ([89], pp. 7.24)

$$\Delta h_{\mathrm{v}} = \Delta h_{v,\mathrm{NBP}} \left(\frac{1 - T_{\mathrm{R}}}{1 - T_{\mathrm{R,NBP}}} \right)^{n} . \tag{A.4}$$

To determine the exponent n the latent heat of evaporation at two distinct points is required, which is taken from the measured data at 20 °C and the normal boiling point

$$n = \frac{\ln\left(\Delta h_{v,20^{\circ}\mathrm{C}}\right) - \ln\left(\Delta h_{v,\mathrm{NBP}}\right)}{\ln\left(1 - T_{\mathrm{R},20^{\circ}\mathrm{C}}\right) - \ln\left(1 - T_{\mathrm{R,NBP}}\right)} . \tag{A.5}$$

In figure A.3 the calculated latent heat of is plotted versus temperature along with measured data. Comparison of the correlation to measured data yields errors smaller than 0.02 kJ kg^{-1}.

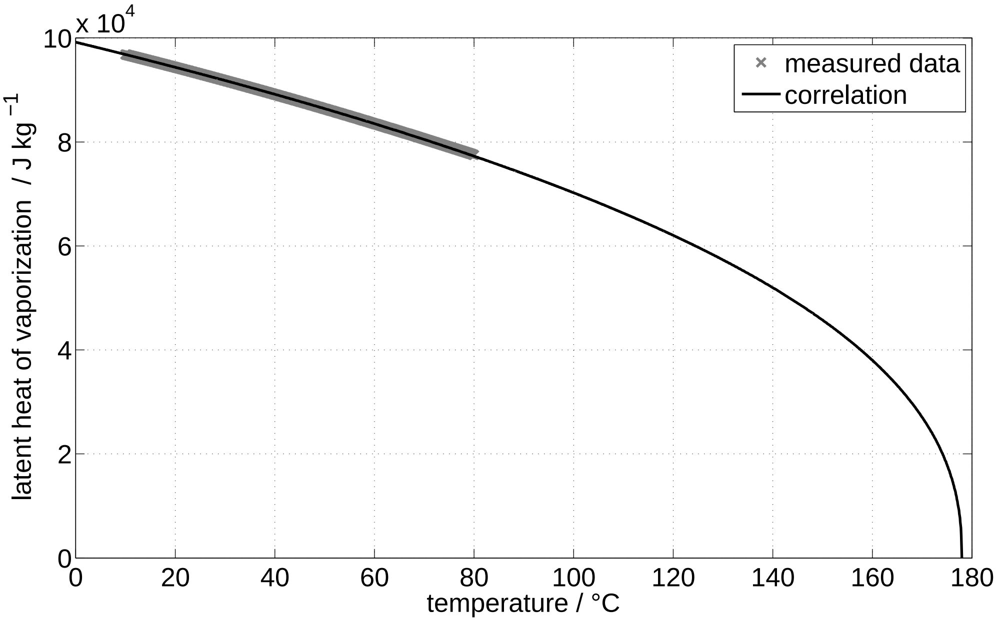

Figure A.3.: Correlation of latent heat of evaporation Δh_{v} versus temperature

A.5 Surface tension

The surface tension is calculated using a correlation suggested by Miller ([89], pp. 12.8)

$$\sigma = {p_{\mathrm{crit}}}^{2/3} {T_{\mathrm{crit}}}^{1/3} Q \left(1 - T_{\mathrm{R}}\right)^{11/9} \cdot 10^{-3} \, \frac{\mathrm{N}}{\mathrm{m\,K\,bar}}, \tag{A.6}$$

with the constant Q being given by

$$Q = 0.1196 \left[1 + \frac{T_{\mathrm{R,NBP}} \ln\left(p_{\mathrm{crit}}/1.013\,25\,\mathrm{bar}\right)}{1 - T_{\mathrm{R,NBP}}} \right] - 0.279. \tag{A.7}$$

In figure A.4 the calculated surface tension is plotted versus temperature along with measured data. Comparison of the correlation to measured data yields errors smaller than $0.15 \cdot 10^{-3}\,\mathrm{N\,m^{-1}}$.

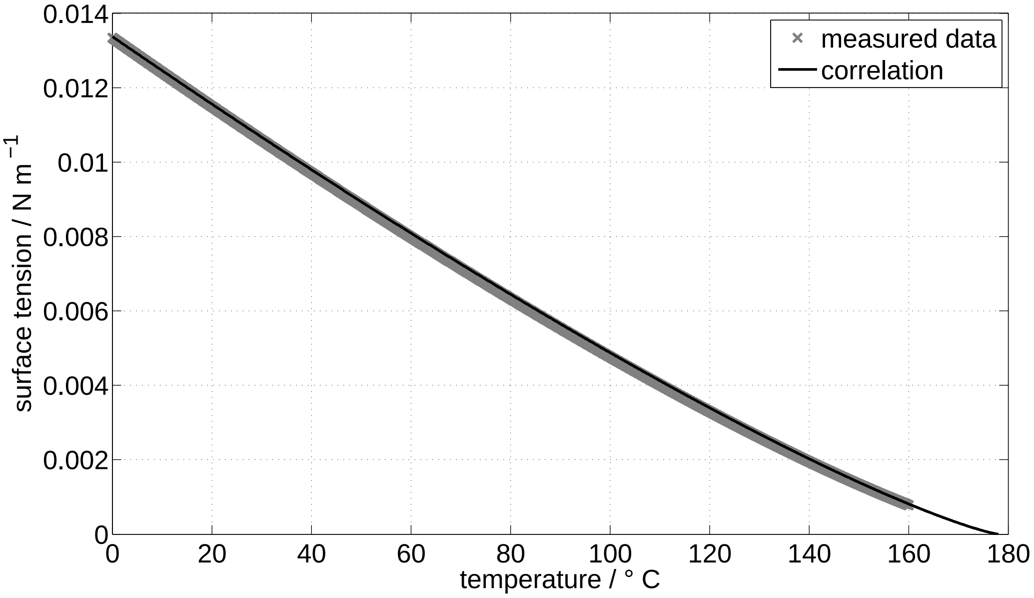

Figure A.4.: Correlation of surface tension σ versus temperature

A.6 Saturated liquid density

The saturated liquid density is calculated from a slightly modified equation proposed by Rackett ([89], pp. 4.35-4.36)

$$\rho_\mathrm{l} = \frac{\rho_\mathrm{l,NBP}}{(0.290\,56 - 0.087\,75\omega)^{\Psi}}, \tag{A.8}$$

with Ψ being determined by

$$\Psi = \left(1 - T_\mathrm{R}\right)^n - \left(1 - T_\mathrm{R,NBP}\right)^n. \tag{A.9}$$

In [89] the exponent n in equation (A.9) is set to $n = 2/7$. This however does not yield acceptable results in the given case. In the original work by Rackett it is stated that “There is no known theoretical basis for Equation 1 or for the specific value selected for this exponent” [91]. For the given case, choosing an exponent of $n = 1/7$ yields an excellent match to the measured data and matches the saturated vapor density at the critical point, which is calculated with a completely different method, extremely well (see section A.7). In figure A.5 the calculated saturated liquid density is plotted versus temperature along with measured data. Comparison of the correlation to measured data yields errors smaller than $10\,\mathrm{kg\,m^{-3}}$.

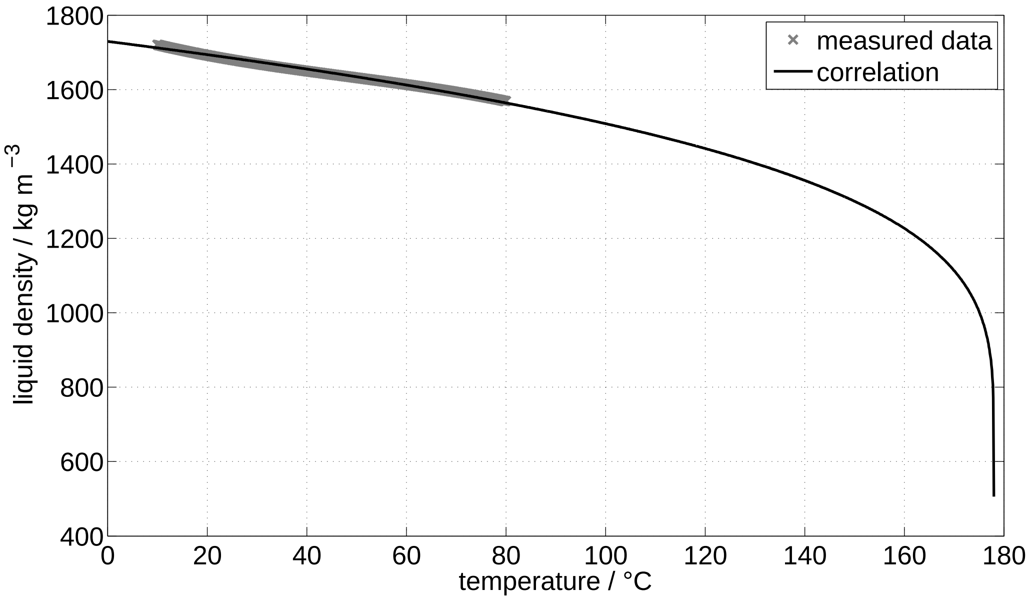

Figure A.5.: Correlation of liquid density ρ_l versus temperature

A.7 Saturated vapour density

The saturated vapour density as a function of temperature is calculated from the Peng-Robinson Equation of State ([89], pp.4.18-4.23)

$$\rho_\text{v} = \frac{\overline{M} p_\text{sat}(T)}{Z\overline{R}T}. \tag{A.10}$$

In this equation Z is the compressibility factor, which accounts for real gas behavior and can be found by solving the cubic equation

$$\begin{aligned} Z^3 + \left(b\frac{p_\text{sat}}{\overline{R}T} - 1\right) Z^2 + \left[ac\frac{p_\text{sat}}{\left(\overline{R}T\right)^2} - 3b^2\left(\frac{p_\text{sat}}{\overline{R}T}\right)^2 - 2b\frac{p_\text{sat}}{\overline{R}T}\right] Z \ldots \\ \ldots - \left[abc\frac{{p_\text{sat}}^2}{\left(\overline{R}T\right)^3} - b^3\left(\frac{p_\text{sat}}{\overline{R}T}\right)^3 - b^2\left(\frac{p_\text{sat}}{\overline{R}T}\right)^2\right] = 0. \end{aligned} \tag{A.11}$$

In equation (A.11) the saturation pressure p_sat can be calculated by solving equation (A.1), while the parameters a,b and c are functions of the accentric factor ω, the reduced temperature T_R and the fluid properties at the critical point

$$a = 0.457\,24\frac{\left(\overline{R}T_\text{crit}\right)^2}{p_\text{crit}}, \tag{A.12a}$$

$$b = 0.0778\frac{\overline{R}T_\text{crit}}{p_\text{crit}}, \tag{A.12b}$$

$$c = \left[1 + \left(0.374\,64 + 1.542\,26\omega - 0.2699\omega^2\right)\left(1 - {T_\text{R}}^{1/2}\right)\right]^2. \tag{A.12c}$$

In figure A.6 the calculated saturated vapour density is plotted versus temperature along with measured data. Comparison of the correlation to measured data yields errors smaller than 1 kg m^{-3}.

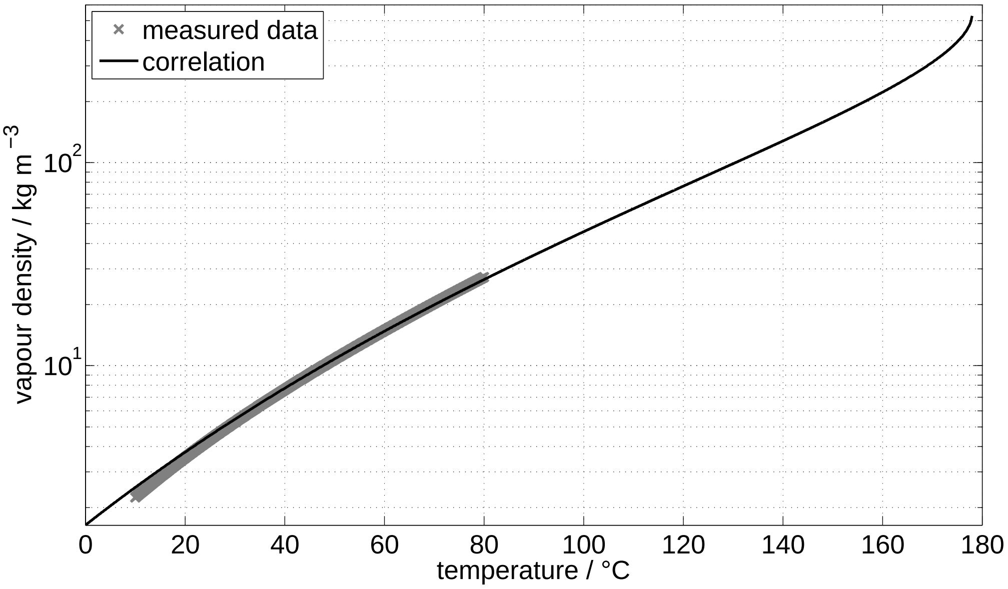

Figure A.6.: Correlation of vapour density ρ_v versus temperature

A.8 Liquid thermal conductivity

The liquid thermal conductivity as a function of temperature is calculated using a method proposed by Jamieson ([89], pp. 10.51-10.52)

$$\lambda_\mathrm{l} = A\left[1 + (1 - T_\mathrm{R})^{2/3} + B\left((1 - T_\mathrm{R})^{1/3} - 3\,(1 - T_\mathrm{R})^{2/3} + 3\,(1 - T_\mathrm{R})\right)\right]. \tag{A.13}$$

To determine the constants A and B two reference measurement values of λ_l are used, which are taken from the measured data at the normal boiling point and at 20 °C

$$A = \frac{\lambda_\mathrm{l,NBP}}{a_\mathrm{NBP} + b_\mathrm{NBP} B}, \tag{A.14}$$

$$B = \frac{a_\mathrm{NBP}\lambda_\mathrm{l,20^\circ C} - a_\mathrm{20^\circ C}\lambda_\mathrm{l,NBP}}{b_\mathrm{20^\circ C}\lambda_\mathrm{l,NBP} - b_\mathrm{NBP}\lambda_\mathrm{l,20^\circ C}}, \tag{A.15}$$

with

$$a_\mathrm{NBP} = 1 + \left(1 - T_\mathrm{R,NBP}\right)^{2/3}, \tag{A.16a}$$

$$a_\mathrm{20^\circ C} = 1 + \left(1 - T_\mathrm{R,20^\circ C}\right)^{2/3}, \tag{A.16b}$$

$$b_\mathrm{NBP} = \left(1 - T_\mathrm{R,NBP}\right)^{1/3} - 3\left(1 - T_\mathrm{R,NBP}\right)^{2/3} + 3\left(1 - T_\mathrm{R,NBP}\right), \tag{A.16c}$$

$$b_\mathrm{20^\circ C} = \left(1 - T_\mathrm{R,20^\circ C}\right)^{1/3} - 3\left(1 - T_\mathrm{R,20^\circ C}\right)^{2/3} + 3\left(1 - T_\mathrm{R,20^\circ C}\right). \tag{A.16d}$$

In figure A.7 the calculated liquid thermal conductivity is plotted versus temperature along with measured data. Comparison of the correlation to measured data yields errors smaller than $2 \cdot 10^{-4}\,\mathrm{W\,m^{-1}\,K^{-1}}$.

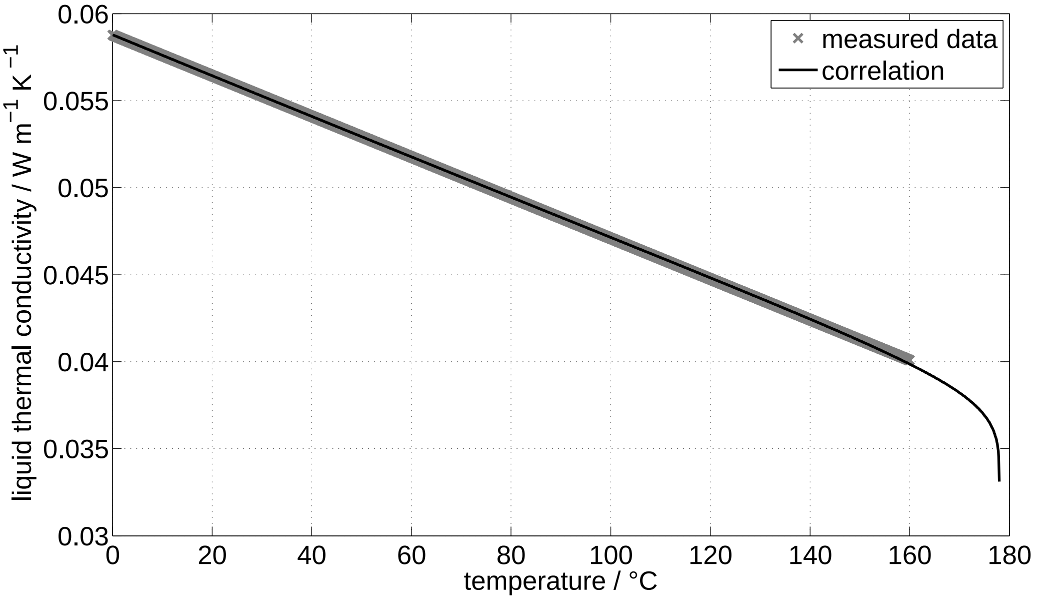

Figure A.7.: Correlation of liquid thermal conductivity λ_l versus temperature

A.9 Vapour thermal conductivity

The vapour thermal conductivity in the low pressure regime as a function of temperature is calculated using the Roy-Thodos method ([89], pp. 10.6-10.10)

$$\lambda_{\mathrm{v},0} = \frac{(\lambda\Gamma)_\mathrm{tr} + (\lambda\Gamma)_\mathrm{int}}{\Gamma}, \tag{A.17}$$

with Γ being the reduced inverse thermal conductivity

$$\Gamma = 210 \left(\frac{T_\mathrm{crit} \overline{M}^3}{{p_\mathrm{crit}}^4} \right)^{1/6}. \tag{A.18}$$

In equation (A.17) the first term $(\lambda\Gamma)_\mathrm{tr}$ is material independent and has been correlated as

$$(\lambda\Gamma)_\mathrm{tr} = 8.757 \left(e^{0.0464 T_\mathrm{R}} - e^{-0.2412 T_\mathrm{R}} \right). \tag{A.19}$$

The second term $(\lambda\Gamma)_\mathrm{int}$ however, contains a material dependent constant C

$$(\lambda\Gamma)_\mathrm{int} = C f\left(T_\mathrm{R}\right), \tag{A.20}$$

with

$$f\left(T_{\mathrm{R}}\right)=-0.152T_{\mathrm{R}}+1.191{T_{\mathrm{R}}}^{2}-0.039{T_{\mathrm{R}}}^{3}. \tag{A.21}$$

Originally Roy and Thodos had proposed a group contribution method to determine the constant C, but in the given case the results of this method are not satisfactory. Therefore, a one-point fit at the normal boiling point is employed to determine C

$$C=\frac{\lambda_{\mathrm{v,NBP}}\Gamma-(\lambda\Gamma)_{\mathrm{tr}}\left(T_{\mathrm{R,NBP}}\right)}{f\left(T_{\mathrm{R,NBP}}\right)}. \tag{A.22}$$

Equation (A.17) does not take the dependency of the thermal conductivity on the gas density into account. Stiel and Thodos introduced a density correction term relevant for high pressures ([89], pp. 10.22)

$$\lambda_{\mathrm{v}}=\frac{1.22\cdot10^{-2}}{\Gamma{Z_{\mathrm{crit}}}^{5}}\left(e^{0.535\rho_{\mathrm{v}}\overline{V}_{\mathrm{crit}}/\overline{M}}-1\right)+\lambda_{\mathrm{v},0}\qquad\text{for}\quad\frac{\rho_{\mathrm{v}}\overline{V}_{\mathrm{crit}}}{\overline{M}}<0.5, \tag{A.23a}$$

$$\lambda_{\mathrm{v}}=\frac{1.14\cdot10^{-2}}{\Gamma{Z_{\mathrm{crit}}}^{5}}\left(e^{0.67\rho_{\mathrm{v}}\overline{V}_{\mathrm{crit}}/\overline{M}}-1.069\right)+\lambda_{\mathrm{v},0}\qquad\text{for}\quad0.5<\frac{\rho_{\mathrm{v}}\overline{V}_{\mathrm{crit}}}{\overline{M}}<2. \tag{A.23b}$$

In equation (A.23) ρ_{v} can be calculated by applying equations (A.10) - (A.12). In figure A.8 the calculated vapour thermal conductivity is plotted versus temperature along with measured data. Comparison of the correlation to measured data yields errors smaller than $1\cdot10^{-4}\,\mathrm{W\,m^{-1}\,K^{-1}}$.

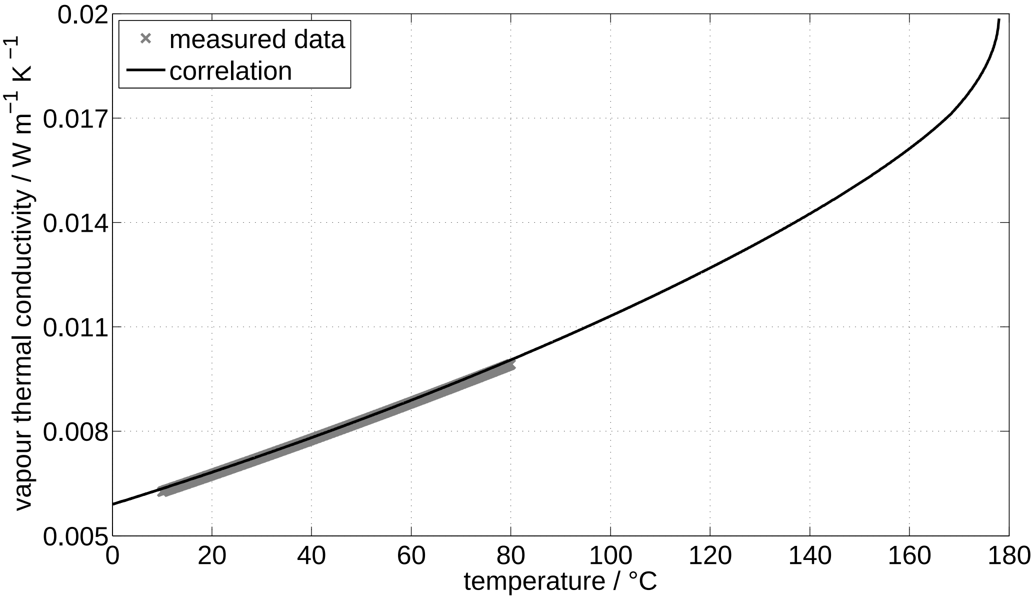

Figure A.8.: Correlation of vapor thermal conductivity λ_{v} versus temperature

A.10 Liquid thermal capacity

The liquid thermal capacity as a function of temperature is calculated using a corresponding states method ([89], pp. 6.22)

$$c_{p,\mathrm{l}} = \left[\left(\frac{\overline{c}_p}{\overline{R}} \right)_0 + \left(\frac{\overline{c}_{p,\mathrm{l}}}{\overline{R}} \right)_\mathrm{R} \right] \frac{\overline{R}}{\overline{M}}. \tag{A.24}$$

In equation (A.24) the first term can be calculated from the equation given in [89], appendix A 40 for n-perfluorohexane

$$\left(\frac{\overline{c}_p}{\overline{R}} \right)_0 = 2.66 + 146.733 \cdot 10^{-3} T - 18.179 \cdot 10^{-5} T^2 + 11.086 \cdot 10^{-8} T^3 - 2.71 \cdot 10^{-11} T^4. \tag{A.25}$$

The second term is depending on the reduced temperature of the liquid and can be calculated as

$$\left(\frac{\overline{c}_{p,\mathrm{l}}}{\overline{R}} \right)_\mathrm{R} = 1.586 + \frac{0.49}{1 - T_\mathrm{R}} + \omega \left[4.2775 + \frac{6.3\,(1 - T_\mathrm{R})^{1/3}}{T_\mathrm{R}} + \frac{0.4355}{(1 - T_\mathrm{R})} \right]. \tag{A.26}$$

In figure A.9 the calculated liquid thermal capacity is plotted versus temperature along with measured data. Comparison of the correlation to measured data yields errors smaller than 10 J kg^{-1} K^{-1}.

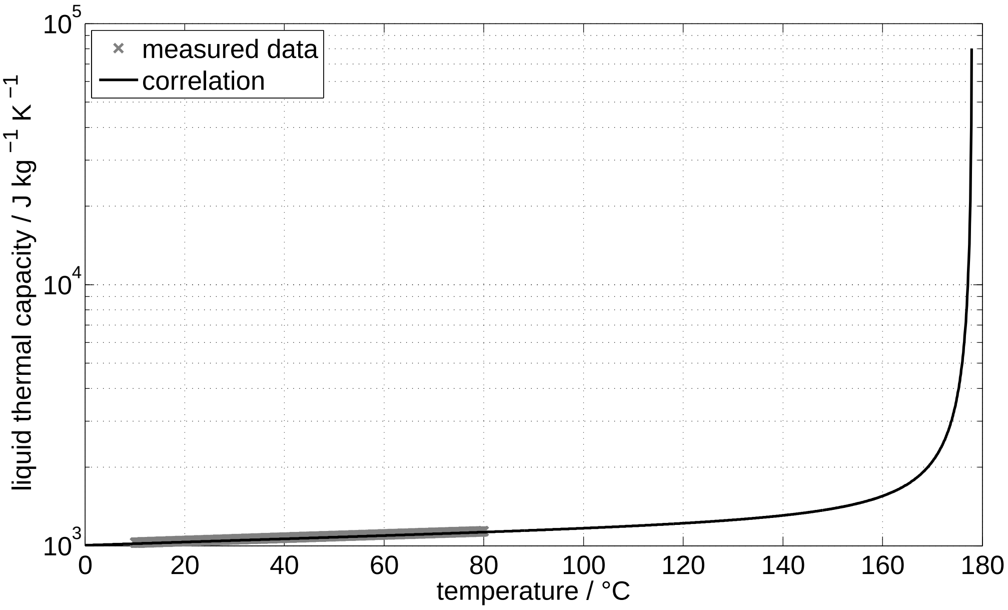

Figure A.9.: Correlation of liquid thermal capacity $c_{p,\mathrm{l}}$ versus temperature

A.11 Vapour thermal capacity

The vapour thermal capacity is calculated with the same method as the liquid thermal capacity, as described in section A.10 ([89], pp. 6.22)

$$c_{p,\mathrm{v}} = \left[\left(\frac{\overline{c}_p}{\overline{R}} \right)_0 + \left(\frac{\overline{c}_{p,\mathrm{v}}}{\overline{R}} \right)_\mathrm{R} \right] \frac{\overline{R}}{\overline{M}}. \tag{A.27}$$

The first term of equation (A.27) is equivalent to the first term of equation (A.24) and can be calculated accordingly using equation (A.25). The second term however is calculated from a method developed by Lee and Kessler [92], which combines the contributions of a “reference fluid” (ref) and a “simple fluid” (sim)

$$\left(\frac{\overline{c}_{p,\mathrm{v}}}{\overline{R}} \right)_\mathrm{R} = \left(\frac{\overline{c}_{p,\mathrm{v}}}{\overline{R}} \right)_\mathrm{R,sim} + \frac{\omega}{\omega_\mathrm{ref}} \left[\left(\frac{\overline{c}_{p,\mathrm{v}}}{\overline{R}} \right)_\mathrm{R,ref} - \left(\frac{\overline{c}_{p,\mathrm{v}}}{\overline{R}} \right)_\mathrm{R,sim} \right]. \tag{A.28}$$

In this equation $\omega_\mathrm{ref} = 0.3978$ is the accentric factor of the reference fluid.
The dimensionless expressions for the isobaric thermal capacity herein can be calculated through the deviation from the isochoric thermal capacity through partial derivatives

$$\left(\frac{\overline{c}_{p,\mathrm{v}}}{\overline{R}} \right)_\mathrm{R,sim} = \left(\frac{\overline{c}_{v,\mathrm{v}}}{\overline{R}} \right)_\mathrm{R,sim} - T_\mathrm{R} \left(\frac{\partial p_\mathrm{R}}{\partial T_\mathrm{R}} \right)^2_{\overline{V}_\mathrm{R},\mathrm{sim}} / \left(\frac{\partial p_\mathrm{R}}{\partial \overline{V}_\mathrm{R}} \right)_{T_\mathrm{R},\mathrm{sim}}, \tag{A.29a}$$

$$\left(\frac{\overline{c}_{p,\mathrm{v}}}{\overline{R}} \right)_\mathrm{R,ref} = \left(\frac{\overline{c}_{v,\mathrm{v}}}{\overline{R}} \right)_\mathrm{R,ref} - T_\mathrm{R} \left(\frac{\partial p_\mathrm{R}}{\partial T_\mathrm{R}} \right)^2_{\overline{V}_\mathrm{R},\mathrm{ref}} / \left(\frac{\partial p_\mathrm{R}}{\partial \overline{V}_\mathrm{R}} \right)_{T_\mathrm{R},\mathrm{ref}}. \tag{A.29b}$$

The partial derivatives for simple and reference fluid can be correlated using the following equations:

$$\begin{aligned} \left(\frac{\partial p_\mathrm{R}}{\partial T_\mathrm{R}} \right)_{\overline{V}_\mathrm{R}} &= \frac{1}{\overline{V}_\mathrm{R}} \left[1 + \frac{b_1 + b_3/{T_\mathrm{R}}^2 + 2b_4/{T_\mathrm{R}}^3}{\overline{V}_\mathrm{R}} - \frac{c_1 - 2c_3/{T_\mathrm{R}}^3}{2{\overline{V}_\mathrm{R}}^2} \dots \right. \\ &\quad \left. \dots + \frac{d_1}{5{\overline{V}_\mathrm{R}}^5} - \frac{2c_4}{{T_\mathrm{R}}^3{\overline{V}_\mathrm{R}}^2} \left(\beta + \frac{\gamma}{{\overline{V}_\mathrm{R}}^2} \right) e^{-\gamma/{\overline{V}_\mathrm{R}}^2} \right], \end{aligned} \tag{A.30a}$$

$$\begin{aligned} \left(\frac{\partial p_\mathrm{R}}{\partial \overline{V}_\mathrm{R}} \right)_{T_\mathrm{R}} &= \frac{T_\mathrm{R}}{{\overline{V}_\mathrm{R}}^2} \left[1 + 2\frac{b_1 - b_2/T_\mathrm{R} - b_3/{T_\mathrm{R}}^2 - b_4/{T_\mathrm{R}}^3}{\overline{V}_\mathrm{R}} + 3\frac{c_1 - c_2/T_\mathrm{R} - c_3/{T_\mathrm{R}}^3}{2{\overline{V}_\mathrm{R}}^2} \dots \right. \\ &\quad \left. \dots + 6\frac{d_1 + d_2/T_\mathrm{R}}{{\overline{V}_\mathrm{R}}^5} + \frac{c_4}{{T_\mathrm{R}}^3{\overline{V}_\mathrm{R}}^2} \left(3\beta + \frac{5\gamma}{{\overline{V}_\mathrm{R}}^2} - \frac{2\beta\gamma}{{\overline{V}_\mathrm{R}}^2} - \frac{2\gamma^2}{{\overline{V}_\mathrm{R}}^4} \right) e^{-\gamma/{\overline{V}_\mathrm{R}}^2} \right]. \end{aligned} \tag{A.30b}$$

The reduced molar volume $\overline{V}_\mathrm{R}$ can be calculated by applying equations (A.10) - (A.12) for the vapour density

$$\overline{V}_\mathrm{R} = \frac{\overline{M}}{\rho_\mathrm{v} \overline{V}_\mathrm{crit}}. \tag{A.31}$$

The final parameters required by equation (A.29) are the dimensionless expressions for the isochoric thermal capacity, which is calculated for simple and reference fluid with

$$\left(\frac{\bar{c}_{v,\mathrm{v}}}{\bar{R}}\right)_{\mathrm{R}} = \frac{2b_3+6b_4/T_\mathrm{R}}{{T_\mathrm{R}}^2\bar{V}_\mathrm{R}} - \frac{3c_3}{{T_\mathrm{R}}^3{\bar{V}_\mathrm{R}}^2} - \frac{3c_4}{{T_\mathrm{R}}^3\gamma}\left[\beta+1-\left(\beta+1+\frac{\gamma}{{\bar{V}_\mathrm{R}}^2}\right)e^{-\gamma/{\bar{V}_\mathrm{R}}^2}\right]. \qquad \text{(A.32)}$$

The constants used in equations (A.30) and (A.32) are different for simple and reference fluid and are listed in table A.3 [92].

In figure A.10 the calculated vapour thermal capacity at constant pressure is plotted versus temperature along with measured data. Comparison of the correlation to measured data yields errors smaller than $10\,\mathrm{J\,kg^{-1}\,K^{-1}}$.

Table A.3.: constants for simple and reference fluid data correlations [92]

Constant	value for simple fluid	value for reference fluid
b_1	$118.1193 \cdot 10^{-3}$	$202.6579 \cdot 10^{-3}$
b_2	$265.728 \cdot 10^{-3}$	$331.511 \cdot 10^{-3}$
b_3	$154.790 \cdot 10^{-3}$	$27.655 \cdot 10^{-3}$
b_4	$30.323 \cdot 10^{-3}$	$203.488 \cdot 10^{-3}$
c_1	$23.6744 \cdot 10^{-3}$	$31.3385 \cdot 10^{-3}$
c_2	$18.6984 \cdot 10^{-3}$	$50.3618 \cdot 10^{-3}$
c_3	0	$16.901 \cdot 10^{-3}$
c_4	$42.724 \cdot 10^{-3}$	$41.577 \cdot 10^{-3}$
d_1	$155.488 \cdot 10^{-7}$	$487.36 \cdot 10^{-7}$
d_2	$623.689 \cdot 10^{-7}$	$74.0336 \cdot 10^{-7}$
β	$653.92 \cdot 10^{-3}$	1.226
γ	$60.167 \cdot 10^{-3}$	$37.54 \cdot 10^{-3}$

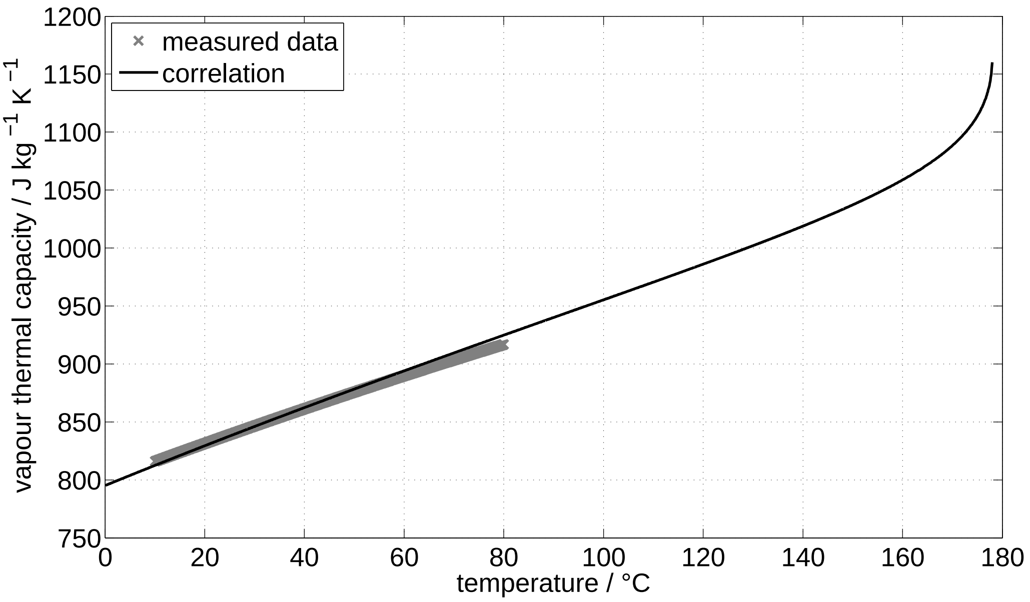

Figure A.10.: Correlation of vapour thermal capacity $c_{p,\mathrm{v}}$ versus temperature

A.12 Liquid kinematic viscosity

The liquid kinematic viscosity is calculated with the Andrade equation ([89], pp. 9.57)

$$\nu_{\mathrm{l}} = \frac{e^{(A/T+B)}}{\rho_{\mathrm{l}}} \cdot 10^{-3} \, \frac{\mathrm{Pa}}{\mathrm{s}}. \tag{A.33}$$

The saturated liquid density used in equation (A.33) can be calculated by applying equations (A.8)-(A.9). The two constants A and B can be determined by applying a two-point fit at the normal boiling point and at 20 °C for the dynamic viscosity of the liquid

$$A = \frac{\ln\left(\mu_{\mathrm{l,20°C}}/\mu_{\mathrm{l,NBP}}\right)}{1/T_{20°\mathrm{C}} - 1/T_{\mathrm{NBP}}}, \tag{A.34a}$$

$$B = \ln\left(\mu_{\mathrm{l,NBP}}\right) - \frac{A}{T_{\mathrm{NBP}}}. \tag{A.34b}$$

In figure A.11 the calculated liquid kinematic viscosity is plotted versus temperature along with measured data. Comparison of the correlation to measured data yields errors smaller than $1 \cdot 10^{-9}\,\mathrm{m}^2\,\mathrm{s}^{-1}$.

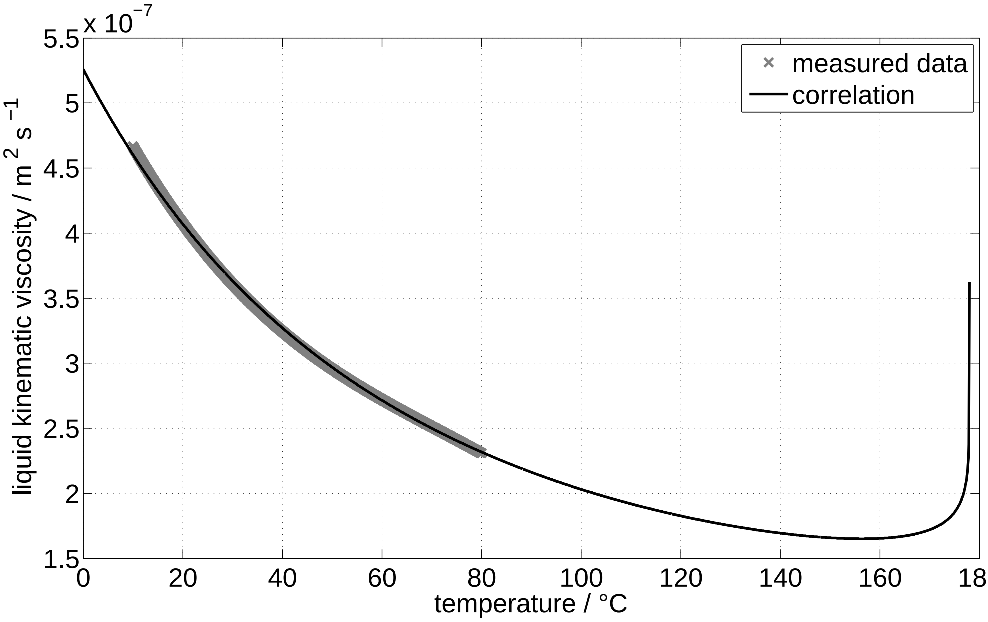

Figure A.11.: Correlation of liquid kinematic viscosity ν_{l} versus temperature

A.13 Vapour kinematic viscosity

The vapour kinematic viscosity is calculated with a method proposed by Chung ([89], pp. 9.5 - 9.8)

$$\nu_{\mathrm{v}} = \frac{40.785 \cdot 10^{-9} C \left(\overline{M} T\right)^{1/2}}{\rho_{\mathrm{v}} \overline{V}_{\mathrm{crit}}^{\;2/3} \Omega_{v}} \frac{\mathrm{m\,kg}^{1/2}}{\mathrm{s\,K}^{1/2}\,\mathrm{kmol}^{1/6}}. \tag{A.35}$$

The constant C is in this case only a function of the accentric factor, as the dipole moment of FC-72 (resp. n-perfluorohexane) is zero ([89], Annex A11) and the fluid is non-polar

$$C = 1 - 0.2756\omega. \tag{A.36}$$

The viscosity collision integral Ω_v is given by

$$\Omega_v = 1.161\,45 T^{*-0.148\,74} + 0.524\,87 e^{-0.7732 T^*} + 2.161\,78 e^{-2.437\,87 T^*}, \tag{A.37}$$

with

$$T^* = 1.2593 T_{\mathrm{R}}. \tag{A.38}$$

In figure A.12 the calculated vapour kinematic viscosity is plotted versus temperature along with measured data. Comparison of the correlation to measured data yields errors smaller than $4 \cdot 10^{-7}\,\mathrm{m^2\,s^{-1}}$.

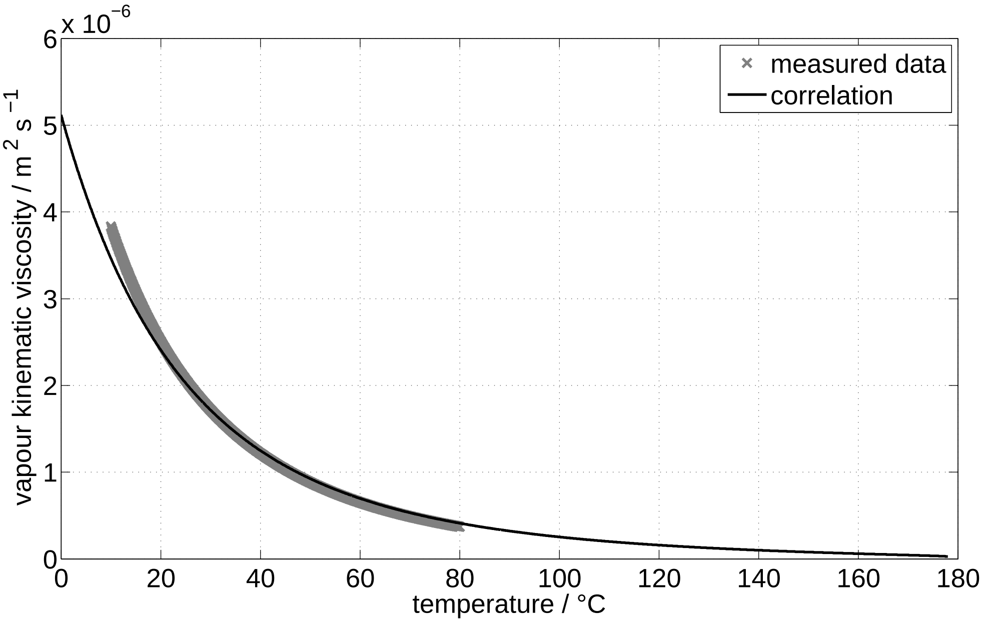

Figure A.12.: Correlation of vapor kinematic viscosity ν_{v} versus temperature

B Details of the experiment setup

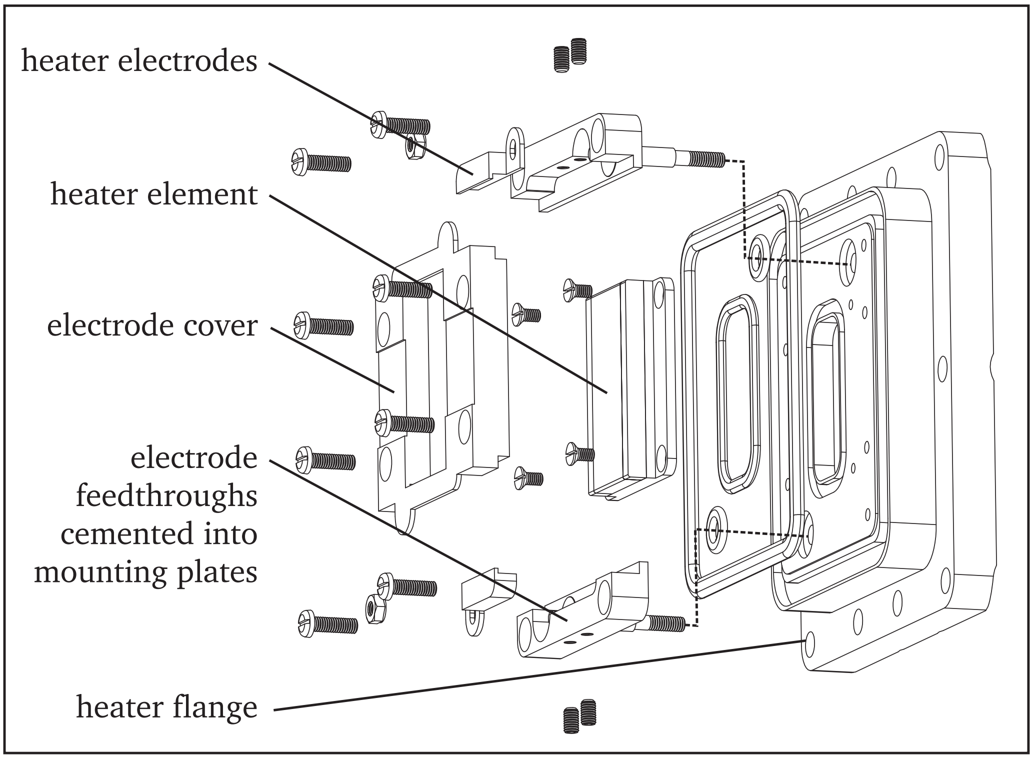

Figure B.1.: Exploded view of the heater flange assembly

In figure B.1 an exploded view of the heater flange assembly is displayed, which accommodates the heater fixation, the heater electrodes and the electrode feedthroughs, as well as a cover for the electrodes. The copper feedthroughs are cemented into PEEK frames to keep them insulated from the heater flange. The copper electrodes themselves provide a polished mating surface to connect the feedthroughs with the chromium heating layer of the experiment heater. The heater is very susceptible to mechanical loads, so the connection with the electrodes must be established with extreme care. To achieve this, the nuts fixing the electrodes on the feedthroughs are only slightly tightened to keep them in place and avoid scratching of the electrodes on the heating layer. Then the connection between electrodes and heating layer is established by carefully tightening the set screws in the feedthrough PEEK frames. Between the screws and the electrodes small elastomer dampers are placed to compensate the difference in thermal expansion between the parts. The electrode cover is needed to form the part of the capillary slot wall, which is not formed by the heater itself and to avoid disturbance of the flow. It provides small cutouts with a depth of 500 µm at the centre of the heater to allow for optical access to the heater surface.

A sectional view of the experiment test section is provided in figure B.2. An exploded view of the experiment test section is provided in figure B.3. In figure B.4 a photography of the core of the experiment setup is displayed. A photography of the complete experiment setup including peripheral components is displayed in figure B.5.

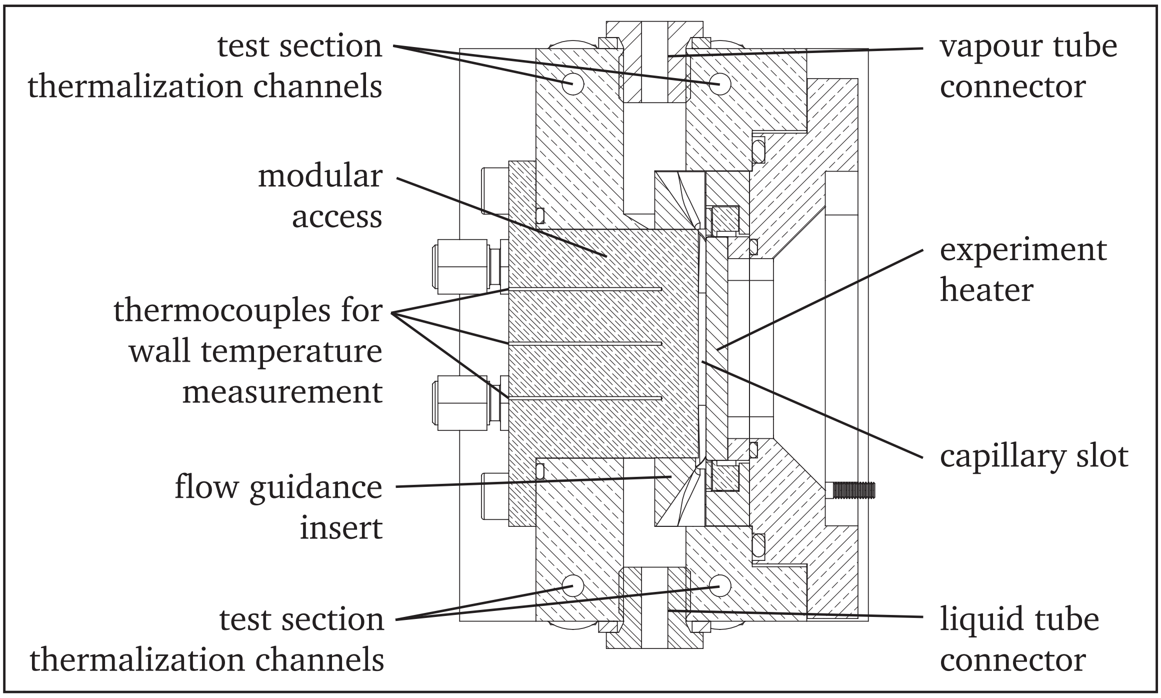

Figure B.2.: Sectional view of the experiment test section

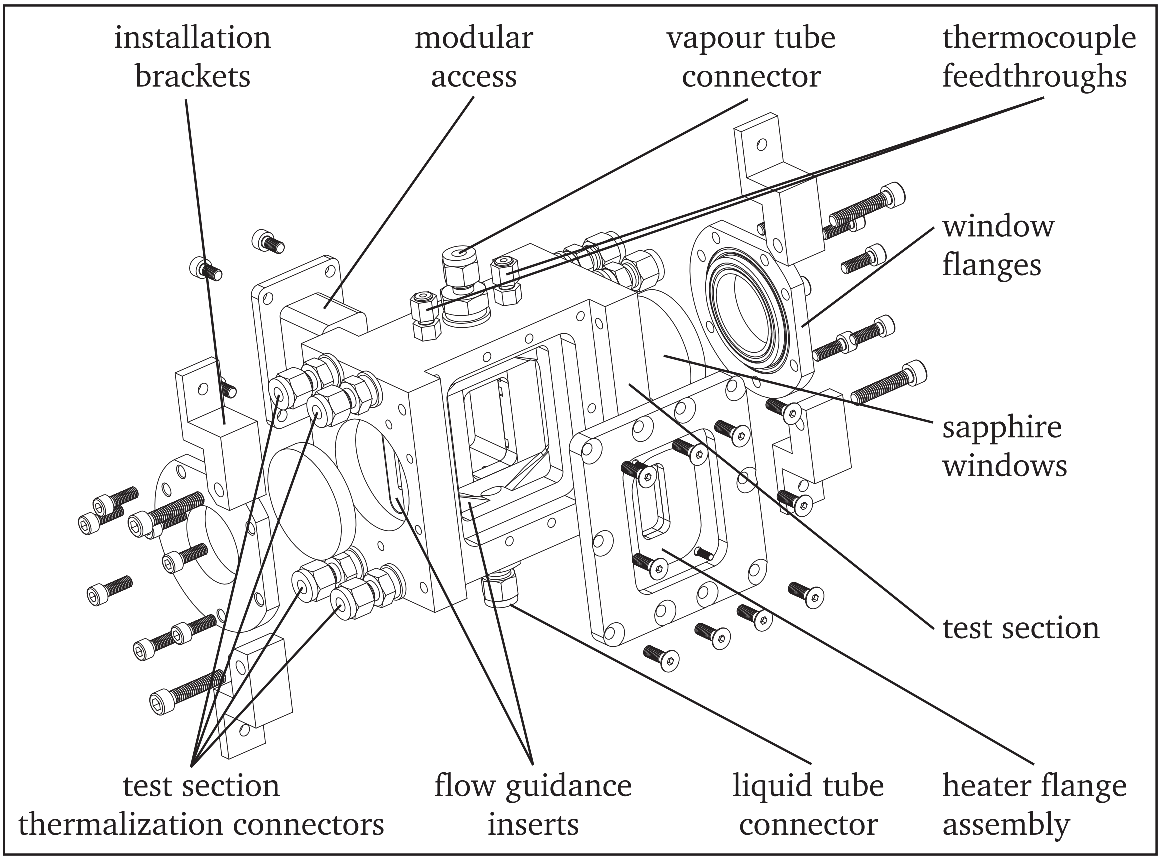

Figure B.3.: Exploded view of the experiment test section

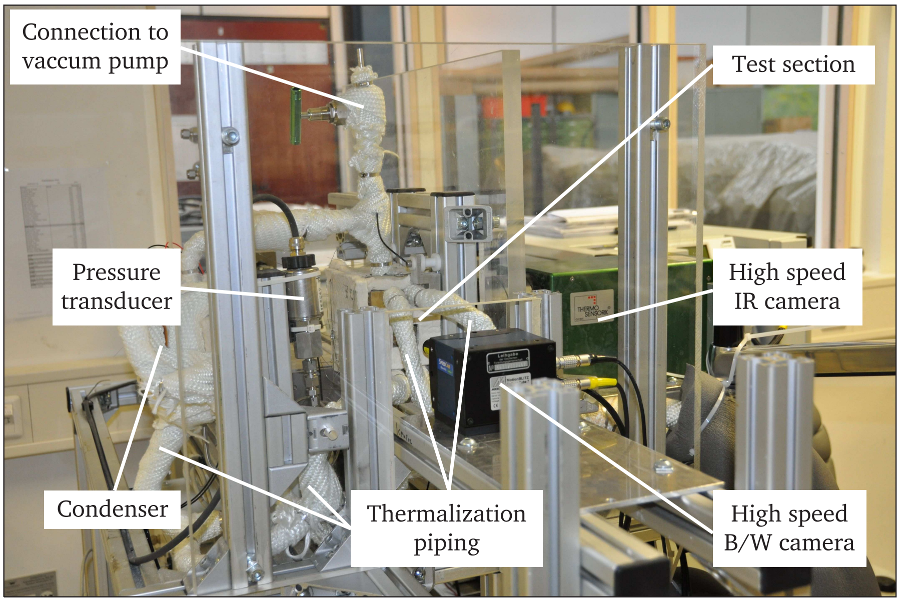

Figure B.4.: Photography of the experiment setup core

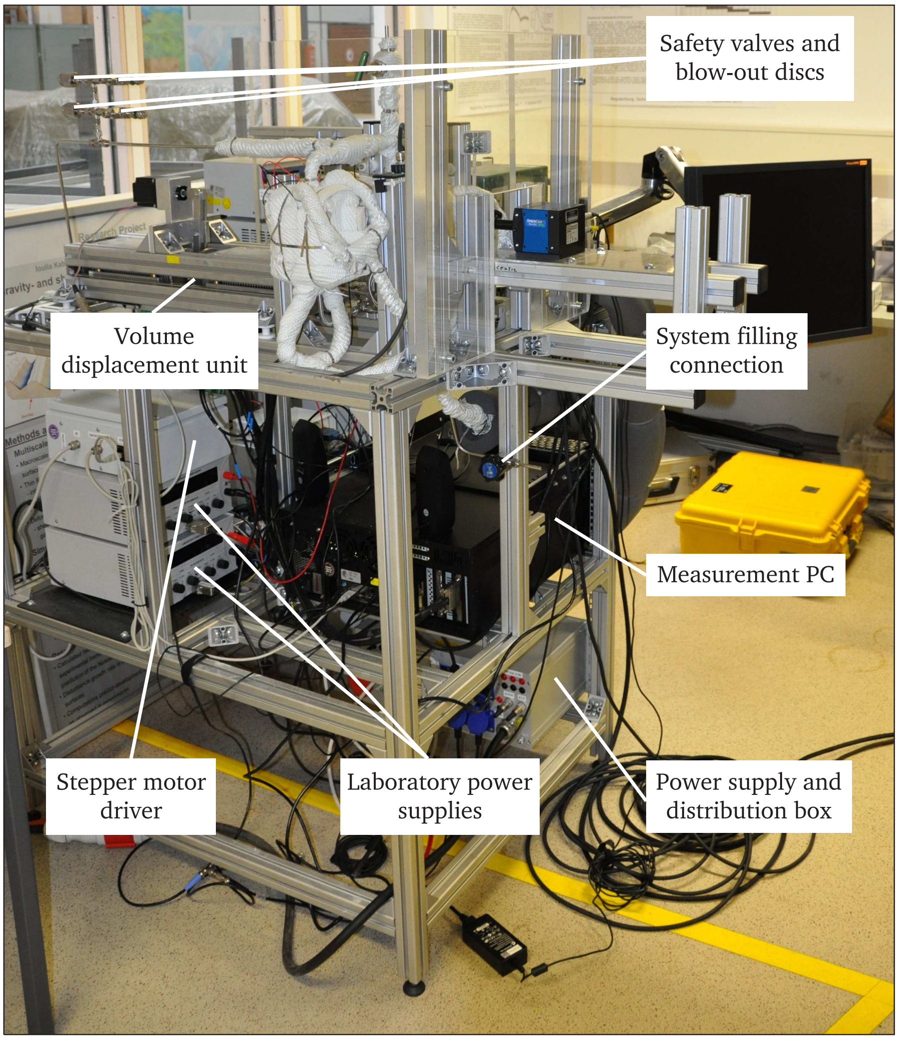

Figure B.5.: Photography of the experiment setup

C Full mass spectra of degassed and not degassed FC-72

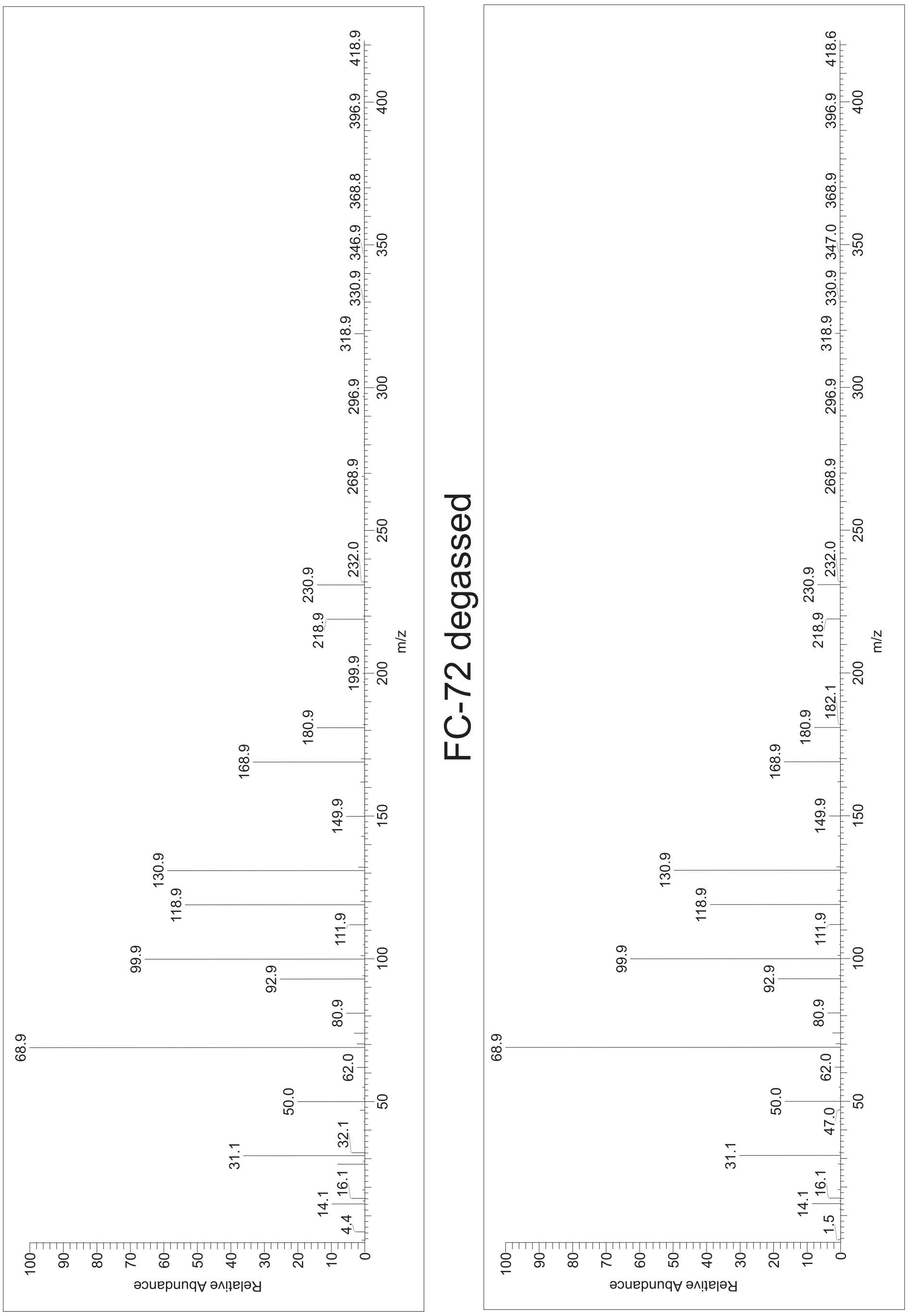

Figure C.1.: Mass spectra from the gas chromatography-mass spectrometry (GC-MS) of a not degassed FC-72 sample (left) and a degassed FC-72 sample (right)

D Other experiments performed by the author using the sputtered heater design

The heater design developed within the frame of this work features some considerable advantages over thin foil heaters (see section 3.2). Slightly altered versions of this heater design (heaters with the same coating composition but different substrate sizes) have therefore been used in two other experimental investigations focussing on the fundamentals of nucleate boiling in a microgravity single bubble experiment and the fundamentals of spray cooling in a single drop impingement experiment, which are shortly outlined below.

D.1 Single bubble cycles under microgravity

This section features some of the results of a single bubble pool boiling experiment conducted under variable gravity conditions, which have been published in [93]. The experiments were conducted during the 1st and 2nd Joint European Partial-g Parabolic Flight Campaign (JEPPF) organized in co-operation by the European Space Agency (ESA), the French space agency Centre National D'Études Spatiales (CNES) and the German space agency Deutsches Zentrum für Luft- und Raumfahrt (DLR). During these two campaigns, the specially equipped A-300 Zero-G aircraft performed parabolic flight profiles to establish stable gravity levels of $a = 0.38\,\mathrm{g}$ (Martian gravity), $a = 0.16\,\mathrm{g}$ (Lunar gravity) and $a = 0\,\mathrm{g}$ (microgravity), with fluctuations less than $\Delta a = \pm 0.05\,\mathrm{g}$. Apart from allowing a parametric study of the influence of gravity onto nucleate boiling, the processes that play a decisive role during an ebullition cycle are considerably slowed down in reduced gravity, due to the reduction of buoyancy forces acting on the bubble. Processes that are too fast or take place on too small scales to be resolved by state-of-the-art measurement techniques under normal gravity, can therefore be resolved in a low gravity environment.

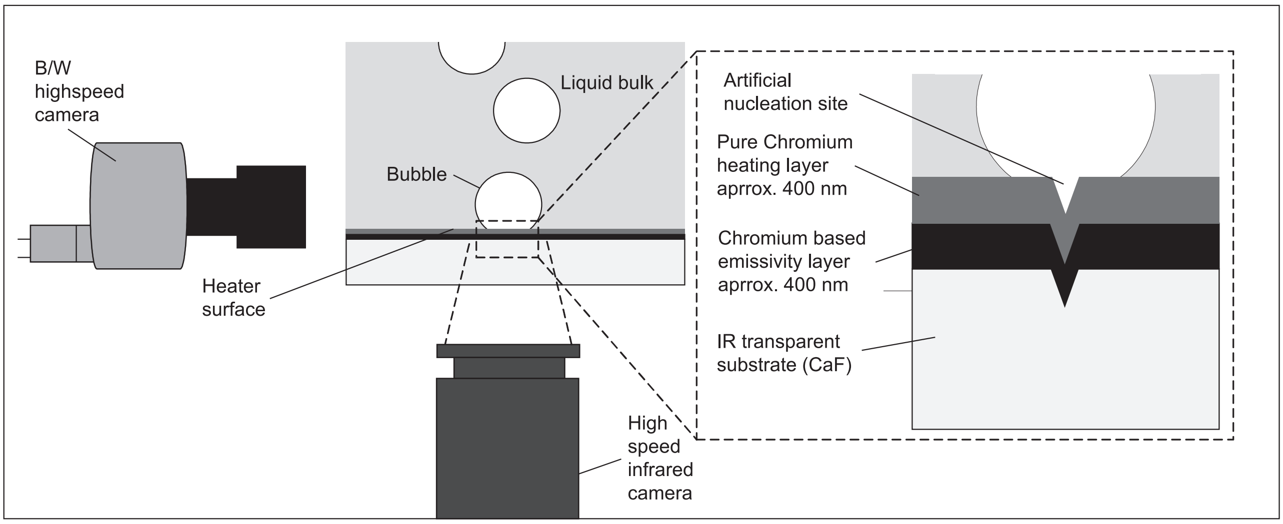

Figure D.1.: Schematics of the experiment on single bubble pool boiling under reduced gravity [93]

In figure D.1 the schematics of the experiment are displayed. The CaF_2 heater substrates with a thickness of 2 mm used in this experiment were equipped with an artificial nucleation site before the two-layer coating composition was applied. The coating-system itself was identical to the one used in the main part of this work. The heater was installed in a dedicated boiling test cell, filled with FC-72/PF-5060 as experiment fluid, which was thremalized by an external water circuit. The experiment fluid was with $t_\mathrm{l} = 39.1\,^\circ\mathrm{C}$ slightly subcooled towards the saturation temperature of $t_\mathrm{sat} = 42.3\,^\circ\mathrm{C}$ at the experiment pressure of $p = 600\,\mathrm{mbar}$.

In figures D.2 and D.3 typical experimental results for a single bubble ebullition cycle are displayed. In the left column the bubble shape acquired with a high speed B/W camera, in the central column the temperature distribution at the heater surface and in the right column the numerically calculated heat flux fields are shown. Figure D.2 features the results during expansion of the bubble foot (corresponding to a receding contact line case), while figure D.3 features the results during contraction of the bubble foot (corresponding to an advancing contact line case).

In between figure D.2 d) and figure D.3 a), no movement of the contact line occurs, as the bubble movement caused by the increasing buoyancy force is counteracted by the still ongoing bubble growth. During the bubble foot expansion phase, the contact line moves across the heater surface at high velocities and removes more energy from the wall material, than can be resupplied through thermal conduction, thus cooling down the wall below the bubble. In the time period in between figures D.2 d) and D.3 a) the wall temperature below the vapour bubble is equalized with the temperature below the liquid bulk through thermal conduction. This leads to an increase of the heat flux transferred at the contact line, as less energy is required by the transient heating up of the wall material below the bubble. The temperature directly below the contact line however stays lower than the average wall temperature, as the on-going contact line evaporation constantly removes energy from the wall. When the contact line movement caused by buoyancy gains dominance over the contact line movement induced by bubble growth, an advancing contact line case is the result (see figure D.3). During this phase, the heat flux transferred at the contact line gradually increases, as additional energy is required to re-establish the thermal boundary layer disturbed by the bubble.

The fact that the heat flux is neither constant at a stationary contact line, nor at a receding contact line, shows, that when investigating highly dynamical systems like growing vapour bubbles, one must take the thermal response of the solid into account. If contact line movement is too fast, the contact line leaves a cold trail behind, as the time-scale of energy removal through near contact line heat transfer can be much smaller than the time-scale on which energy can be transferred through instationary thermal conduction in the solid.

A more in-detail description of the experiment is given in [93].

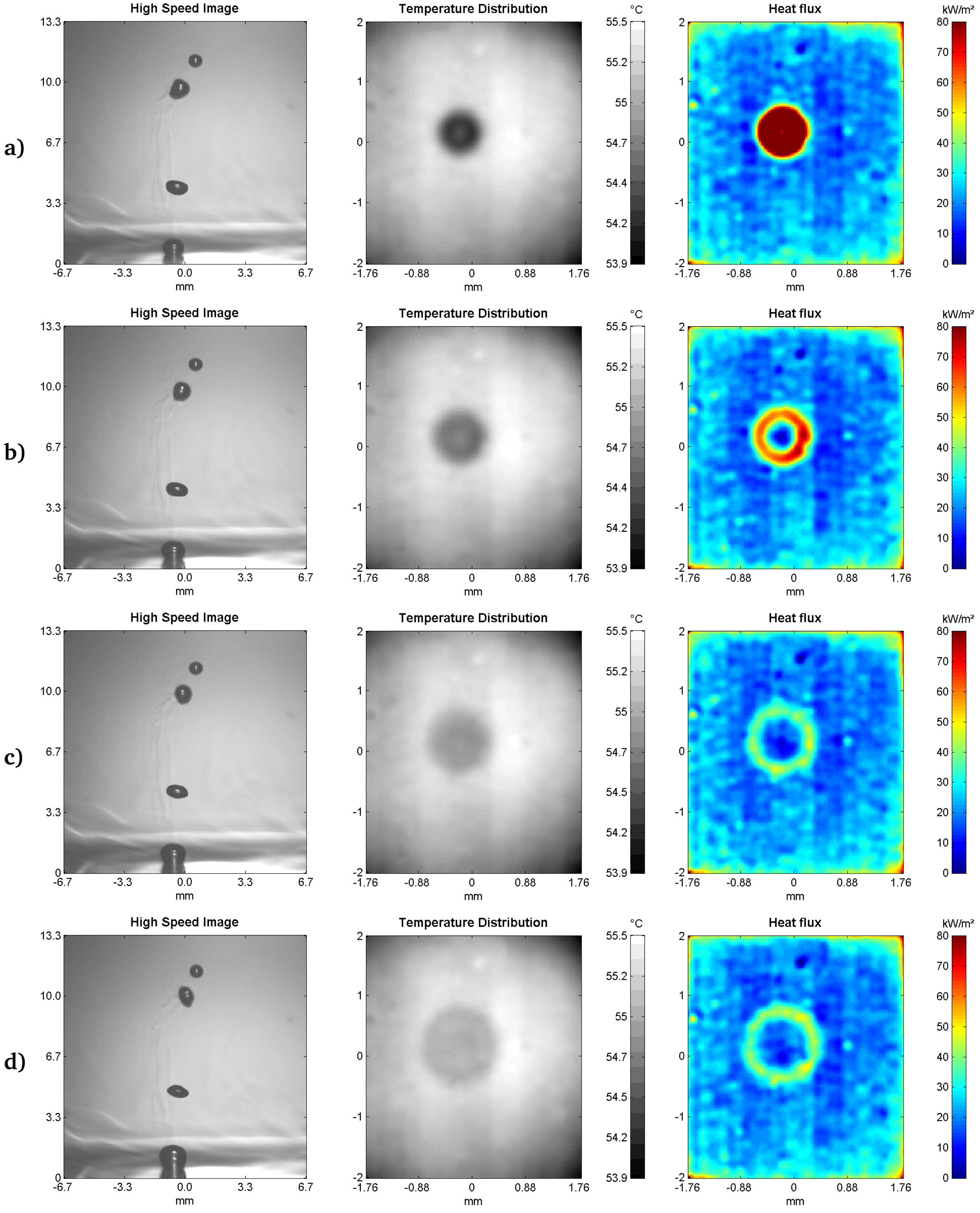

Figure D.2.: Black and white image (left), temperature (centre) and heat flux distribution (right) at a single bubble with expansion of the bubble foot at τ = 1 ms (a), τ = 2 ms (b), τ = 3 ms (c) and τ = 5 ms (d) after nucleation of the bubble under lunar gravity (0.16 g) [93]

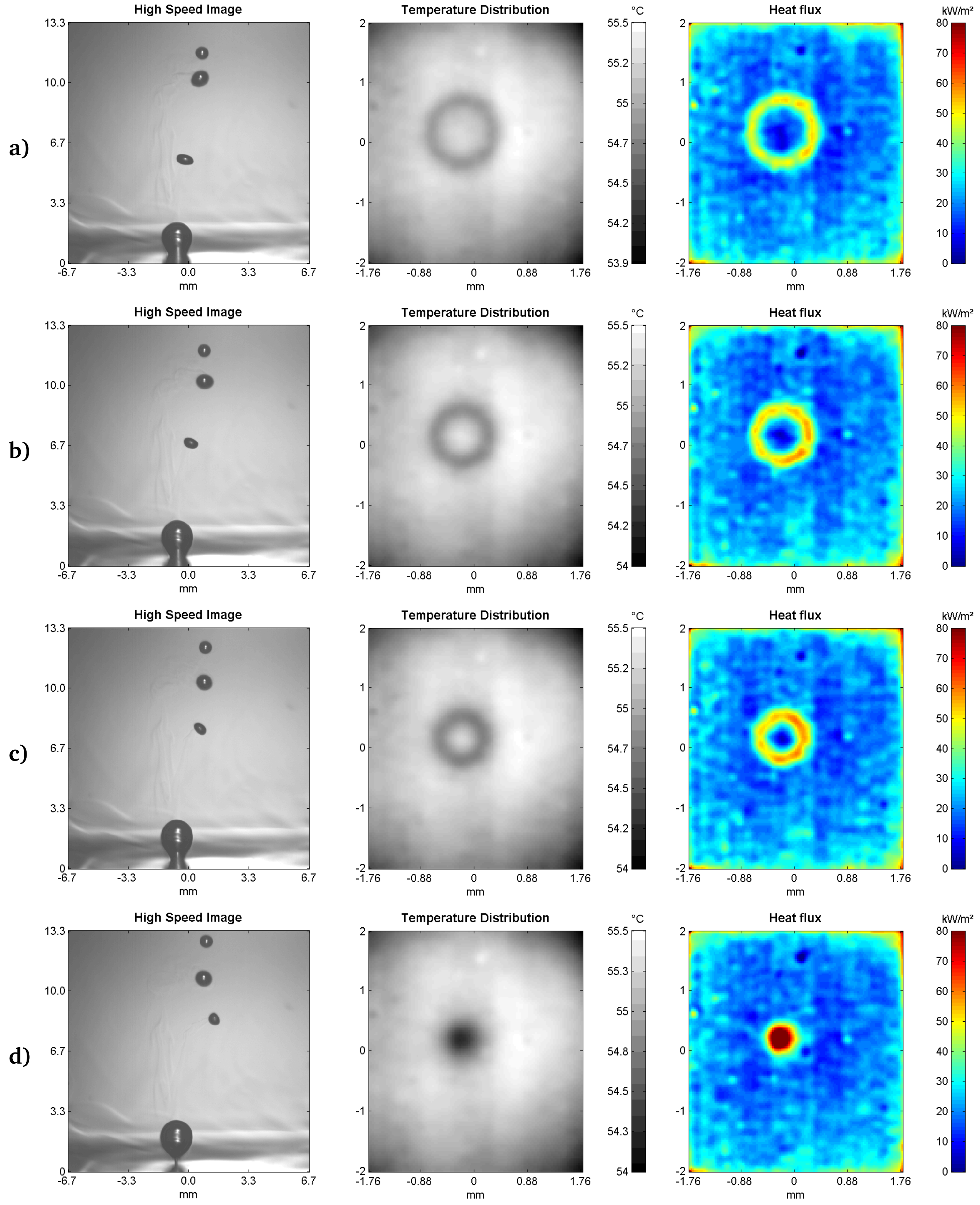

Figure D.3.: Black and white image (left), temperature (centre) and heat flux distribution (right) at a single bubble with contraction of the bubble foot at τ = 12 ms (a), τ = 19 ms (b), τ = 26 ms (c) and τ = 34 ms (d) after nucleation of the bubble under lunar gravity (0.16 g) [93]

D.2 Single drop impingement

This section features results of single drop impingement experiments, that have been published in [94]. In figure D.4, the schematics of the experiment are depicted. Core of the experiment is the sputtered heater design, as introduced in section 3.2. While the coating system is unaltered to the one used in the single capillary slot experiment, a smaller heater thickness of 2 mm was employed to save computational time of the heat flux calculation procedure. The heater is installed in a dedicated brass test cell, which is equipped with an external water thermalization circuit flowing through the test cell walls.

In a first step the test cell was filled with the experiment fluid FC-72 and the wall temperature of the test cell is adjusted to temperatures slightly above its saturation temperature at ambient pressure ($p = 1\,\mathrm{bar}$) of $t_{\mathrm{sat}} = 56.6\,°\mathrm{C}$. Due to the onset of nucleate boiling at the test cell walls, the test cell fills with an air/vapour mixture. By removing the atmosphere within the test cell using a vacuum pump the vapour content inside the test cell is constantly increased. Fluid lost by removal of the mixture inside the cell is added from a reservoir, until the temperature measured at eight locations inside the gaseous phase of the test cell matches the saturation temperature of the fluid and the boiling process stops. At non-heated regions at the test cell bottom a small pool of liquid remains at a constant volume, indicating thermodynamic equilibrium between liquid and vapour phase.

With the help of a pressure equalization membrane the pressure inside the test cell is kept constant at ambient pressure. A syringe is placed above the heater, which is unheated and therefore slightly subcooled towards the saturation temperature of the fluid. Vapour re-condenses at the syringe and accumulates at the syringe tip, until the gravity forces of the forming droplet overcome the surface tension forces and it detaches from the syringe. This method of droplet generation results in highly reproducible droplet diameters of $d_{\mathrm{D}} = 0.965\,\mathrm{mm}$ ... $1.008\,\mathrm{mm}$. Droplet impact velocity can be varied in the range of $v_{\mathrm{D}} = 0.27\,\mathrm{mm\,s^{-1}}$ ... $0.58\,\mathrm{mm\,s^{-1}}$ by changing the height of the syringe.

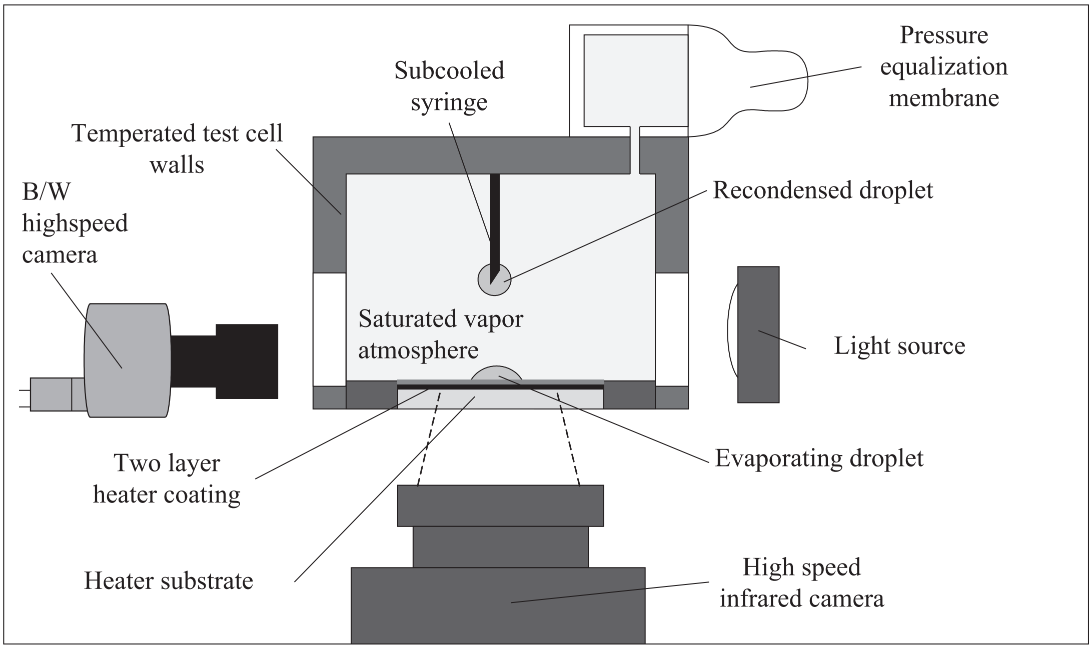

Figure D.4.: Schematics of the experiment on single drop impingement [94]

In figures D.5 and D.6 a typical drop impact event with a droplet Reynolds number of $\mathrm{Re_D} = 2040$ and a droplet Weber number of $\mathrm{We_D} = 65$ is shown between $\tau = 1\,\mathrm{ms}$ (figure D.5 a)) after impact until a sessile state is reached at $\tau = 39\,\mathrm{ms}$ (figure D.6 d)). In the left column the droplet shape acquired with a high speed B/W camera, in the central column the temperature distribution at the heater surface and in the right column the numerically calculated heat flux fields are shown. Directly after impact, a high heat flux is reached on the whole wetted area of the heater, which indicates the dominance of single phase convective heat transfer from the superheated wall to the droplet.

Already 4 ms after impact a distinctive heat flux maximum develops at the outer rim of the droplet, close to the three-phase contact line (see figure D.5 b)), which indicates the increasing importance of contact line heat transfer. Like in the boiling experiment described in section D.1, the heat flux peak at the rim of the droplet is accompanied by a local temperature minimum, as energy is constantly removed from the solid through on-going contact line evaporation. In the centre of the droplet a second high heat flux plateau arises, which slowly decays over time, as liquid from the rim of the droplet flows back inward and the spreading radius decreases (see figure D.5 c) - d)). Though thin film evaporation could be responsible for this high heat flux plateau in the centre of the droplet, one should keep in mind, that the liquid flowing across the surface in this region originates from regions of the droplet, that are by far colder than the wall and can therefore also be caused by transient heat transfer to the liquid.

During contraction of the droplet (figure D.5 d) - figure D.6 d)) the overall heat flow transferred to the droplet gradually decreases. The ratio of contact line heat transfer to total heat transfer on the other hand constantly increases, until contact line evaporation is clearly the dominant heat transfer mode at the sessile droplet.

A more in-detail description of the experiment is given in [94].

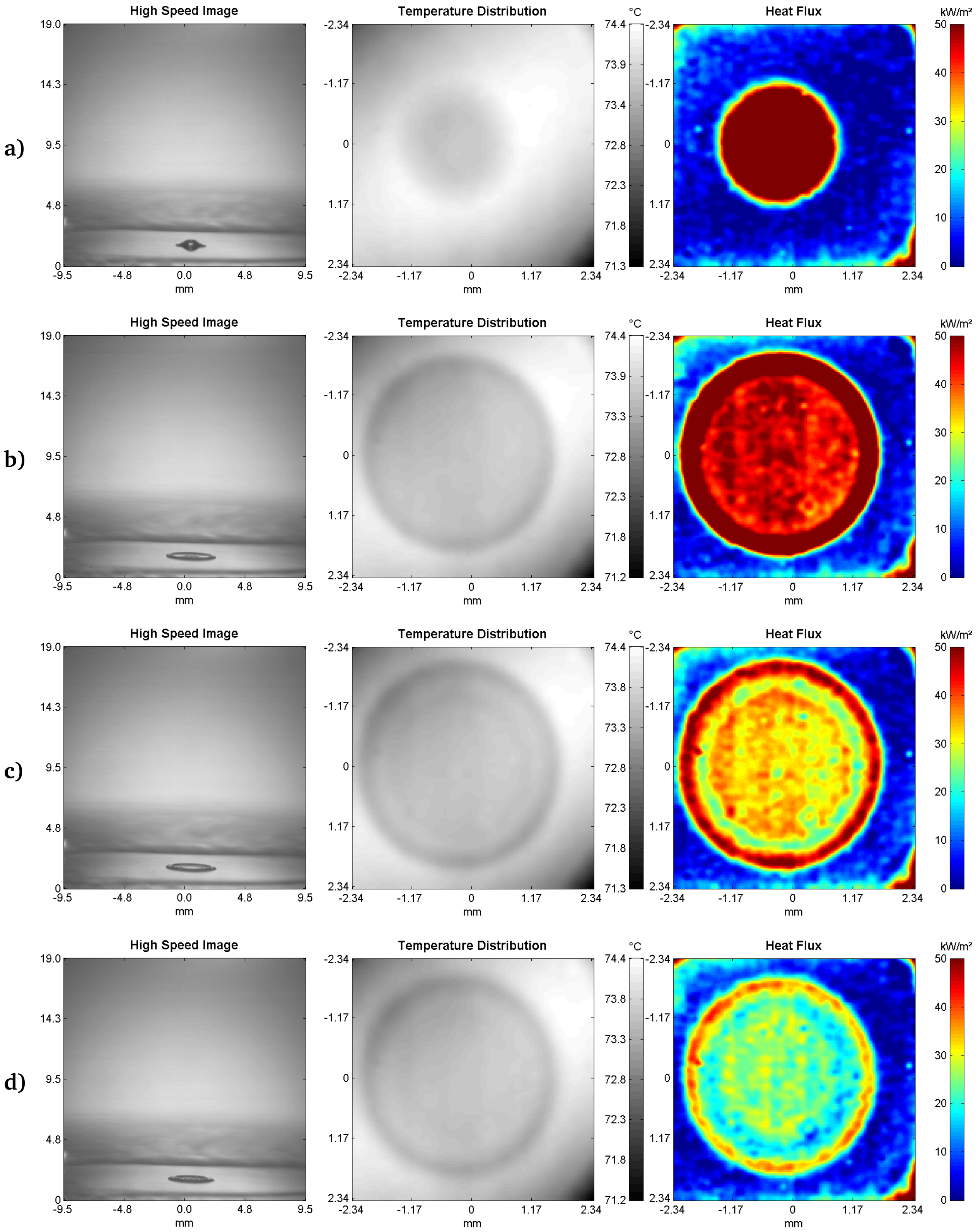

Figure D.5.: Black and white image (left), temperature (centre) and heat flux distribution (right) during single drop impingement at τ = 1 ms (a), τ = 4 ms (b), τ = 7 ms (c) and τ = 10 ms (d) after impact [94]

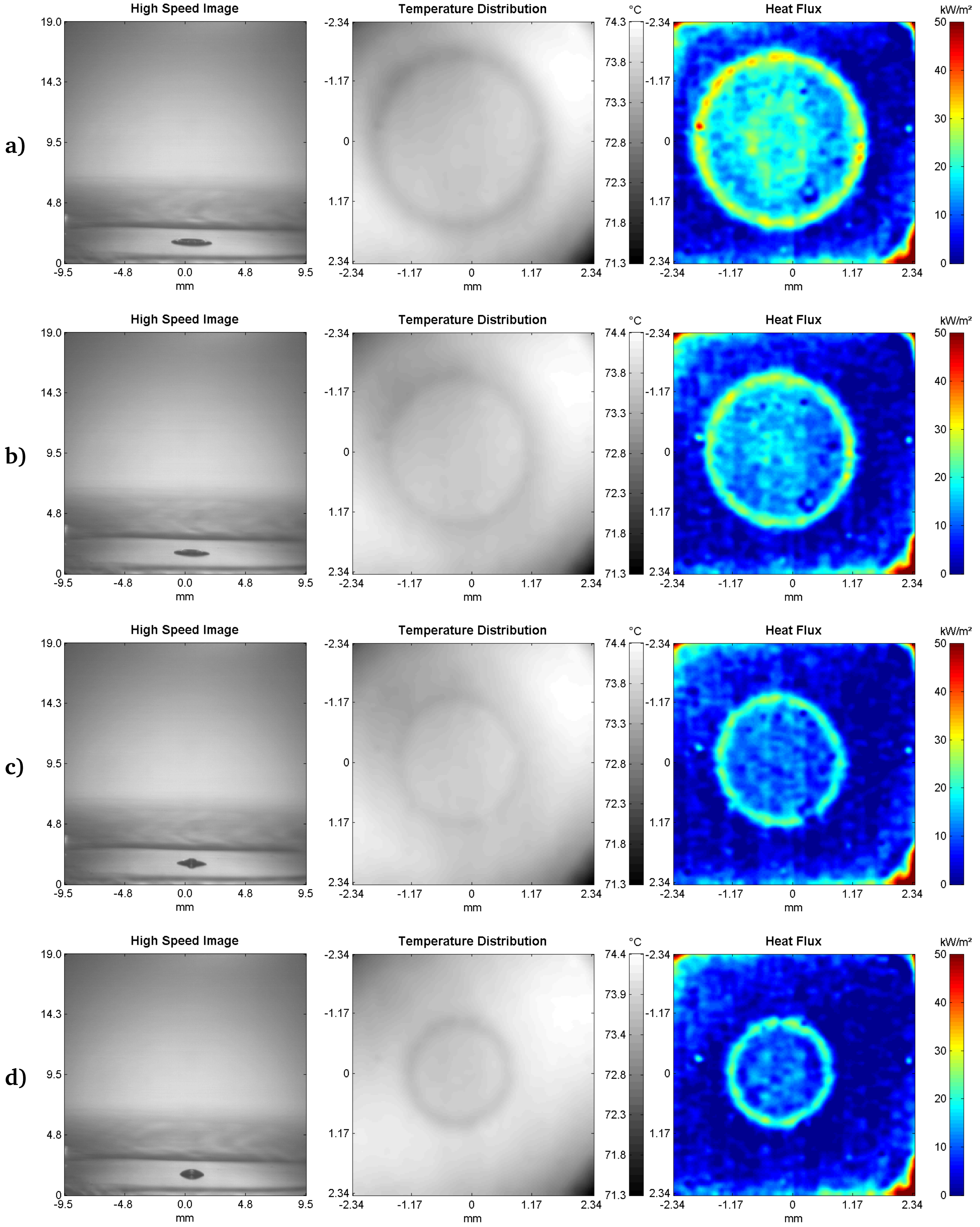

Figure D.6.: Black and white image (left), temperature (centre) and heat flux distribution (right) during single drop impingement at τ = 13 ms (a), τ = 16 ms (b), τ = 19 ms (c) and τ = 39 ms (d) after impact [94]

Curriculum vitae

Personal information

Name	Sebastian Fischer
Date of birth	December 1st, 1983
Place of birth	Wiesbaden, Germany
Marital status	unmarried

Professional career

since 04/2010	Research and teaching assistant at the Institute of Technical Thermodynamics of Technische Universität Darmstadt, with focus of research on experimental investigation of contact line evaporation phenomena
05/2009 - 11/2009	Preparation of diploma thesis at EADS Astrium Space Transportation GmbH, topic of thesis: Coordination and Performance of Breadboarding Programme for the Fluid-Physics Experiment EC Rubi to be executed on the International Space Station ISS

Studies of Mechanical Engineering

10/2004 - 11/2009	Studies of mechanical engineering at Technische Universität Darmstadt (emphasis on thermodynamics, fluid mechanics and aeronautic engineering)

Military service

10/2003 - 03/2004	Served in the flight safety group of Jagdbombergeschwader 33 of the German Luftwaffe at Büchel, Germany
07/2003 - 09/2003	German Luftwaffe basic training in the Luftwaffenausbildungsregiment 1 at Budel, Netherlands

Education

08/1994 - 07/2003	Secondary school (Gymnasium am Mosbacher Berg, Wiesbaden)
08/1990 - 08/1994	Elementary school (Grundschule Wiesbaden Breckenheim)

List of publications

1. S. Fischer, St. Herbert, A. Sielaff, E. M. Slomski, P. Stephan, and M. Oechsner. Experimental Investigation of Nucleate Boiling on a Thermal Capacitive Heater Under Variable Gravity Conditions. *Microgravity Science and Technology*, 24(3):139−146, 2012.
2. S. Fischer, E. M. Slomski, P. Stephan, and M. Oechsner. Enhancement of nucleate boiling heat transfer by micro-structured chromium nitride surfaces. *Journal of Physics: Conference Series*, 395:012128, 2012.
3. S. Fischer, S. Herbert, E. M. Slomski, P. Stephan, and M. Oechsner. Local Heat Flux Investigation During Pool Boiling Single Bubble Cycles Under Reduced Gravity. *Heat Transfer Engineering*, 35(5):482−491, 2014, also published in *Procedings of the 8th International Conference on Boiling and Condensation Heat Transfer*, 2012.
4. P. Stephan, A. Sielaff, S. Fischer, J. Dietl, and S. Herbert. A contribution to the basic understanding of nucleate boiling phenomena: generic experimental and numerical simulations. In *Proceedings of the 3rd International Forum on Heat Transfer*, 2012.
5. E. M. Slomski, S. Fischer, H. Scheerer, M. Oechsner, and P. Stephan. Textured CrN thin coatings enhancing heat transfer in nucleate boiling processes. *Surface and Coatings Technology*, 215:465−471, 2013.
6. S. Herbert, S. Fischer, T. Gambaryan-Roisman, and P. Stephan. Local heat transfer and phase change phenomena during single drop impingement on a hot surface. *International Journal of Heat and Mass Transfer*, 61:605−614, 2013.
7. S. Fischer, S. Herbert, T. Gambaryan-Roisman, and P. Stephan. Local heat flux investigation during single drop impingement onto a heated wall. In *Proceedings of the 25th European Conference on Liquid Atomization and Spray Systems (ILASS-Europe 2013)*, 2013.
8. S. Fischer, S. Batzdorf, T. Gambaryan-Roisman, and P. Stephan. High Resolution Heat Transfer Measurements at the Three Phase Contact Line of a Moving Single Meniscus. In *Proceedings of the 15th International Heat Transfer Conference*, 2014.